UNIVERSITÀ DEGLI STUDI FIRENZE

DOTTORATO DI RICERCA IN SCIENZE DELLA TERRA

CICLO XXXI

COORDINATORE Prof. Lorella Francalanci

"Behaviour of S-bearing compounds (H₂S and SO₂) emitted in air from natural emissions in hydrothermal-volcanic systems"

Settore Scientifico Disciplinare GEO/08

Dottoranda	**Tutore**
Dott.ssa Chiara Caponi	Prof. Franco Tassi

Co-Tutori
Dr. Lorenzo Fusi

Prof. Andri Stefánsson

Coordinatore
Prof. Lorella Francalanci

Anni 2015/2018

«E quindi uscimmo a riveder le stelle.»
(Dante Alighieri, Divina Commedia
Inferno, Canto XXXIV, 139)

Abstract

The main sources of SO_2 and H_2S in air consist of (i) natural fluid emissions from active/quiescent volcanoes and (ii) anthropogenic activities. These gas compounds have a strong impact on air quality, since they are toxic and climate forcing agents. Notwithstanding, the behaviour of these S-compounds in air is poorly known, since relatively scarce are the available thermodynamic data as well as those deriving from direct measurements. Hydrogen sulphide is the main S-compounds of low-temperature emissions in hydrothermal systems and, in the atmosphere, tends to be oxidized to SO_2 by photochemical reactions. Oxidation processes are also affecting atmospheric SO_2, which is the main S-compounds of high-temperature emissions in volcanic systems, since about 65% is transformed to SO_4^{2-} whilst the remaining 35% is removed by dry deposition. This PhD research project was aimed to provide insights into the chemical-physical processes affecting H_2S and SO_2 in plumes discharged from hydrothermal fluid emissions which control the spatial distribution of these gases in air. The empirical approach carried out in Iceland, where a number of hydrothermal emissions related to different volcanic/geothermal systems occurs, followed a measurement strategy optimized during two first field campaign at Vulcano Island (Aeolian Archipelago) and at La Solfatara (Phlegrean Fields). Hydrogen sulphide and SO_2 measurements in air were performed using a Thermo Scientific 450i Analyzer positioned at increasing distance along patterns downwind from the emission sources, in order to obtain a "snapshot" of the H_2S and SO_2 concentrations within the plume. A mathematical model of the spatial distribution of the two air pollutants, coupled with a statistical elaboration of the measured data, was applied to the measured data to i) describe the evolution of H_2S and SO_2 within the plume with distance observed in the field,

ii) determine the rate of loss of H_2S and SO_2 at increasing distances from the source, and iii) discriminate the effects of physical (i.e. dilution) and chemical (e.g., oxidation of H_2S to SO_2) mechanisms controlling the spatial and temporal dispersion of the S-bearing gases. The results show that dilution by air affect both H_2S and SO_2 at a lower extent with respect to the chemical degradation processes. Simulations carried out using the mathematical model show that, at distances >100 meters from the emitting source, the H_2S and SO_2 concentrations were below (<5 ppb by vol.) those of the guidelines of WHO (World Health Organization). Remarkably, the reaction rates of oxidation processes (i.e. homogeneous gas-phase reactions via OH radical) in air for both H_2S and SO_2 calculated by the model are faster than those suggested in literature. This implies that the H_2S and SO_2 removal mechanism from the plume mostly consist of heterogenous and multiphase reactions that, on their turn, depends on different variables, e.g., presence of water droplets and plume temperature. Different SO_2/H_2S ratios were measured at each geothermal system, as well as at the same system in the proximity of different gas emissions, suggesting that these SO_2/H_2S variations were not related to the deep magmatic source, but, more likely, to secondary shallow processes.

Contents

iv

Chapter 1

Introduction

Sulphur occurs in Earth's atmosphere as a variety of compounds (e.g., SO_2, H_2S, DMS, OCS) either in gaseous or aerosol forms, emitted from both natural and anthropogenic sources. The latter give the higher contribution, forming 70% of all sulphur emissions (60-100 Mt(S) yr^{-1}), while the remainder is released from oceanic plankton (13-36 Mt(S) yr^{-1}), volcanoes (6-20 Mt(S) yr^{-1}), biomass burning (1-6 Mt(S) yr^{-1}) and land biota and soils (0.4-5.6 Mt(S) yr^{-1}) (Penner et al., 2001). The anthropogenic fraction is much higher on a regional scale, particularly over NE America, Europe and SE Asia (Stevenson et al., 2003). Anthropogenic sulphur is almost exclusively emitted as sulphur dioxide (SO_2) and is associated with fossil fuel and industrial activity (Benkovitz et al., 1996), while hydrogen sulphide (H_2S) is mainly natural (about 90% of the total H_2S in the atmosphere; US Environmental Protection Agency, EPA, 1993), although it can be also derived from the production of coking coal, cellulose, fertilizers, refinement of crude petroleum, tanning of skins and treatment of waste water (Bates et al., 1992; Kourtidis et al., 2004, 2008; Colomer et al., 2012). Sulfur dioxide and H_2S are the main sulphur gases emitted from volcanic activity, although traces of other sulphur gases can also be released (e.g., COS and CS_2). Sulfur dioxide (SO_2) is the main high-temperature volcanic gas (>400 °C) at atmospheric pressure. Within hydrothermal systems, "magmatic" SO_2 reacted during the fluid ascent to surface, producing sulphuric acid (H_2SO_4) and H_2S (Giggenbach, 1996); the latter is, consequently, the dominant S-bearing gas compound in low-temperature emissions (<100 °C) and in water dominated geothermal systems (<350 °C). Neverthless, the main source of S in most volcanic geothermal systems is suggested to be related to dissolution of sulfur (Mizutani and Sugiura, 1966; Giggenbach, 1987; Chiodini et al.,

1993; Marini et al., 2011; Stefánsson et al., 2015; Gunnarsson-Robin et al., 2017) instead of direct degassing of melt. This could explain the absence of SO_2 in most <350 °C volcanic geothermal systems and low SO_4 in the reservoir fluids, which, on the contrary, increases as soon as there is "magmatic" SO_2 input from cooling melt. Gases emitted during large eruptions (e.g., Pinatubo, Philippines) can be carried tens of kilometres up into the upper atmosphere and cause strong effects on climate, atmospheric and terrestrial environment, from local to global scale and over a period of few years up to 1 Myr (Oppenheimer et al., 2003a). Large amounts of gases can also be released during quiescent (non-eruptive) periods through visible (i.e. fumaroles, solfataras and plumes) and non-visible (i.e. diffuse soil degassing) emanations. The contribution from this type of emissions can be substantial, as they can persist for prolonged periods of time: from years to decades and centuries (Chiodini et al., 1994, 2000, 2005; Hansell and Oppenheimer, 2004). After H_2O and CO_2, SO_2 and H_2S are the most prevalent gas species emitted from active volcanic- and geothermal systems, respectively, and their atmospheric concentrations in these areas represent a significant hazard to human health (Sigurdsson et al., 2015). Both SO_2 and H_2S caused many fatalities in volcanic areas worldwide, although CO_2 has been responsible for the great majority of casualties (e.g., Hansell and Oppenheimer, 2004; McDougall and Garland, 1954; Witham, 2005; Cook and Weinstein, 2011; Williams-Jones and Reimer, 2015). Using an empirical approach, this study aims to investigate the behaviour of H_2S and SO_2 once they are released into the atmosphere from the main hydrothermal fluid discharges of Iceland, i.e. fumaroles, boiling and mud pools. Iceland represents a perfect location for S-measurements, since geothermal activity is widely spread throughout the country and H_2S concentration in air is of great concern for health and environmental hazards (WHO, 2000). The H_2S and SO_2 measurements strategy has been firstly developed and defined at Vulcano Island and La Solfatara crater (Italy), the data of which will be discuss here for comparison and ascertaining the potential hazards in these locations, being the sites of tourist attractions for thousands of people and densely inhabited, respectively. In Iceland, air measurements of H_2S and SO_2 were carried out using a Thermo Scientific 450i Analyzer positioned at 4-6 fixed points at increasing distance

and downwind from the emission sources, under different weather conditions. Due to its high-sensitivity, the device allows the detection of SO$_2$ and H$_2$S at very low concentrations (down to 2 ppb), other than real-time and high-frequency measurements. Volatile Organic Compounds (VOCs) were also measured using solid traps equipped with portable pumps. The methods are accurately described in Chapter 4. Thanks to the collaboration with the Department of Mathematics "U. Dini" (University of Florence), a mathematical model, developed by using a simple mass balance equation and by the fitting with the experimental data (Chapter 6), was also applied to i) determine the rate of loss of H$_2$S and SO$_2$ at increasing distances from the source, and ii) discriminate the effects of physical (i.e. dilution) and chemical (e.g., oxidation of H$_2$S to SO$_2$) processes controlling the spatial and temporal dispersion of the S-bearing gases. While the model is of great importance to predict quantitatively the environmental impact of hydrothermal gas plumes, the measured data, obtained in the field surveys, represent an exclusive dataset of H$_2$S and SO$_2$ concentrations in air within Icelandic geothermal areas.

1.1 H$_2$S and SO$_2$ air measurements: previous works

As mentioned above, hydrogen sulphide is mainly natural and it is emitted from geothermal areas in relative high amounts during quiescent periods, while SO$_2$ is a typical magmatic gas released during volcanic activity. Hydrogen sulphide, as well as SO$_2$, is emitted into the air as a mixture of gas and particles, which forms "volcanic plumes", rising and moving depending on the wind. Because of its potentially hazardous effects on human health and the surrounding environment (Webster, 1995; WHO, 2000, 2003; Bates et al., 2002), H$_2$S in the air, water, soils and vegetation is sufficient to be of environmental concern for areas that host geothermal fields. On the other hand, SO$_2$ is mainly studied in urban areas for air quality regulations and in volcanic systems for volcanic monitoring (SO$_2$/H$_2$S ratio): volcanic activity at quiescent volcanoes can be preceded or accompanied by an increase of SO$_2$ relative to hydrothermal H$_2$S (e.g., Aiuppa et al., 2006). While eruptive stratospheric volcanic plumes and their atmospheric impacts have extensively been studied (e.g., Robock, 2000; Robock and Oppenheimer, 2003),

the impacts of tropospheric emissions from quiescent volcanoes are by far less characterised. However, it is becoming clear that, on local to regional environmental/health impacts in a long-term period, weaker and continuous emissions can have the same importance of large and short-lived volcanic eruptions (e.g., Delmelle, 2003; Mather et al., 2003a). As a consequence, studies and research projects on gas dispersion in geothermal areas, carried out mainly by energy companies, have increased from the 1930s, stimulated by stricter environmental control regulations. In recent years, air dispersion studies have taken place at numerous locations to calculate the dispersal of air pollutants through "air dispersion models" based on Gaussian modelling of a continuous, buoyant plume of air. These mathematical models allow the prediction of H_2S concentrations in the atmosphere from the emitting sources, the risks of exposure and impacts on human health and the environment (e.g., in the Imperial Valley in California, Gudiksen, 1979; in Cerro Prieto in Mexico, Gallegos-Ortega et al., 2000; in Rotorua, New Zealand, Horwell et al., 2004; and in Iceland: at Svartsengi, Kollikho, 1998; at Nesjavellir, Gíslason, 2000; at Nesjavellir, Nyagah, 2006 and at Hellisheidi power-plant, Ólafsdóttir, 2007). However, these models are essentially "physical models", as they do not take into account paths and rates of chemical reactions in tropospheric volcanic plumes, which can be a matter of particular interest for highly reactive acidic gaseous volatile species such as SO_2 and H_2S (Symonds et al., 1994). While other species (e.g., CO_2) are considered relatively inert during atmospheric dilution, these reactive species, once emitted from the vent, are cooled and mixed with the atmosphere (characterized by different temperatures, humidity and aerosol content; Gerlach, 2004) and can be involved in different types of reactions i.e. gas-only and gas-liquid-solid. However, the behaviour of SO_2 and H_2S in air is poorly known, since relatively scarce are the available thermodynamic data as well as those deriving from direct measurements. When hydrogen sulphide is discharged into the atmosphere, it can partially be dissolved into surface waters, absorbed into soils (Cihacek and Bremner, 1993) and plant foliage (De Kok et al., 1988), or it can precipitate as elemental sulphur (Cihacek and Bremner, 1993) and oxidized in air into other sulphur compounds, e.g., SO_2 (Davis et al., 1979). The latter has been the matter of considerable debates, as scarce is the knowledge about the fate and the conversion of geothermally-sourced

H$_2$S into SO$_2$ in the atmosphere. Cox and Sandalls (1974) suggested that photo-oxidation of H$_2$S to SO$_2$ is the major loss process for H$_2$S in the atmosphere, whereas other authors (Brown and Webster, 1994; Kristmannsdóttir et al., 1999) claimed that this mechanism is relatively slow and only a small fraction of H$_2$S is oxidized in air. In a dry and sunny climate, a great amount of H$_2$S can be oxidized to SO$_2$, whereas under dark, dry and relatively cold conditions the efficiency of the conversion seems to decrease significantly (Spedding and Cope, 1984). On the other hand, oxidation processes also affect SO$_2$. About 65% of SO$_2$ is indeed transformed to SO$_4{}^{2-}$ whilst the remaining 35% is removed by dry deposition (Yu et al., 2017). If the oxidation of H$_2$S to SO$_2$ is as fast as suggested and if H$_2$S from geothermal power plants and hydrothermal areas is efficiently converted to SO$_2$, important consequences on local pollution (e.g., for plants protection), volcanic monitoring (e.g., presence of SO$_2$ not just related to volcanic activity) and also global pollution (e.g., emission of SO$_2$ into the atmosphere) are to be considered. In this respect, the question of the possible conversion or rate of conversion of H$_2$S to SO$_2$ is of major concern. Processes affecting SO$_2$ and H$_2$S in air are described in detail in Chapter 2.

Chapter 2

S-bearing compounds: H_2S and SO_2

2.1 Chemical processes involving H_2S and SO_2 in air

Sulfur compounds exist in both reduced and oxidized states, with oxidation numbers from -2 (H_2S) to +6 (H_2SO_4), the latter being the most stable form in the presence of O_2. Most sulfur species are released to the atmosphere primarily in a chemically reduced state and then, generally oxidized to +4 oxidation state (SO_2) (Fig. 2.1). Approximately 65% of sulfur dioxide is later converted to SO_4^{2-}, whereas the remaining 35% is removed as dry deposition. The higher the oxidation state of sulfur the greater the affinity to water, favoring its removal from the atmosphere by wet deposition (Wallace and Hobbs, 2006).

The most important sulfur gases in the atmosphere are SO_2, H_2S, dimethyl-sulfide (DMS), carbonyl sulfide (COS) and carbon disulfide (CS_2). Most sulfur compounds have a short residence time in the troposphere (few days), with the exception of COS, which is more stable (two-year residence time) (Wallace and Hobbs, 2006).

The oxidation processes of atmospheric SO_2 are relatively well-known (e.g., Davis et al., 1979; McKeen and Liu, 1984), whereas little is known those affecting the reduced sulfur forms, e.g., H_2S, DMS.
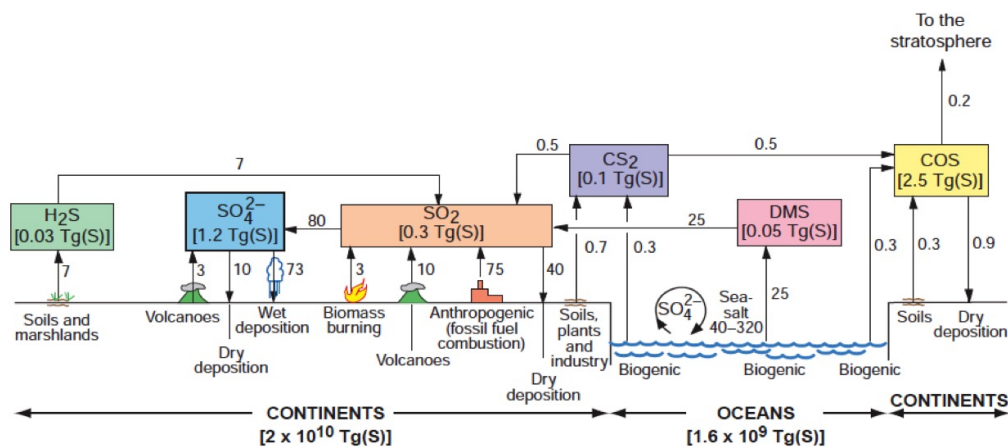
FIGURE 2.1: *Principal sources and sinks of sulfur-containing gases in the troposphere. Fluxes are in Tg(S) per year. The global sulfur budget is significantly affected by human activities (78 Tg(S)). For clarity, wet and dry removal are shown only over the continents, although they also occur over the oceans (from Hobbs, 2000).*

2.1.1   Hydrogen sulfide oxidation processes

Reduced sulfur compounds are relatively low soluble in water compared to the oxidized species and, for this reason, the oxidation in cloud droplets is probably not significant. The main process affecting both DMS and hydrogen sulfide in the atmosphere is likely the photochemical oxidation to SO$_2$ (e.g., Cox and Sandalls, 1974; Wallace and Hobbs, 2006). A direct photo-oxidation of H$_2$S and DMS is unlikely to occur in the lower atmosphere since none of such gases absorb the UV radiation at wavelength greater than 260 nm (Cox and Sandalls, 1974). Oxidation of H$_2$S involving O$_3$ and O$_2$ is possible, but it is too slow under atmospheric conditions to be significant (Frenklach et al., 1981). Cox and Sandalls (1974) suggested the importance of OH radicals in the photo-oxidation of H$_2$S, which is likely proceeding in the daylight, as follows (Norrish and Zeelenberg , 1957; Stuhl, 1974; Perry et al., 1976; Graedel, 1977a):
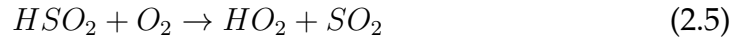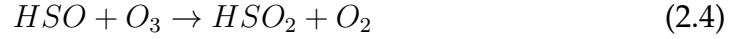
$$OH + H_2S \rightarrow H_2O + HS \tag{2.1}$$

HS then reacts with O$_3$ or NO$_2$ to form HSO (Graedel, 1977b; Leu and Smith, 1982):

$$HS + O_3 \rightarrow HSO + O_2 \tag{2.2}$$

$$HS + NO_2 \rightarrow HSO + NO \tag{2.3}$$

HSO is then converted to SO₂:

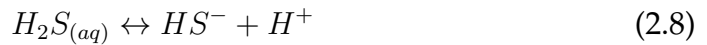$$HSO + O_3 \rightarrow HSO_2 + O_2 \tag{2.4}$$

$$HSO_2 + O_2 \rightarrow HO_2 + SO_2 \tag{2.5}$$

Laboratory experiments conducted by Cox and Sandalls (1974) showed that, with low-intensity light source, no detectable oxidation of H₂S was observed after 1 h of irradiation, either alone or in the presence of NO. Furthermore, in dark conditions, the H₂S decay was similar to that expected from dilution, indicating that oxidation processes are probably less efficient in the absence of light. As a consequence, in nighttime, when no OH radicals are expected to act as oxidants, H₂S is suggested to be oxidized via nitrate radical, as follows (Yin et al., 1990; Finlaysson-Pitts and Pitts, 2000):

$$H_2S + NO_3 \rightarrow HS + HNO_3 \tag{2.6}$$
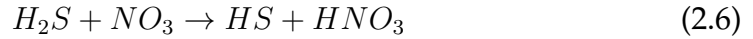
In aqueous solutions, hydrogen sulfide is a weak diprotic acid and dissociates via the following reactions (Arnorsson et al., 1982):

$$H_2S_{(g)} \leftrightarrow H_2S_{(aq)} \tag{2.7}$$

$$H_2S_{(aq)} \leftrightarrow HS^- + H^+ \tag{2.8}$$

$$HS^- \leftrightarrow H^+ + S^{2-} \tag{2.9}$$

where $H_2S_{(g)}$ and $H_2S_{(aq)}$ are hydrogen sulfide in the gas and the aqueous phase respectively. The dissociation constants for reactions (2.8) and (2.9) are K_{a1} = 10 $^{-6.99}$ and K_{a2} = 10 $^{-17.07}$, respectively. The reactivity of $H_2S_{(aq)}$ is largely dependent on the pH of the acid solution. Ball and Liss (1983) reported that at pH of 5-6, H₂S is a gas of moderate solubility, but as the pH increased most H₂S is dissolved. The constant rate of H₂S consumption has not been definitely determined and many authors have proposed different

values for reaction (2.1), estimated by the application of various methods (e.g., theoretical computations and direct measurements), while rates for all the reaction sequences [(2.2), (2.4) and (2.5)] are described in Atkinson et al. (1992). If oxidation by OH radical is a major mechanism in H_2S removal (Cox and Sandalls, 1974), an estimate of the atmospheric residence time of hydrogen sulfide can be made on the basis of its reactivity with hydroxyl radicals. Using rate constants for the reaction of OH radicals with H_2S, various authors calculated the lifetime of H_2S in the troposphere ranging from 12 to 27 h (Perry et al., 1976; Sprung, 1977; Graedel, 1977; Eggleton and Cox, 1978; Jaeschke et al, 1979; Wine et al., 1981; Servant and Delaport, 1982), which was confirmed by H_2S and SO_2 field measurements carried by Henry and Hidy (1980).

Laboratory experiments carried out by Perry et al. (1976) showed a reaction rate of OH with H_2S of 5.2×10^{-12} cm^3 molecule^{-1} s^{-1} (at T = 297-427 K and with an estimated initial concentration of OH $\approx 10^{11}$ molecule cm^3) and a calculated H_2S half-life in the lower troposphere of 0.5 day (using an average OH radical concentration of 3×10^6 molecule cm^3). Similarly, Wine et al. (1981), as the results of a flash photolysis-resonance fluorescence kinetics study, reported a temperature-independent (in the range 244-367 K) rate constant of $5.35 (\pm 0.40) \times 10^{-11}$ cm^3 molecule^{-1} s^{-1} and a half-life for H_2S in the troposphere of 27 h (considering a concentration of OH = 2×10^6 molecule cm^3). Jaeschke et al. (1980) proposed a mean lifetime of H_2S above tidal mudflats of 12.2 h, while other studies carried out by the same group in the Mt. Etna volcanic plume, as far as the H_2S removal was concerned, a reaction rate ten times faster (k = 2.1×10^{-4} s^{-1}; Jaeschke et al., 1982) was estimated. Cox and Sandalls (1974), using both the average (24 h) OH concentration in the lower atmosphere calculated by Levy (1971, 1973) and the Stuhl's rate constant for reaction (2.1) (k = 3.1×10^{-12} cm^3 molecule^{-1} s^{-1}; Stuhl 1973), predicted a H_2S life-time of 1.3 days. Spedding and Cope (1984), in their experiments in a geothermal gas plume (New Zealand), computed a life time of about 8 h in both summer and winter and a mean rate constant for H_2S oxidation to SO_2 of $(3.5 \pm 1.3) \times 10^{-3}$ min^{-1}. The results suggested that, in geothermal plumes, H_2S lifetimes in the atmosphere were markedly lower than those deduced from the experimental runs where H_2S was oxidized with OH radicals. Thus, field measurements demonstrated that the

oxidation of H$_2$S was faster. Studies carried out by Hitchcock (1977, 1978) in Monroe County (Florida) and near salt marshes on Wallops Island (Virginia), suggested that the oxidation rates of H$_2$S and SO$_2$ were much greater than those supposed to occur in the atmosphere, with residence times for both the S-compounds of 1-2 h, rather than 12 h or greater. Other authors (Bottenheim and Strausz, 1980) suggested that H$_2$S can persist up to 42 days during wintertime. More reaction rates for (2.1) reaction are shown in Fig. 2.2.

| λ/cm^3 molecule^{-1} s^{-1}	Temp./K	Reference
Absolute Rate Coefficients		
$5.6 \times 10^{-12} \exp(-57/T)$	245–450	Lin *et al.,* 1985[1]
$(4.4 \pm 0.7) \times 10^{-12}$	299	
$1.32 \times 10^{-11} \exp[-(394 \pm 190)/T]$	294–463	Lafage *et al.,* 1987[2]
$(3.3 \pm 0.5) \times 10^{-12}$	294	
Relative Rate Coefficients		
$(5.2 \pm 0.8) \times 10^{-12}$	300	Barnes *et al.,* 1986[3]
Reviews and Evaluations		
$6.3 \times 10^{-12} \exp(-80/T)$	200–300	IUPAC, 1989[4]
$6.0 \times 10^{-12} \exp(-75/T)$	200–300	NASA, 1990[5]

FIGURE 2.2: *Rate coefficient data proposed by various authors for the H₂S oxidation reaction via the OH radical (from Atkinson et al., 1992). The preferred values by the IUPAC Subcommittee are k = 4.8 × 10⁻¹² cm³ molecule⁻¹ s⁻¹ at 298 K and k = 6.3 × 10⁻¹² exp(-80/T) cm³ molecule⁻¹ s⁻¹ over the temperature range 200-300 K.*

Recently, some authors (i.e. Badalamenti et al., 2001; Carapezza et al., 2003; D'Alessandro et al., 2009; Somma et al., 2017; Gudjónsdóttir et al., 2018) explained both the decrease of H$_2$S concentration from emitting sources and the presence of SO$_2$ in geothermal systems by photo-oxidation processes of H$_2$S to SO$_2$. Badalamenti et al. (2001) claimed that the low H$_2$S/SO$_2$ ratio (1–0.1) measured in the atmosphere, compared to the same ratio in the fumarolic gases (100), clearly indicated that H$_2$S suffered oxidation during the transport in the atmosphere. The same conclusions were argued by Carapezza et al. (2003) to justify the presence of SO$_2$ at Cava dei Selci (Roma), which was absent in the source gas, and the air enrichment of the inert CO$_2$ with respect to H$_2$S. Measurements carried out by passive samplers

(Radiello$^{®}$) by D'Alessandro et al. (2009) suggested that the decrease in concentration of atmospheric H_2S observed in summer, respect to the winter period, cannot entirely be ascribed to a simple dilution process and photochemical reactions were invoked as the main mechanism that consumed the emitted H_2S.

The effects of meteorological factors on H_2S concentration were also studied to some extent. Results obtained by Ólafsdóttir et al. (2014), on the dependency of hydrogen sulfide concentration on weather parameters, showed that wind direction was one of the prevailing factors controlling the atmospheric concentration and distribution of H_2S. Furthermore, high H_2S concentration in Reykjavik from the nearby geothermal power plants were observed with high air stability, low wind speed and absence of precipitation. Marani et al. (2000) observed similar results at the Olkaria geothermal power station (Kenya), since the highest concentrations of H_2S were recorded with low wind, high humidity and low atmospheric temperatures. Studies on geothermal plumes distribution, carried out by Ólafsdóttir and Gardarsson (2013), showed that the H_2S plume in mountainous areas is heavily dependent on the topography, especially during neutral and stable air conditions. These authors argued that, since H_2S can be transported over long distances, the depletion of H_2S from the atmosphere must be a slow process.

Other processes can be responsible for the removal of gaseous H_2S from the atmosphere. Soils can adsorb considerable amounts of H_2S from the air (Cihacek and Bremner, 1993) and formation of elemental sulfur deposits around fumarolic vents is frequently observed in geothermal systems, related to hot rising gases that cool to <100 °C (Lee et al., 2005), according to the reaction:

$$2H_2S + SO_2 \leftrightarrow 3S + H_2O \qquad (2.10)$$
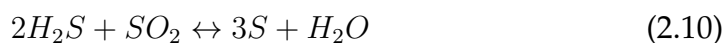
2.1.2   Sulfur Dioxide oxidation processes

Although much information is now available about the atmospheric SO_2 oxidation in anthropogenic plumes and free atmosphere, SO_2 lifetime for tropospheric volcanic plumes has not still determined and the estimated degradation rates vary widely (from 1 to >99% per hour) (McGonigle et al., 2004). In free atmosphere, sulfur dioxide is known to be converted into sulfate particles (or condensation nuclei) by a number of chemical processes (Urone and

Schroeder, 1969; Sethi, 1971; Sidebottom et al., 1972; Freiberg, 1975), which are of environmental concern since they cause visibility degradation. The gas conversion to aerosol can occur through three different paths: i) condensation, which involves gas-phase molecules combining or condensing with existing condensation nuclei; ii) nucleation, i.e. gases interacting and combining with Aitken nuclei (particles with a diameter < 0.1 mm) to form larger aerosols; iii) coagulation, which occurs when aerosols collide and aggregate, yielding larger particles (Friedlander, 1977; Finlayson-Pitts et al., 1986).

In volcanic plumes, sulfur dioxide can be involved in three types of reactions, which lead to the formation of particulate sulfate: i) gas-phase homogeneous reactions (mainly via hydroxyl radicals), ii) aqueous-phase reactions and iii) heterogeneous reactions on the surface of solid particles (i.e. gas and aerosol; Eatough et al. 1994), with reaction rates increasing with temperature, relative humidity, UV insolation, and aerosol density (Eatough et al., 1994). Gas-phase homogeneous reactions are driven by oxidation of gaseous SO_2 by OH, which is considered the main oxidant for $SO_{2(g)}$ in daytime conditions (Finlayson-Pitts and al., 1986; Xie, 1992):
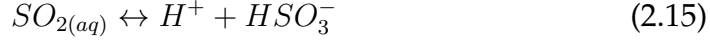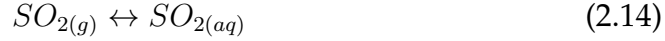
$$OH + SO_2 + M \rightarrow HOSO_2 + M \qquad (2.11)$$
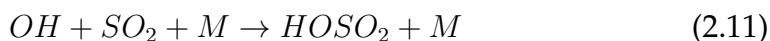
Where the third body M is any inert molecule (in the atmosphere is generally O_2 or N_2). Equation (2.11) can be followed by (Stockwell and Calvert, 1983):

$$HOSO_2 + O_2 \rightarrow SO_3 + HO_2 \qquad (2.12)$$

$$SO_3 + H_2O \rightarrow H_2SO_4 \qquad (2.13)$$

The final oxidation product, H_2SO_4, has a very short lifetime in the atmosphere since it is rapidly converted to particulate-phase species through condensation and nucleation mechanisms. Finally, sulfate particles are removed from the stratosphere by gravitational sedimentation.

Since sulfur dioxide is readily soluble in water, $SO_{2(g)}$ can be adsorbed into water droplets according to the following aqueous-phase reactions (Erickson et al., 1977; Eatough, 1997):

$$SO_{2(g)} \leftrightarrow SO_{2(aq)} \tag{2.14}$$

$$SO_{2(aq)} \leftrightarrow H^+ + HSO_3^- \tag{2.15}$$

$$HSO_3^- \leftrightarrow H^+ + SO_3^{2-} \tag{2.16}$$

with $K_{1(25°C)} = 1.32 \times 10^{-2}$ M and $K_{2(25°C)} = 6.42 \times 10^{-8}$ M for equations (2.15) and (2.16), respectively. Heterogeneous reactions on solid surfaces are generally considered to play a minor role in converting $SO_{2(g)}$ to particulate sulfate, compared to those involving hydroxyl radicals and aqueous reactions, although they can become important in volcanic plumes where high particle densities (>100 μg/m³) are often dominant (Cocks et al., 1983; Cheng et al., 1987; Delmelle, 2003). Sulfur dioxide can be adsorbed and then oxidized on various types of surfaces such as graphite, soot particles, fly ash, dust, MgO, Fe_2O_3 or MnO_2 (Finlayson-Pitts and al., 1986; Parungo et al., 1992; Yu et al., 2017). Möller (1980) reported constant rates values of $\approx 1.2 \times 10^{-4}$ s⁻¹ for SO₂ oxidation via gas phase, $\geq 5 \times 10^{-5}$ s⁻¹ via aqueous phase and $\approx (0.1$–$10) \times 10^{-5}$ s⁻¹ via particle surface reactions in the (non-volcanic) troposphere.

In tropospheric volcanic plumes, few investigations were carried out to estimate the conversion rate of SO₂ and different reaction rates were proposed. Hobbs et al. (1982) suggested a gas-to-particle conversion rates in the range between 1.9×10^{-7} and 1.6×10^{-6} s⁻¹ during the Mount St. Helens eruption, USA. Martin et al. (1986) inferred rates between 2.2×10^{-6} and 4.0×10^{-5} s⁻¹ for the Mt. Etna plumes, consistent with similar measurements carried out at Kilauea (Hawaii, USA) by Porter et al. (2002), who proposed SO₂ oxidation rates ranging from 2.0 to 5.5×10^{-5} s⁻¹. Jaeschke et al. (1980) computed a reaction rate constant in the range of 1.7×10^{-4} and 7.8×10^{-4} s⁻¹ for the 1978 and 1979 Mt. Etna volcanic plumes. Significantly higher SO₂ loss rates, exceeding 10^{-3} s⁻¹, were also observed in the tropospheric volcanic plume associated with the lava dome eruption at Soufriere Hills volcano (Montserrat) (Oppenheimer et al., 1998b). This relatively fast conversion was possibly the result of particular conditions: either the presence of a warm, moist, boundary layer and dense clouds or the content of hygroscopic ash in the plume,

probably favored by rapid condensation of steam. Consequently, SO_2 diffusion and dissolution in droplets increased. However, similar reaction rates were also observed at Mt. Etna (Fig. 2.3).
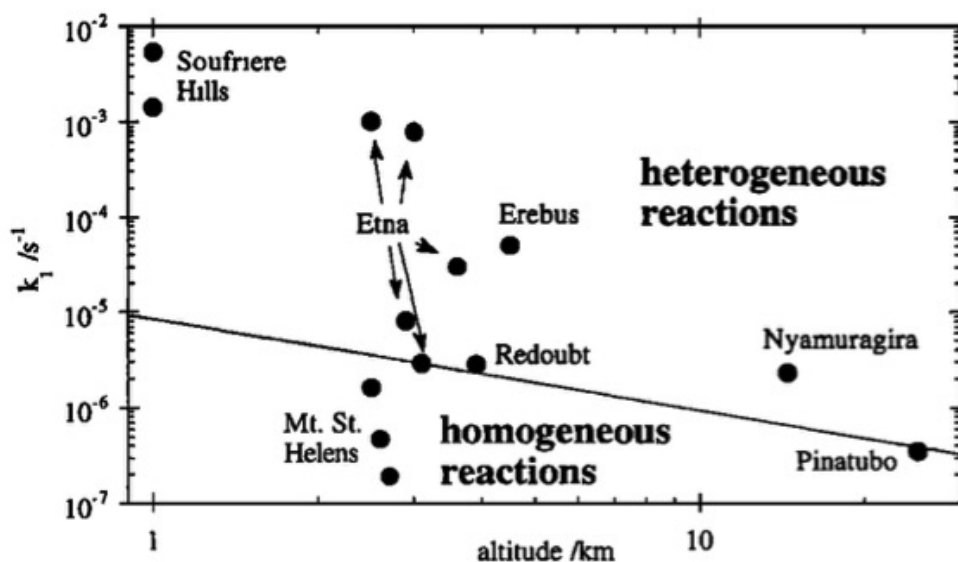

FIGURE 2.3: *Sulfur dioxide loss rates (s^{-1}) plotted against volcanic plume altitude (km). The transition between homogeneous gas phase oxidation via hydroxyl radicals and heterogeneous multiphase reactions is also represented (black line; data from Eatough et al., 1994; Thornton et al., 1996). Variations can occur according to solar radiation levels (from Oppenheimer et al., 1998).*

Additional removal mechanisms of SO_2, which remain still poorly known in volcanic environments, are wet and dry deposition (Aiuppa et al., 2001; Delmelle et al., 2001; Delmelle, 2003). Dry deposition depends on various factors such as reactivity (of the gaseous or particulate form), the nature of the surface of deposition, wind speed, atmospheric stability and so forth (e.g., Wesely and Hicks, 2000), which make difficult the direct measurements of this process. Studies carried out by Delmelle et al. (2001) at Masaya volcano (Nicaragua) in the dry season suggested a SO_2 dry deposition of about 10% of the total daily volcanic emission of SO_2. Similar trends were recognized in industrial plumes: the measured or modeled amount of SO_2 deposited as dry deposition is about 2-8% of the total SO_2 emitted into the atmosphere (Freedman and Hutchinson, 1980; Borque, 1996). Wet precipitation (e.g., acidic rain and fog) was considered as a minor scavenging process in the surrounding areas of Mt. Etna by Aiuppa et al. (2011) since only a

small fraction (0.3 ± 1.2%) of the atmospheric discharge of the volcano was affected by this process. About the influence of meteorological conditions on SO_2 depletion in tropospheric volcanic plumes, Eatough et al. (1994) suggested that the rates of SO_2 conversion to sulfate, via homogenous and/or heterogeneous processes, increase together with the temperature, insolation and relative humidity. When plumes are characterized by high particle density (>400 $\mu g/m^3$) or plumes are entrained into cloud or fog (as the case of Oppenheimer et al., 1998, see above), depletion rates are faster. On the contrary, studies carried out by McGonigle et al. (2004) at Masaya volcano showed that SO_2 removal rates from the tropospheric volcanic plume are minimal and no significant changes were observed for different relative humidity conditions (from 40 to 100%). Other reaction rates estimated by various authors for different SO_2 oxidation processes in free atmosphere are shown in Fig. 2.4 and 2.5.
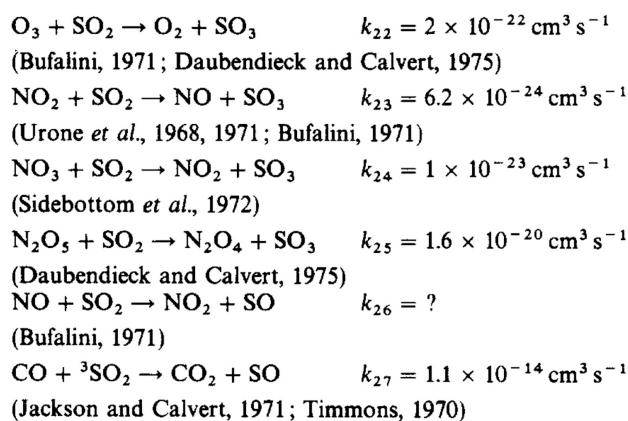
$$O_3 + SO_2 \rightarrow O_2 + SO_3 \qquad k_{22} = 2 \times 10^{-22}\,cm^3\,s^{-1}$$
(Bufalini, 1971; Daubendieck and Calvert, 1975)
$$NO_2 + SO_2 \rightarrow NO + SO_3 \qquad k_{23} = 6.2 \times 10^{-24}\,cm^3\,s^{-1}$$
(Urone *et al.*, 1968, 1971; Bufalini, 1971)
$$NO_3 + SO_2 \rightarrow NO_2 + SO_3 \qquad k_{24} = 1 \times 10^{-23}\,cm^3\,s^{-1}$$
(Sidebottom *et al.*, 1972)
$$N_2O_5 + SO_2 \rightarrow N_2O_4 + SO_3 \qquad k_{25} = 1.6 \times 10^{-20}\,cm^3\,s^{-1}$$
(Daubendieck and Calvert, 1975)
$$NO + SO_2 \rightarrow NO_2 + SO \qquad k_{26} = ?$$
(Bufalini, 1971)
$$CO + {}^3SO_2 \rightarrow CO_2 + SO \qquad k_{27} = 1.1 \times 10^{-14}\,cm^3\,s^{-1}$$
(Jackson and Calvert, 1971; Timmons, 1970)

FIGURE 2.4: *SO_2 oxidation with molecules (from Möller et al., 1980).*

$$O + SO_2 + M \rightarrow SO_3 + M^* \qquad k_{16} = 3.5 \times 10^{-14}\, cm^3\, s^{-1}$$
(Graedel *et al.*, 1976)
$$HO_2 + SO_2 \rightarrow OH + SO_3 \qquad k_{17} = 9 \times 10^{-16}\, cm^3\, s^{-1}$$
(Cox, 1974; Warneck, 1974)
$$RO_2 + SO_2 \rightarrow RO + SO_3 \qquad k_{18a} = 9 \times 10^{-16}\, cm^3\, s^{-1}$$
(Harker, 1975)
$$CH_3O_2 + SO_2 \rightarrow CH_3O + SO_3 \qquad k_{18b} = 4.3 \times 10^{-15}\, cm^3\, s^{-1}$$
(Cox and Penkett, 1971; Cox, 1974)
$$OH + SO_2 + M \rightarrow HOSO_2 + M \qquad k_{19} = 1.1 \times 10^{-12}\, cm^3\, s^{-1}$$
(Dubrovnik, 1977)
$$HOSO_2 + (O_2, NO, RH) \rightarrow HOSO_2O_xH_y + (NO_2, R) \quad k_{20} \gg k_{19}$$
(Smith and Urone, 1974; Cox, 1975)
possible destroy after:
$$HOSO_2O_xH_y \rightarrow SO_3 + (HO_2, OH, H_2O)$$
$$HOSO_2 + NO_2 \rightarrow HOSO_2ONO$$
(Schroeder and Urone, 1978)

FIGURE 2.5: *SO_2 oxidation with radicals. [M] = 4.5 $\times$ 10^{19} cm^{-3}
(from Möller et al., 1980).*

2.2 Guidelines in ambient air

2.2.1 H$_2$S guidelines

The World Health Organization (WHO, 2003) defines hydrogen sulfide as a colorless, flammable, poisonous gas that is soluble in water and organic solvents with a characteristic odor of rotten eggs. Human exposure to H_2S is principally via inhalation because of its gaseous form and it is rapidly adsorbed through the lungs, but unlikely bio-concentrates in the food-chain because it is expelled through the urine, intestines and expired air (WHO, 2003). The H_2S toxicity for humans is a proven fact at certain concentrations (WHO, 2003). At about 0.03 ppm it causes nuisance whilst at higher concentrations (1-4 ppm) symptoms such as lack of vigor, loss of appetite and restlessness, are usually found in exposed elderly, young children and asthmatic individuals (WHO, 2003), whereas the respiratory function in healthy humans is not affected. Serious health effects during short-term exposures occur at much higher levels: it can irritate and injure eyes (10 ppm), the upper respiratory tracts (50-100 ppm) and causes loss of smell (150 ppm). Furthermore, being a gas denser than atmospheric air (similarly to carbon dioxide), it can accumulate in topographic depressions reaching concentrations lethal to humans and animals (>700 ppm; WHO, 2000, 2003) . The effects of hydrogen sulfide on humans are summarized in Fig. 2.6. While the hazards caused

by high concentrations of hydrogen sulfide are relatively well known, scanty information is available on the effects caused to humans when exposed to very low concentrations. Studies carried out at Rotorua geothermal area (New Zealand) by Bates et al. (2002) suggested that long-term exposures to low H$_2$S concentrations can have severe health consequences on respiratory, cardiovascular and nervous systems. Air quality guidelines from the World Health Organization (WHO, 2000) suggested a guideline value of 0.15 mg/m^3 (about 0.10 ppm) [1] for H$_2$S in ambient air with an averaging time of 24 h. To avoid significant odor annoyance, hydrogen sulfide concentrations should not be allowed to exceed 7 μg/m^3 (about 4.6 ppb), with a 30-minute averaging period (Fig. 2.7). Background concentrations of H$_2$S in ambient unpolluted air were estimated to be between 0.14 and 0.4 μg/m^3 (about 0.1 and 0.3 ppb respectively; US EPA, 1993); the typical concentration in urban area is instead about one order of magnitude higher (1.0–3.0 μg/m^3 or 0.7-2 ppb; Kurtidis et al., 2008).

Hydrogen sulfide concentration		Effect	Reference
mg/m^3	ppm		
1400-2800	1000-2000	Immediate collapse with paralysis of respiration	*(2)*
750-1400	530-1000	Strong CNS stimulation, hyperpnoea followed by respiratory arrest	*(2)*
450-750	320-530	Pulmonary oedema with risk of death	*(2)*
210-350	150-250	Loss of olfactory sense	*(11)*
70-140	50-100	Serious eye damage	*(11)*
15-30	10-20	Threshold for eye irritation	*(11)*

FIGURE 2.6: *Dose-effect relationships of hydrogen sulfide (from WHO, 2000). (2) Hydrogen sulfide, Geneva, World Health Organization, 1981 (Environmental Health Criteria, No. 19). (11) Savolainen, H. Nordiska expert gruppen for gransvardes dokumentation. 40. Dihydrogensulfid (Nordic expert group for TLV evaluation. 40. Hydrogen sulfide) Arbeta och hdlsa, 31: 1-27 (1982).*

---

[1] **Conversion factors (WHO, 2000)**:
1 ppm (20 °C, 1013 hPa) = 1.5 mg/m^3
1 mg/m^3 = 0.670 ppm

Country / Agency	Level	Averaging period	Notes	Ref.
WHO	$7 \ \mu g/m^3$	30 min	To avoid odour annoyance.	a
	$150 \ \mu g/m^3$	24 hours	This guideline was obtained by dividing the threshold for eye irritation of 15,000 $\mu g/m^3$ by a factor of 100.	
Iceland	$50 \ \mu g/m^3$	24 hours	The limit may be exceeded 5 times per year. From 1st July 2014, the limit may not be exceeded.	b
New Zealand	$7 \ \mu g/m^3$	1 hour	The hydrogen sulphide value is based on odour nuisance and may be unsuitable for use in geothermal areas.	c
USEPA California	$43 \ \mu g/m^3$	1 hour	In 1969, the Air Resources Board adopted this standard and in 1984, the ARB retained this standard.	d
	100 g/MW-hr	-	From any geothermal power plant.	
	1 kg/hr	-	From any miscel. steam supply operation.	e
Bay Area	2.5 kg/hr	-	From any geothermal well.	
	35% of full flow	1 hour	In a scheduled outage.	
	35% of full flow	4 hour	In an unscheduled outage.	

a. WHO, 2000: Air quality guidelines for Europe, 2nd ed. Copenhagen.
b. Regulation 514/2010, Annex 1. *http://www.government.is* .
c. Ministry for the Environment of New Zealand 2002. Ambient air quality guidelines. 2002 Update.
d. California EPA, Air Resources Board 1984: Sulphide ambient air quality standard.
e. Bay Area Air Quality Managem. District, 1982. Regulation 9, Rule 5: Hydrogen sulphide from geothermal power plants.

FIGURE 2.7: *The allowable thresholds concentration in ambient air according to the World Health Organization (WHO) guidelines and countries regulations where geothermal energy is developed (e.g., New Zealand and Iceland) (from WHO, 2000). This is because H_2S is strongly present in geothermal areas and in the vicinity of geothermal plants, since it is one of the main constituents of the geothermal fluid.*

2.2.2 SO$_2$ guidelines

Sulfur dioxide is a colorless gas, highly reactive, that is readily soluble in water (WHO, 2000). The most serious concerns related to this air pollutant are experienced in large urban areas where SO_2 and particulate matter, derived from the combustion of fossil fuels, are emitted in large quantities. Natural background concentrations of sulfur dioxide in Europe rural areas are generally below 5 $\mu g/m^3$ (1.8 ppb)[2], whereas in urban areas the annual mean concentrations are mainly in the range of 20–60 $\mu g/m^3$ (7–21 ppb), with occasionally daily mean values >125 $\mu g/m^3$ (44 ppb) (WHO, 2000). Similar to H_2S, human exposure to sulfur dioxide mainly occurs via inhalation, which is the only effect considered in terms of health hazard. Epidemiological studies suggest that SO_2 can affect the respiratory system and lung functions, causing coughing, mucus secretion, aggravation of asthma and chronic bronchitis, as well as more propensity to infections of the respiratory tract. Irritation of the eyes is also observed (WHO, 2000). Experiments

---

[2]**Conversion factors (WHO, 2000)**:
1 ppm (20 °C, 1013 hPa) = 2860 $\mu g/m^3$
1 mg/m^3 = 0.350 ppm

in controlled chamber on volunteers for short exposure periods (from few minutes up to 1 h) indicated changes in pulmonary function and respiratory symptoms only after 10 minutes (accentuated in asthmatic groups). Based on this evidence, a guideline value of 500 μg/m^3 (0.175 ppm) should not be exceeded over averaging periods of 10 minutes. For 24-h and long-term exposure, the 1987 guidelines recommended values of 125 μg/m^3 (0.044 ppm) and 50 μg/m^3 (0.017 ppm) (WHO, 2000), respectively. Sulfur dioxide has also important effects on natural environments: it contributes to acidic deposition, causing negative consequences on aquatic (rivers and lakes) ecosystems. A major concern is related to the damage to forests and acidification of rain and soils. As a consequence, European air quality limit values for SO$_2$, defined by the 2008 Air Quality Directive (EU, 2008c), are also given for vegetation protection, with threshold values of 20 μg/m^3 (7 ppb) over a year (Fig. 2.8).

Objective	Averaging period	Limit or threshold value	Number of allowed exceedances
Human health	One hour	350 µg/m³	24 hours per year
Human health	One day	125 µg/m³	3 days per year
Alert (^{a})	One hour	500 µg/m³	
Vegetation	Calendar year	20 µg/m³	
Vegetation	Winter (1 October–31 March)	20 µg/m³	

Note: (^{a}) To be measured over three consecutive hours at locations representative of air quality over at least 100 km² or an entire zone or agglomeration, whichever is the smaller.

FIGURE 2.8: *Sulfur dioxide threshold values for human health and vegetation protection given by the 2008 Air Quality Directive (from EU, 2008c).*

Chapter 3

Study areas

The presence of extensive geothermal/hydrothermal activity favors the release of large quantities of sulfur compounds in the atmosphere, which are essentially in the form of hydrogen sulfide (H_2S). This means that in these environments we can study almost "pure" sources of H_2S and its physical (i.e. for simple dispersion) and chemical (i.e. for oxydation processes) behaviour. For this reasons, Iceland has been selected as the perfect environment for this study, being characterized by an extensive volcanic-geothermal activity across the country. Air measurements have been also carried out at Vulcano Island (Aeolian Archipelago) and at La Solfatara (Phlegraean Fields), where the methods and sampling strategies have been developed for the first time. This section consists of a brief general introduction on main features that characterized a geothermal system and then, a description of the study areas is subsequently reported.

Geothermal systems typically consist of the following three main components: i) permeable reservoir rock (mainly created by tectonic and hydrothermal fracturing), ii) convection of groundwater which carry heat and solutes from the reservoir to the surface and iii) a heat source. Most of the geothermal systems also have an overlying cap-rock that partially isolates them from the shallow groundwater regime (Goff and Janik, 2000). Geothermal systems occurs in a range of geological setting: most of them are generally located along or near convergent plate boundaries, transform plate boundaries, within rift systems (which are poorly known being submarine), spreading centers and over mantle hot spots. Neverthless, a smaller fraction of geothermal resources comes from fault circulation systems and sedimentary basin. There are three main types of geothermal systems exploiting

natural reservoir of hot water (generally called hydrothermal systems), according to geological setting, temperatures, geophysical and hydrologic criteria: i) volcanic systems or young igneous systems, ii) tectonic systems and iii) geopressured systems. The first type is associated with volcanic activity (along plate boundaries and within hot spots), it is generally the hottest ($\leq$370 °C) and with shallow reservoir depths ($\leq$1.5 km, even if some can be deeper). The second is characterized by an high heat flow with reservoir temperature of $\leq$250 °C, even though devoids of igneous activity; it is usually associated with elevated seismicity due to Quaternary faulting and occurs in backarc environments, crustal extension regions, along collision and fault zones. The third type refers to hot, overpressured reservoirs formed in sedimentary basins by subsidence and burial of fluid-bearing strata and are characterized by a lower heat flow (50 to 190 °C) (Goff and Janik, 2000). The first type is that considered in this study and it is schematically represented in Fig. 3.1. The heat is provided by a shallow magmatic intrusion (<6 km) by heat conduction, allowing the fluid circulation in the overlying hydrothermal realm. The magma chamber is isolated from the permeable reservoir by low-permeability rocks, even if some magmatic water and volatiles can be transferred directly to the geothermal system. On the other hand, a clay seal at the top of the hydrothermal realm limits direct communication with shallow groundwater. If the rising hydrothermal fluids are sufficiently hot, they can depressurize resulting in the separation of liquid and vapor phases (i.e., boiling). The extent of the boiling zone is controlled essentially by host rock permeability (Norton and Knight, 1977).

Most geothermal systems are liquid dominated, namely characterized by liquid water in fractures and pores, although bubbles of steam and gas can be also present (two-phase conditions). Less commonly, steam-dominated conditions prevail in major fractures when the systems is strongly isolated from circulating groundwaters (e.g., Geysers in USA, Larderello in Italy). The aqueous fluids within geothermal systems usually consists of ancient to modern meteoric precipitation, even thought seawater, or a mixture of seawater and meteoric water, can be the main fluid source in some rift and coastal locations (e.g., Reykjanes geothermal system in Iceland). These fluids provide basal recharge to the system and the hot fluids flows up as a buoyant plume relative to a hydrostatic gradient. The gaseous component
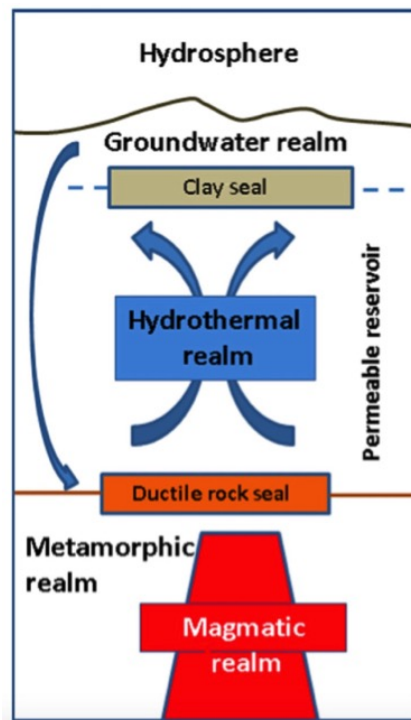
FIGURE 3.1: *Schematic representation of magmatic intrusion, hydrothermal circulation and shallow groundwater flow realms.*
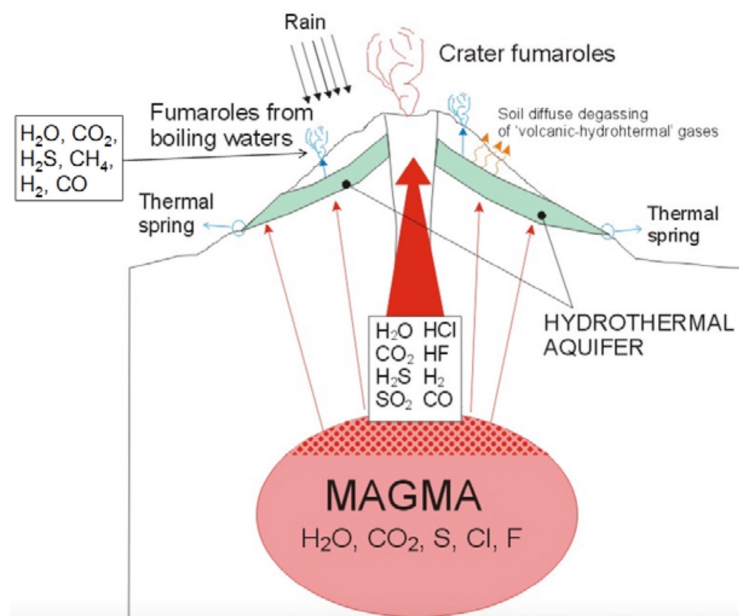
FIGURE 3.2: *A typical volcano-hydrothermal system. Magma degassing processes at depth both feed high temperature fumaroles and supply fluid and thermal energy to the hydrothermal aquifers (from Fisher and Chiodini 2015 – The Encyclopedia of Volcanoes).*

in geothermal fluids derives from magma contributions, fluid-rock interaction processes, contribution from air-saturated meteoric water and thermal breakdown in reservoir rocks. The main component and thermal carrier is H_2O (usually >95% by vol.; Italiano et al., 1998), which can exceed 99% by vol. in fumarolic gases discharging from geothermal areas. Respect to vulcanic gases, geothermal gases usually contain i) more CO_2; ii) less total sulfur, which is essentially in H_2S reduced form; iii) higher contents of CH_4, NH_3 and N_2 and rarely contain acid halides (Giggenbach, 1996; Goff and Janik, 2000) (Fig. 3.2).

3.1 Vulcano Island

Vulcano island is an active volcanic system located at the center of the Aeolian volcanic island arc in the southern Tyrhenian Sea (Italy) within a graben structure (Barberi et al., 1994) linked to NNW-SSE dextral strike slip fault, the Tindari-Letojanni discontinuity, which dissects the arc (Fig. 3.3).

The Aeolian archipelago developed on the Calabro-Peloritano continental margin and its volcanism is entirely of recent age (the oldest is dated at approximately 1.02 M.y.; Santo et al., 1995) and Vulcano Island belongs to its last cycle of volcanic activity (Cioni and D'Amore, 1984). The exposed part of Vulcano is entirely built up of high-K calc-alcaline (HKCA), shoshonitic (SHO) and leucite tephrite or potassic (KS) rocks, ranging from basalts to rhyolites (Keller, 1980; Ellam et al., 1988; De Astis, 1995). The active volcanic cone is 391 m high a.s.l. and it is placed at the center of a caldera called "La Fossa" or "Gran Cratere", a volcano-tectonic pull-apart-like structure (Ventura, 1994; Mazzuoli et al., 1995). Since the latest explosive eruption in 1888-90, Vulcano Island has been dominated by fumarolic activity of various intensity and time changes (i.e. from 200 °C in 1913 up to 615 °C in 1923 at La Fossa; Sicardi, 1955), mainly localized on a N-S trending fracture zone on which the volcanoes La Fossa, the Faraglione and Vulcanello are aligned (Fig. 3.3) (Keller, 1970). Currently, the main manifestations in the area consist of: i) fumaroles at Gran Cratere, which are located inside, outside and on the crater rim of the NW flank, with temperatures from 98 to >300 °C (Capasso et al., 1997; Bellucci, 2003); ii) submarine and aerial fumaroles on the shoreline of Baia di Levante, along the isthmus that connects Vulcano to
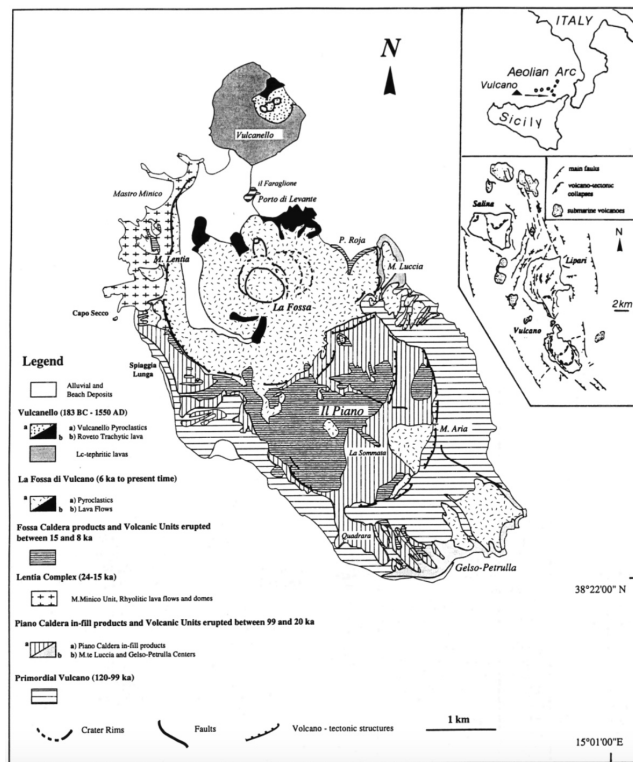
FIGURE 3.3: *Schematic geological map of Vulcano Island. Top inset is the location of the Aeolian Arc; bottom inset: structural map of the Vulcano-Lipari-Salina islands (from De Astis, 1995).*

Vulcanello, with a N-S trend alignment and with temperatures close to 100 °C (Honnorez et al., 1973; Capaccioni et al., 2001); iii) fumaroles and thermal springs at Vulcano Porto and Faraglioni area (i.e. the "Vasca degli Ippopotami" mud pool). The presence of a magma body at a depth of 2–3 km beneath Vulcano was inferred from geophysical and geochemical investigations (Ferrucci et al., 1991), also carried out for geothermal purposes (e.g., Todesco, 1997 and references therein) while the main geochemical evidence of a magmatic contribution to the fumarolic gases of La Fossa is related to their chemical composition, helium isotope ratio (R/Ra = 5-6.5; Tedesco et al., 1995; Italiano and Nuccio, 1997) and ^{3}He output (Italiano et al., 1997). Furthermore, the fluid composition of La Fossa crater fumaroles is typical of high temperature magmatic fluid: H_2O and CO_2 represent the main gases (more than the 99 vol%) while SO_2, H_2S, N_2, HCl, HF, and H_2, are significantly occurring. Carbon monoxide, He e CH_4 are subordinate. Several studies of the gas chemistry have allowed to propose a number of interpretative models. Each model suggests a mixing between deep magmatic

and shallow fluids. Carapezza et al. (1981) hypothesized the presence of a pressurized biphase reservoir (liquid-vapor) of meteoric origin at a depth of about 2 km, feeding the crater fumaroles. Cioni and D'Amore (1984) proposed a "dry monophase model", later confirmed by Chiodini et al. (1991; 1992a; 1993), suggesting that the fluids discharged from the crater were due to a mixing between a deep magmatic component and shallower fluids; the origin of these fluids was apparently related to an evaporation process of seawater or saline hydrothermal fluids, entering from lateral aquifers into a low pressure, high temperature zone surrounding the uprising conduits of the deep component. However, other autors (i.e. Mazor et al., 1988) suggested that the fumarolic system was mainly influenced by the contribution of seawater while the magmatic contribution should have beed considered negligible, or, on the contrary, none contribution from seawater was involved (i.e. Bolognesi and D'Amore, 1993). A thermal aquifer primarily fed by meteoric water partially mixed with seawater was recognized beneath the Vulcano Porto area, at the base of the La Fossa volcanic cone (Carapezza et al., 1983; Capasso et al., 1992). Geothermal exploration in the 1950's (Sommaruga, 1984) carried out by AGIP (Italian oil and geothermal company), identified a multilevel hydrothermal system, which was comprising a shallower water aquifer (7–14 m depth) at a temperature of about 100 °C and feeding the thermal mainifestations on the seashore, an intermediate water aquifer (at 90–95 m depth) at about 136 °C, and a deep-water body (185–236 m depth) at about 200 °C and with a composition close to that of seawater (Fig. 3.4). The gas emissions showed a typical low-temperature hydrothermal fluid composition, with relatively high concentration of CO_2, CH_4 and H_2S and low concentration of CO; no SO_2 was detected (e.g., Chiodini et al., 1995; Capaccioni et al., 2001). H_2S and SO_2 air measurements carried out in this study were concentrated on the Vulcano-Vulcanello hydrothermal system and at the Vulcano Porto (Fig. 3.3).
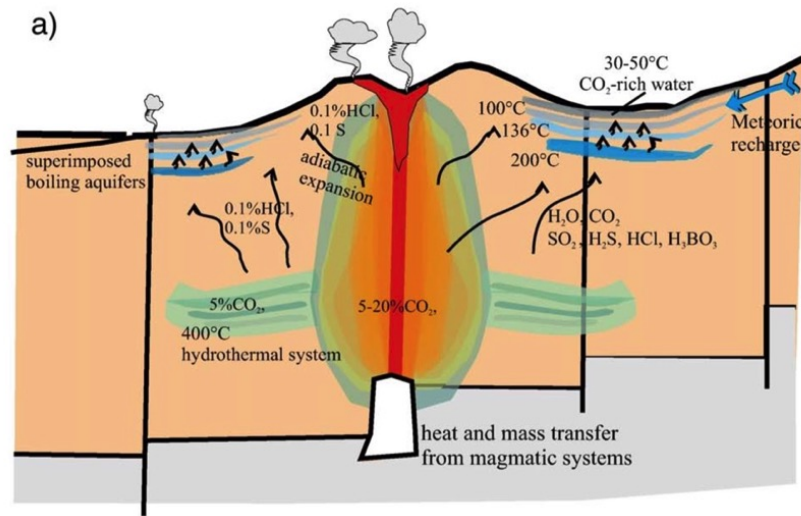
FIGURE 3.4: *Geochemical conceptual model of the volcanic-hydrothermal system of Vulcano Island (from Federico et al., 2010).*

3.2 La Solfatara (Phlegreaen Fields)

La Solfatara volcano is a tuff cone affected by widespread fumarolic activity, located within the densely-populated area of the Phlegreaen Fields caldera (12 km in diameter), NW of Naples in the Campanian region (South Italy) (Fig. 3.5). The Phlegrean Fields volcanic complex covers an area of about 100 km^2 and is characterized by a series of monogenic volcanoes and a large caldera depression, mainly formed after one of the world's largest late Quaternary volcanic eruptions, which produced the largest pyroclastic deposit (about 80 km^3 of solid rock; Thunell et al., 1979) of the Campanian area: the Campanian Ignimbrite.

The most recent eruptive event occurred in 1538 A.D. at Monte Nuovo, a monogenic tuff cone located close to the center of the caldera depression (e.g., Rosi and Santacroce, 1984; Di Vito et al., 1987; Rosi and Sbrana, 1987). Continuous emissions of hydrothermal fuids and ground deformation are among the most remarkable effects associated with the volcanic activity in this area: phases of slow aseismic subsidence were periodically alternated to remarkable, though short, episodes of ground uplift (bradyseism) and seismic activity, one of which preceded the A.D. 1538 eruption and caused a total vertical displacement of 7 m (Dvorak and Berrino, 1991; Dvorak and Gasparini, 1991; Dvorak and Mastrolorenzo, 1991). Three main uplift phases
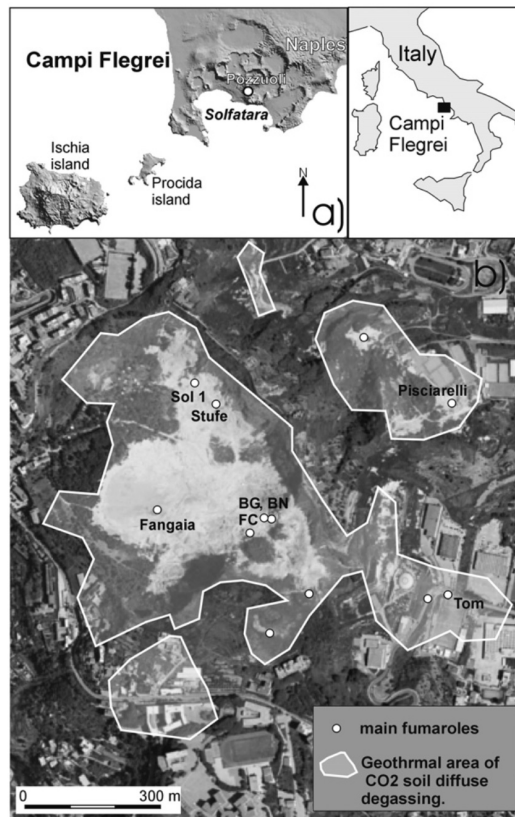
FIGURE 3.5: *(a) Location of the Phlegreaen Fields caldera. Solfatara crater, Procida and Ischia Islands are also indicated. (b) Location of the main fumaroles, mud pools (La Fangaia) and the area of diffuse degassing within the Solfatara crater (from Caliro et al., 2007).*

were recorded: i) 1950-1952, ii) 1969–1972 and iii) 1982–1984, when the town of Pozzuoli was partially evacuated (Barberi et al., 1984). In addition, four "mini" uplift periods occurred in 1989, 1994, 2000 and 2006. Since 1538 A.D., the Phlegrean Fields volcanic area has remained in a solfataric stage, mostly concentrated at Pisciarelli and inside the Solfatara crater, these two sites presenting the most impressive fumarolic gas discharges associated with the underlying geothermal system, from where the thermal release was estimated in about 100 MW (Chiodini et al., 2001a), that makes this system one of the largest fumarolic manifestations of the world. The outlet temperatures of the fumarolic discharges are from 140 to 165 °C (Todesco et al., 2003) and a mixture of H_2O and CO_2 with minor amounts of H_2S, $N2_2$, H_2 and CH_4 is released. No typical magmatic species are detected (i.e. SO_2) so far. A conceptual geochemical model of such geothermal system was first proposed

by Cioni et al. (1984) and then improved by Cioni et al. (1989), Chiodini et al. (1992, 1996), Chiodini and Marini (1998), Chiodini et al. (2000a, 2001a) and Caliro et al. (2007): the heat source of the hydrothermal system is a cooling magma located at depth (at 3-5 km below the surface; Armienti et al., 1983), which supplies heat to the overlying aquifer(s), causing boiling and separation of a gas phase at conditions of maximum enthalpy for saturated steam (236 °C, 31 bar; Cioni et al., 1984), which occupies the shallower part of the system. The extimated temperatures for this "vapor zone", indicated by gas equilibria in the CO_2–CO–CH_4–H_2O–H_2 system, varies from 200 to 240 °C and P_{H_2O} from 1 to 20 bar (Chiodini and Marini, 1998; Chiodini et al., 2001a). A deeper mixing zone (2000–2500 m depth), which likely represents the conditions at the bottom of the hydrothermal system, with higher temperatures (360 °C) and with a 200–250 bar pressure was suggested by Caliro et al. (2007). In this deep zone, magmatic and meteoric component mix with an estimated ratio of 1:4 (Caliro et al., 2007), leading to the formation of a plume mainly composed of a gas phase that migrates towards the surface (Fig. 3.6). In this study, the measurements were mainly carried out around "La Fangaia" emission, a bubbling mud pool made up of rainwater and vapour condensate (Fig. 3.5).
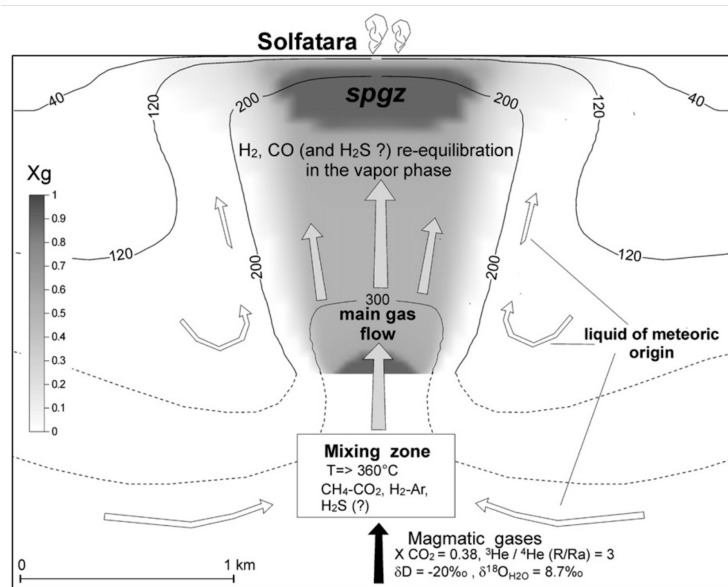
FIGURE 3.6: *Geochemical conceptual model of Solfatara (from Caliro et al., 2007). The zones of deep mixing and the H_2, CO and H_2S re-equilibration in the vapor phase are also reported. The gas/liquid mass fraction is indicated as Xg and is described in detail in Chiodini et al. (2003) and Todesco et al. (2003).*

3.3   Iceland

Iceland is a unique geological system representing the subaerial expression of the Mid-Atlantic Ridge that connects the Eurasian and North American plates, having a spread of approximately 18 mm per year (Sæmundsson, 1979), and lying on the top of a hotspot presumed to be fed by a deep mantle plume (Einarsson, 2008). The buoyancy of this hot spot and the associated high volcanic production are the main causes of Iceland being subaerial. By a geological point of view, Iceland is almost entirely made up of Tertiary plateau lavas (3.3-16 Ma, Hardarson et al., 1997), Plio-Pleistocene lavas (0.78-3.3 Ma) and hyaloclastites (0.01-0.78 Ma), formed subglacially, and Holocene lavas (<0.01 Ma) (Hardarson et al., 2008). Approximately 85-90% of the volume of Iceland above sea level is characterized by igneous rocks whereas 10-15% consists of consolidated sediments. Intrusive and plutonic rocks are less than 0.5% of the surface (Sæmundsson, 1980; Jóhannesson and Sæmundsson, 1998). Quaternary formations are found along the margins of the rift zone while Tertiary basalts predominate away from the rift zone to the east

and west. The lithospheric plate boundary has slowly been migrating west-wards relative to the mantle plume (Vink et al., 1985), producing the shift of the Icelandic volcanic belts (Óskarsson et al., 1985; Einarsson, 1989) from eastern Greenland (about 55 Ma ago) to the present position (Fig. 3.7) (Vink, 1984).
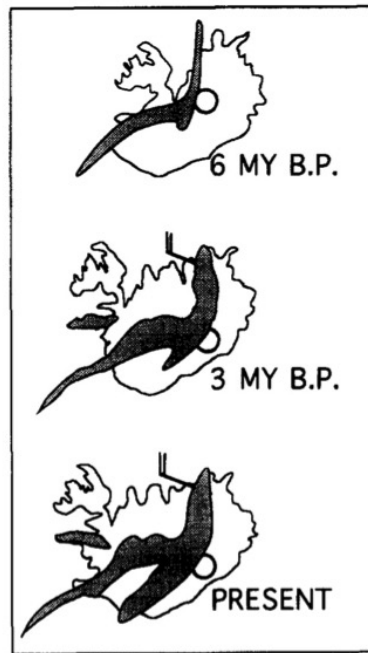
FIGURE 3.7: *Evolution of the volcanic belts in Iceland. Circle shows the location of the mantle plume (from Oskarsson et al., 1985).*

Currently, the plate boundary curves from a NNW-SSE direction in northern Iceland to an almost E-W direction on the Reykjanes Peninsula in southwestern Iceland. New Icelandic crust is generated at four main segments of the spreading axes (volcanic belts): the Reykjanes Volcanic Zone (RVZ), the Western Volcanic Zone (WVZ), the Northern Volcanic Zone (NVZ), and the South-Eastern Volcanic Zone (SEVZ), the latter being the youngest province (about 2 Ma) and is gradually replacing the WVZ as the center of rifting in South Iceland. The transform motion between the on-land continuation of the Reykjanes Ridge (the RVZ) and the SEVZ is bridged by the South Iceland Seismic Zone (SISZ) (Sæmundsson, 1979). Two subsidiary belts also occur on Snæfellsnes (SVB), active 13-8 Ma ago, and in the Öræfajökull area (ÖVB) (Fig. 3.8).
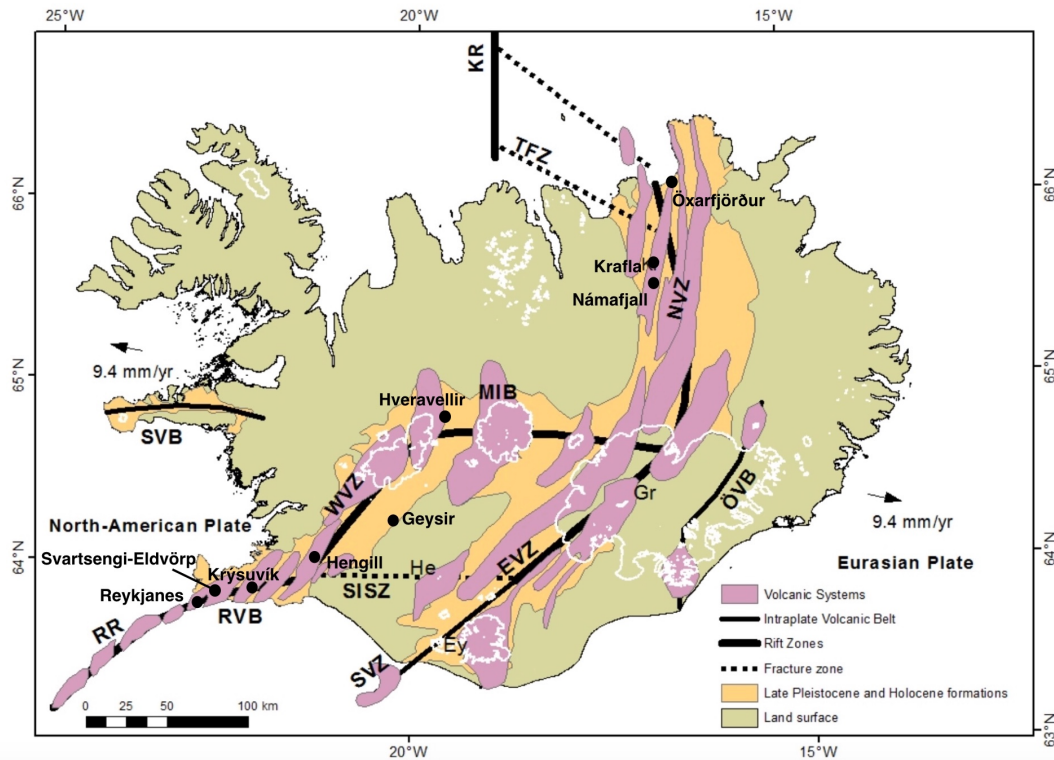
FIGURE 3.8: *Icelandic volcanic systems. The main high-temperature geothermal systems were also indicated (modified from Guðjónsdóttir et al., 2018).*

Geophysical studies and seismic measurements indicated that the center of the mantle plume lies under the region northwest of Vatnajökull (Fig. 3.8), where a low-velocity anomaly (P- and S-wave velocities), in the upper 400 km, has been identified (Tryggvason et al., 1983). This anomaly can extend even deeper, as hypothesized by recent tomographic models (French and Romanowicz, 2015), which suggested the presence of lower mantle plume conduits close to the Iceland hotspot. In this region, characterized by the thickest crust ($\approx$ 35-45 km), an high ^{3}He/^{4}He domain has been identified (Harðardóttir et al., 2017), which continues southward along the highly active and propagating ERZ. Along ERZ, the plume flows at shallow, sublithospheric depths, until it reaches the surface with limited mixing with the surrounding mantle material (Harðardóttir et al., 2017). The highest ^{3}He/^{4}He ratios has been measured in Vestfirðir (West Fiords), which is characterized by a thick crust (30 km), suggesting that the present plume head is actively affecting this region along the plume track or it is extended at

sub-lithosferic levels (Richards et al., 1989; Larson and Ekström, 2001) from central Iceland to northwest.

Guðmundsson (2003) suggested that the unusually high density of Icelandic crust probably results from higher degrees of melting and so to the frequent occurrence of intrusive dykes and sills. Shallow partially molten magma chambers can be also formed and major volcanic complexes with the associated fissure swarms, resulting from tensional fractures and normal faults, can extend above these reservoirs. Volcanic eruptions on the Reykjanes Peninsula, however, are probably directly fed from magma reservoirs in the mantle due to the absence of a shallow magma chamber and, consequently, shallow level intrusions are dominant (Guðmundsson, 1987). Each volcanic system is generally associated with a geothermal system, usually divided into high- and low-temperature systems, depending on the geological setting and temperature data from drill holes (Bödvarsson, 1961). In Iceland, the high-temperature geothermal activity is commonly associated with active volcanic complexes (i.e. active volcanoes and fissure swarms) located along the rift and characterized by >200 °C reservoir temperatures and at 1 km depth (namely "base temperature"), whereas low-temperature systems are related to off-rift activity (i.e. in Quaternary and Tertiary formations) and have reservoir temperatures lower than 150 °C at 1 km depth (Fridleifsson, 1979). Few Icelandic geothermal fields located close to the margin of the volcanic belts, have reservoir temperatures in the range of 150-200 °C and can be considered as medium-temperature fields (Sæmundsson et al., 2011). Due to the tectonic drift and the process of crustal accretion, the central volcanic complexes, together with their associated geothermal systems, will eventually be disconnected from their magmatic heat source. As a result, the volcano becomes extinct and the geothermal system gradually cools down, becoming a low temperature geothermal system outside the volcanic zones (Arnórsson et al., 2010). K/Ar dating and paleomagnetic studies indicated that each central volcano has a life span of 0.3-1.0 Ma after which the center of activity shifts to a new location along the plate boundary (Arnórsson et al., 1995). Twenty high-temperature areas have been recognized in Iceland (Pàlmason et al., 1974; Georgsson et al., 1993) but only in eight areas geothermal wells were drilled: Reykjanes, Svartsengi, Eldvörp, Krýsuvík, Hengill,

Námafjall, Krafla and Öxarfjörður (Fig. 3.8 and 3.9). Although they are hydrologically connected, they seem to have separate heat sources (Björnsson and Steingrimsson, 1991). All these areas are being exploited with the exception of Eldvörp and Krýsuvík. Few areas, such as Geysir and Hveravellir, were defined by Bödvarsson (1961) as borderline between high- and low-temperature areas, but now they are considered as high-temperature systems (Pàlmason et al., 1985) on the basis of subsurface temperature estimates by chemical geothermometry (Arnórsson, 1995). Finally, Reykir, Leira and Reykholt belong to the low-temperature group.
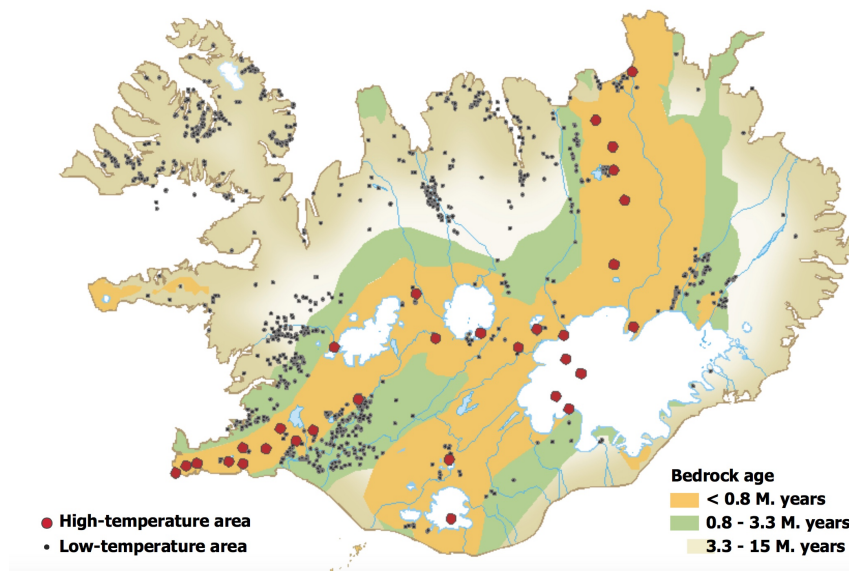
FIGURE 3.9: *Distribution of high- and low-temperature geothermal systems in Iceland. The high-temperature systems lie within the active volcanic zones (from National Energy Authority, 2014; Armarsson, 2015).*

Icelandic thermal fluids have a meteoric and seawater origin or a mixture in between, with temperatures from 10 up to 450 °C and pH between 2 and 10 (Kaasalainen and Stefánsson, 2012; Ármannsson, 2015; Kaasalainen et al., 2015; Stefánsson et al., 2016b). The concentration of major components, except mobile elements like chloride, is controlled by thermodynamic equilibria between the geothermal minerals and fluids (e.g., Giggenbach, 1980, 1981; Arnórsson et al., 1985; Stefánsson and Arnórsson, 2002). Most high-temperature areas are located on high ground and very young permeable rocks. As a result, the groundwater table in the high-temperature areas is deep and surface manifestations are mostly steam vents. In areas

such as Geysir, Hveravellir and the Hveragerdi field of the Hengill area, the geothermal groundwater table reaches the surface and sinter deposits can be found around the hot springs (Arnórsson, 1985). The geothermal systems (i.e. Reykjanes) where the heat source derives from dyke swarm and intrusions, water does not receive enough heat to boil at the base of the convection cell. On the other hand, the heat source of those systems associated with central volcanic complexes (i.e. Krafla, Námafjall, Hengill) is extensive and the low permeability structures allow the water at deep levels to boil. The rising supercritical fluid has sufficient enthalpy to produce a mixture of water and steam, which, due to its low density, rapidly rises to the surface, also favored by the high permeability of the geological formations (Arnórsson, 1985).

3.3.1 Krafla

The Krafla high-temperature geothermal system is located within the active caldera of the Krafla central volcano, originated less than 500.000 years ago (Sæmundsson, 1991), in the neovolcanic zone of the axial rifting in N-Iceland (Fig. 3.8). The Krafla central volcano (300–500 m elevation) extends over an area of 21 by 17 km and is associated with a 5-10 km wide and 100 km long NNE–SSW trending fissure swarm which intersects the caldera (Sæmundsson, 1991; Hjartardóttir et al., 2012). Volcanic activity is extensive and there have been several fissure eruptive episodes during the last few thousand years; during the most recent event, which started in late 1975 after a quiet period of about 250 years, nine eruptions took place, the last one occurring in September 1984 (Björnsson, 1985). The rifting episode was characterized by long inflation periods, during which magma accumulated at shallow depth into the magma reservoir below the caldera region (Björnsson et al., 1979), and subsidence events, when the magma laterally migrated away from the chamber into the fissure swarms or extruded at the surface (Björnsson, 1985; Einarsson, 1991).

Seismic studies (Einarsson, 1991; Brandsdóttir et al., 1997), during the beginning of the rifting episode (Ewart et al., 1991), evidenced the presence of a shallow-level magma chamber (2-3 km N-S, 8-10 km E-W wide and 0.7-1.8 km thick) located at 3 km depth beneath the Krafla caldera. More recently, tomographic results obtained by Schuler et al. (2015) recognized two distinct low-V_p anomalies at 2–3 km depth b.s.l. under Víti and east of

Hvannstóð, which matched with the two attenuating bodies inferred from S wave shadows, as suggested by Einarsson (1978) during the Krafla fires. Furthermore, Schuler et al. (2015) associated the very low-V_p/V_s region found underneath the geothermal field with the superheated steam layer, which lies between the host rock and the felsic melt. The presence of a shallow magma chamber is responsible of the very high temperatures (>300 °C) in the Krafla reservoir system and represents the heat source of the geothermal reservoir (Böðvarsson et al., 1984). Presently, the region hosts a 60MW power plant (Björnsson, 2006) and the shallow magma body was twice intercepted during drilling, the last time in 2009 at 2104 m depth (Elders et al., 2011; Pope et al., 2013; Zierenberg et al., 2013). The drill cuttings showed layers of hyaloclastites alternated with lava successions and small intrusions of dykes and sills, dominating the upper 1200–1400 m of the Krafla geothermal system. Below 1800 m larger intrusive bodies of gabbro and occasional granophyre are the dominant lithologies (Guðmundsson, 1983; Ármannsson et al., 1987). Geothermal manifestations are extensive in the Krafla area with steaming, altered ground, fumaroles and mudpools which cover an area of about 15 km^2 (Stefánsson, 1981; Ármannsson et al., 1987). The high-T area can be divided into four separate fields: Leirhnukur, in the centre of the caldera, Leirbotnar, Suðurhlíðar, separated by a semi-linear series of explosive craters called Hveragil, and Hvíthólar fields, the latter lying near the southern caldera margin at 2 km south of Leirbotnar (Fig. 3.10).

The three latter were drilled and revealed a complex geothermal system (Stefànsson, 1981; Ármannsson et al., 1987) consisting of: i) Leirbotnar, a relatively cool (190-220 °C) water-dominated upper zone, which extends from about 200 m below the surface down to about 1100 m and a hot (300-350 °C) lower boiling reservoir; ii) Suðurhlíðar, a system characterized by a boiling temperature-pressure curve at all depths suggesting a single zone of production, probably boiling near the surface and iii) Hvíthólar, a boiling upper part that extends from the surface to 600 m with a temperature of 250-260 °C and below, a cooler water-satured zone where the temperature is 170-190 °C at 1200 m and then gradually increases to 240-250 °C at 1800 m. Further to the south, along the boundary of the central volcano, another wellfield produces from the Námafjall geothermal region (Fig. 3.11) (Ármannsson et al., 1987).
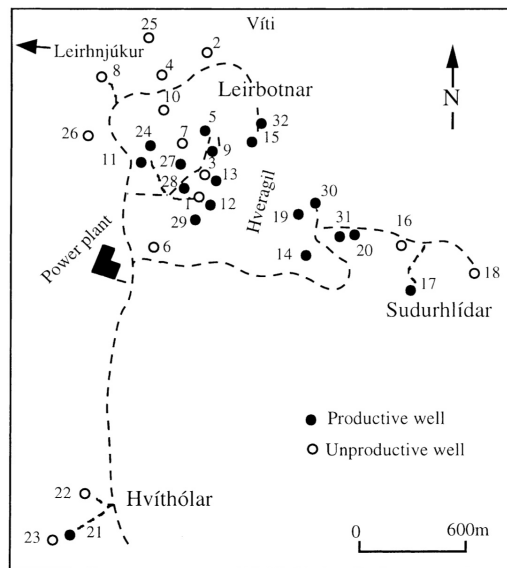
Fig. 2. The three wellfields at Krafla.

FIGURE 3.10: *The Krafla area with the three main wellfields. The productive and unproductive wells were also indicated (from Guð-mundsson and Arnórsson, 2002).*
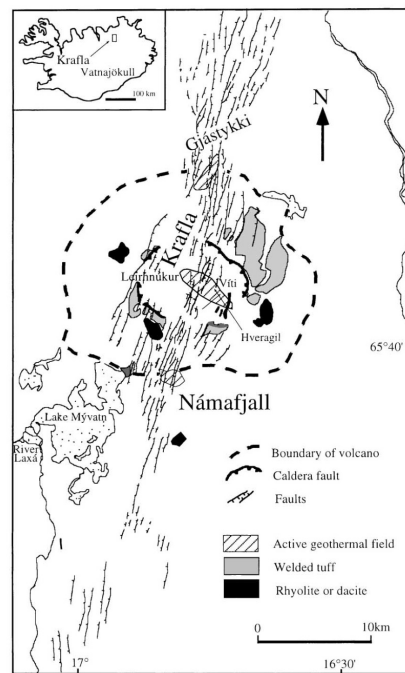
FIGURE 3.11: *The Krafla and Námafjall geothermal areas with the associated fissure swarms (from Guðmundsson and Arnórsson, 2002).*

During the 1975-1984 volcanic-rifting episode at Krafla, parts of the geothermal system were severly affected by magmatic gases, with an increase of the gas content (mostly CO_2) of the steam-rich fumaroles, probably due to the new degassing magma intruded into the roots of the geothermal system (Ármannsson et al., 1989). This magmatic contribution has decreased with time. Only at Leirbotnar field, changes in gas concentration were detected and at present some of the wells around Hveragil are still affected by gas from this new magma batch. The Suðurhlíðar and Hvíthólar fields seemed not to be affected (neither an excess of volcanic gas nor heating was observed; Ármannsson et al., 1987) and that of Námafjall was, though at a limited extent, and only temporarily after the laterally intrusion of magma from the chambers under Krafla into the Námafjall geothermal system. The water discharged from wells at Krafla is very dilute (900–1500 mg/L as total dissolved solids) and typical of meteoric-dominated Icelandic geothermal systems, resulting from limited Cl availability in basalt-hosted systems (Arnórsson, 1995). In the hottest wells, the total gas concentration far exceeded that of the solids. Pope et al. (2014) suggested that there is only one primary geothermal fluid source, locally derived from nearby meteoric waters from the north. The large spatial variation in the stable isotope composition of geothermal fluids observed at Krafla is the result of localized boiling, phase separation with variable mobilization of the vapor and liquid fractions of the fluids and mixing with magmatic gases released from shallow magmatic intrusions into the caldera. The fumarole gas composition in the area was relatively stable from 1871 to 1975 when the Krafla fires started. Carbon dioxide is the most abundant gas, followed by H_2S, H_2 and N_2 (Guðmundsson and Arnórsson, 2002). Measurements of H_2S and SO_2 were mainly carried out in two wellfields of the Krafla geothermal area: Leirbotnar and Hvíthólar (Fig. 3.12 and 3.13).

3.3.2 Námafjall

Námafjall high-temperature geothermal field (Fig. 3.8) lies outside the Krafla caldera in the southern half of the fissure swarm that is associated with Krafla central volcano (Fig. 3.11) (Pálmason and Sæmundsson, 1974; Sæmundsson, 1991; Guðmundsson and Arnórsson, 2002). The Krafla and Námafjall high-T geothermal areas have been exploited for steam production

FIGURE 3.12: *The fumarole gas emission measured at Hvíthólar geothermal field within Krafla system.*

FIGURE 3.13: *The fumarole gas emission measured at Leirbotnar geothermal field within Krafla system.*

since the 1970s and estimation of the initial aquifer steam fraction and pressure logging showed that Krafla and Námafjall geothermal reservoirs are liquid dominated (Guðmundsson and Arnórsson, 2002). A total of 12 wells were drilled at Námafjall, providing steam for drying diatomaceous earth extracted from the bottom of the nearby Lake Myvatn and operating a 3 MW back-pressure turbine unit (Ragnars et al., 1970). Only three of these

wells are presently productive, because most of them were damaged or destroyed in September 1977 during seismic movements of the active fissures and faults and intrusions of magma into the geothermal system (Sigurdsson, 1993). The boreholes at Hverir were abandoned and some developed into powerful fumaroles that are now a tourist attraction. The highest temperatures recorded downhole at Námafjall were 320 °C and the deepest well was drilled down to 1950 m. The eruption history of the Námafjall and Krafla areas is closely related since they belong to the same fissure system. Námafjall is thought to be the "parasitic" system of the Krafla volcanic field (Arnórsson, 1995): as mentioned above, magma from the Krafla caldera likely intruded horizontally in the Námafjall direction along fissures and fractures, serving as the heat source for the hydrothermal system. As an evidence, during the Krafla eruption in 1977, well B4 in Námafjall discharged magma (Larsen, 1978 cited in Isabirye, 1994). The Námafjall field is characterized by the Námafjall ridge, about 2.5 km long and 0.5 km wide, which is part of the NNE-trending larger hyaloclastite ridge called Námafjall-Dalfjall-Leirhnjúkur, about 15 km long and 1 km wide; it is bounded by two main faults, namely the Krummaskard and Grjótagja faults, along which surface manifestations are associated (Mortensen et al., 2008). The subsurface geology at Námafjall, as shown in drill cuttings, is characterized by an upper succession, which represents the aquifer rock, mainly made of subglacially formed hyaloclastites and interglacial basaltic lavas intersected by intrusions (Ármannsson et al., 1987; Guðmundsson, 1993a). The lower succession is mainly composed of lava from shield volcanoes intercalated with hyaloclastite layers while intrusive formations dominate below about 1500 m depth. The geothermal area at Námafjall has a surface of about 3–4 km^2 (Sæmundsson, 1991), where steaming ground, mud pools, fumaroles and large quantities of native sulphur deposits are widely spread. The thermal manifestations are mainly located on the Námafjall hill (150 m above surroundings) and on the low ground east and west of the Námafjall Ridge: Hverarönd and Bjarnarflag (Fig. 3.14) (Ragnars et al., 1970; Ármannsson et al., 1987; Mortensen et al., 2008; Ármannsson, 2011). Temperature logs and subsurface hydrothermal alteration reveal temperatures at around 300 °C below 1000 m depth, slightly increasing with depth (Hjartarson et al., 2004; Guðmundsson, 1993). The main upflow zone of the geothermal system is
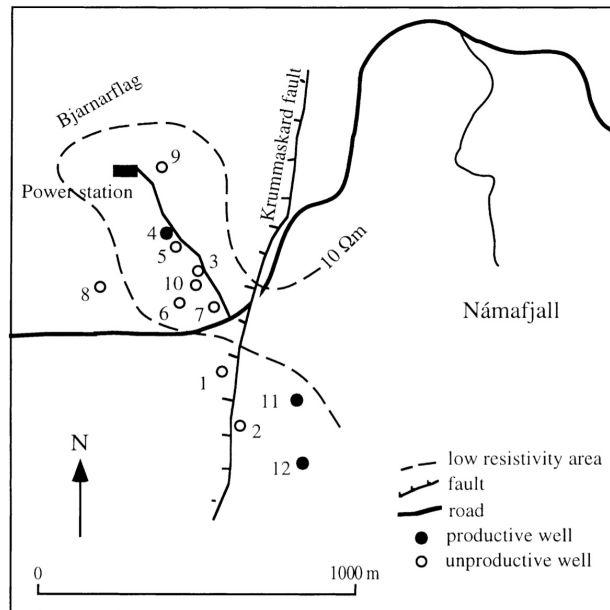
Fig. 3. Wells in the Bjarnarflag field of the Námafjall geothermal area.

FIGURE 3.14: *Wells in the Bjarnaflag field of the Námafjall geother-
mal area (from Guðmundsson and Arnórsson, 2002).*

located under Mt. Námafjall, as evidenced by the presence of a high resis-
tivity area. Smaller secondary upflow zones can be found in the NW part of
the field. Fluid and several gas samples were collected from surface mani-
festations in the period 1952-1993 (Ármannsson, 1993) and several geother-
momethers were used to estimate reservoir temperatures in the Námafjall
geothermal systems, which resulted: i) > 300 °C at Hverarönd (Hverir), east
of Námafjall ridge; ii) close to 280 °C east of the Krummaskard fault and
gradually decreasing westwards; iii) up to 240-260 °C at Bjarnaflag, west
of the Námafjall ridge where most wells were drilled (Guðmundsson and
Arnórsson, 2002). During the beginning of the 1975-1984 volcanic episode,
the fumarolic activity at Námafjall increased, likely due to the increased boil-
ing of a two-phase aquifer fluid. On the other hand, no changes in the gas
content of well discharge and fumarole steam were observed (Arnórsson
and Gunnlaugsson, 1985), suggesting that the magma intruded from the
chambers below Krafla was already largely degassed. Furthermore, wells
drilled at Námafjall prior the volcanic episode showed temperatures follow-
ing the boiling point curve with depth, while in wells drilled after, temper-
atures at the top of the reservoir were sub-boiling. This is probably due to

the ingression of cold shallow groundwater into the reservoir, facilitated by fractures activated during the volcanic-rifting event. After 1988, the initial conditions seemed to be restored (Guðmundsson and Arnórsson, 2002). The highly permeability of the system is mainly due to young and fractured lava fields transacted by numerous faults (i.e. Krummaskard and Grjótagja fractures) and for this reason, all the precipitations within the area likely penetrate underground (Kristmannsdóttir and Ármannsson, 2004). The Námafjall geothermal system is considered hydrologically independent from that of Krafla and the water recharge is thought to be of meteoric origin (Arnórsson et al., 1983) that feeds the local groundwater system in the vicinity of the system seeping through the fissures and fractures (Fig. 3.15)(Arnórsson, 1995). At Námafjall, the relative gas concentrations are different respect to
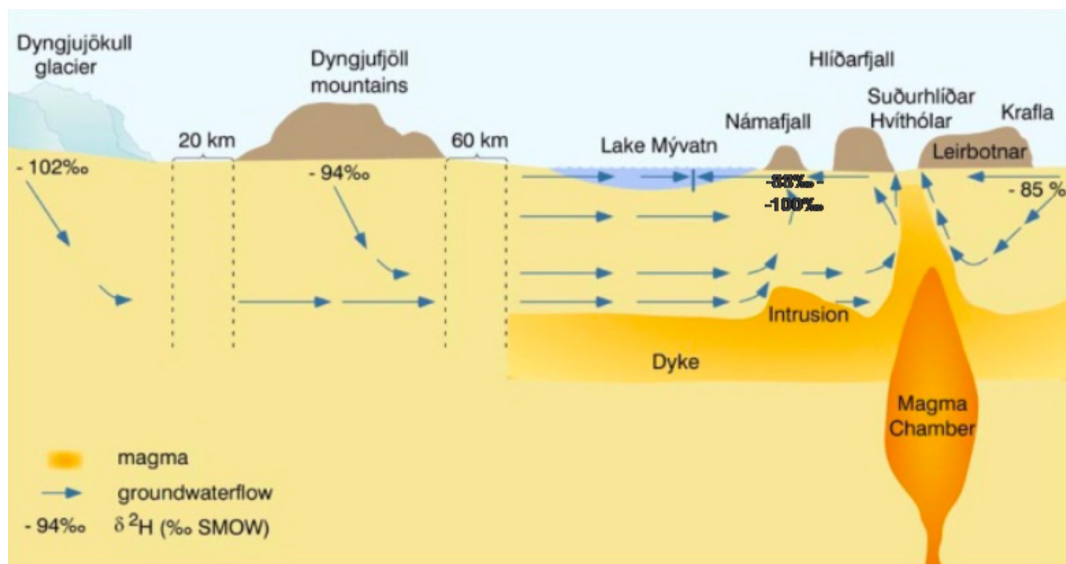
FIGURE 3.15: *Groundwater flow conceptual model of Námafjall and Krafla geothermal systems (from Guðmundsson et al., 2010).*

those of Krafla: CO_2 is less abundant and correspondingly, H_2 and H_2S are more abundant (Ármannsson, 1993). The high H_2 concentration is considered to be due to the relatively high fraction of equilibrium steam in the reservoir (Arnórsson, 1995). Transient pulses, like during the Krafla fires, can double or even triple the CO_2 concentration. A substantial increase of methane was also observed in 1979 and attributed to the Krafla fires (Ármannsson, 2016). The $\delta^{13}C\text{-}CO_2$ is consistent with a magmatic origin for the gas according to Ármannsson et al. (1998). In this study, the H_2S and SO_2

measurements were carried out at the Hverir and Bjarnaflag geothermal areas (Fig. 3.16 and 3.17).
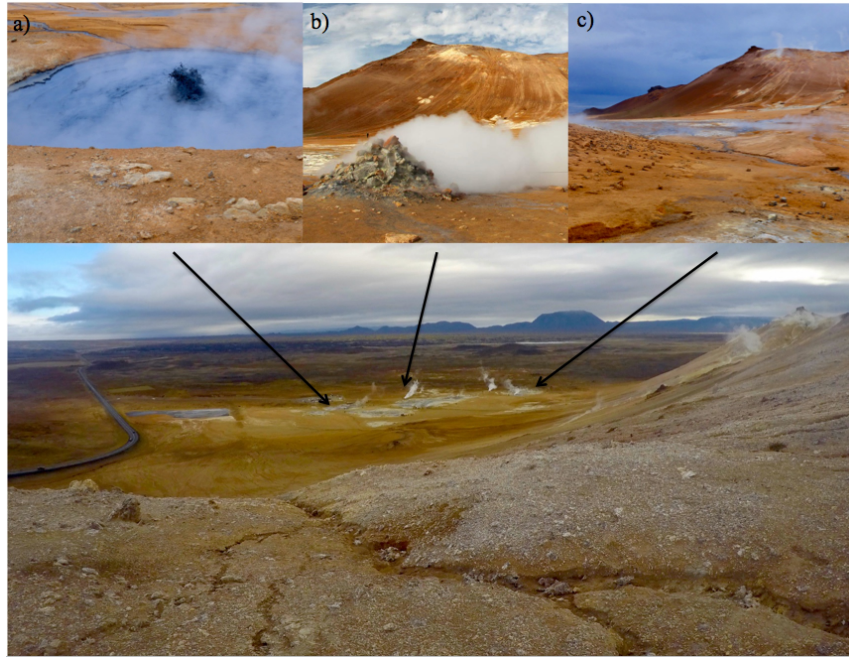
FIGURE 3.16: *The Námafjall Hverir geothermal area with the different type of gas emission measured in this study: (a) the big boiling mud pool, (b) the borehole and (c) the small boiling mud pools.*

FIGURE 3.17: *The gas emission measured in this study in the Bjarnaflag geothermal area.*

3.3.3 Reykjanes Peninsula

The Reykjanes Peninsula (RP) is the southwestern tip of Iceland and represents the landward extension of the slow spreading Mid-Atlantic Ocean Ridge (MAR). The RP segment of the rift became active at 6-7 Ma (Sæmundsson, 1979), and is 65 km long (Peate et al., 2009). It is connected with the submarine Reykjanes Ridge (RR) to the west and with the Hengill triple junction to the east (Fig. 3.8). The Reykjanes Peninsula is the most active region as far as the microearthquakes are concerned (Ward and Björnsson, 1971) and is dominated by estensional tectonics that formed a rift valley (graben) associated with an intense NE-SW trending fault zone (Björnsson et al., 1970). The RP lacks central volcanoes with shallow magma chambers and it is built up by young, highly fractured basaltic formations, low relief lava fields, as well as scoria and tuff cones formed during episodic fissure eruption volcanism (Jakobsson et al., 1978; Thordarson and Larsen, 2007). The most recent volcanic eruptions occurred between the 12th and the 13th century, and were likely fed from fissures tapping magma reservoirs in the mantle (Thordarson and Larsen, 2007).

As a result of the extremely high rock permeability and low hydrostatic heads on the land side, seawater easily percolates through the shallow post-glacial lavas, which cover the low-lying western half part of the Reykjanes Peninsula. In this part of the peninsula, the ground-water table level is very low, only 1.5 m above sea level (unpublished data by the National Energy Authority), whilst in the eastern part the level is lower because of the higher elevation of this area (200-400 m) and the abundant presence of Quaternary lower permeability rocks. At the same time, also rainwater can enter the system easily and outside of the Reykjanes geothermal area a thin fresh water lens (<30 m thick) float on seawater-derived groundwater (Sigurdsson, 1986). The geothermal activity seems to be controlled by the complex local tectonics and magmatic activity (Jakobsson et al., 1978; Arnórsson, 1995), which facilitate the circulation of groundwater and seawater through the basaltic crust and permit quite uniform temperatures below the boiling zone (Jónsson, 1968; Fridriksson et al., 2006). The main volcanic systems are, from west to east, Reykjanes (partially submarine, 56 km^2), Svartsengi (115 km^2), Krýsuvík (133 km^2) and Brennisteinsfjöll (142 km^2) (Fig. 3.18) (Peate et al., 2009, Sæmundsson and Sigurgeirsson, 2013). Each system hosts a geothermal field, all of them lying on the plate boundary (Björnsson et al., 1977) and whose heat is provided through dykes and sills intruded at depth, which are extensively fractured due to active crustal rifting (Guðmundsson, 1995). They might be more similar to the systems on the submarine extension of the volcanic belts, the Mid-Atlantic Ridge, than to the other high-temperature geothermal fields in Iceland because of the absence of differentiated volcanic and caldera structures.
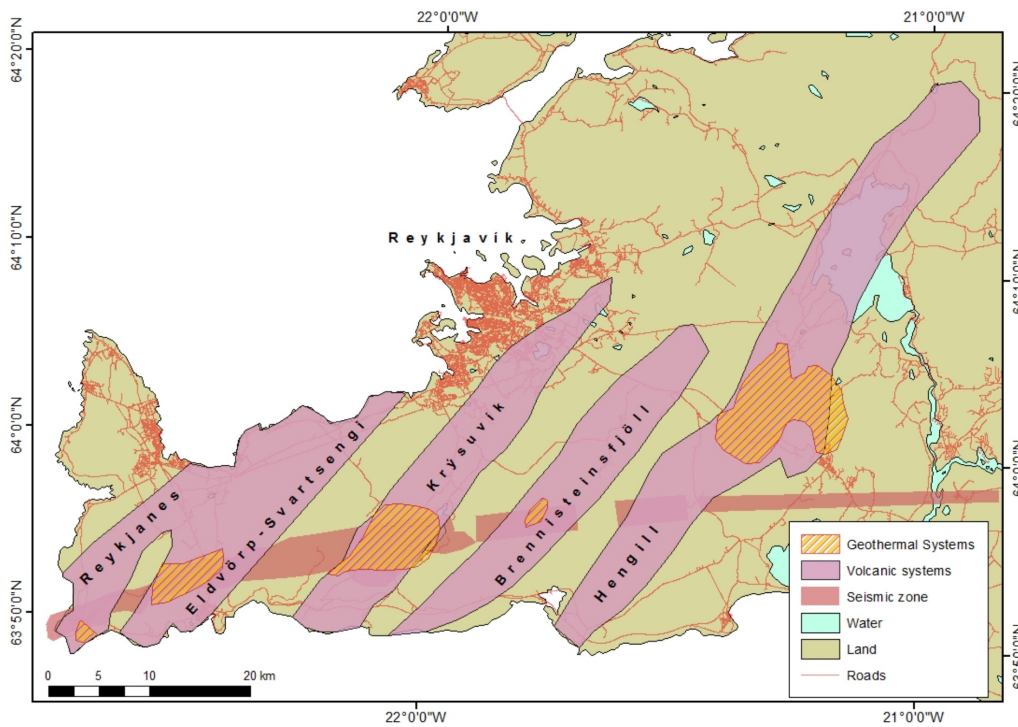
FIGURE 3.18: *Volcanic systems on the Reykjanes Peninsula (pink
color) and the relative geothermal areas (stiped) (from Guðjónsdóttir
et al., 2018).*

Most aquifers intercepted by the production wells showed temperatures
between 140 and 290 °C, the highest values being recorded at Reykjanes and
lowest ones at Svartsengi (Björnsson et at., 1972; Arnórsson et al., 1975); the
only exception is the aquifer of well RN-10, which had temperatures of about
315 °C (Björnsson et al., 2004). The fluids discharged from the wells showed
a large variation in salinity. It is higher and close to that of seawater in the
Reykjanes geothermal field, in the south-west tip of the peninsula, while
it decreases, towards the Krýsuvík area, which is farthest east of the three
drilled fields (Arnórsson et al., 1978).

Reykjanes

The Reykjanes geothermal area is located at the center of the Reykjanes vol-
canic system (Jakobsson et al., 1978) in the south-western tip of the Reykjanes
Peninsula and it is the westernmost system of Iceland volcanic zones (Fig.
3.18). It is a basalt-hosted, seawater dominated, active hydrothermal system
and it is one of the smallest high-temperature fields in Iceland, with surface

manifestations and altered ground, covering an area of $\sim$2 km^2 (Björnsson et al.,1972; Pálmason et al., 1985), although most of the current surface activity is concentrated in an area of approximately 0.2 km^2. The uppermost 1 km of the geothermal area is characterized by a porous layer of hyaloclastite tuffs, breccias, and tuffaceous and marine sediments, which, below 400–500 m, form a cap-rock for the geothermal system preventing the inflow of relatively cold saline ground waters; the deeper part is dominated (50-60%) by basaltic lavas and intrusive rocks. Surface geothermal manifestations at Reykjanes include steam vents, steam heated mud pools, and steam emanating fractures, which strongly depend on local seismic events for mode and intensity. A shallow freshwater lens is localized in the upper 30 m of the geothermal system due to the penetration of surface waters through highly faulted permeable rocks (Sigurðsson, 1986). Thirteen small aquifers were identified in the well RN12, all cased off, but three main feeding zones were inferred at depths of 1000, 1300 and 2200 m. The Reykjanes geothermal system lacks a shallow magma chamber but a low resistivity anomaly at 10 km depth was recently found by MT surveys and interpreted as a dense, partially molten, dyke complex or a large cooling gabbroic intrusion, which is suggested to be the heat source of the shallower hydrothermal system (Friðleifsson et al., 2011; Friðleifsson and Richter., 2010). Franzson et al. (2002) suggested that there is a primary upflow zone in the area below the wells RN12, RN21 and the Gunnuhver thermal area (Fig. 3.19), which is the larger, most active and intensely altered part of the geothermal area and contains steam vents, boiling mud pools and characterized by intense argillic alteration.
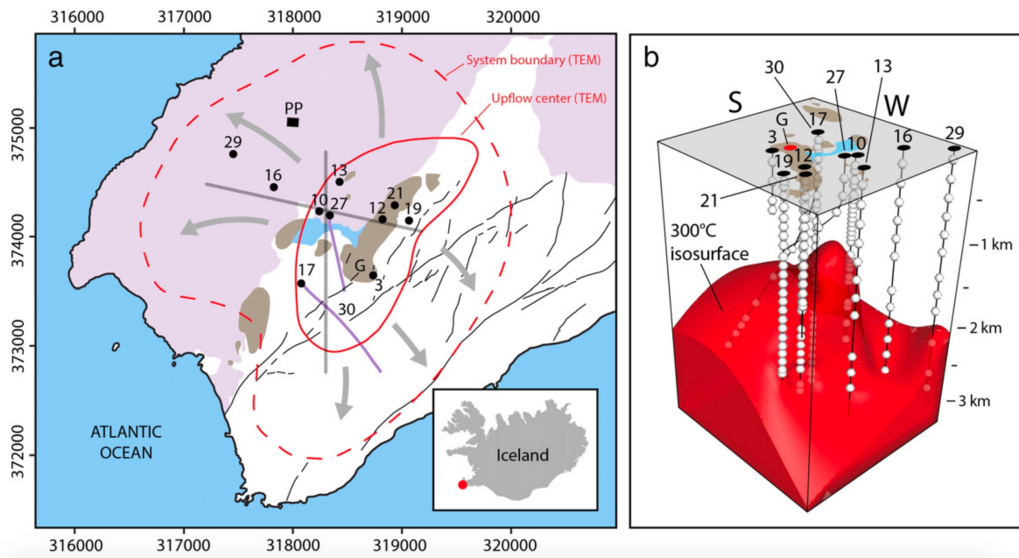
FIGURE 3.19: *(a) The Reykjanes geothermal field. The dashed line delimits an area where the low resistivity cap reaches a depth of 800-1000 m; the red line the upflow center; the gray arrows the inferred outflow paths; the black lines fractures and faults; the brown areas indicate altered ground; PP = Reykjanes geothermal power plant; G = Gunnuhver thermal area. (b) 3D well map showing sample locations (spheres) and the measured 300 °C isosurface (from Libbey and Williams-Jones, 2016).*

The bigger steam vent of Gunnuhver is the one considered in this study together with a small fumarole nearby (Fig. 3.20 and 3.21). Measured reservoir temperatures at Reykjanes are commonly in the range of 280 to 300 °C. However, the well RN10, west of RN12, shows higher temperatures ($\sim$320 °C; Franzson et al., 2002; Björnsson et al., 2004) at 1 km depth, while RN17B and RN30 shows temperatures as high as 345 °C and 350 °C (Friðleifsson et al., 2011; Friðriksson et al., 2015), respectively, suggesting that the present upflow can be extended towards the west and to the south (Fig. 3.19) (Libbey et al., 2016). This upflow zone is tectonically controlled by the intersection of the main NE–SW trending zone of normal faults and fissures, with a short N–S fracture and an unmapped NW–SE transform fault that cross the Gunnuhver thermal area (Sigurðsson, 2010).

FIGURE 3.20: *Gunnuhver steam vent measured in this study at Reykjanes geothermal area.*

FIGURE 3.21: *The small fumarole close to the Gunnuhver steam vent measured in this study at Reykjanes geothermal area.*

Pope et al. (2009) suggested a major upflow around well RN10 and a first boil of the upflowing geothermal fluids at a temperature of 320 °C at a depth of ~1.3 km below the water table (Franzson et al., 2002; Arnórsson et al., 2007; Friðleifsson et al., 2014). It is therefore expected that below about 1.3 km, geothermal fluids are in a liquid phase (sub-boiling), whereas above this depth are into two-phase and follow the boiling point curve until they reach the cap-rock (Flóvenz and Sæmundsson, 1993; Franzson et al., 2002; Pope et al., 2009). Away from the thermal area around RN10, first boiling occurs at shallower depths, but always below 500 m within the main geothermal field. Deeper in the reservoir, up to 2.5 km, a convective heat transfer dominates, while at increasing depth, temperature increases by conduction (Franzson et al., 2002, Friðriksson et al., 2015). The present-day hydrothermal fluids of Reykjanes are characterized by a Total Dissolved Solids (TDS) and chloride content higher than most geothermal waters in Iceland and water chemistry closely resembles that of seawater (Björnsson et al., 1972; Arnórsson, 1978) due to both the proximity to the coast and the highly permeable and strongly fractured basaltic host-rocks, which facilitate the influx of the saline water into the hydrothermal system (Björnsson et al., 1972; Arnórsson et al., 1978, 1995). Other major elements, including SiO_2, Ca, and K, suggested that fluids were affected by substantial chemical modification through boiling, water–rock interaction, and possibly evaporation (Lonker et al., 1993; Arnórsson, 1995; Pope et al., 2009). Moreover, the lighter hydrogen isotopic content with respect to that of seawater, fluids inclusion analyses and stratigraphic studies indicated that meteoric/sea water ratio varied through time (Sveinbjörnsdóttir et al., 1986; Pope et al., 2009), suggesting that glacially-derived freshwater dominated the system at some time during the Pleistocene. The dry gas concentrations showed CO_2 to be the dominant gas, while H_2S, $H_2$2 (reflecting the temperature of the aquifers) and CH_4 (indicating organic contribution) were relatively low when compared to those of fluids from other Icelandic geothermal areas (Ármannsson, 2016). The significantly high N_2 concentrations were related to shallow contribution. The $\delta^{13}C$ values in CO_2 suggest a magmatic origin for these gases (Ármannsson et al.,1998).

Krýsuvík

Krýsuvík is a high-temperature geothermal system, located in the center of the RP, covering an area of 40–60 km^2 (Guðmundsson et al., 1975). This system can be divided into 6 sub-areas: Sandfell, Trölladyngja, Köldunámur, Austurengjar, Hveradalir and Seltún (Fig. 3.22). The main surface hydrothermal activity occurs in the last three areas and mainly consists of hot and altered ground with mud pools, fumaroles and solfataras. The geothermal activity is associated with two hyaloclastite ridges: Vesturháls and Sveifluháls, and a fault passing through Austurengjar, east of the Sveifluháls ridge (Fig. 3.22).
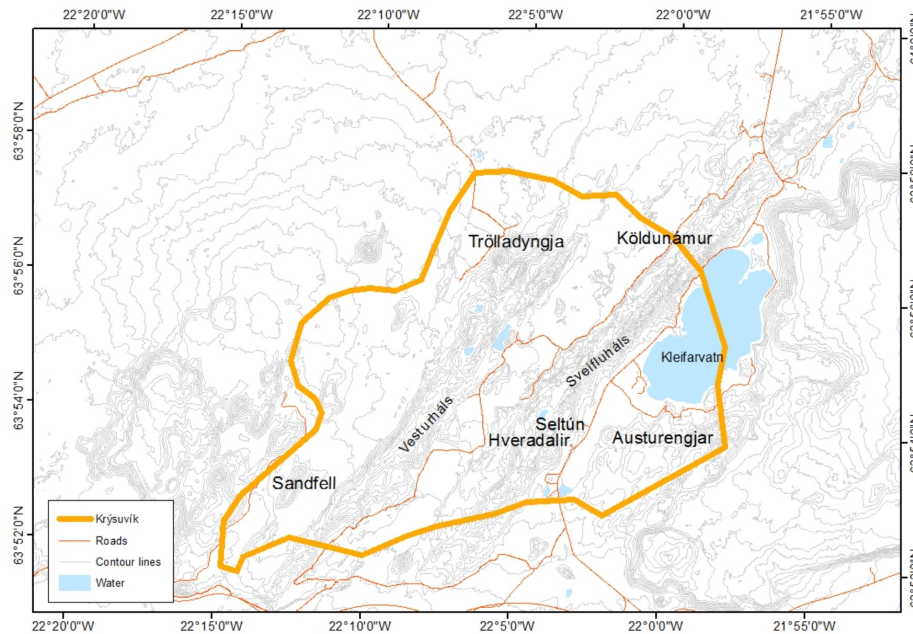
FIGURE 3.22: *Krýsuvík high-temperature system identified by resistivity surveys (orange line). The two hyaloclastite ridges, Sveifluháls and Vesturháls, associated with the geothermal activity in Krýsuvík, are also reported (from Guðjonsdottir et al., 2018).*

The Krýsuvík system, as the whole RP area, is not connected to a major magma chamber but it was dominated by rift volcanism (Arnórsson et al., 1975) with the last volcanic eruption occurring in the 12th century (Sæmundsson and Sigurgeirsson, 2013). The heat source of this geothermal area

is considered to be related to dyke intrusions (Arnórsson et al., 1975; Arnórsson, 1987) and the equilibrium temperature suggested by gas geothermometers ranges between 200-300 °C for the Krysuvik geothermal system (Arnórsson et al., 1975). Two upflows were suggested by Arnórsson (1987), one in the southern end of Lake Kleifarvatn Krýsuvík subarea and the other in the Trölladyngja subarea. Recent resistivity measurements showed a conductive body at approximately 2 to 5 km depth (Didana, 2010; Hersir et al., 2013) beneath the central part of the Krýsuvík geothermal area, with an approximate extension of 10 km^2 (Michalczewska et al., 2012; Hersir et al., 2013). The lack of S-wave attenuation in the region suggested the presence of a gas or supercritical fluid at 6 km depth (Adelinet et al., 2011) and not the presence of large volumes of molten materials. An enormous amount of hot water exists within the system (Guðmundsson et al., 1975). This thermal water is characterized by high variations in the TDS content from the different subareas as a result of distinct proportions in the mixing between hot and saline and fresh water at depth (Guðmundsson et al., 1975). Steam- and CO_2-dominated emissions with subordinate H_2S, $\delta^{13}C$ values in CO_2 and high Helium isotopic ratios (Poreda et al., 1992) suggested that a magmatic source was feeding the hydrothermal system (Ármannsson et al., 1998). H_2S and SO_2 measurements were carried out in the Seltùn touristic area, mainly around a boiling pool emission (Fig. 3.23).

FIGURE 3.23: *The boiling pool considered in this study in the Seltùn thermal area.*

3.3.4 Hengill area

The Hengill Area is located 20 km SE of Reykjavík at the meeting point between the Reykjanes Peninsula Volcanic Zone (RP), the Western Volcanic Zone (WVZ) and the South Iceland Seismic Zone (SISZ), which is a transform zone (Fig. 3.8) (e.g., Hersir et al., 1984, 1990; Steingrimsson et al., 1986; Árnason et al., 1987; Foulger, 1988a, b; Foulger and Toomey, 1989; Walker, 1992). The vast Hengill geothermal system is one of the largest high-temperature geothermal areas in Iceland and is an important power source since it provides electricity to Reykjavík and surroundings for both domestic and industrial use, as well as for heating needs (Björnsson et al., 2003; Franzson et al., 2005). Extensive geological, geophysical and geochemical surveys were carried out in the Hengill area for geothermal exploration from the 1940s until the 1980s, after which two main geothermal power plant were built: Nesjavellir and Hellisheidi, still active and located at NE and SW of the Hengill volcano, respectively (Björnsson et al., 2003; Franzson et al., 2005). The Hengill complex is centred in a 70-80 km long fissure system with an associated graben structure. It hosts three main volcanic centres, which are, listed in decreasing age and from E to W: Grændalur, Hrómundartindur (Ölkelduháls) and the 800 m high Hengill central volcano, which topographically dominates the system (Fig. 3.24). Each system is NE-SW alinged along the fissure swarms towards the Thingvallavatn lake following parallel trends. Both Hrómundartindur and Hengill have erupted in post-glacial times. Hrómundartindur last erupted about 11000 years ago and Hengill, 5000 and 2000 years ago (Árnason et al., 1987a). At present day, the Grensdalur and Hrómundartindur systems are almost extinct as a result of migration of the locus of spreading to the currently active Hengill system. The most recent magmatic activity at Hengill occurred in 1789, with intrusive volcanism, i.e. dyke injection (Sæmundsson, 2006) combined with an intense earthquake swarm that affected 30 km of the fissure from Mt. Hengill north to Thingvellir (Palsson, 1945). Silicic lava can be found in the Hengill volcanic system suggesting an evolved magma chamber (Trønnes, 2012). However, seismic tomography and gravity studies provided no evidence for a substantial shallow magma body beneath Mt. Hengill (Tryggvason et al., 2002) like the one suggested for the Krafla caldera in north Iceland (Brandsdóttir et al. 1997). Magnetotelluric measurements made at
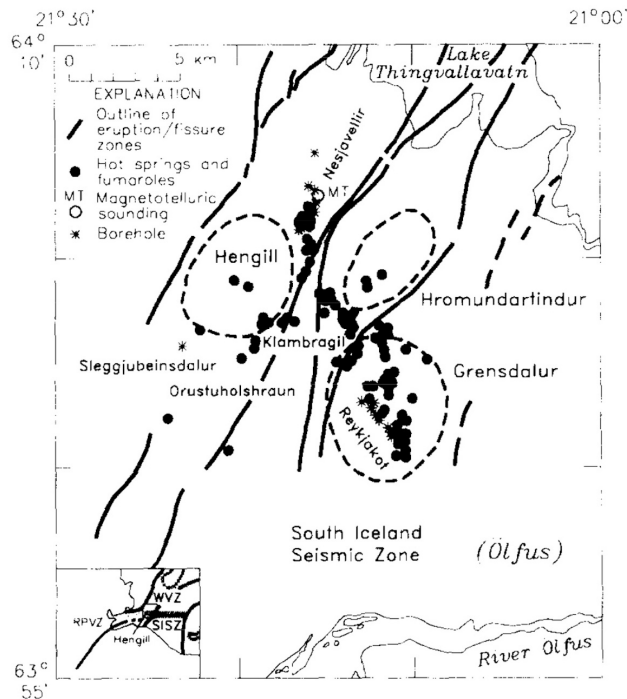
FIGURE 3.24: *The Hengill area. The three volcanic systems (Grens-dalur, Mt. Hengill and Hromundartindur; dashed lines) are shown with the associated fissure swarms (from Foulger, 1984).*

Nesjavellir detected an aseismic high-conductivity layer and low-velocity body few km thick at a depth of 7.5 km beneath and to NE of Mt. Hengill (Hersir et al., 1990). This was interpreted to be an isolated body partially melt above the top of a seismic layer, elongated parallel to the fissure swarm (Foulger and Toomey, 1989; Foulger and Arnott, 1993). This body was activated or formed during the most recent magmatic event in 1789. On the other side, Tryggvason et al. (2002) observed that the reduction in the P-wave velocity was larger than the S-wave velocities and suggested that the low-velocity anomaly found at dephts beneath the Hengill volcanic system was not caused by partial melting but by supercritical fluids, meteoric water and fluids of magmatic origin, which are present in a strongly fractured volcanic fissure system. However, this model did not exclude the possible presence of small quantity of melt (0.01 km^3), invisible to tomography, beneath the Hrómundartindur volcano, as suggested by Sigmundsson et al. (1997). Gas geochemistry and distribution of the thermal-cracking earthquakes indicated that separate heat sources underlie each volcanic system, rather than

a common heat source connected to a shallow magma chamber located beneath the Hengill central volcano, as was previously assumed (Böðvarsson et al., 1990). The heat source for the system was believed to be a complex of solidified dykes, sills and intrusions that became dominant above 1.5 km depth and associated with an eruptive fissure active during the Holocene (Árnason et al., 2010; Scott et al., 2013). Deep circulation of groundwater in highly fractured rocks were suggested to transfer the heat upwards (Franzson et al., 2010). The geothermal area is mainly dominated by hyaloclastites and the typical surficial emissions of the area are fumaroles, clayey ground and pools with muddy or turbid water. The temperatures of the fumarole steam at Hengill are at the boiling point of water at the Hengill elevation ($\sim$100 °C) and show a typical hydrothermal composition, with H_2O as a major constituent (meteoric origin), followed by CO_2, H_2S, H_2, N_2, CH_2, and He, while CO and acid gases SO_2, HCl, and HF are practically absent (Marty et al. 1991). The whole Hengill volcanic system is characterized by a source having a mean R/R_a of 14.4 $\pm$ 1.6, higher than the normal mid-ocean ridge (8 $\pm$ 1), suggesting hot-spot helium for Hengill (Marty et al. 1991) and a mantle source for volatiles and gases at the surface environment in this system. The natural emissions measured in this study were located i) to the south of Hengill volcanic centre, at Hengill Skidaskali, close to the Hellisheidi power plant and ii) to the east of Hengill volcanic centre, in the geothermal field of Ölkelduháls (in the core area of the Hrómundartindur volcanic complex) (Fig. 3.24). The emissions measured consisted mainly of mud boiling pools and fumaroles in both systems (Fig. 3.25 and 3.26).

In the Ölkelduháls geothermal field, three wells were drilled, two with 200-210 °C temperatures and marginal to the volcanic axis, and one closer and hotter (280 °C) (Arnórsson, 2016). The wells were characterized by extremely permeable formations especially at 1000-1200 m depth. Discrepancies in gas geothermometer temperatures and especially a considerable CO_2 flow from depth was interpreted as being due to a hotter system at depth than at the drilled depths (Björnsson, 2007). The Hydrothermal conceptual model of western Ölkelduháls geothermal area is reported in Fig. 3.27.

FIGURE 3.25: *Fumaroles and mud boiling pools measured in this study in the geothermal area of Ölkelduháls.*

FIGURE 3.26: *The mud boiling pool measured in this study at the thermal area of Skidaskali.*

3.3.5   Geysir

The Geysir geothermal area in Haukadalur is one of the Icelandic high-temperature areas and one of the most famous tourist attractions for the phenomenon of the erupting hot spring, hence the name "geyser". The Geysir area is located in southern Iceland, just east of the western volcanic
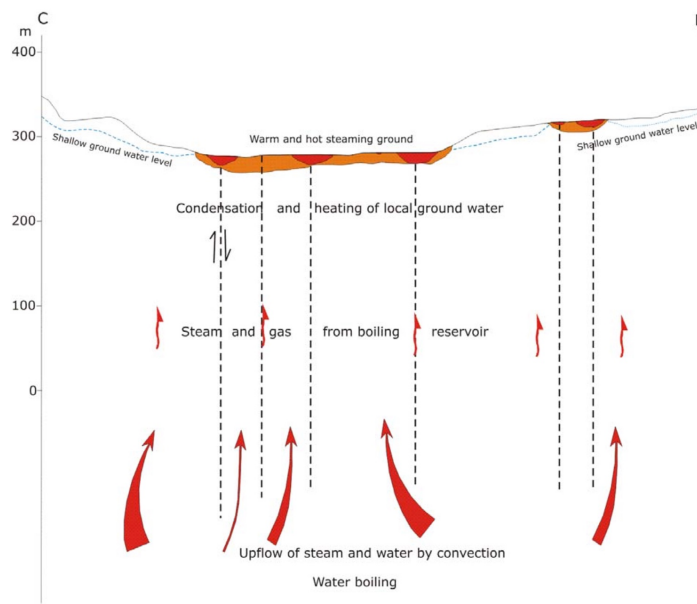
FIGURE 14: Hydrothermal model of western Ölkelduháls field along line C-D

FIGURE 3.27: *Hydrothermal conceptual model of western Ölkel-*
duháls geothermal area (from Gebrehiwot, internal report n7, 2005).

rift zone (WRZ, Fig. 3.8), about 110 km from Reykjavik at approximately
100 m a.s.l., in a shallow NS-oriented valley. During the last 10,000 years no
volcanic activity was recorded and the geothermal system is likely driven
by volcanic intrusions located at a shallow level in the crust, in the roots
of an extincted central volcano (Sæmundsson, 1979). Geysir is one of the
four geothermal areas (i.e. Torfajökull, Kerlingafjöll and Askja) character-
ized by major silicic rock formations, whereas the others in Iceland are dom-
inated by basaltic rocks. Most of the geothermal activity (i.e. hot springs,
geyser activity, steam vents and mud pools) occurs in an intensively altered
area, which is only a few hundred metres across, but thermal manifestations,
mostly in the form of warm springs, spread over an area of approximately 6
km^2, and distributed along the main NNE-SSW-oriented regional direction.
From 1968 until 1998 no significant changes were observed in the chemical
composition of the Geysir geothermal water as it remained constant from
the first records (Barth, 1950). The dry gas chemistry is characterised by
high CO_2 and low H_2S and H_2 concentrations compared to those recorded in
other high-temperature geothermal areas from Iceland: the removal of H_2S

is suggested to be related to condensation and oxidation in the upflow. Water temperatures at the surface are between 20 and 100 °C, whereas equilibriun temperatures at depth were estimated at 230–260 °C (Arnórsson, 1995; Kaasalainen and Stefánsson, 2012). The pH of the Geysir waters ranges between 3.3 and 9.1 at surface temperatures, and the δD-δ^{18}O relationship for hot and cold water indicates that the groundwater is of local meteoric origin. In the Geysir area there are three main larger geysers: Konungshver, Geysir and Strokkur (Fig. 3.28), but only the last one still regularly erupt every 4-8 minutes. These hot spring lies at the bottom of the eastern slope of the rhyolitic dome Laugarfjall, which rises to 187 m a.s.l. (Fig. 3.28). There are a number of records which showed changes in the hot springs during earthquake episodes (Thorkelsson, 1925), the latest taking place in 2000 after a major earthquake in the southern part of Geysir. This likely indicates a rejuvenation process in temrs of permeability in the upflow zone caused by tectonic movements. In this study, only Konungshver and Geysir were considered (Fig. 3.29 and 3.30). The Geysir hot spring and its outlet stream are located near the eastern border of the geothermal area. The circular pool is 20 m in diameter and a shallow rim (<2 cm high) and lies at the top of a regular dome-shaped morphology consisting of silica sinter. The pool water has a temperature of 90 °C. The stream temperature decreases to 20 °C over a distance of 40 m (Geilert et al., 2015). The Konungshver hot spring and outflow stream are situated on a small hill between the Geysir and Haihver streams. The hot spring temperatures varies between 70 °C in the center and 67 °C at the rim of the pool. Stream water temperatures decrease to 16 °C over a distance of 20 m (Geilert et al., 2015).
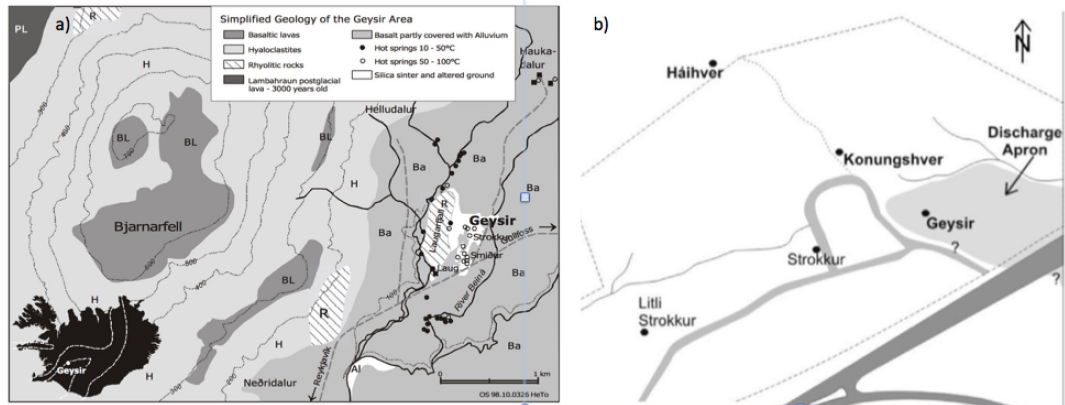
FIGURE 3.28: *a) Schematic geological map of the Geysir geothermal area and its surroundings (Torfason, 1985). b) Location of the three main larger geysers, Konungshver, Geysir and Strokkur, in the Geysir geothermal area (Geilert et al., 2015).*

FIGURE 3.29: *Konungshver pool at Geysir geothermal area*

FIGURE 3.30: *Geysir pool at Geysir geothermal area*

Chapter 4

Methods

4.1 H_2S and SO_2 measurements

The chemical composition of volcanic-hydrothermal gases is commonly determined by direct sampling at the emission vent by using gas-sampling bottles containing a solution of 4N NaOH (Giggenbach, 1975). This sampling procedure, coupled with that proposed by Piccardi (1982), allows the determination of SO_2 and H_2S at very low concentrations (0.01 mg/L as $SO_4{}^{2-}$). However, whilst several gas species can simultaneously be measured with this method, post-collection chemical determinations in laboratory are required, precluding any real-time continuous monitoring of volcanic activity. Furthermore, the result of the analysis is influenced by the ability of the operator in the gas sampling. For this reason, in recent years, remote spectroscopic techniques, from both satellites and ground-based instruments, have been introduced (i.e. COSPEC, Stoiber et al., 1980; Bluth et al., 1993; FTIR, Francis et al., 1998; DOAS, Galle et al., 2003), allowing real-time measurements of volcanic gas composition from remote stations. However, CO_2 and H_2S, two main constituents of volcanic gases, are spectroscopically difficult to be determined and the corresponding volcanogenic emission rates can only indirectly be derived. Furthermore, this approach is generally expensive and requires frequent instrument calibration.

More recently, field-portable gas analyzers, i.e., Multi-GAS (e.g., Aiuppa et al., 2009 and references therein, Ilyinskaya et al., 2015), for real-time determination of CO_2, SO_2 and H_2S were developed and presently they are widely used for studying volcanic-hydrothermal systems. The Multi-component Gas Analyzer System station can be equipped with electrochemical SO_2 and

H_2S sensors that work at ppm level (0–100 ppmv and 0-50 ppmv respectively) and, for this reason, this instrumentation can efficiently work close to volcanic gas emissions where the concentrations of S-compounds are relatively high. Nevertheless, the most applied technique for monitoring air pollutant is the passive/diffusive technique. This techinque has long been used in both volcanic and anthropogenic environment and allows measurements in air of gaseous compounds such as combustion products (e.g., SO_2 and NO_x), reduced gases (e.g., H_2S and NH_3), O_3, Hg and volatile organic compounds (VOCs) (e.g., Shooter et al., 1995; Flores et al., 1996; Bernard et al., 1999; Tang et al., 2002; Klanova et al., 2006; Campos et al., 2010; Nash and Leith, 2010; Zabiegala et al., 2010; Byanju et al., 2012; Colomer et al., 2012; D'Alessandro et al., 2013; Pavilonis et al., 2013; Al-Awadhi, 2014; Huang et al., 2014). The benefit of these passive traps is that, being low cost and with no power supply requirements, they can be located in multiple locations at the same time, easily obtaining a general view of the spatial distribution of the air pollutants (Hangartner, 2000). However, passive samplers need long exposure time (up to several days) and as a consequence, short-term temporal variations cannot be recorded (Krupa and Legge, 2000). Furthermore, their efficiency is strongly affected by several environmental factors, e.g., temperature, humidity and wind speed (Brown, 2000; Krupa and Legge, 2000; Delgado-Saborit and Esteve-Cano, 2006), whose effects are difficult to be quantified. In this study, real-time, high-frequency and high-sensitive SO_2-H_2S measurements were carried out by using a Thermo 450*i* analyzer, as described in detail in the next section.

4.1.1   Scientific equipment

The Thermo Scientific 450*i* Hydrogen Sulfide–Sulfur Dioxide Analyzer has been widely used worldwide to measure ambient concentration of the main gaseous sulfur species (H_2S and SO_2) in air (Thermo Scientific, 2008), due to its broad detection range, sensitivity, durability, and reasonable cost (Blunden and Aneja, 2008; Heber et al., 2009; Li et al., 2011; Akdeniz et al., 2011, 2012; Liu et al., 2012; Lin et al., 2012; Ni et al., 2012; Lim et al., 2012; Liu et al., 2013; Janni et al., 2014). Furthermore, the instrument was already used in Reykjavik (Iceland) for monitoring H_2S concentrations resulting from two nearby geothermal power plants (Thorsteinsson et al., 2013). The Model 450*i*

operates on the principle that H$_2$S is converted to SO$_2$: sulfur dioxide is measured by pulsed fluorescence, while H$_2$S is converted to SO$_2$ with a molybdenum catalyst prior to detection (Fig. 4.1). This is possible because the influx air (regulated by a pump operating at 1 L/min) is separated into two internal flow lines: a Combined Sulfur line (CS line) and a SO$_2$ line (Thermo Fisher Scientific, 2008). The CS line directs the gas sample through a converter unit, consisting of the Mo-catalyst working at variable temperatures between 310 and 340 °C, where H$_2$S is oxidized to SO$_2$ (efficiency >80%). Consequently, the detector measures the sum of H$_2$S and SO$_2$ (CS). Conversely, the SO$_2$ line bypasses the converter, directly measuring the gas sample. The instrument is equipped with a valve to alternate between the two lines, allowing the determination of both SO$_2$ and CS. Both lines end in the fluorescence chamber, where pulsating UV light excites the SO$_2$ molecules, which decaying to lower energy states and emits a UV light that is proportional to the SO$_2$ concentration. Finally, a photomultiplier tube (PMT) detects the UV light emission of the decaying SO$_2$ molecules. The difference between the CS and SO$_2$ signals allows to compute the H$_2$S content (Thermo Scientific, 2008).

The Model 450*i* outputs the SO$_2$-H$_2$S-CS ranges concentration in ppb to the front panel display and although the duration of a single measurement is 1 s, a satisfactory precision ($\pm$1%; Thermo Scientific, 2008) is obtained in 1 min, by averaging the results of 60 repeated measurements (linearity $\pm$1%; Thermo Scientific, 2008). The detection limit under field conditions is 1 ppb and the working range is between 0.05 and 10 ppm (Thermo Scientific, 2008).

4.1.2 Measurement strategy

The measurements of H$_2$S and SO$_2$ in air were carried out in ten main areas located in Italy and Iceland, as described in the third chapter. The studied emissions were mainly gas manifestations (i.e. steam vents, fumaroles, hot and mud bubbling pools). Several repeated measurements were carried out in each selected area, over a period of 4 months in Iceland (autumn 2017 and spring 2018) and about 10 days in Italy, in order to validate the data and to investigate the effect of different weather conditions (i.e. wind speed and direction, temperature, humidity, rainy and sunny day) on S-compounds concentration and distribution in the atmosphere. At each area, a gas emission was selected according to accessibility, topography, ability to move around
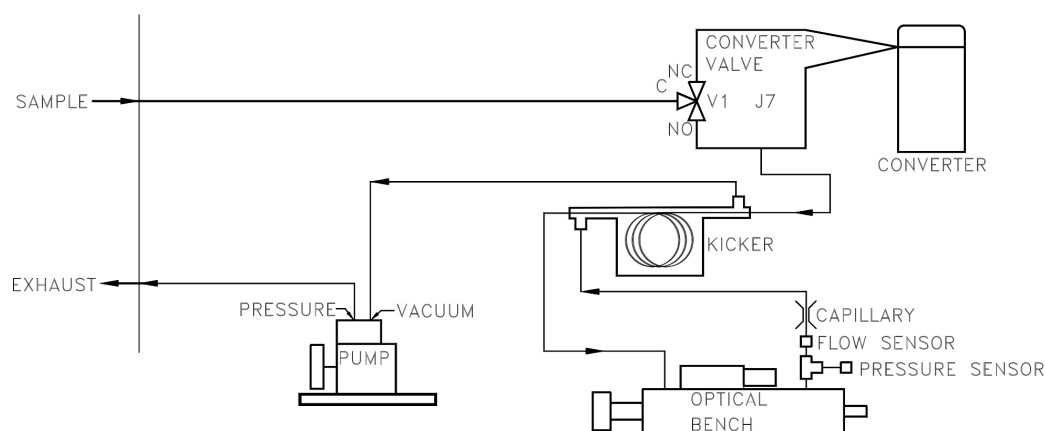
FIGURE 4.1: *The sample, either coming directly from the inlet or processed in the converter, flows through a hydrocarbon kicker that removes hydrocarbons from the sample by forcing the hydrocarbon molecules to differentially permeate through the tube wall. The sample then flows into the fluorescence chamber, where pulsating UV light excites the SO_2 molecules. As the excited SO_2 molecules decay to lower energy states, they emit UV light that is proportional to the SO_2 concentration. The band-pass filter only allows the wavelengths emitted by the excited SO_2 molecules to reach the photomultiplier tube (PMT).*

the source with the instrument and permissions obtained by the local authority or private owners. At least 4 days were spent in each area with an average of 6-7 hours of measurements per day, during which 5-6 fix spots were chosen to carry out H_2S and SO_2 measurements at different distances from the source. The measurements were carried out downwind from the most distant fix spot from the source to the closest one (e.g., from lower to higher concentrations) to i) minimize possible memory effects and ii) to catch "snapshot" of the H_2S-SO_2 concentrations within the plume (Fig. 4.2). The first and the last fix spots were basically selected according to the topography and the source flux, i.e. the stronger the flux of the source the more distant the first and last fix spot. During the data acquisition, a certain regularity and equidistance between the fix spots was maintained as much as possible. In addition, due to Icelandic regulations on the protection of the natural environment, the equipment was moved by hand (about 50 kg weight) during the measurements, whereas at La Solfatara and Vulcano Island a car was used. In the field, the Thermo 450i analyzer was equipped

with a 3 m long PVC tube, which allowed S-measurements at 1.5 m from the ground, and 3 gel batteries with a durability of about 3 hours each. Furthermore, a Davis Vantage Vue mobile weather station was installed to regularly and continuously measure air humidity and temperature, wind direction and speed (Fig. 4.3). The location of each measured fix spots are shown in the next chapter.
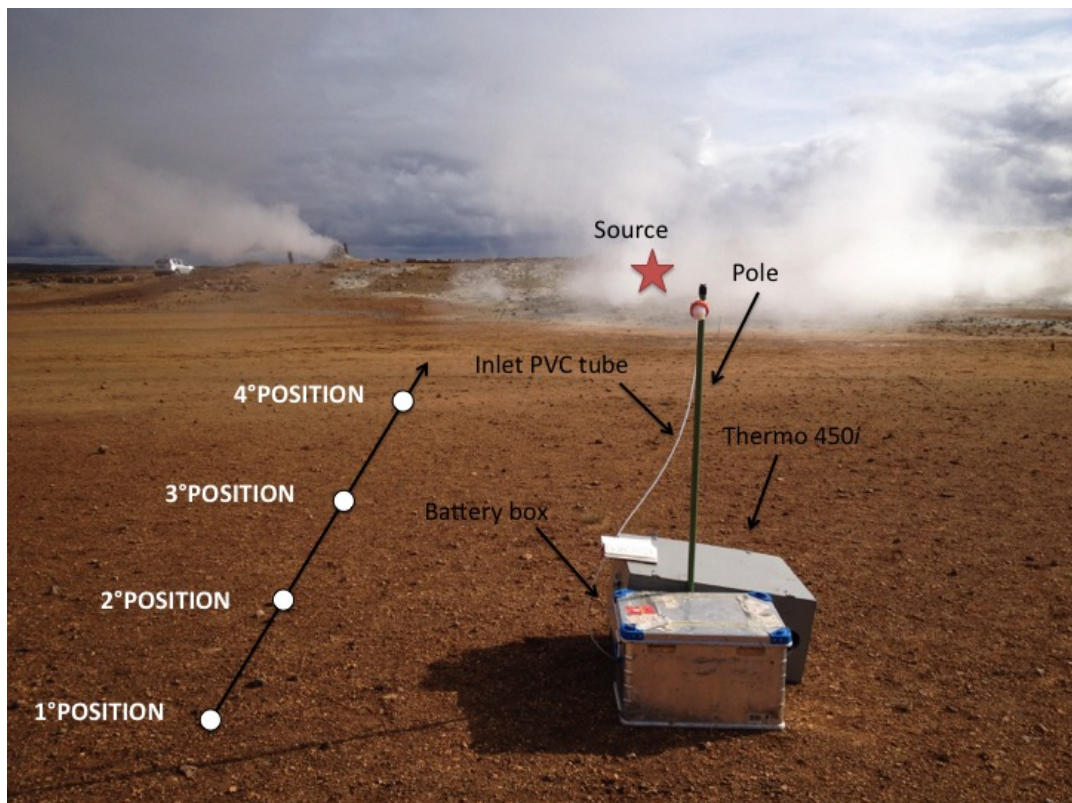
FIGURE 4.2: *Representation of the H₂S and SO₂ measurement strategy in air. The sampling equipment is also reported. The wind direction is towards the observer.*
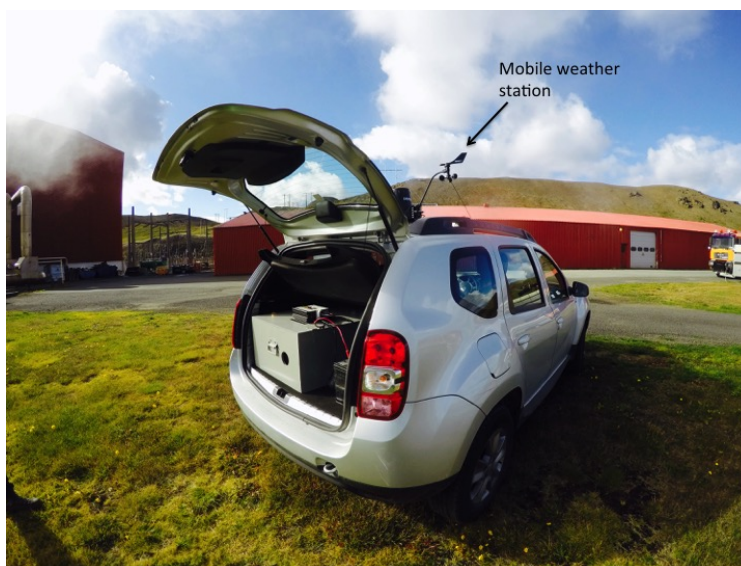
FIGURE 4.3: *Measuring equipment stored in the car, including the mobile weather station.*

4.2   VOCs measurements

The H_2S-SO_2 measurements were coupled with those of VOCs (non-methane Volatile Organic Compounds) for the organic characterization of the Icelandic natural sources. Because they are present at very low concentrations in air, dedicated advanced sampling techniques were required. The methodological approaches normally applied are based on absorbent materials (organic and inorganic) or passive samplers (Wang et al., 2006). In this study, the Solid Trap (ST) method was used (Tassi et al., 2012c): a stainless-steel tube (9 cm long and 0.5 cm of diameter) packed with 3-phase (Carbosieve 111, Carboxen B, Carboxen C) absorbent material was connected to a portable pump (Tecora® AYRON 5), which allowed a constant low-flux through the trap. During the 2017 sampling field in Iceland, at each measurement site, a single ST was used. The solids traps equipped with the portable pump were located at about 50 cm from the ground, downwind respect to the source, operating at a constant flux of 250 cc/min and over a period of 2-3 hours (Fig. 4.4). In the laboratory, the VOCs trapped in the ST were i) firstly desorbed at 250 °C for 20 min by using a DANI Master thermal desorber (TD), ii) absorbed by a quartz 3-phase focusing trap at 5 °C, iii)

desorbed for 2 min at 220 °C and, eventually, iv) injected, through a transfer line maintained at 220 °C, in the column headspace of a Thermo Trace GC Ultra gas chromatograph coupled to a Thermo DSQ Quadrupole Mass Spectrometer (GC–MS, Fig. 4.5). Retention times of the chromatographic peaks and the mass spectra were both used to identify VOCs detected by the quadrupole detector, using the mass spectra database of the NIST05 library (NIST, 2005) for comparison. Quantitative analyses were carried out by external standard calibration procedure using Accustandard mixtures in methanol or, alternatively, hexane solvent (Tassi et al., 2012c). Relative Standard Deviation (RSD), calculated from five replicate analyses of the standard mixtures, was <5%.The limit of quantification (LOQ) was determined by linear extrapolation from the lowest standard in the calibration curve using the area of a peak having a signal/noise ratio of 5 (Tassi et al., 2012b). Analytical errors were <5%.

Tecora AYRON 5 pump   3-phase ST
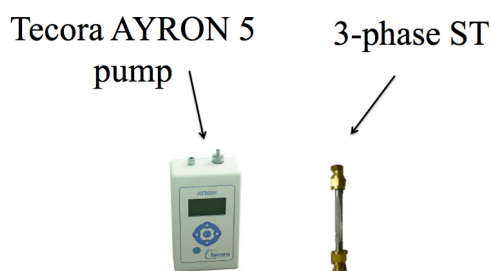
FIGURE 4.4: *(The two main components for VOCs sampling.*

FIGURE 4.5: *Thermo Trace GC Ultra gas chromatograph and Thermo DSQ Quadrupole Mass Spectrometer (GC-MS) for the analysis of VOCs.*

Chapter 5

Results

In this Chapter, all the H_2S-SO_2 data in air, together with those of VOCs (when available), are presented. Each geothermal system was considered separately in a dedicated sub-chapter. Since the weather conditions and wind direction stability were not always favorable during the field surveys, part of the data are likely not representative of the H_2S-SO_2 evolution at increasing distance from the emitting source within the hydrothermal plume. Consequently, the most representative data were used to develop the mathematical model and are presented in detail in Tables 5.1-5.17, while the others are here described and discussed in the next chapter. The background values for H_2S and SO_2 in clean air were measured in all the systems (at Vulcano Island, La Solfatara and in Icelandic geothermal systems) and values of 1.5-2.0 ppbv were found for SO_2, whereas H_2S concentrations were mainly below the instrument detection limit. As mentioned in Chapter 4, the Thermo Scientific 450*i* detection limit under field conditions is 1 ppb and the working range is between 0.05 and 10 ppm (Thermo Scientific, 2008). For each system, SO_2-H_2S maximum and minimum values were presented and, when possible, the fix spots of measure were represented graphically in a SO_2 vs. H_2S diagram, as shown in the example in Fig. 5.1 for the Krýsuvík geothermal system. The first fix spot is the closest one to the source, whereas the last one is the more distant, as described in Chaper 4. The SO_2-H_2S values generally are lined up along a straight line, with higher values close to the source and gradually decreasing with distance.
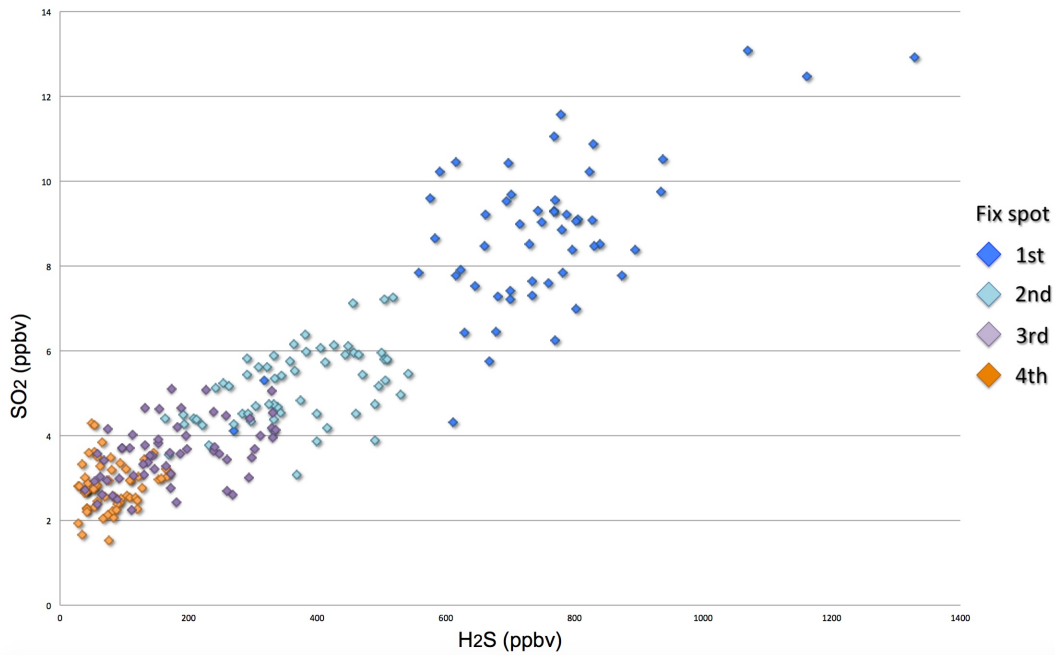
FIGURE 5.1: *SO$_2$-H$_2$S binary diagram for Krýsuvík geothermal system, KRY(A). The four fix spots are indicated with different colors.*

5.1   Vulcano Island

At Vulcano Island, the H$_2$S-SO$_2$ measurements in air were carried out in 2016 at the Vulcano Porto hydrothermal area, at the base of La Fossa volcanic cone. A series of 3 fix spots of measurements: VULC(A) (Fig. 5.2), and 4 fix spots: VULC(B) (Fig. 5.4), were performed downwind the Faraglioni sub-marine fumarolic emissions and Vasca Ippopotami bubbling pool. The higher H$_2$S and SO$_2$ values measured in this area were 5611 and 90 ppbv, respectively. The VULC(A) data showed SO$_2$ values in the range of 2.0-29 ppbv and 5.1-839 ppbv for H$_2$S (Fig. 5.3); sulfur dioxide of VULC(B) varied from 1.2 to 27 ppbv while H$_2$S was from 3 to 584 ppbv (Fig. 5.5).

FIGURE 5.2: *Location of 1-3 fix spots (red dots) respect to the emitting sources (in yellow) at Vulcano Porto.*
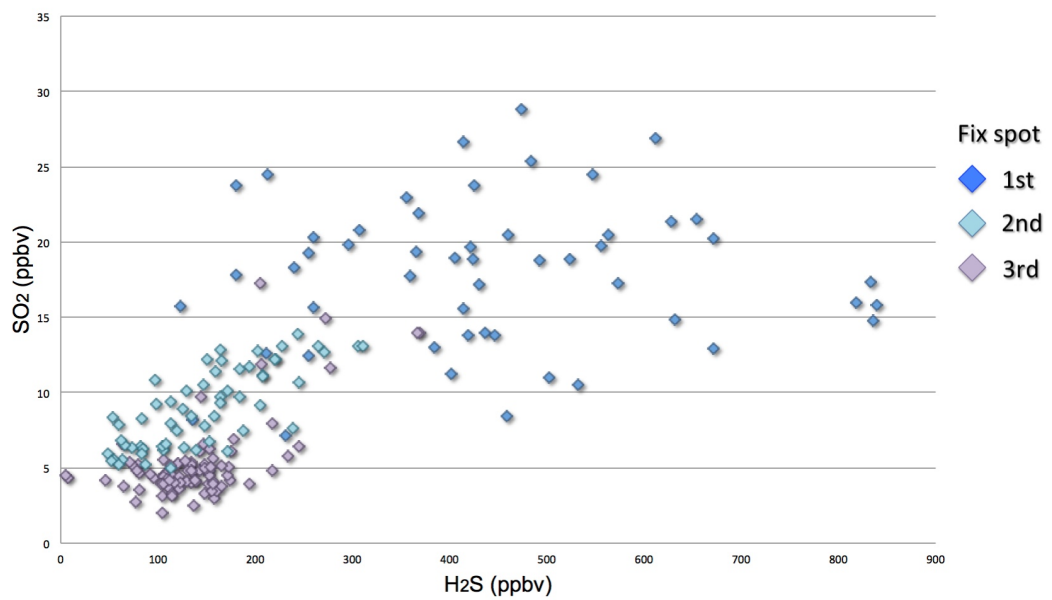
FIGURE 5.3: *SO_2-H_2S binary diagram for VULC(A). The three fix spots are indicated with different colors.*

FIGURE 5.4: *Location of 1-4 fix spots (red dots) respect to the emitting sources (in yellow) at Vulcano Porto.*
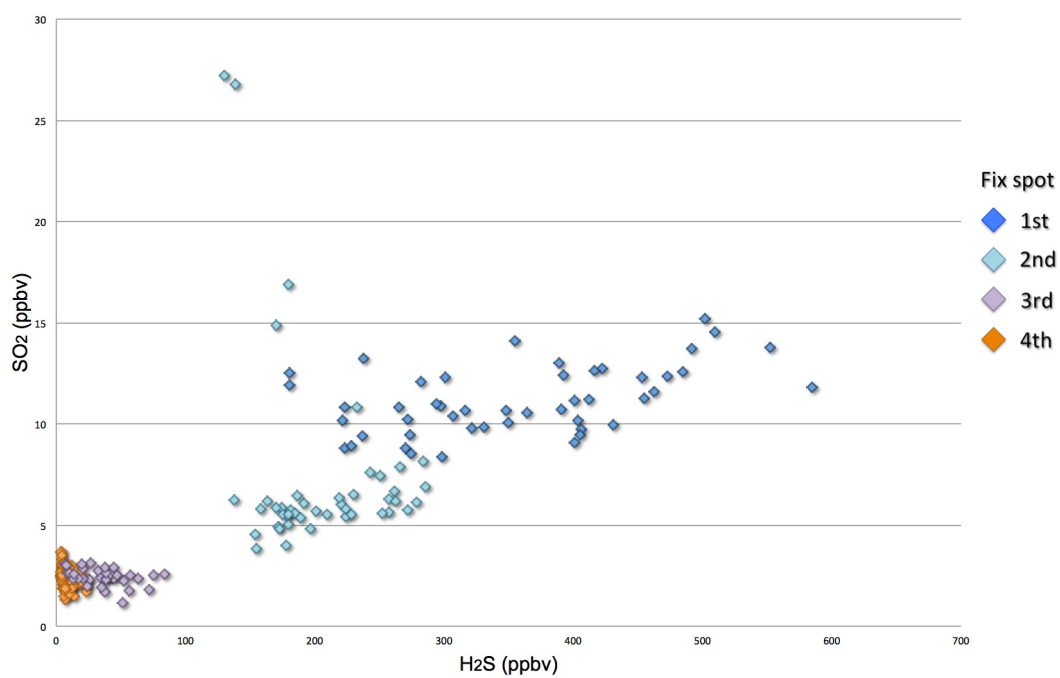
FIGURE 5.5: *SO_2-H_2S binary diagram for VULC(B). The four fix spots are indicated with different colors.*

5.2 La Solfatara

Within La Solfatara crater, the H_2S-SO_2 measurements were carried out in 2016 at different distances (4 fix spot of measurements) and downwind respect to the "Fangaia" bubbling pool (Fig 5.6). The SO_2 values varied from 1.0 to 152 ppbv, while H_2S was from 1.4 to 1329 ppbv (Fig. 5.7).
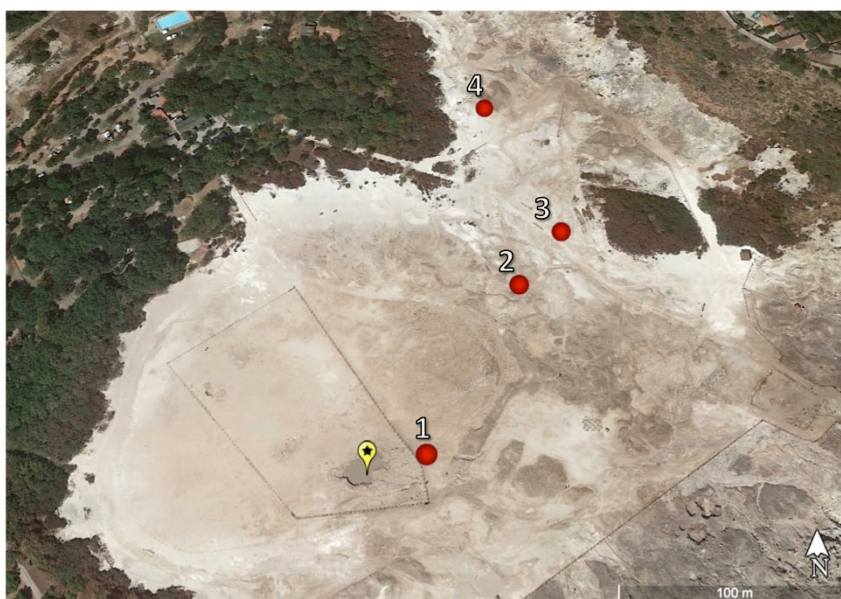
FIGURE 5.6: *Location of 1-4 fix spots (red dots) respect to the emitting source Fangaia (in yellow) within La Solfatara crater.*
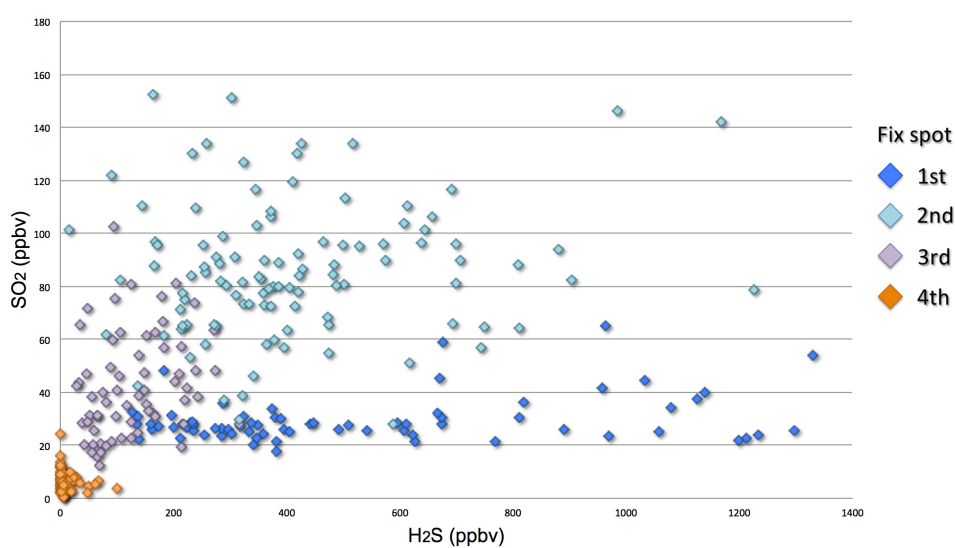
FIGURE 5.7: *SO_2-H_2S binary diagram for La Solfatara (SOLF). The four fix spots are indicated with different colors..*

5.3   Krafla

Two main geothermal areas were considered at Krafla high-temperatures geothermal system: Leirbotnar (Hveragil) and Hvíthólar (Fig. 3.8 and 3.10). In Hvíthólar, the measurements were carried out in autumn 2017 and indicated as HVITH(B) and characterized by 5 fix spots (Fig. 5.8). The measurements were repeated in spring 2018, HVITH(C) and HVITH(E), the latter characterized by 6 fix spots (Fig. 5.11). Considering all the measured fix spots, in HVITH(C), sulfur dioxide varied from 1.8 to 22 ppbv, while H_2S ranged from 3.3 to 1082 ppbv (Fig. 5.10). The H_2S-SO_2 data for HVITH(B) and HVITH(E) are reported in Table 5.1 and 5.2 and Fig. 5.9 and 5.12, respectively. In Leirbotnar (LEIRB), the measurements were only performed in 2018. Since the area is characterized by difficult access and topography, the H_2S-SO_2 analyzer was positioned in a single fix spot for six hours. The H_2S ranged between 15 and 2511 ppbv, while SO_2 spanned between 1.8 and 18 ppbv (Fig. 5.13).

Among VOCs, the aromatic compounds are dominant (46.5%), followed by alkanes (20.3%), O-bearing (16.2%), S-bearing (7.6%), alkenes (4.4%), cyclics (4.2%) and halocarbons (0.9%) (Fig. 5.14, Table 5.3).
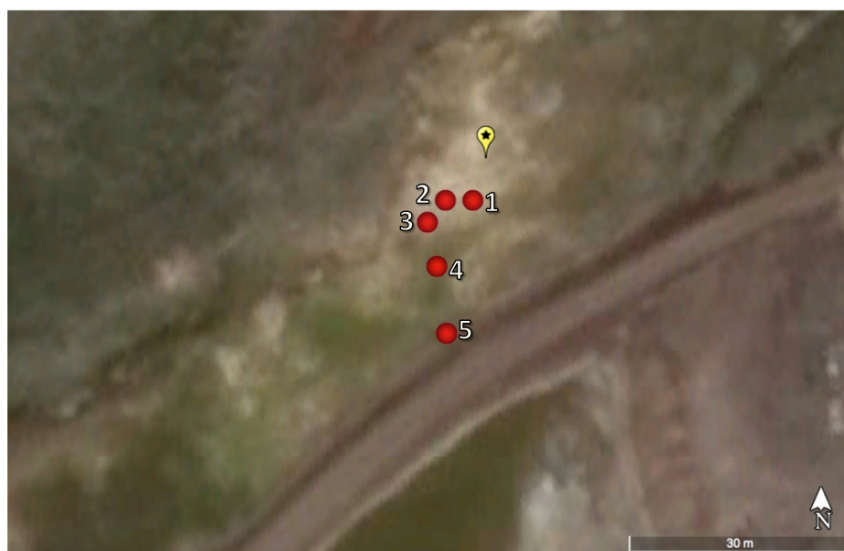
FIGURE 5.8: *Location of 1-5 fix spots (red dots) with respect to the emitting source (in yellow) for HVITH(B). The mean wind velocity is 7.4 m/s.*
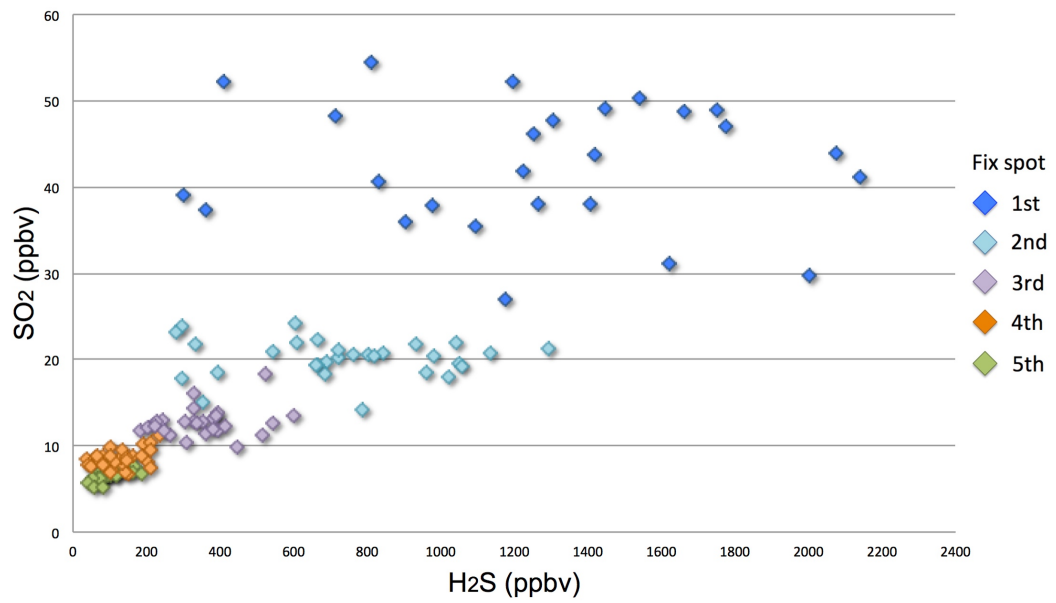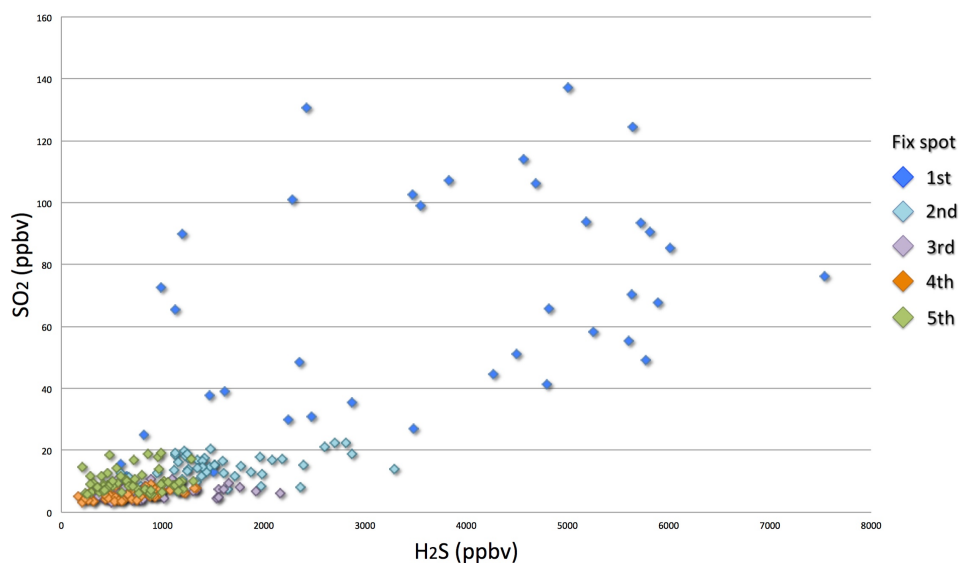
FIGURE 5.9: *SO_2-H_2S binary diagram for HVITH(B). The five fix spots are indicated with different colors.*

Fix spot	S-compound	MAX (ppbv)	MIN (ppbv)	AVERAGE (ppbv)	MEDIAN (ppbv)	SD
1	H_2S	2140	301	1256	1258	503
	SO_2	54	27	42	43	7.3
2	H_2S	1294	842	946	946	147
	SO_2	24	14	20	20	2.2
3	H_2S	598	184	349	335	109
	SO_2	18	9.9	13	13	1.6
4	H_2S	235	38	129	130	57
	SO_2	11	6.8	8	8.5	1.1
5	H_2S	187	40	97	85	38
	SO_2	8.2	5.2	6.6	6.6	0.7

TABLE 5.1: H_2S and SO_2 maximum, minimum, average, median and standard deviation values for each fix spot of measurements in HVITH(B) in 2017. The location of 1-5 fix spots is shown in Fig. 5.8
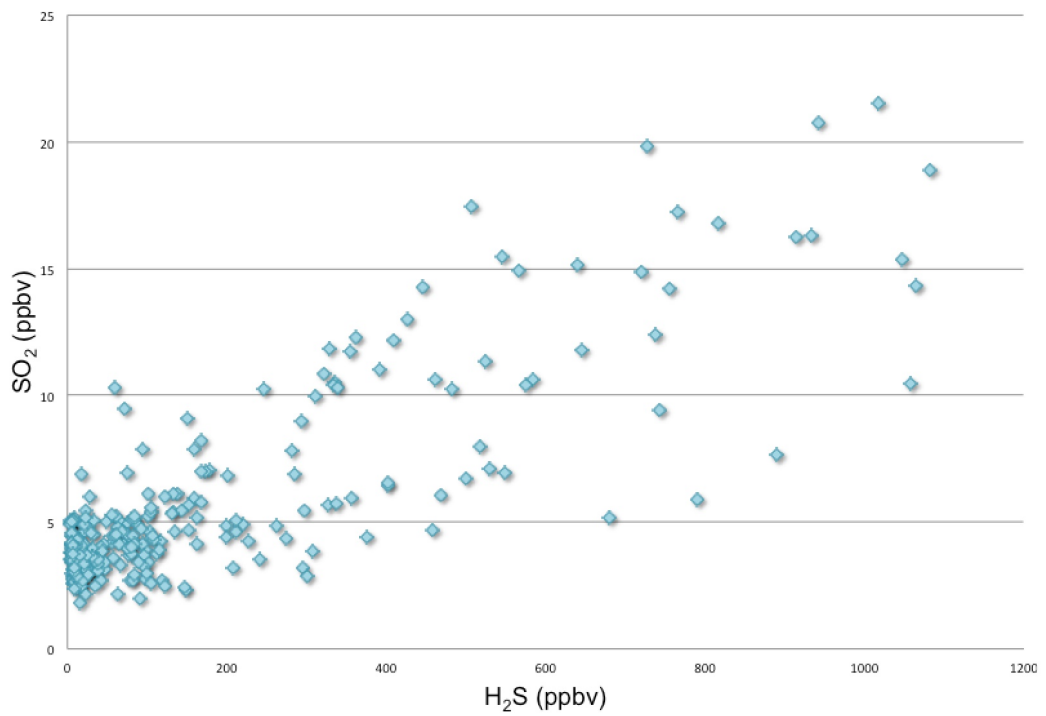
FIGURE 5.10: *SO$_2$-H$_2$S binary diagram for HVITH(C). The blue dots represent all the fix spots.*

FIGURE 5.11: *Location of 1-6 fix spots (red dots) with respect to the emitting source (in yellow) for HVITH(E). The mean wind velocity is 4.6 m/s.*
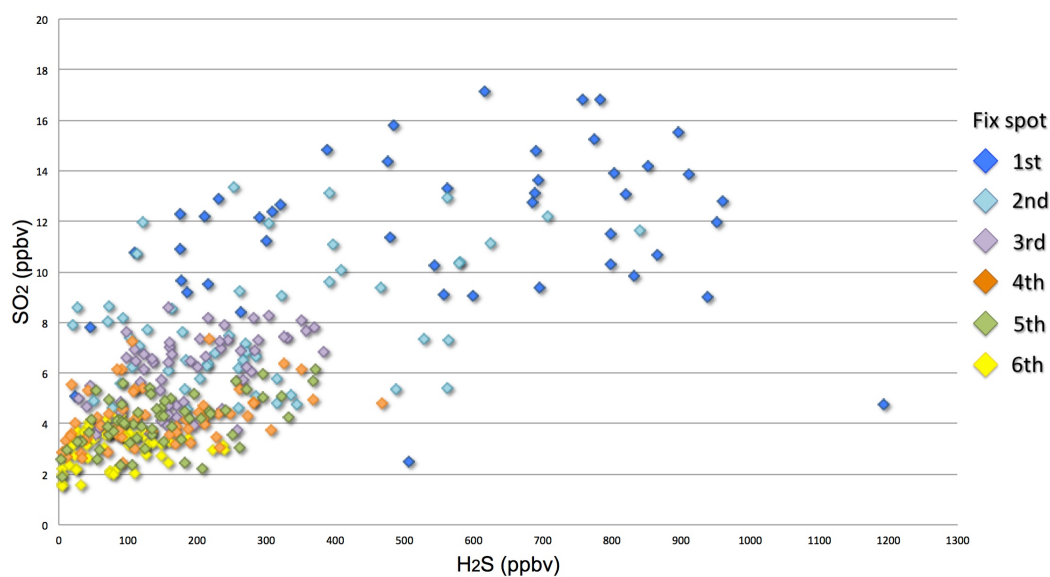
FIGURE 5.12: *SO₂-H₂S binary diagram for HVITH(E). The six fix spots are indicated with different colors.*
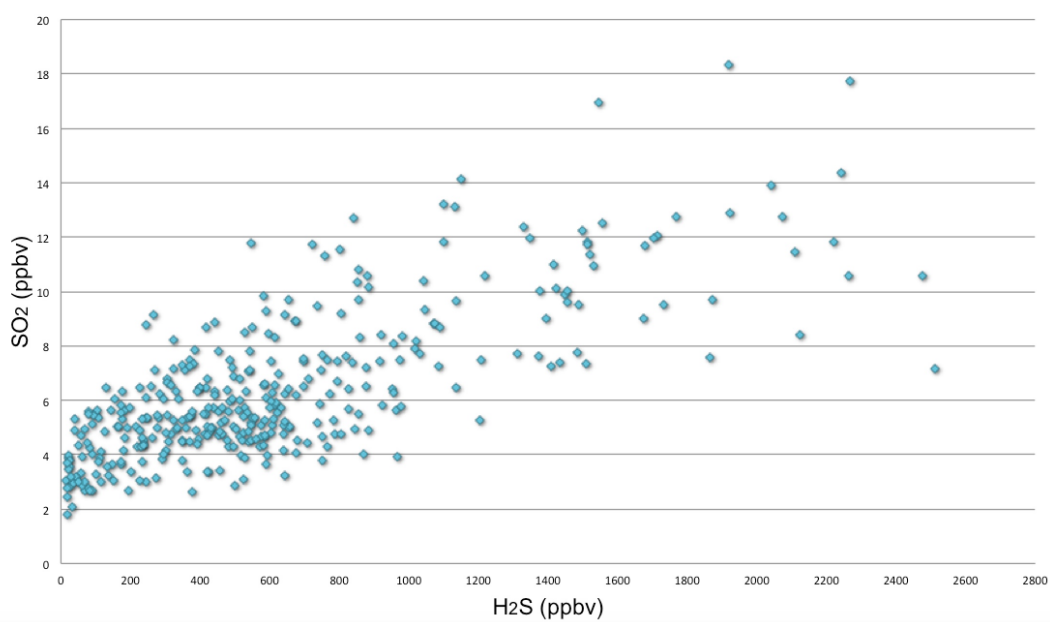
FIGURE 5.13: *SO₂-H₂S binary diagram for LEIRB.*

Fix spot	S-compound	MAX (ppbv)	MIN (ppbv)	AVERAGE (ppbv)	MEDIAN (ppbv)	SD
1	H_2S	1193	23	557	580	294
	SO_2	17	2.5	12	12.2	3.1
2	H_2S	840	20	284	260	186
	SO_2	13	4.6	7.8	7.3	2.5
3	H_2S	383	28	188	170	88
	SO_2	8.6	3.5	6.0	6.4	1.4
4	H_2S	467	5.9	139	109	106
	SO_2	7.3	2.4	4.2	3.9	1.1
5	H_2S	372	3.6	147	132	90
	SO_2	6.2	1.9	4.1	4.1	1.0
6	H_2S	240	4.6	86	83	57
	SO_2	4.4	1.5	3.1	3.2	0.7

TABLE 5.2: H_2S and SO_2 maximum, minimum, average, median and standard deviation values for each fix spot of measurements in HVITH(E) in 2018. The location of 1-6 fix spots is shown in Fig. 5.11

VOCs	nmol/mol
Alkanes	2.9
Aromatics	6.7
Cyclics	0.6
Alkenes	0.6
S-bearing	1.1
O-bearing	2.3
Terpenes	-
Halocarbons	0.1

TABLE 5.3: VOCs chemical composition (in nmol/mol) of Hvíthólar geothermal system.
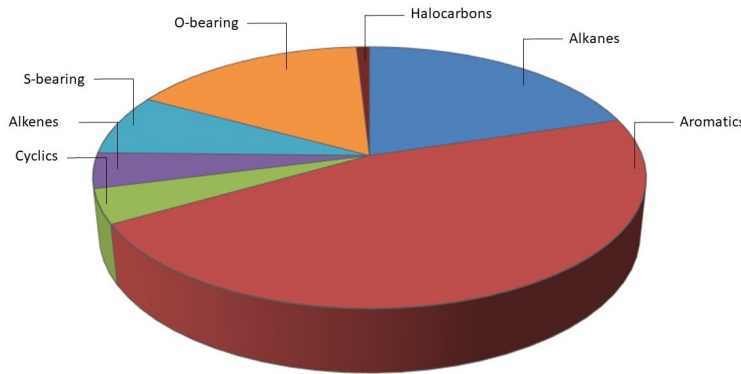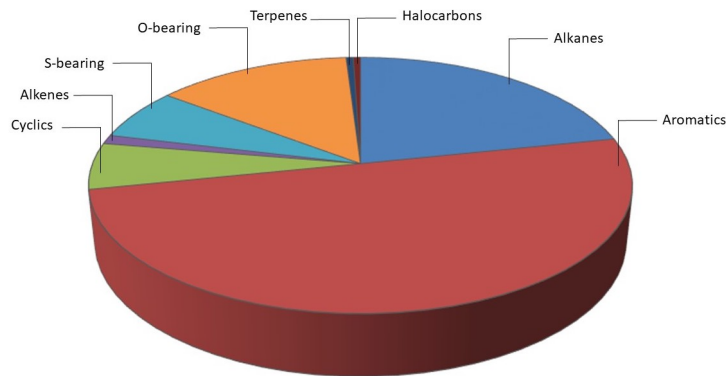

FIGURE 5.14: *Pie diagram showing relative VOC % with respect to the total VOCs composition. The corresponding % is, as follows: aromatics (46.5%), alkanes (20.3%), O-bearing (16.2%), S-bearing (7.6%), alkenes (4.4%), cyclics (4.2%) and halocarbons (0.9%).*

5.4 Námafjall

At Námafjall Hverir, within the Námafjall geothermal system (Fig. 3.8), H_2S and SO_2 emitted from different natural emission were measured at: i) small bubbling pools field, indicated as NAM(A), and borehole emissions, indicated as NAM(B), in 2017; ii) big bubbling pool, named NAM(C), and borehole emissions, named NAM(D), in 2018 (Fig. 3.16). Considering all the measured fix spots, in NAM(A) sulfur dioxide varied from 2.6 to 22 ppbv, while H_2S ranged from 36 to 4080 ppbv (Fig. 5.15); in NAM(B), sulfur dioxide was varying from 3.2 to 52 ppbv, while H_2S ranged from 12 to 5463 ppbv (Fig. 5.16); in NAM(C), sulfur dioxide was between 10 and 66 ppbv, while H_2S spanned from 7.1 to 4263 ppbv (Fig. 5.17). The NAM(D) data are shown

in Table 5.4 and represented in Fig. 5.19, whereas the fix spots location is shown in Fig. 5.18.

Among VOCs, the aromatic compounds are dominant (50%), followed by alkanes (14.4%), cyclics (11.1%), O-bearing (9.7%), S-bearing (6.8%), alkenes (6.3%), halocarbons (1.4%) and terpenes (0.3%) (Fig. 5.20, Table 5.5).
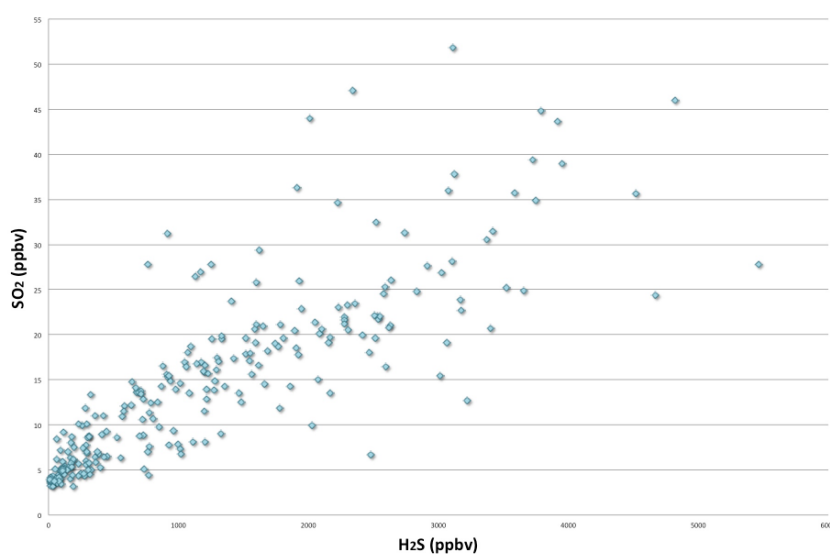
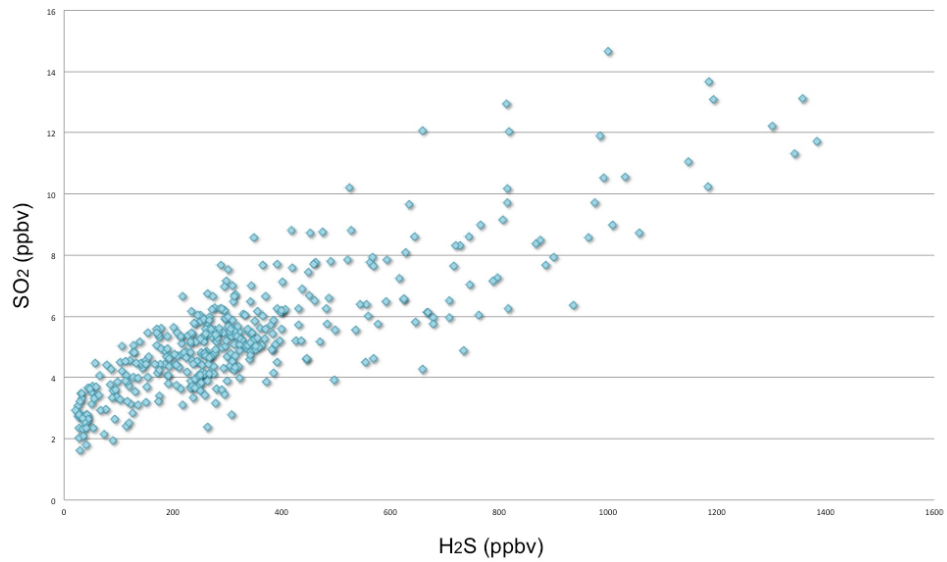FIGURE 5.15: *SO_2-H_2S binary diagram for NAM(A). The blue dots represent all the fix spots.*
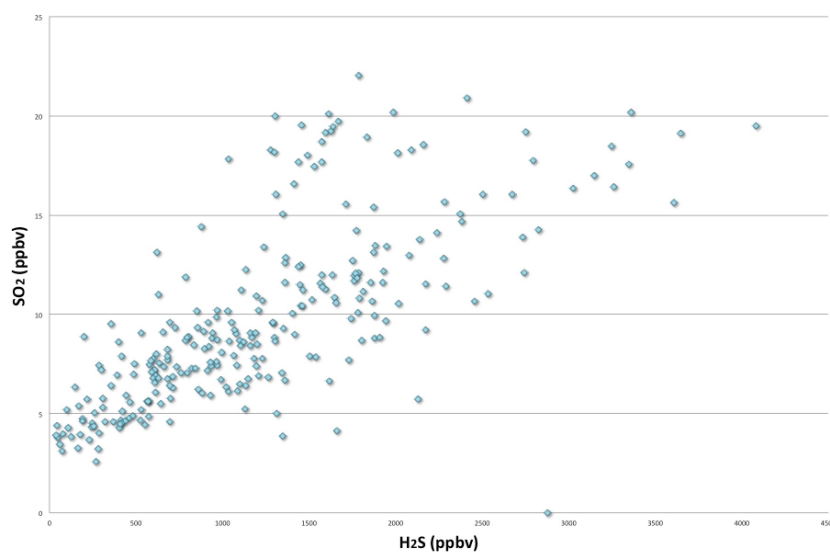
FIGURE 5.16: *SO_2-H_2S binary diagram for NAM(B). The blue dots represent all the fix spots.*
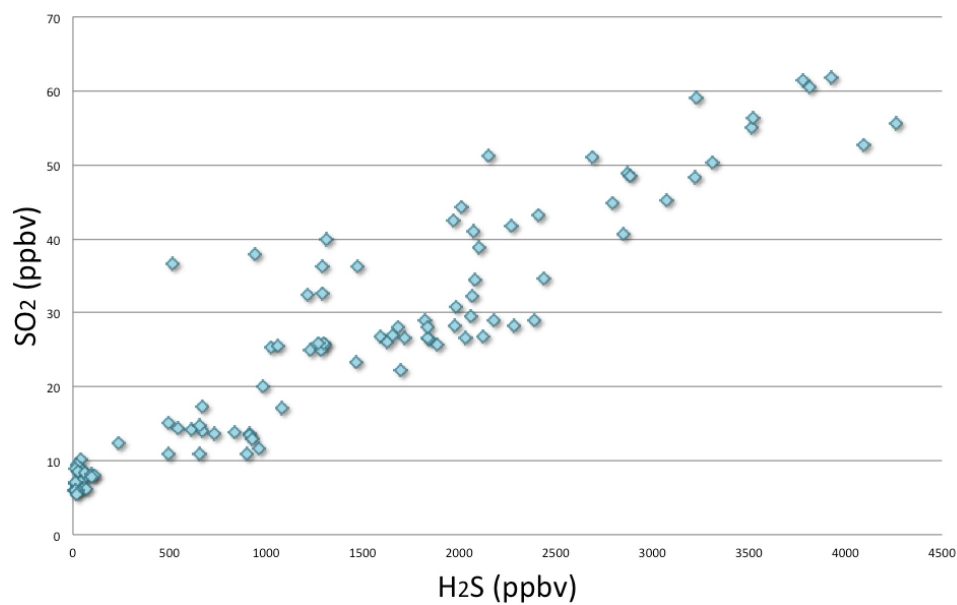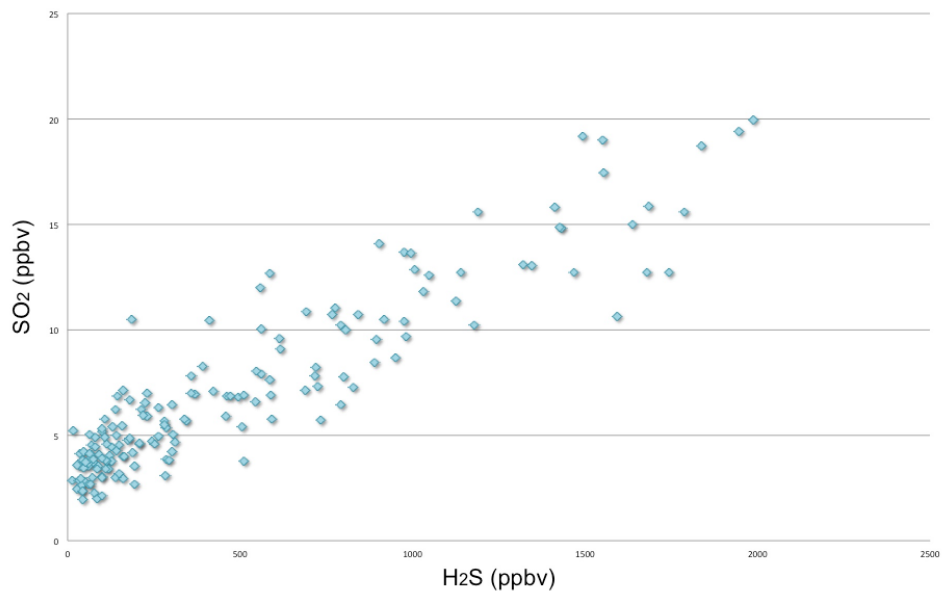
FIGURE 5.17: *SO_2-H_2S binary diagram for NAM(C). The blue dots represent all the fix spots.*
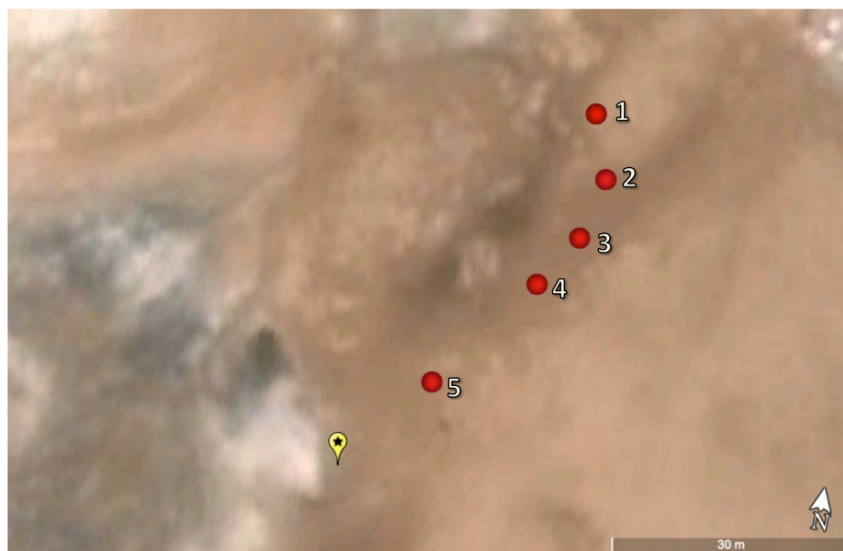
FIGURE 5.18: *Location of 1-5 fix spots (red dots) respect to the emitting source (in yellow) for NAM(D). The mean wind velocity is 4.9 m/s.*

FIGURE 5.19: *SO₂-H₂S binary diagram for NAM(D). The five fix spots are indicated with different colors.*
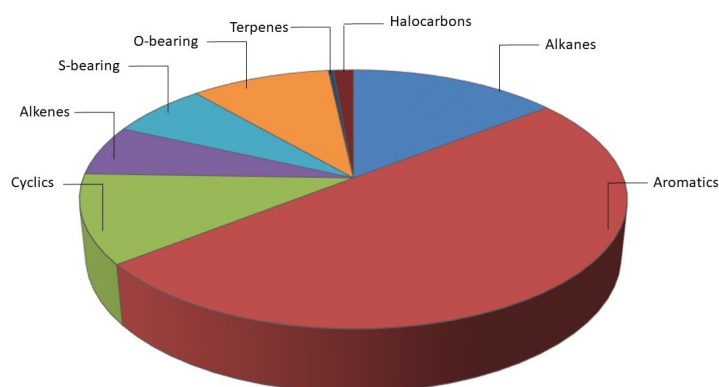
FIGURE 5.20: *Pie diagram showing relative VOC % with respect to the total VOCs composition. The corresponding % is, as follows: aromatics (50%), alkanes (14.4%), cyclics (11.1%), O-bearing (9.7%), S-bearing (6.8%), alkenes (6.3%), halocarbons (1.4%) and terpenes (0.3%).*

Fix spot	S-compound	MAX (ppbv)	MIN (ppbv)	AVERAGE (ppbv)	MEDIAN (ppbv)	SD
1	H_2S	7535	588	3583	3688	1953
	SO_2	142	16	71	70	35
2	H_2S	3290	572	1443	1331	612
	SO_2	27	9.2	18	18	4.9
3	H_2S	2159	230	830	696	450
	SO_2	15	7.7	11	10	1.6
4	H_2S	1334	168	722	760	281
	SO_2	14	7.9	10	10	1.6
5	H_2S	1303	239	694	659	295
	SO_2	16	10	13	13	1.6

TABLE 5.4: H_2S and SO_2 maximum, minimum, average, median and standard deviation values for each fix spot of measure in NAM(D) in 2018. The location of 1-5 fix spots is shown in Fig. 5.18.

VOCs	nmol/mol
Alkanes	4.6
Aromatics	15.9
Cyclics	3.6
Alkenes	2.0
S-bearing	2.2
O-bearing	3.1
Terpenes	0.1
Halocarbons	0.4

TABLE 5.5: VOCs chemical composition (in nmol/mol) of Námafjall Hverir geothermal system.

5.5 Bjarnaflag

Within the Bjarnaflag geothermal area (Fig. 3.14), measurements around the same natural emission were done in 2017 (Fig. 5.21): BJARN(A) and 2018 (Fig. 5.23): BJARN(C) close to the Bjarnaflag Blue Lake. The data are shown in Tables 5.6 and 5.7 and represented in Fig. 5.22 and 5.24 with SO_2 vs. H_2S binary diagrams.

Among VOCs, the aromatic compounds are dominant (50.1%), followed by alkanes (21.7%), O-bearing (13.7%), S-bearing (6.6%), cyclics (5.9%), alkenes (1.1%), halocarbons (0.5%) and terpenes (0.5%) (Fig. 5.25, Table 5.8).

FIGURE 5.21: *Location of 1-5 fix spots (red dots) with respect to the emitting source (in yellow) for BJARN(A).*
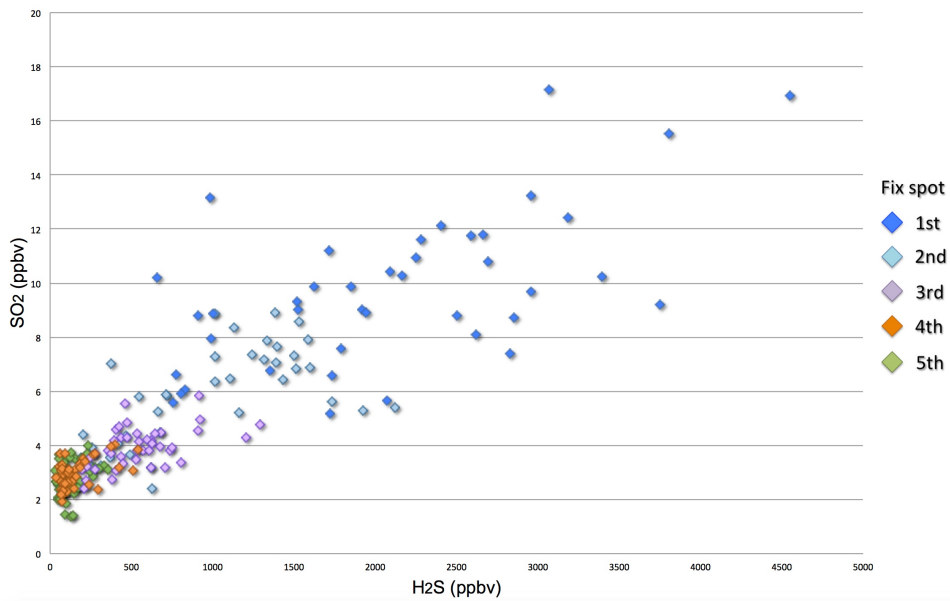
FIGURE 5.22: *SO₂-H₂S binary diagram for BJARN(A). The five fix spots are indicated with different colors.*

FIGURE 5.23: *Location of 1-4 fix spots (red dots) with respect to the emitting source (in yellow) for BJARN(C). The mean wind velocity is 6.4 m/s.*
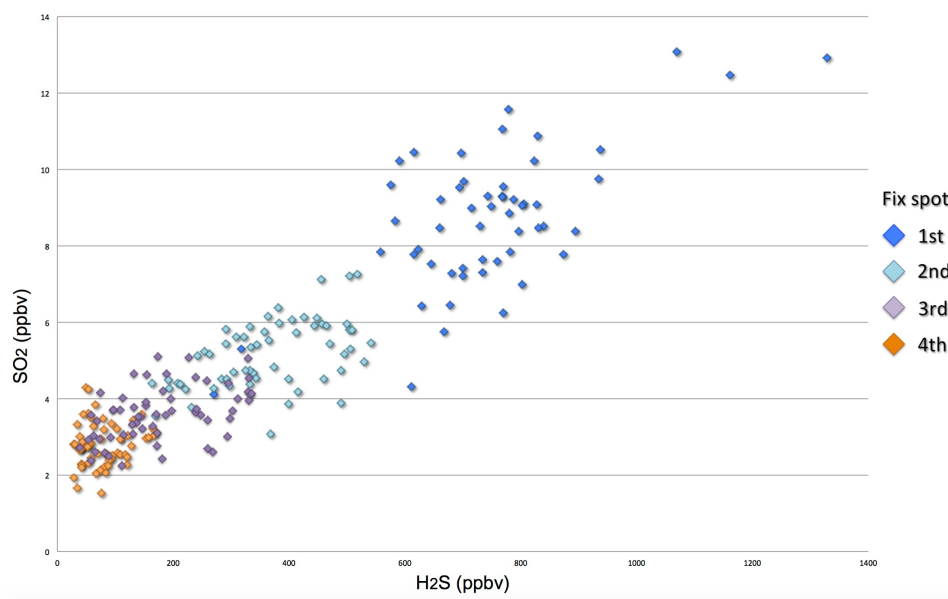
Fix spot	S-compound	MAX (ppbv)	MIN (ppbv)	AVERAGE (ppbv)	MEDIAN (ppbv)	SD
1	H_2S	4551	655	2099	2072	943
	SO_2	17	5.2	9.7	9.3	2.9
2	H_2S	2120	189	935	1014	554
	SO_2	8.9	2.4	5.7	5.8	1.8
3	H_2S	1289	195	536	501	253
	SO_2	5.8	2.4	3.9	3.8	0.7
4	H_2S	539	39	157	108	124
	SO_2	4.0	1.9	2.9	3.0	0.5
5	H_2S	360	30	133	116	80
	SO_2	4.0	1.4	2.8	2.7	0.6

TABLE 5.6: H_2S and SO_2 maximum, minimum, average, median and standard deviation values for each fix spot of measure in BJARN(A) in 2018. The location of 1-5 fix spots is shown in Fig. 5.21
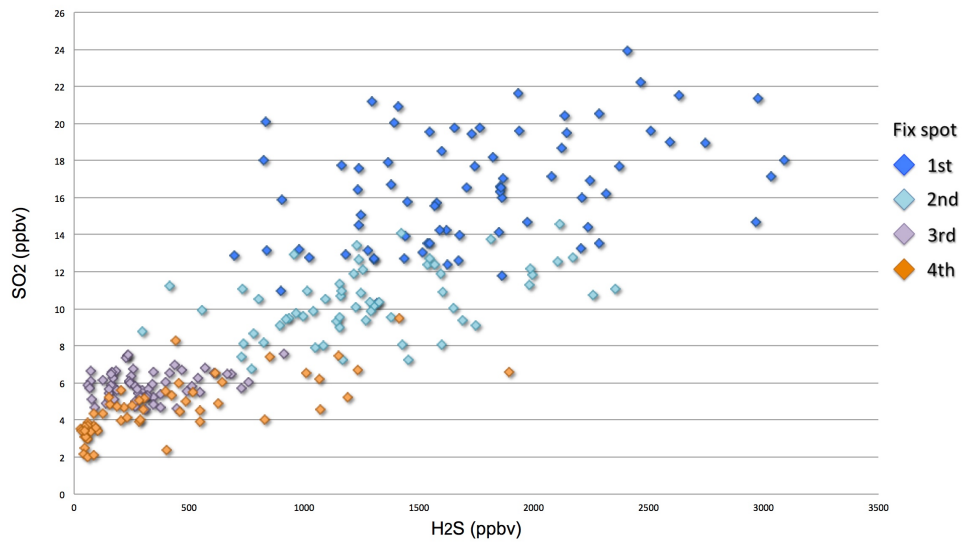
FIGURE 5.24: *SO$_2$-H$_2$S binary diagram for BJARN(C). The four fix spots are indicated with different colors.*

FIGURE 5.25: *Pie diagram showing relative VOC % with respect to the total VOCs composition. The corresponding % is, as follows: aromatics (50.1%), alkanes (21.7%), O-bearing (13.7%), S-bearing (6.6%), cyclics (5.9%), alkenes (1.1%), halocarbons (0.5%) and terpenes (0.5%).*

Fix spot	S-compound	MAX (ppbv)	MIN (ppbv)	AVERAGE (ppbv)	MEDIAN (ppbv)	SD
1	H_2S	3090	696	1751	1675	559
	SO_2	24	10	16	16	3.1
2	H_2S	2357	294	1288	1230	454
	SO_2	15	6.8	10.4	10	1.8
3	H_2S	1892	29	403	268	420
	SO_2	9.5	2.0	4.6	4.5	1.5
4	H_2S	910	59	316	271	189
	SO_2	7.6	4.6	5.9	5.9	0.8

TABLE 5.7: H_2S and SO_2 maximum, minimum, average, median and standard deviation values for each fix spot of measure in BJARN(C) in 2018. The location of 1-4 fix spots is shown in Fig. 5.23

VOCs	nmol/mol
Alkanes	4.7
Aromatics	10.9
Cyclics	1.3
Alkenes	0.2
S-bearing	1.4
O-bearing	3.0
Terpenes	0.1
Halocarbons	0.1

TABLE 5.8: VOCs chemical composition (in nmol/mol) of Bjarnaflag geothermal system.

5.6 Reykjanes

Within the high-temperature geothermal system of Reykjanes (Fig. 3.8), two main emissions were considered: the Gunnuvher big steam vent and a small fumarole nearby (Fig. 3.20 and 3.21). The two sites were measured in 2017: REYK(A) and REY(C), respectively, whereas in 2018 only the second site was measured with two double measurements indicated as REY(D) (Fig. 5.28) and REY(E) (Fig. 5.30). In REY(A), considering all the fix spots, sulfur dioxide ranged from 1.6 to 15 ppbv, while H_2S from 21 to 1384 ppbv (Fig. 5.26). In REYK(C), SO_2 values was in the range of 2-20 ppbv, while those of H_2S were between 13 and 1989 ppbv (Fig. 5.27). The H_2S-SO_2 data for REY(D) and REY(E) are shown in detail in Tables 5.9 and 5.10 and represented in Fig. 5.29 and Fig. 5.31.

Among VOCs, the aromatic compounds are dominant (49.5%), followed by alkanes (25%), alkenes (6.9%), O-bearing (6.3%), S-bearing (5.5%), cyclics (4.9%), and halocarbons (1.9%) (Fig. 5.32, Table 5.11).
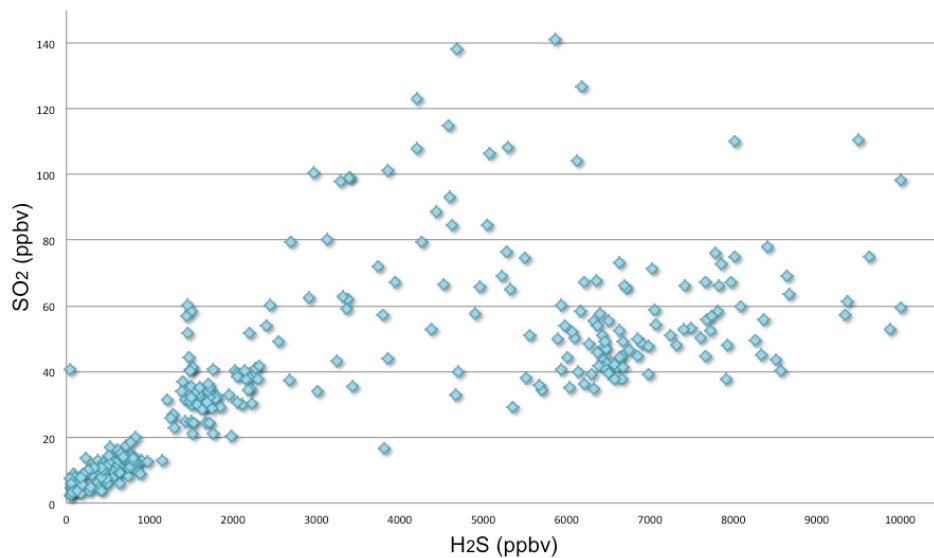
FIGURE 5.26: *SO$_2$-H$_2$S binary diagram for REYK(A). The blue dots represent all the fix spots.*
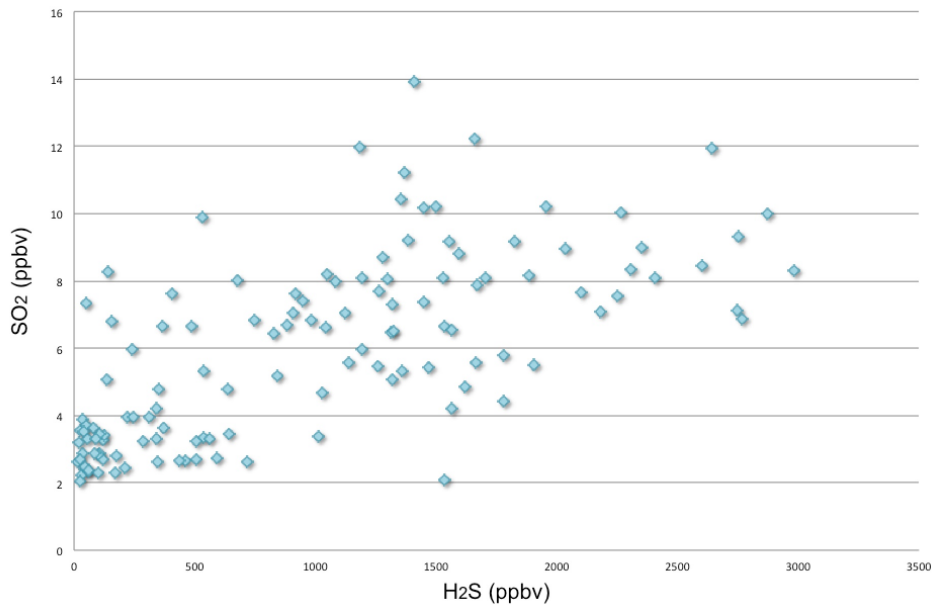

FIGURE 5.27: *SO$_2$-H$_2$S binary diagram for REYK(C). The blue dots represent all the fix spots.*

FIGURE 5.28: *Location of 1-4 fix spots (red dots) with respect to the emitting source (in yellow) for REYK(D). The mean wind velocity is 6 m/s. The Gunnuhver steam vent is also indicated.*
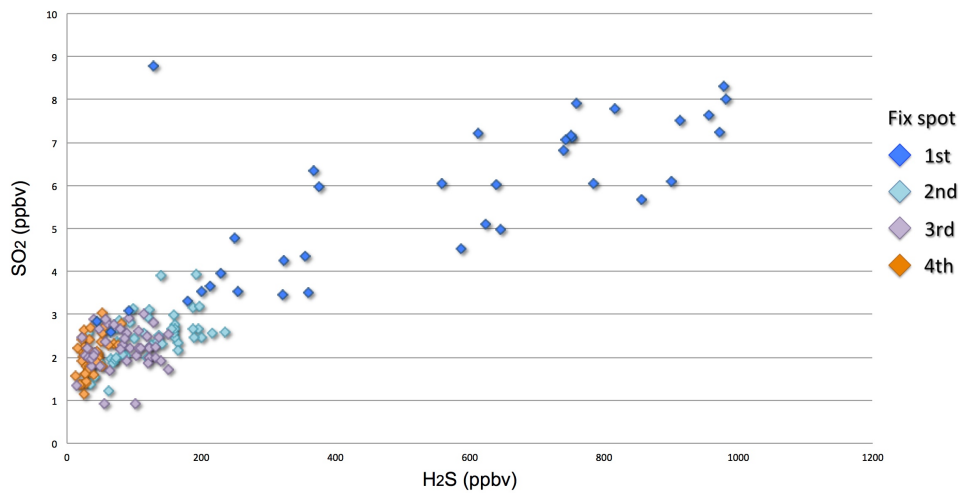
FIGURE 5.29: *SO_2-H_2S binary diagram for REYK(D). The four fix spots are indicated with different colors.*

Fix spot	S-compound	MAX (ppbv)	MIN (ppbv)	AVERAGE (ppbv)	MEDIAN (ppbv)	SD
1	H_2S	981	45	537	600	301
	SO_2	8.8	2.6	5.6	6.0	1.8
2	H_2S	236	32	123	122	54
	SO_2	3.9	1.2	2.5	2.5	0.5
3	H_2S	151	14	85	87	39
	SO_2	3.0	0.9	2.2	2.2	0.5
4	H_2S	81	13	36	32	15
	SO_2	3.0	1.2	2.0	2.1	0.4

TABLE 5.9: H_2S and SO_2 maximum, minimum, average, median and standard deviation values for each fix spot of measure in REYK(D) in 2018. The location of 1-4 fix spots is shown in Fig. 5.28

FIGURE 5.30: *Location of 1-5 fix spots (red dots) with respect to the emitting source (in yellow) for REYK(E). The mean wind velocity is 4.4 m/s. The Gunnuhver steam vent is also indicated.*
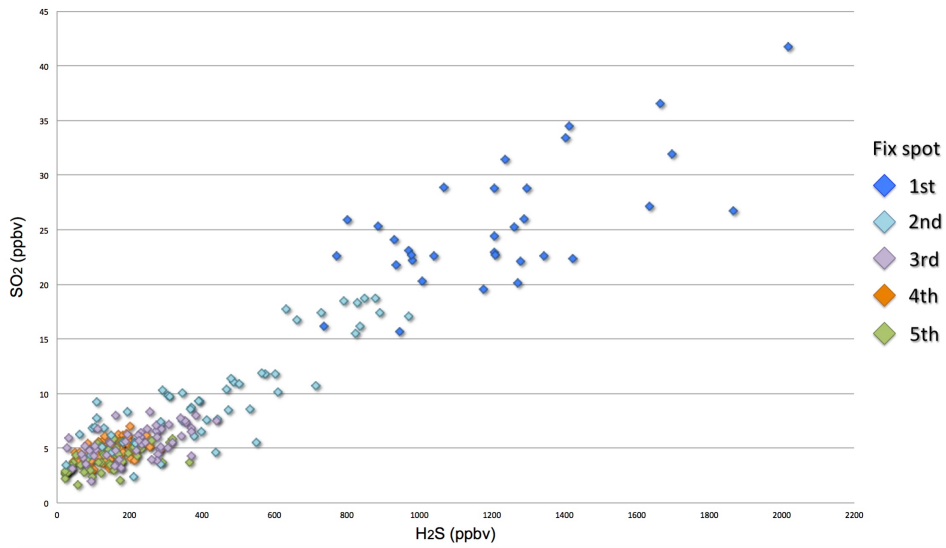
FIGURE 5.31: *SO_2-H_2S binary diagram for REYK(E). The five fix spots are indicated with different colors.*

Fix spot	S-compound	MAX (ppbv)	MIN (ppbv)	AVERAGE (ppbv)	MEDIAN (ppbv)	SD
1	H_2S	2018	736	1217	1207	308
	SO_2	42	16	25	24	5.6
2	H_2S	971	25	423	392	251
	SO_2	19	2.4	9.7	8.7	4.5
3	H_2S	440	27	217	229	103
	SO_2	8.3	2.0	5.5	5.5	1.4
4	H_2S	285	45	154	150	55
	SO_2	7	3.0	4.8	4.8	0.9
5	H_2S	365	21	138	139	85
	SO_2	5.8	2.6	3.9	4.0	0.7

TABLE 5.10: H_2S and SO_2 maximum, minimum, average, median and standard deviation values for each fix spot of measure in REYK(E) in 2018. The location of 1-5 fix spots is shown in Fig. 5.30

VOCs	nmol/mol
Alkanes	9.8
Aromatics	19.4
Cyclics	1.9
Alkenes	2.7
S-bearing	2.1
O-bearing	2.5
Terpenes	-
Halocarbons	0.7

TABLE 5.11: VOCs chemical composition (in nmol/mol) of
Reykjanes geothermal system.
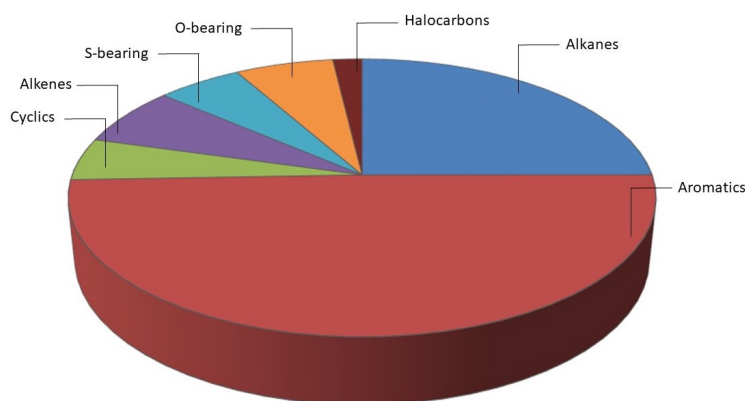
FIGURE 5.32: *Pie diagram showing relative VOC % with respect
to the total VOCs composition. The corresponding % is, as follows:
aromatics (49.5%), alkanes (25%), alkenes (6.9%), O-bearing (6.3%),
S-bearing (5.5%), cyclics (4.9%), and halocarbons (1.9%).*

5.7   Krýsuvík

At the high-temperature geothermal system of Krýsuvík (Fig. 3.8), the mea-
surements were carried out along two transects (indicated as KRY(A) and
KRY(C), respectively) in the touristic area of Seltùn in 2017 (Fig. 5.33 and
Fig. 5.35). No measurements were repeated in 2018. The H_2S-SO_2 data are
reported in detail in Tables 5.12 and 5.13 and represented in Fig. 5.34 and
Fig. 5.36.

FIGURE 5.33: *Location of 1-4 fix spots (red dots) with respect to the emitting source (in yellow) for KRY(A). The mean wind velocity is 3.6 m/s.*
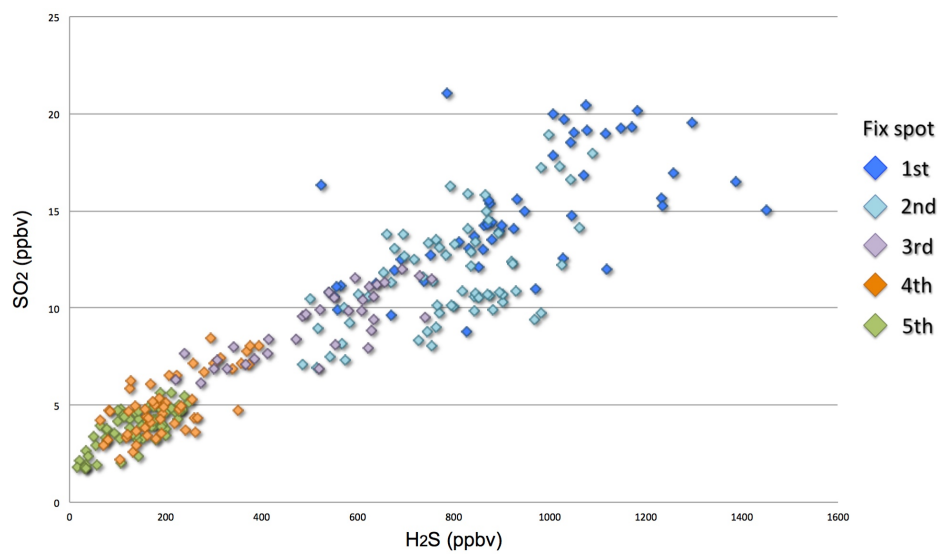

FIGURE 5.34: *SO_2-H_2S binary diagram for KRY(A). The four fix spots are indicated with different colors.*

Fix spot	S-compound	MAX (ppbv)	MIN (ppbv)	AVERAGE (ppbv)	MEDIAN (ppbv)	SD
1	H_2S	1329	270	744	746	165
	SO_2	13	4.1	8.7	8.8	1.9
2	H_2S	541	163	364	361	102
	SO_2	7.3	3.1	5.1	5.2	0.9
3	H_2S	335	38	176	165	87
	SO_2	5.1	2.2	3.6	3.6	0.7
4	H_2S	170	28	80	75	39
	SO_2	4.3	1.5	2.8	2.8	0.6

TABLE 5.12: H_2S and SO_2 maximum, minimum, average, median and standard deviation values for each fix spot of measure in KRY(A) in 2017. The location of 1-4 fix spots is shown in Fig. 5.33

FIGURE 5.35: *Location of 1-4 fix spots (red dots) with respect to the emitting source (in yellow) for KRY(C). The mean wind velocity is 3.7 m/s.*
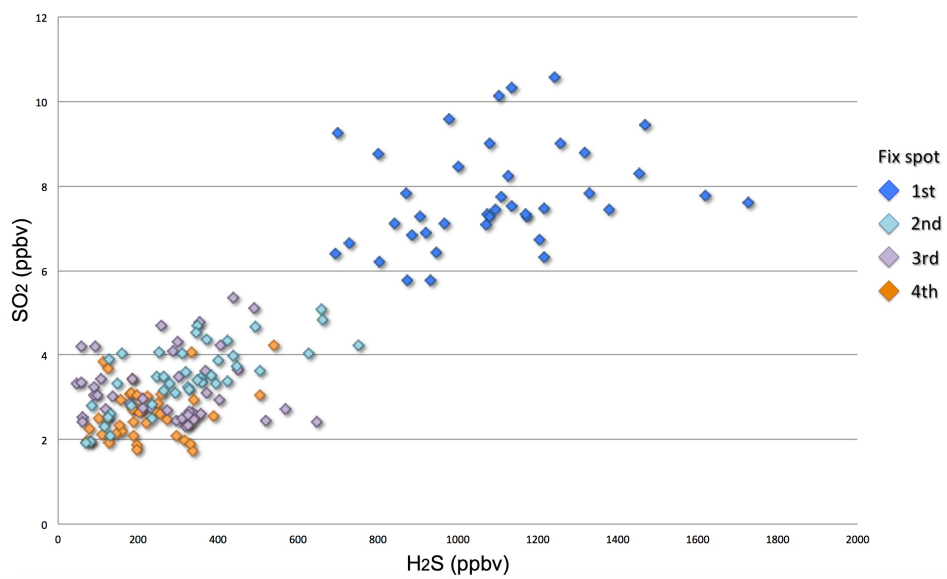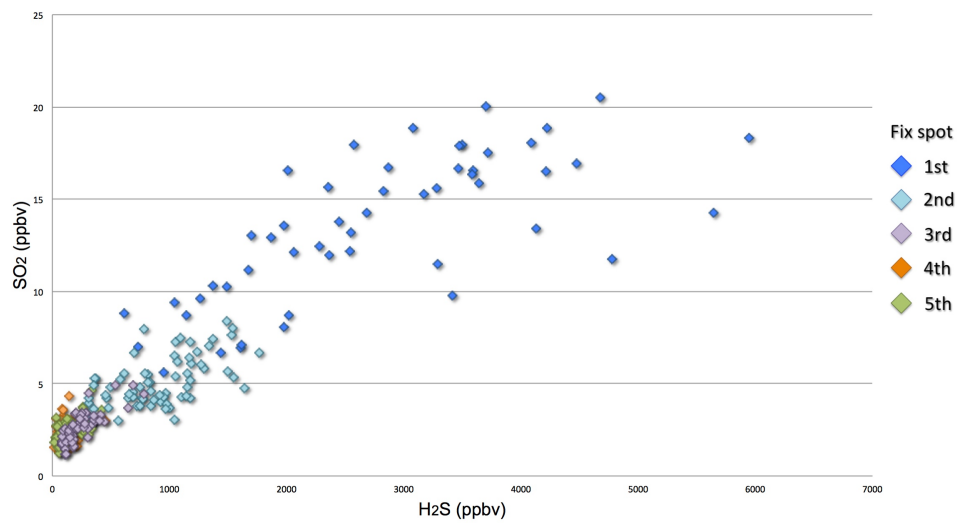

FIGURE 5.36: *SO_2-H_2S binary diagram for KRY(C). The four fix spots are indicated with different colors.*

Fix spot	S-compound	MAX (ppbv)	MIN (ppbv)	AVERAGE (ppbv)	MEDIAN (ppbv)	SD
1	H_2S	1727	693	1090	1087	238
	SO_2	10	5.8	7.8	7.5	1.2
2	H_2S	750	69	320	321	165
	SO_2	5.1	1.9	3.5	3.5	0.8
3	H_2S	646	47	272	296	151
	SO_2	5.4	2.3	3.2	3.0	0.8
4	H_2S	540	73	223	197	103
	SO_2	4.2	1.7	2.6	2.6	0.6

TABLE 5.13: H_2S and SO_2 maximum, minimum, average, median and standard deviation values for each fix spot of measure in KRY(C) in 2017. The location of 1-4 fix spots is shown in Fig. 5.35

5.8 Hengill Skidaskali

At Hengill Skidaskali, part of the Hengill volcanic geothermal area (Fig. 3.8), a mud boiling pool was selected for H_2S-SO_2 measurements in both 2017, named SKI(B) and SKI(C), and 2018, named SKI(D). In SKI(C) sulfur dioxide was between 1.2 and 141 pbbv, while H_2S ranged from 36 to 10804 ppbv (Fig. 5.37). Lower concentrations of SO_2 and H_2S were measured in SKI(D), being comprised between 2.1 and 14 pbbv and 16.0 and 2984 ppbv, respectively (Fig. 5.38). The H_2S-SO_2 values for SKI(B) are reported in detail in Table 5.14 and represented in Fig. 5.40, whereas the location of the six fix spots is shown in Fig. 5.39.

FIGURE 5.37: *SO_2-H_2S binary diagram for SKI(C). The blue dots represent all the fix spots.*

FIGURE 5.38: *SO$_2$-H$_2$S binary diagram for SKI(D). The blue dots represent all the fix spots.*

FIGURE 5.39: *Location of 1-6 fix spots (red dots) with respect to the emitting source (in yellow) for SKI(B). The mean wind velocity is 6.3 m/s.*

Fix spot	S-compound	MAX (ppbv)	MIN (ppbv)	AVERAGE (ppbv)	MEDIAN (ppbv)	SD
1	H_2S	6893	2277	4376	4284	1010
	SO_2	56	18	35	33	8.8
2	H_2S	3541	1559	2457	2425	450
	SO_2	32	10	22	21	4.1
3	H_2S	2533	1196	1684	1643	308
	SO_2	21	12	16	16	2.1
4	H_2S	1018	580	755	734	87
	SO_2	12	6.1	8.7	8.6	1.3
5	H_2S	1027	574	731	718	103
	SO_2	12	5.0	8.5	8.3	1.2
6	H_2S	514	245	401	402	54
	SO_2	8.1	3.8	5.4	5.3	0.9

TABLE 5.14: H_2S and SO_2 maximum, minimum, average, median and standard deviation values for each fix spot of measure in SKI(B) in 2017. The location of 1-6 fix spots is shown in Fig. 5.39
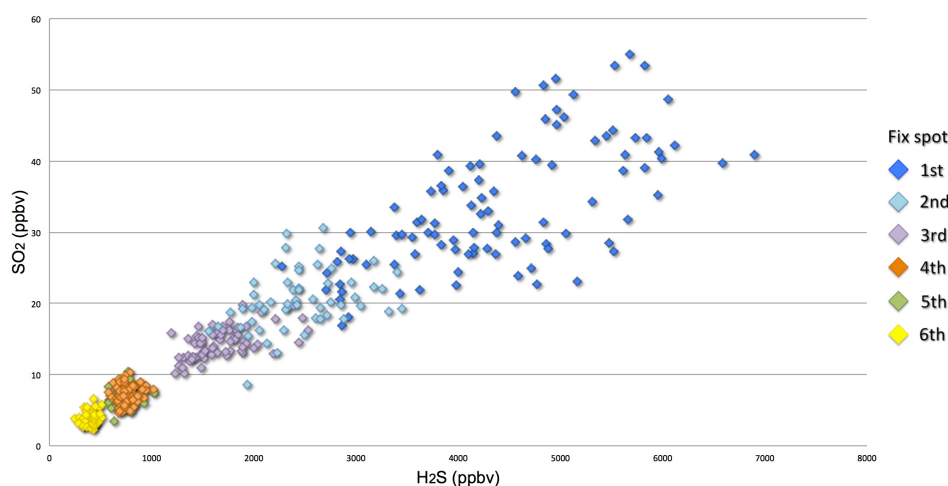
FIGURE 5.40: *SO$_2$-H$_2$S binary diagram for SKI(B). The six fix spots are indicated with different colors.*

5.9   Hengill Ölkelduháls

Within the Ölkelduháls geothermal area, located SE of Hengill volcano (Fig. 3.24), the H$_2$S-SO$_2$ measurements were mainly carried out around several mud bubbling pools in both 2017 and 2018. The 2017 measurements are indicated in this study as OLK(A) (Fig. 5.41) and OLK(C) (Fig. 5.43), while those recorded in 2018 are indicated as OLK(E) (Fig. 5.45). The H$_2$S-SO$_2$ data for OLK(A), OLK(C) and OLK(E) are shown in detail in Tables 5.15, 5.16 and 5.17 and represented in Fig. 5.42, Fig. 5.44 and Fig. 5.46, respectively. The higher H$_2$S-SO$_2$ concentrations of OLK(A) respect to OLK(C) are related to the different distances of the fix spots from the emitting source: in OLK(A) the first fix spot was positioned at 3 meters and the last fix spot at 12 meters from the source, whereas in OLK(C) the first fix spot was at 13 meters and the last at 55 meters from the source (Fig. 5.41, Fig. 5.43).

FIGURE 5.41: *Location of 1-5 fix spots (red dots) with respect to the emitting source (in yellow) for OLK(A). The mean wind velocity is 3.1 m/s.*
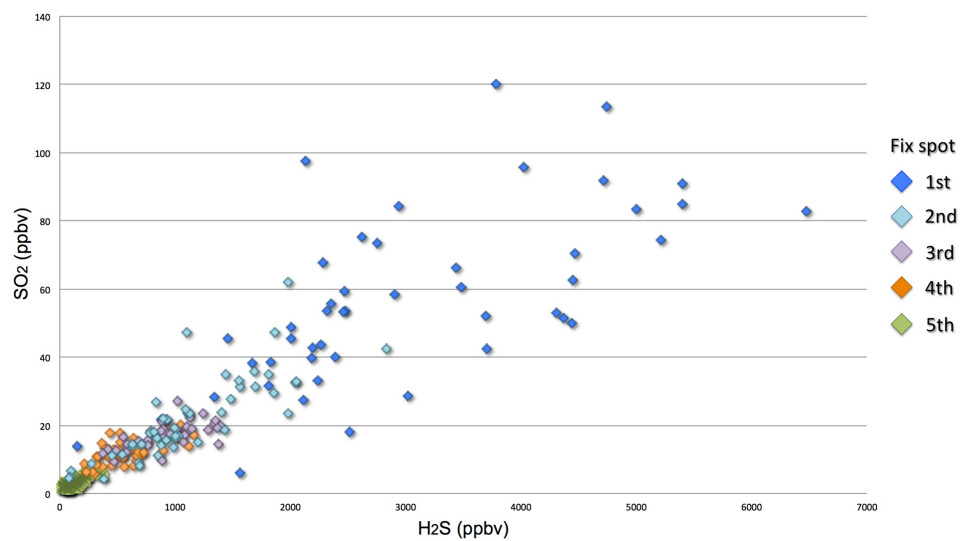
FIGURE 5.42: *SO_2-H_2S binary diagram for OLK(A) in 2017. The five fix spots are indicated with different colors.*

Fix spot	S-compound	MAX (ppbv)	MIN (ppbv)	AVERAGE (ppbv)	MEDIAN (ppbv)	SD
1	H_2S	6476	148	3031	2514	1357
	SO_2	120	5.9	57	53	26
2	H_2S	2837	75	1104	999	583
	SO_2	62	4.2	22	19	12
3	H_2S	1389	376	916	912	292
	SO_2	27	9.2	17	18	3.9
4	H_2S	1158	210	604	555	256
	SO_2	20	5.9	12	12	3.6
5	H_2S	369	19	122	116	78
	SO_2	6.0	1.2	3.1	2.8	1.3

TABLE 5.15: H_2S and SO_2 maximum, minimum, average, median and standard deviation values for each fix spot of measure in OLK(A) in 2017. The location of 1-5 fix spots is shown in Fig. 5.41

FIGURE 5.43: *Location of 1-5 fix spots (red dots) with respect to the emitting source (in yellow) for OLK(C). The mean wind velocity is 9 m/s.*

FIGURE 5.44: *SO_2-H_2S binary diagram for OLK(C) in 2017. The five fix spots are indicated with different colors.*

Fix spot	S-compound	MAX (ppbv)	MIN (ppbv)	AVERAGE (ppbv)	MEDIAN (ppbv)	SD
1	H_2S	1450	525	933	900	221
	SO_2	21	8.8	14.9	14.4	3.3
2	H_2S	1088	33	265	200	179
	SO_2	19	6.9	11.8	10.9	2.7
3	H_2S	754	222	514	545	151
	SO_2	12	6.1	9.1	9.5	1.8
4	H_2S	395	64	205	187	87
	SO_2	8.4	2.2	5.0	4.8	1.5
5	H_2S	248	16	141	150	64
	SO_2	5.6	1.7	3.9	4.0	1.0

TABLE 5.16: H_2S and SO_2 maximum, minimum, average, median and standard deviation values for each fix spot of measure in OLK(C) in 2017. The location of 1-5 fix spots is shown in Fig. 5.43.

FIGURE 5.45: *Location of 1-5 fix spots (red dots) with respect to the emitting source (in yellow) for OLK(E). The mean wind velocity is 2.2 m/s.*

FIGURE 5.46: *SO_2-H_2S binary diagram for OLK(E) in 2018. The five fix spots are indicated with different colors.*

Fix spot	S-compound	MAX (ppbv)	MIN (ppbv)	AVERAGE (ppbv)	MEDIAN (ppbv)	SD
1	H_2S	5944	615	2767	2573	1251
	SO_2	20	5.6	13.5	13.6	3.9
2	H_2S	1767	279	894	870	376
	SO_2	8.4	3.0	5.1	4.8	1.4
3	H_2S	783	81	242	209	147
	SO_2	4.9	1.2	2.7	2.7	0.8
4	H_2S	457	19	136	123	78
	SO_2	4.3	1.3	2.5	2.6	0.6
5	H_2S	418	20	152	137	100
	SO_2	4.6	1.2	2.5	2.5	0.6

TABLE 5.17: H_2S and SO_2 maximum, minimum, average, median and standard deviation values for each fix spot of measure in OLK(E) in 2018. The location of 1-5 fix spots is shown in 5.45.

5.10   Geysir

At Geysir geothermal area (Fig. 3.8), two natural emissions were considered: Konungsvher and Geysir (Fig. 3.29 and 3.30). The measurements were only carried out in 2017. The H_2S-SO_2 concentrations were the lowest ones among the investigated high-temperature geothermal systems. The SO_2 values were varying from 1.2 to 5.6 ppbv in Konungsvher and from 0.6 to 3.2 ppbv in Geysir, while those of H_2S were from 35 to 274 ppbv in Konungsvher and from 3.6 to 92 pbbv in Geysir (Fig. 5.47). Because of the very low H_2S-SO_2 concentrations, Geysir data were not used in the mathematical model.

Among VOCs, the cyclic compounds are dominant (30.6%), followed by aromatics (26.5%), alkanes (24%), O-bearing (10.1%), terpenes (5.4%) and alkenes (3.5%) (Fig. 5.48, Table 5.18).
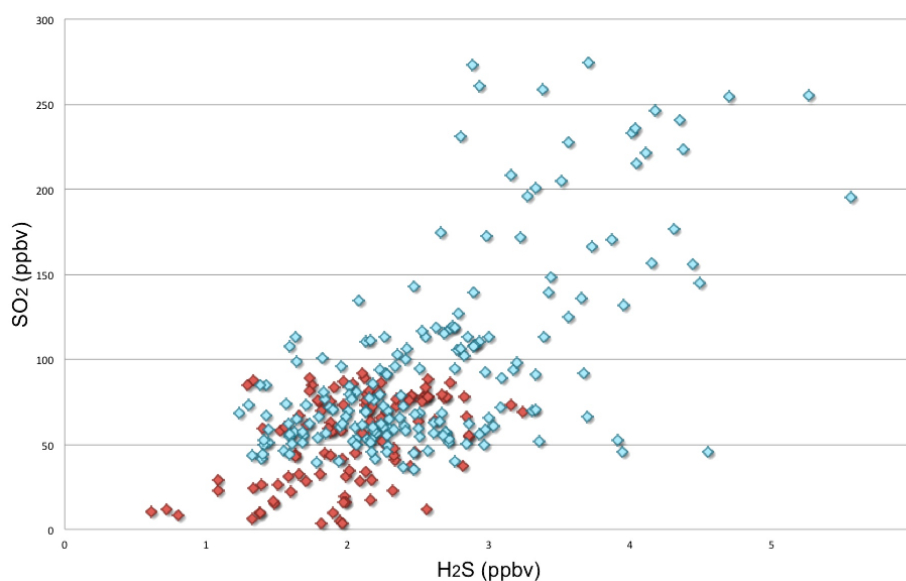
FIGURE 5.47: *SO$_2$-H$_2$S binary diagram for Konungsvher (blue dots) and Geysir (red dots) emissions.*

VOCs	nmol/mol
Alkanes	0.8
Aromatics	0.8
Cyclics	1.0
Alkenes	0.1
S-bearing	-
O-bearing	0.3
Terpenes	0.2
Halocarbons	-

TABLE 5.18: VOCs chemical composition (in nmol/mol) of Geysir geothermal area.
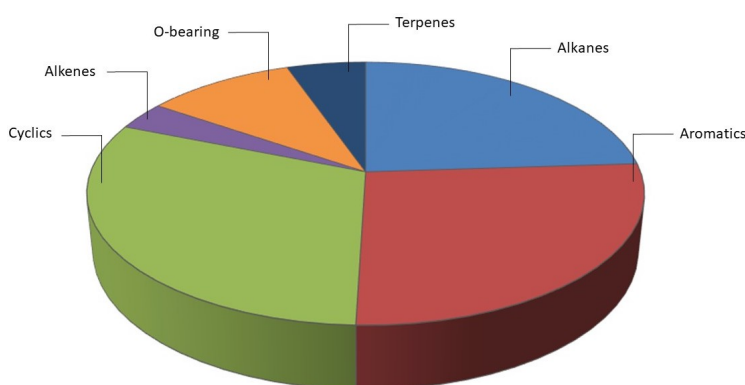
FIGURE 5.48: *Pie diagram showing relative VOC % with respect to the total VOCs composition. The corresponding % is, as follows: cyclics (30.6%), aromatics (26.5%), alkanes (24%), O-bearing (10.1%), terpenes (5.4%) and alkenes (3.5%).*

Chapter 6

Mathematical Model

6.1 The mathematical model: the laminar model

In this Chapter, a mathematical model is proposed to describe the evolution of the concentration $c(\mathbf{x}, t)$ of SO_2 and H_2S in the vicinity of a fumarolic source placed at the origin of a coordinate system $\{\mathbf{O}, x_1, x_2, x_3\}$. The overall mass balance yields

$$\frac{\partial c}{\partial t} + \operatorname{div} \mathbf{j}_c = Q(c) \tag{6.1}$$

where $\mathbf{j}_c$ is the vector flux of SO_2 or H_2S and $Q(c)$ is the rate of production (if $Q > 0$) or consumption (if $Q < 0$) of SO_2 or H_2S. If $Q(c) < 0$ for all positive c then we must require $Q(0) = 0$, meaning that when $c = 0$ the evolution of the system stops since there is no SO_2 or H_2S to be consumed. The specific form of $Q(c)$ should be inferred from the mechanism that produces the consumption/production of the species c. Therefore, if c is consumed because of a reaction then, Q should represents the reaction rate. If c is diluted, then Q should reflect the dilution rate and so forth. The flux $\mathbf{j}_c$ is typically formed by a convective term $\mathbf{j}_{cv}$ and by a diffusive term $\mathbf{j}_D$ where

$$\mathbf{j}_{cv} = c(\mathbf{x}, t)\mathbf{v}(\mathbf{x}, t) \qquad \mathbf{j}_D = -D\nabla c(\mathbf{x}, t). \tag{6.2}$$

In (6.2) the vector field $\mathbf{v}(\mathbf{x}, t)$ represents the velocity at some point $\mathbf{x}$ and at some time t, while the flux $\mathbf{j}_D$ represents the classical Fickian diffusion. The velocity $\mathbf{v}(\mathbf{x}, t)$ must be determined solving the momentum balance equation for the air (which can be treated as a fluid). We recall that the divergence of a vector field $\mathbf{v} = (v_1, v_2, v_3)$ in an Eulerian coordinate system is given by:

$$\mathrm{div}\, \mathbf{v} = \frac{\partial v_1}{\partial x_1} + \frac{\partial v_2}{\partial x_2} + \frac{\partial v_3}{\partial x_3}.$$

The physical meaning of the divergence (notice that the divergence is a scalar) of the velocity $\mathbf{v}$ is the rate at which material volumes change during the flow. Indeed, if the fluid is incompressible div $\mathbf{v} = 0$. The form of $\mathbf{j}_D$ simply states that the species with concentration c migrates along the direction of the maximum growth (the gradient) of the species according to a proportionality factor D called diffusivity. In principle D may also depend on c, but this typically occurs when the range in which c spans is fairly large. As a first approximation we may assume that D is a positive constant. From equation (6.2) we derive:

$$\frac{\partial c}{\partial t} + \mathrm{div}\left(c\mathbf{v} - D\nabla c\right) = Q(c), \tag{6.3}$$

or equivalently:

$$\frac{\partial c}{\partial t} + c\,\mathrm{div}\,\mathbf{v} + \nabla c \cdot \mathbf{v} - D\Delta c = Q(c). \tag{6.4}$$

Indeed:

$$\mathrm{div}\,(c\mathbf{v}) = \sum_{i=1}^{3} \frac{\partial(cv_i)}{\partial x_i} = \sum_{i=1}^{3}\left(c\frac{\partial v_i}{\partial x_i} + \frac{\partial c}{\partial x_i}v_i\right) = c\,\mathrm{div}\,\mathbf{v} + \nabla c \cdot \mathbf{v}$$

The operator Δ is called the Laplacian and it is given by:

$$\Delta c = \frac{\partial^2 c}{\partial x_1^2} + \frac{\partial^2 c}{\partial x_2^2} + \frac{\partial^2 c}{\partial x_3^2}$$

Therefore, the equation that governs the evolution of the species c is given by (6.4). Let's now suppose to take a material volume[1] Ω_t of air. Its mass is given by:

---

[1]With the term material we intend a volume that is constituted by the same particles at each time.

$$M(\Omega_t) = \int_{\Omega_t} \rho(\mathbf{x}, t)d\mathbf{x}.$$

where $\rho(\mathbf{x}, t)$ is the density of the fluid that transports the species with concentration c. If no mass of air is added or removed into the volume during its flow, the mass must remain constant and hence, the time derivative of $M(\Omega_t)$ must be zero (conservation of mass principle). Hence:

$$\frac{dM(\Omega_t)}{dt} = \frac{d}{dt} \int_{\Omega_t} \rho(\mathbf{x}, t)d\mathbf{x} = 0.$$

According to the Reynolds transport theorem (Gurtin, 1981) we obtain:

$$\frac{dM(\Omega_t)}{dt} = \int_{\Omega_t} \frac{\partial \rho}{\partial t}d\mathbf{x} + \int_{\partial\Omega_t} \rho\mathbf{v} \cdot \mathbf{n}d\sigma = 0.$$

where $\partial\Omega_t$ is the boundary of Ω_t and $\mathbf{n}$ its outward normal derivative. On applying the divergence theorem we find:

$$\frac{dM(\Omega_t)}{dt} = \int_{\Omega_t} \frac{\partial \rho}{\partial t}d\mathbf{x} + \int_{\Omega_t} \mathrm{div}\left(\rho\mathbf{v}\right)d\mathbf{x} = 0. \tag{6.5}$$

Because of the arbitrariness of Ω_t we have that relation (6.5) must hold locally. This leads to the famous "continuity" equation:

$$\frac{\partial \rho}{\partial t} + \mathrm{div}\left(\rho\mathbf{v}\right) = 0. \tag{6.6}$$

When the density ρ is constant then div $\mathbf{v} = 0$ and the fluid is said to be incompressible. In this case equation (6.4) reduces to:

$$\frac{\partial c}{\partial t} + \nabla c \cdot \mathbf{v} - D\nabla c = Q(c). \tag{6.7}$$

The vector field $\mathbf{v}$ must be determined imposing the linear momentum balance (in other words Newton's second law for a continuum). This balance law can also be written for a material volume Ω_t,

$$\frac{d}{dt} \underbrace{\int_{\Omega_t} \rho \mathbf{v} d\mathbf{x}}_{\text{linear momentum}} = \mathbf{R}^{(s)} + \mathbf{R}^{(e)}.$$

The right hand side of the above equation is the resultant of the surface forces $\mathbf{R}^{(s)}$ acting on Ω_t and the external forces $\mathbf{R}^{(e)}$ (e.g., gravity) acting on Ω_t. The surface forces are represented through a second order symmetric tensor $\mathbf{T}$ called the Cauchy stress (actually it can be proven that the tensor is symmetric applying the balance of angular momentum), so that we can write:

$$\frac{d}{dt} \underbrace{\int_{\Omega_t} \rho \mathbf{v} d\mathbf{x}}_{\text{linear momentum}} = \int_{\partial\Omega_t} \mathbf{T}\mathbf{n} d\sigma + \int_{\Omega_t} \rho \mathbf{f} d\mathbf{x}$$

where $\mathbf{f}$ is the resultant of the specific external forces. Applying again the Reynolds theorem we find:

$$\int_{\Omega_t} \rho \left(\frac{\partial \mathbf{v}}{\partial t} + (\nabla \mathbf{v})\mathbf{v} \right) d\mathbf{x} = \int_{\Omega_t} \text{div } \mathbf{T} + \rho \mathbf{f} d\mathbf{x}$$

For the arbitrariness of Ω_t we end up with:

$$\rho \left(\frac{\partial \mathbf{v}}{\partial t} + (\nabla \mathbf{v})\mathbf{v} \right) = \text{div}\mathbf{T} + \rho \mathbf{f}, \tag{6.8}$$

that represents the local form of the momentum balance. The tensor $\mathbf{T}$ must be specified by the particular type of considered fluid (constitutive equation). For a Newtonian fluid the tensor assumes the form:

$$\mathbf{T} = -p\mathbf{I} + \mu(\nabla \mathbf{v} + \nabla \mathbf{v}^T)$$

where μ is a positive constant called viscosity and p is the so-called hydrostatic pressure. When $\rho = const$ equation (6.8) becomes:

$$\rho \left(\frac{\partial \mathbf{v}}{\partial t} + (\nabla \mathbf{v})\mathbf{v} \right) = -\nabla p + \mu \Delta \mathbf{v} + \rho \mathbf{f}, \tag{6.9}$$

also known as the Navier-Stokes equation. When written component-wise we obtain:

$$\rho\left(\frac{\partial v_1}{\partial t} + v_1\frac{\partial v_1}{\partial x_1} + v_2\frac{\partial v_1}{\partial x_2} + v_3\frac{\partial v_1}{\partial x_3}\right) = -\frac{\partial p}{\partial x_1} + \mu\left(\frac{\partial^2 v_1}{\partial x_1^2} + \frac{\partial^2 v_1}{\partial x_2^2} + \frac{\partial^2 v_1}{\partial x_3^2}\right) + \rho f_1,$$

$$\rho\left(\frac{\partial v_2}{\partial t} + v_1\frac{\partial v_2}{\partial x_1} + v_2\frac{\partial v_2}{\partial x_2} + v_3\frac{\partial v_2}{\partial x_3}\right) = -\frac{\partial p}{\partial x_2} + \mu\left(\frac{\partial^2 v_2}{\partial x_1^2} + \frac{\partial^2 v_2}{\partial x_2^2} + \frac{\partial^2 v_2}{\partial x_3^2}\right) + \rho f_2,$$

$$\rho\left(\frac{\partial v_3}{\partial t} + v_1\frac{\partial v_3}{\partial x_1} + v_2\frac{\partial v_3}{\partial x_2} + v_3\frac{\partial v_3}{\partial x_3}\right) = -\frac{\partial p}{\partial x_3} + \mu\left(\frac{\partial^2 v_3}{\partial x_1^2} + \frac{\partial^2 v_3}{\partial x_2^2} + \frac{\partial^2 v_3}{\partial x_3^2}\right) + \rho f_3,$$

Consequently, when the velocity field $\mathbf{v}$ is constant (equilibrium solution) the Navier-Stokes equation produces the trivial equation:

$$\nabla p = \rho\mathbf{f},$$

which states that the hydrostatic pressure is balanced by the external forces acting on the fluid. Assuming for instance that $\mathbf{f}$ is gravity, i.e. $\mathbf{f} = g\mathbf{e}_3$ we obtain the system:

$$\begin{cases} \dfrac{\partial p}{\partial x_1} = 0 \\[2mm] \dfrac{\partial p}{\partial x_2} = 0 \\[2mm] \dfrac{\partial p}{\partial x_3} = \rho g \end{cases}$$

whose solution is given by $p = p_o + \rho g x_3$, where p_o is the pressure at level $z = 0$. We have introduced the Navier-Stokes equation because it allows to determine a number that tells us whether we are in a laminar or in a turbulent regime. This is important as equations (6.7) and (6.9) are valid only when this number, called the Reynolds number, is less than a fixed value. The Reynolds number can be defined for various situations in which a fluid is in relative motion with respect to a surface (flow in a duct, flow over a surface, etc). To define this number we set $\mathbf{f} = \mathbf{g} = g\mathbf{e}_3$, meaning

that the body force is gravity (directed along $\mathbf{e}_3$). Then, we can introduce the non-dimensional variables:

$$\mathbf{x} = L\tilde{\mathbf{x}} \qquad t = T\tilde{t} \qquad p = P\tilde{p} \qquad \mathbf{v} = U\tilde{\mathbf{v}}, \qquad (6.10)$$

where L, T, P and U are characteristic length, time, pressure and velocity, respectively. The choice of these reference quantities must be suggested by the "physics" of the problem and we shall shortly see how to select them. Substituting (6.10) into (6.9) we find:

$$\left(\frac{\rho U^2}{L}\right)\left[\left(\frac{L}{UT}\right)\frac{\partial\tilde{\mathbf{v}}}{\partial\tilde{t}} + (\tilde{\nabla}\tilde{\mathbf{v}})\tilde{\mathbf{v}}\right] = -\left(\frac{P}{L}\right)\tilde{\nabla}\tilde{p} + \left(\frac{\mu U}{L^2}\right)\tilde{\Delta}\tilde{\mathbf{v}} + \rho g\mathbf{e}_z,$$

or equivalently:

$$\left[\left(\frac{L}{UT}\right)\frac{\partial\tilde{\mathbf{v}}}{\partial\tilde{t}} + (\tilde{\nabla}\tilde{\mathbf{v}})\tilde{\mathbf{v}}\right] = -\left(\frac{P}{\rho U^2}\right)\tilde{\nabla}\tilde{p} + \left(\frac{\mu}{\rho U L}\right)\tilde{\Delta}\tilde{\mathbf{v}} + \left(\frac{gL}{U^2}\right)\mathbf{e}_z, \quad (6.11)$$

We define $T_t = L/U$ the characteristic time (this indeed is the time taken by a particle that travels at speed U to cover a length L). Then, we define:

$$Eu = \frac{P}{\rho U^2} \qquad \text{(Euler number)} \qquad Re = \frac{\rho U L}{\mu} \qquad \text{(Reynolds number)}$$

$$Fr = \frac{U}{\sqrt{gL}} \qquad \text{(Freude number)}$$

Choosing as characteristic time $T = T_t$, the system (6.11) can be rewritten as:

$$\left[\frac{\partial\tilde{\mathbf{v}}}{\partial\tilde{t}} + (\tilde{\nabla}\tilde{\mathbf{v}})\tilde{\mathbf{v}}\right] = -Eu\tilde{\nabla}\tilde{p} + \frac{1}{Re}\tilde{\Delta}\tilde{\mathbf{v}} + \frac{1}{Fr^2}\mathbf{e}_z, \qquad (6.12)$$

The non-dimensional number Eu is called the Euler number and it measures the ratio between the pressure and the inertial forces. The non-dimensional

number Fr is called the Freude number and it measures the ratio between gravity and the inertial forces. The non-dimensional number Re is called the Reynolds number and it measures the ratio between the inertial and the viscous forces. Taking as typical values for air:

$$\rho \approx 1.2\,\frac{Kg}{m^3} \qquad \mu \approx 1.5 \cdot 10^{-5}\,\frac{Kg}{m \cdot s} \qquad U = 3\frac{m}{s} \qquad L = 20\,m$$

we see that:

$$Re = O(10^6)$$

meaning that we are essentially in a turbulent regime. This is consistent with experimental evidence that shows that air is inherently turbulent. In this case, the Navier-Stokes equations are no longer valid and velocity cannot be determined by solving (6.9).

6.2 Modeling the turbulent flow and turbulent diffusion

The typical feature of turbulence is that the fluid velocity varies significantly and irregularly in both position and time. As a result, turbulence is a statistical phenomenon and is best described with statistical techniques. If the turbulent motions are subsonic, the flow can often be approximately treated as being incompressible. Such flows are subject to fluid instabilities that can easily produce swirling motions on many different scales. To take into account these instabilities the Reynolds decomposition can be used as it refers to the separation of flow variables (e.g., velocity, pressure etc.) into the mean (time-averaged) component and the fluctuating component. As a consequence, we write:

$$\mathbf{v} = \bar{\mathbf{v}} + \mathbf{v}' \qquad p = \bar{p} + p' \tag{6.13}$$

The averaging method considers the mean value at a fixed point in space and averaged over a time interval large enough so that the mean values are independent of it. In conclusion:

$$\overline{\mathbf{v}} = \frac{1}{\Delta t} \int\limits_{t_o}^{t_o+\Delta t} \mathbf{v}\,dt \qquad \overline{p} = \frac{1}{\Delta t} \int\limits_{t_o}^{t_o+\Delta t} p\,dt$$

The time-average of the fluctuating values are supposed to be zero, i.e.:

$$\overline{\mathbf{v}'} = 0 \quad \overline{p'} = 0.$$

Notice that for any scalar quantity φ:

$$\overline{\frac{\partial \varphi}{\partial x_j}} = \frac{\partial \overline{\varphi}}{\partial x_j}$$

Hence, the substitution of (6.13) into the mass balance yields:

$$\frac{\partial \overline{v}_1}{\partial x_1} + \frac{\partial \overline{v}_2}{\partial x_2} + \frac{\partial \overline{v}_3}{\partial x_3} = 0.$$

The substitution into (6.9) is trickier, but at the end we get:

$$\rho\left(\frac{\partial \overline{v}_1}{\partial t} + \overline{v}_1\frac{\partial \overline{v}_1}{\partial x_1} + \overline{v}_2\frac{\partial \overline{v}_1}{\partial x_2} + \overline{v}_3\frac{\partial \overline{v}_1}{\partial x_3}\right) = -\frac{\partial \overline{p}}{\partial x_1} + \mu\Delta\overline{v}_1 + \rho f_1 - \rho\left(\frac{\partial \overline{v'_1 v'_1}}{\partial x_1} + \frac{\partial \overline{v'_1 v'_2}}{\partial x_2} + \frac{\partial \overline{v'_1 v'_3}}{\partial x_3}\right),$$

$$\rho\left(\frac{\partial \overline{v}_2}{\partial t} + \overline{v}_1\frac{\partial \overline{v}_2}{\partial x_1} + \overline{v}_2\frac{\partial \overline{v}_2}{\partial x_2} + \overline{v}_3\frac{\partial \overline{v}_2}{\partial x_3}\right) = -\frac{\partial \overline{p}}{\partial x_2} + \mu\Delta\overline{v}_2 + \rho f_2 - \rho\left(\frac{\partial \overline{v'_2 v'_1}}{\partial x_1} + \frac{\partial \overline{v'_2 v'_2}}{\partial x_2} + \frac{\partial \overline{v'_2 v'_3}}{\partial x_3}\right),$$

$$\rho\left(\frac{\partial \overline{v}_3}{\partial t} + \overline{v}_1\frac{\partial \overline{v}_3}{\partial x_1} + \overline{v}_2\frac{\partial \overline{v}_3}{\partial x_2} + \overline{v}_3\frac{\partial \overline{v}_3}{\partial x_3}\right) = -\frac{\partial \overline{p}}{\partial x_3} + \mu\Delta\overline{v}_3 + \rho f_3 - \rho\left(\frac{\partial \overline{v'_3 v'_1}}{\partial x_1} + \frac{\partial \overline{v'_3 v'_2}}{\partial x_2} + \frac{\partial \overline{v'_3 v'_3}}{\partial x_3}\right),$$

In a more compact form we can write:

$$\rho\frac{D\overline{v}_i}{Dt} = -\frac{\partial \overline{p}}{\partial x_i} + \mu\Delta v_i + \rho f_i - \rho\left(\sum_{j=1}^{3} \frac{\partial \overline{v'_i v'_j}}{\partial x_j}\right), \qquad\qquad (6.14)$$

Equations (6.14) are sometimes referred to as the Reynolds averaged Navier-Stokes equations (RANS). We may therefore re-write the total shear stress as:

$$T_{ij} = -p\delta_{ij} + \mu \left(\frac{\partial v_i}{\partial x_j} - \rho \overline{v_i' v_j'} \right),$$

where δ_{ij} is the Kronecher delta. If we compare (6.14) to the Navier-Stokes equations (6.9) we notice that besides the viscous part an additional term was added to the total shear stress. This term results from the time-average and is generally the dominant part of the total shear stress. Since the term only appears due to the Reynolds average, it is called "Reynolds stress" or "apparent turbulent shear stress". To obtain the closure of the system, the form of the Reynolds stresses must be specified, which sets, in relation, the apparent shear stresses with the velocity field of the average flow. Boussinesq hypothesis yields:

$$-\overline{v_i' v_j'} = \nu_t \left(\frac{\partial \bar{v}_i}{\partial x_j} + \frac{\partial \bar{v}_j}{\partial x_i} - \frac{2}{3} \frac{\partial \bar{v}_k}{\partial x_k} \delta_{ij} \right) - \frac{2}{3} K \delta_{ij}$$

where:

$$K = \frac{1}{2} \overline{v_i' v_i'}.$$

Other choices are of course possible. Let us now focus on the advection-diffusion equation (6.7) and let us decompose the concentration c in the mean and fluctuating parts (as we have done for the velocity field):

$$c = \bar{c} + c'. \tag{6.15}$$

Substitution of (6.15) into (6.7) leads to:

$$\frac{\partial}{\partial t}(\bar{c} + c') + \nabla(\bar{c} + c') \cdot (\bar{\mathbf{v}} + \mathbf{v}') = D\Delta(\bar{c} + c') + Q(\bar{c} + c'). \tag{6.16}$$

Let us now suppose, for simplicity that Q is linear and let us time-average equation (6.16). After some calculation we get:

$$\frac{\partial \overline{c}}{\partial t} + \nabla \overline{c} \cdot \overline{\mathbf{v}} = D\Delta \overline{c} - \nabla(\overline{c'\mathbf{v}'}) + Q(\overline{c}). \qquad (6.17)$$

or in an analogous way:

$$\frac{\partial \overline{c}}{\partial t} + \nabla \overline{c} \cdot \overline{\mathbf{v}} = \mathrm{div}(D\nabla \overline{c} - \overline{c'\mathbf{v}'}) + Q(\overline{c}). \qquad (6.18)$$

It is easy to see that the term $D\nabla \overline{c} - \overline{c'\mathbf{v}'}$ in the parenthesis on the r.h.s. represents the mass transport. The first is due to molecular diffusion (Fick's law) and the second is the turbulent flow that arises because of the correlation between $\mathbf{v}'$ and c'. Since D is typically a very small quantity we have that:

$$\|\overline{c'\mathbf{v}'}\| \gg \|D\nabla c\|$$

and the molecular diffusion term can be neglected compared to the turbulent flux. It is however to remark that, at smaller scales, the molecular diffusion is still an important mechanism for mixing. At this point it can be useful to drop the bar and re-write equation (6.18) and:

$$\frac{\partial c}{\partial t} + \nabla c \cdot \mathbf{v} = -\nabla(c'\mathbf{v}') + Q(c). \qquad (6.19)$$

The above equation cannot be solved because the quantities c' and $\mathbf{v}'$ are unknown. Once again, we have to "close" the problem. In common engineering problems this is circumvented with the "eddy diffusivity coefficients". In other words, we write:

$$c'\mathbf{v}' = -K_1 \frac{\partial c}{\partial x_1} - K_2 \frac{\partial c}{\partial x_2} - K_3 \frac{\partial c}{\partial x_3}, \qquad (6.20)$$

or equivalently:

$$c' \mathbf{v}' = - \begin{pmatrix} K_1 & 0 & 0 \\ & & \\ 0 & K_2 & 0 \\ & & \\ 0 & 0 & K_3 \end{pmatrix} \nabla c, \qquad (6.21)$$

where K_j are the "eddy diffusivity coefficients". In general, these coefficients depend on some mean properties of the flow. Various empiric correlations have been proposed to model the form of the eddy coefficients. Equation (6.19) becomes:

$$\frac{\partial c}{\partial t} + v_1 \frac{\partial c}{\partial x_1} + v_2 \frac{\partial c}{\partial x_2} + v_3 \frac{\partial c}{\partial x_3} =$$

$$= \frac{\partial}{\partial x_1} \left(K_1 \frac{\partial c}{\partial x_1} \right) + \frac{\partial}{\partial x_2} \left(K_2 \frac{\partial c}{\partial x_2} \right) + \frac{\partial}{\partial x_3} \left(K_3 \frac{\partial c}{\partial x_3} \right) + Q(c). \qquad (6.22)$$

The K_j coefficients have the same dimensions of molecular diffusivity, i.e. a square length over a time. As a consequence, the mass flux (6.20) can be interpreted as "turbulent diffusion". Turbulent diffusion can be defined as a diffusion process by which substances are transported in the atmosphere or in any fluid system due to eddy motion (random and chaotic time dependent motions) and it greatly accelerates the transport and the decrease of concentrations of passive contaminants in a fluid or environment. Consequently, turbulent diffusion is responsible for the dilution of H_2S and SO_2 in the atmosphere according to a parameter K called "eddy diffusivity coefficient". On the other hand, the Q(c) term represents the production (or consumption) of H_2S and SO_2, namely the rate of increase (or decrease) of the two pollutants initial concentration once they are released from the emitting source. By data observations, we assume that consumption outweighs on production and consequently, the Q(c) will be preceded by a minus sign. Furthermore, we assume that this consumption is mainly due to chemical reactions that involve both H_2S and SO_2 in air by various reagents, since the two pollutants are highly reactive acidic species in the atmosphere. The types of these chemical reactions will be discussed in detail in Chapter 8.

6.3   1D model with negligible diffusion

As a first attempt to solve how SO_2 or H_2S evolved with time and distance, we may assume that velocity is constant **v** so that the RANS are automatically satisfied. Let's suppose that the fumarole produces SO_2 or H_2S from a source point $x = 0$ and that turbulent diffusion is negligible ($K_1 = K_2 = K_3 = 0$). In this case the measured SO_2 or H_2S concentration is given by $c(x, t)$, where x represents the distance from the fumarole and t is time. The equation for the concentration is given by:

$$\frac{\partial c}{\partial t} + v\frac{\partial c}{\partial x} = Q(c) \qquad x \in [0, L] \ \ t \geqslant 0 \tag{6.23}$$

where $v > 0$ is the longitudinal constant averaged velocity of the wind ($v = v_1$) and $Q(c) < 0$ is the rate of disappearance of SO_2 or H_2S (due to possible reaction processes). The intent is that to model the specific form of $Q(c)$ in order to have a simulation model to predict the concentration of SO_2 or H_2S at a given distance from the fumarole at a given time. The first attempt we make is to assume that:

$$Q(c) = -\alpha c$$

where α is a parameter that has to be determined to validate the model with experimental data. The dimension of α is the inverse of a time (t^{-1}). The domain of the equation (6.23) is shown in Fig. 6.1.
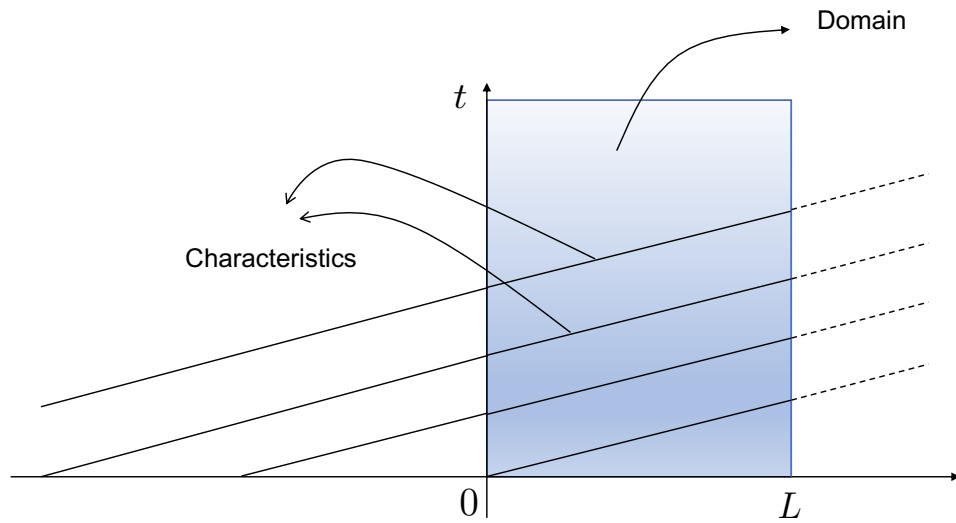
FIGURE 6.1: *Sketch of the domain*

Equation (6.23) must be coupled with the boundary and initial conditions:

$$c(0,t) = c_f(t) \qquad c(x,0) = c_{in}(x)$$

where $c_f(t)$ is the concentration of the fumarole at time t and $c_{in}(x)$ is the initial profile of the SO_2 concentration. Problem (6.23) can be solved by the method of characteristics (Samarskii and Tikhonov, 1963). This approach indeed considers the differential system provided by the coefficients of equation (6.23):

$$\begin{cases} \dfrac{dt}{d\tau} = 1 & t(0) = t_o \\[2mm] \dfrac{dx}{d\tau} = v & x(0) = x_o \\[2mm] \dfrac{dc}{d\tau} = -\alpha c & c(0) = c(x_o, t_o); \end{cases} \qquad (6.24)$$

Integration of (6.24) yields:

$$\begin{cases} t = \tau + t_o \\[2ex] x = v\tau + x_o \\[2ex] \ln c = \ln c(0) - \alpha\tau \end{cases} \tag{6.25}$$

Setting $t_o = 0$, from the first two of (6.25) we get the equation of the characteristics:

$$x - vt = x_o \tag{6.26}$$

while from the 6.26 we find:

$$c = c(x_o, 0)e^{-\alpha t}$$

The solution is therefore given by:

$$c(x, t) = c(x_o, 0)e^{-\alpha t} = c_{in}(x_o)e^{-\alpha t} = c_{in}(x - vt)e^{-\alpha t} \tag{6.27}$$

where x_o is given by (6.26).

As shown by Fig. 6.1 the characteristic passing from some point (x, t) may intersect the $x-$axis at some point $(x_o, 0)$ with $x_o < 0$. Therefore we must extend the function $c_{in}(x)$, which is only defined for $x \geq 0$, also to the half space $x < 0$. This is to be done in a way such that when $x = 0$ we get $c(0, t) = c_f(t)$. Therefore, the following function can be defined:

$$c_{in}^{ext}(x) = \begin{cases} c_{in}(x) & x \geq 0, \\[2ex] \bar{c}_{in}(x) & x < 0, \end{cases}$$

so that:

$$c(x, t) = c_{in}^{ext}(x - vt)e^{-\alpha t}. \tag{6.28}$$

Then we impose that:

$$c(0,t) = c_{in}^{ext}(-vt)e^{-\alpha t} = \bar{c}_{in}(-vt)e^{-\alpha t} = c_f(t). \qquad (6.29)$$

Defining $-vt = \xi$ we find:

$$\bar{c}_{in}(\xi) = c_f(-\frac{\xi}{v})e^{-\frac{\alpha \xi}{v}} \qquad (6.30)$$

In conclusion the solution $c(x,t)$ is given by (6.28) with:

$$c_{in}^{ext}(x) = \begin{cases} c_{in}(x) & x \geq 0, \\ \\ c_f(-\frac{x}{v})e^{-\frac{\alpha x}{v}} & x < 0, \end{cases}$$

or analogously:

$$c(x,t) = \begin{cases} c_{in}(x - vt)e^{-\alpha t} & x \geq 0, \\ \\ c_f(t - \frac{x}{v})e^{-\frac{\alpha x}{v}} & x < 0, \end{cases}$$

6.4 2D model with non-negligible turbulent diffusion

Let us go back to equation (6.22) and let us make the following assumptions:

- velocity and eddy diffusion coefficients are uniform in x_2 (where x_2 represents the cross-wind direction);

- the sink term Q is linear in c, i.e. term $Q(c) = -\alpha c$;

- longitudinal diffusion is negligible with respect to the advection transport term in the x_1 direction;

- vertical velocity v_3 is negligible.

Integrating (6.22) in y from $-\infty$ to ∞ with the boundary conditions $c = 0$ for $y \to \pm\infty$ we get:

$$\frac{\partial c^\gamma}{\partial t} + v_1 \frac{\partial c^\gamma}{\partial x_1} = \frac{\partial}{\partial x_3}\left(K_3 \frac{\partial c^\gamma}{\partial x_3}\right) - \alpha c^\gamma \tag{6.31}$$

where c^γ is the integrated cross-wind concentration. For simplicity we re-write (6.31) setting $c = c^\gamma$, $v_1 = v$, $x_1 = x$, $x_3 = z$ and $K = K_3$, obtaining:

$$\frac{\partial c}{\partial t} + v \frac{\partial c}{\partial x} = \frac{\partial}{\partial z}\left(K \frac{\partial c}{\partial z}\right) - \alpha c \tag{6.32}$$

Once again we suppose that v (the mean velocity) is constant and given (measured). Consequently, the momentum equations are automatically satisfied. It can be pinpointed that eq. (7.8) differs from that (6.23) because of the vertical diffusion. The problem is definitely more involved than (6.23), because now the system is 2D in space and different boundary conditions have to be specified. Moreover, the problem (7.8) can be solved only numerically, since in this case no analytical solutions are available. The problem (7.8) must be solved in the domain:

$$\Omega = [0, L] \times [0, h] \times [0, T]$$

where L is the distance from the fumarole, h is the maximum height of the atmospheric layer under consideration and T is the maximum time of the simulation. Equation (7.8) is parabolic in z (second order PDE) and of the first order in x. Therefore, we must impose the boundary conditions on $z = 0$, $z = h$ and $x = 0$. The initial condition is the concentration at time $t = 0$. Following Moreira et al. (2016), we impose that the flux is null on $z = 0$ and $z = h$, namely:

$$K \frac{\partial c}{\partial z}(x, 0, t) = 0 \qquad\qquad K \frac{\partial c}{\partial z}(x, h, t) = 0$$

while on $x = 0$ we write:

$$c(0, z, t) = f(z, t)$$

where $f(z, t)$ represents the concentration at the fumarole location as a function of time and as a function of the altitude z. Finally, we write the initial condition:

$$c(x, z, 0) = g(x, z).$$

6.4.1 Numerical solution

To determine the solution of (7.8), we re-write the problem in a non-dimensional form introducing the following non-dimensional variables:

$$t = T_c \tilde{t} \quad x = L\tilde{x} \quad z = h\tilde{z},$$

where T_c is a characteristic time still to be selected. Notice that c is not rescaled since it is non-dimensional (it is measured in ppb). We introduce the characteristic times:

$$T_t = \left(\frac{L}{v}\right) \quad T_d = \left(\frac{h^2}{K}\right) \quad T_r = \left(\frac{1}{\alpha}\right).$$

which represent the reference transport time, the reference diffusive time and the reference reaction time, respectively. Selecting $T_c = T_t$ we re-write the problem for the concentration in the following form:

$$
\begin{cases}
\dfrac{\partial c}{\partial \tilde{t}} + \dfrac{\partial c}{\partial \tilde{x}} = a\dfrac{\partial^2 c}{\partial \tilde{z}^2} + bc, \\[2mm]
\dfrac{\partial c}{\partial \tilde{z}}(\tilde{x}, 0, \tilde{t}) = \dfrac{\partial c}{\partial \tilde{z}}(\tilde{x}, 1, \tilde{t}) = 0, \\[2mm]
c(0, \tilde{z}, \tilde{t}) = f(\tilde{z}, \tilde{t}), \\[2mm]
c(\tilde{x}, \tilde{z}, 0) = g(\tilde{x}, \tilde{z}),
\end{cases}
\tag{6.33}
$$

where:

$$a = \left(\frac{T_t}{T_d}\right) = \left(\frac{Lh^2}{vK}\right) \qquad b = \left(\frac{T_t}{T_r}\right) = \left(\frac{L}{\alpha v}\right)$$

To solve (6.33) we write an implicit numerical scheme based on finite differences. We discretize the domain by means of a grid (we drop the tildas for simplicity) where each a point (x, y, t) is approximated by (x_i, z_j, t_k):

$$x_i = i\delta x \qquad z_j = j\delta z \qquad t_k = k\delta t,$$

with $i = 0, ..., n_x$, $j = 0, ..., n_z$ and $k = 0, ..., n_t$. The function c is computed at each point of the grid and we write:

$$c(x_i, z_j, t_k) = c_{i,j}^k$$

The derivatives in the partial differential equation $(6.33)_1$ are approximated by linear combinations of function values at the grid points. In particular we write:

$$\frac{\partial c}{\partial t} \approx \frac{c_{i,j}^k - c_{i,j}^{k-1}}{\delta t}$$

$$\frac{\partial c}{\partial x} \approx \frac{c_{i,j}^k - c_{i-1,j}^k}{\delta x}$$

$$\frac{\partial^2 c}{\partial z^2} \approx \frac{c_{i,j+1}^k - 2c_{i,j}^k + c_{i,j-1}^k}{\delta z^2}$$

The partial differential equation becomes:

$$\frac{c_{i,j}^k - c_{i,j}^{k-1}}{\delta t} + \frac{c_{i,j}^k - c_{i-1,j}^k}{\delta x} = a\frac{c_{i,j+1}^k - 2c_{i,j}^k + c_{i,j-1}^k}{\delta z^2} + bc_{i,j}^k$$

After rearranging we get:

$$c_{i,j}^k\left(1 + \frac{\delta t}{\delta x} + \frac{2a\delta t}{\delta z^2} + b\delta t\right) + c_{i,j-1}^k\left(-\frac{a\delta t}{\delta z^2}\right) + c_{i,j+1}^k\left(-\frac{a\delta t}{\delta z^2}\right) + c_{i-1,j}^k\left(-\frac{\delta t}{\delta x}\right) = c_{i,j}^{k-1}$$

Setting:

$$p = \left(-\frac{\delta t}{\delta x} \right) \qquad q = \left(-\frac{a\delta t}{\delta z^2} \right) \qquad r = \left(1 + \frac{\delta t}{\delta x} + \frac{2a\delta t}{\delta z^2} + b\delta t \right)$$

we end up with:

$$r \cdot c_{i,j}^k + q \cdot c_{i,j-1}^k + q \cdot c_{i,j+1}^k + p \cdot c_{i-1,j}^k = c_{i,j}^{k-1} \tag{6.34}$$

Equation (6.34) represents the implicit (centered in z and backwards in x) numerical scheme that must be implemented to obtain the solution $c_{i,j}^k$. At the time step $k-1$, the problem (6.34) reduces to a linear system of the type:

$$Ax = \mathbf{b}$$

whose solution provides the values of $c_{i,j}^k$ defined on the mesh grid at the time step k. Proceeding in this way, we determine the numerical solution of the problem. The free parameters of the model (i.e. the eddy diffusivity coefficient K and the reaction rate α) are hidden in the parameters a and b. We shall fit these parameters with the experimental data. In Fig. 6.2 the stencil adopted for the numerical scheme is shown.
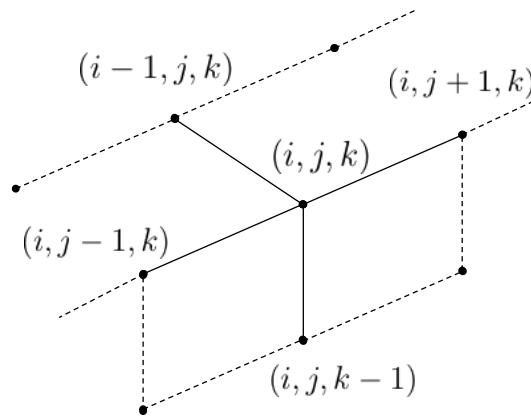
FIGURE 6.2: *Stencil for the numerical scheme*

6.5   Error evaluation

To investigate the efficiency of our model we could make use of the root means square error (RMSE), also known as standard deviation, defined as:

$$RMSE = \sqrt{\frac{\sum_{i=1}^{N}(P_i - O_i)^2}{N}},$$

where O_i are the measured values and P_i the values calculated by the model. This is an absolute quantity and can be misleading when the numerical values of the observation are small. A more reliable measure of the accuracy of the model is given by the Nash-Sutcliffe efficiency EF. This coefficient, proposed by Nash and Sutcliffe (1970), is defined as one minus the sum of the absolute squared differences between the predicted and observed values normalized by the variance of the observed values during the period under investigation. It is calculated as:

$$EF = 1 - \frac{\sum_{i=1}^{N}(P_i - O_i)^2}{\sum_{i=1}^{N}(O_i - \overline{O})^2}, \tag{6.35}$$

where $\overline{O}$ is the arithmetic average of the observed values. From the definition of EF it is evident that the optimal value for EF is 1. Moreover, we observe that positive values of EF indicate that the values of the model are better than the average of the observations. We shall use EF to evaluate the accuracy of our model.

Chapter 7

Discussion

7.1 Statistical Analysis: frequency distribution of H$_2$S and SO$_2$

The first step of data processing was related to the graphical frequency distribution of H$_2$S and SO$_2$ in order to gather insights on the generating processes and associated phenomena (Aitchison, 1982; Ott, 1990; Azzalini and Capitanio, 1999; Reimann and Filzmoser, 1999; Buccianti and Pawlowsky-Glahn, 2005; Buccianti et al., 2006). The frequency distribution provides indication about the probability density function, which describes the occurrence of different possible events; in other words, the probability distribution describes random phenomena, i.e. the probability that an event may occur. A "random phenomenon" is a sequence of "random variables", which follow an evolution described by probability distributions instead of a deterministic pattern (Ott, 1990). Many authors reported that the distribution of geochemical parameters measured in the environment (e.g., those concerning air and water quality, indoor measurements, trace metals) often appears "log-normal" rather than "normal" (Ahrens, 1954; Davis, 1966; Larsen, 1971; Ward Alter and Oswald, 1983). The log-normal distribution is a type of continuous probability distribution resulting by the multiplicative product of many independent random variables, each of which is positive. It is different with respect to the normal (or Gaussian or Laplace-Gauss) distribution, which results by the summation of many independent continuous random variables. The explanation for log-normal (or right-skewed) concentration distributions in nature was firstly published by Kapteyn in 1903 with the "Law of Proportionate Effects" and later by Ott (1990), with the "Theory of

Successive Random Dilutions", a special application of the Kapteyn's law. Ott (1990) proposed the beaker experiment example to explain successive random ("stochastic") processes (Fig. 7.1): an experimenter starts to dilute a pollutant, dispersed within a 250 ml beaker of water with an initial concentration of 1000 ppm, by taking 50 mL of solution from the initial beaker into a new one (Beaker 1) and adding 200 mL of fresh water; the process is then repeated for Beaker 2, 3 and 4, every time taking 50 mL of solution from the previous baker; the final concentration in Beaker 4 will be the product of the initial concentration and the four dilution factors; if no errors in the dilution occurred, the experiment is called "deterministic" because the dilution ratios are fixed and no variation is observed if the experiment is repeated (Fig. 7.1); if the experimenter commits some error in each dilution, the experiment becomes "stochastic", because dilutions will be varying every time the experiment is repeated and the final pollutant quantities for each repetition will have a log-normal frequency distribution rather than a single value (Fig. 7.2).
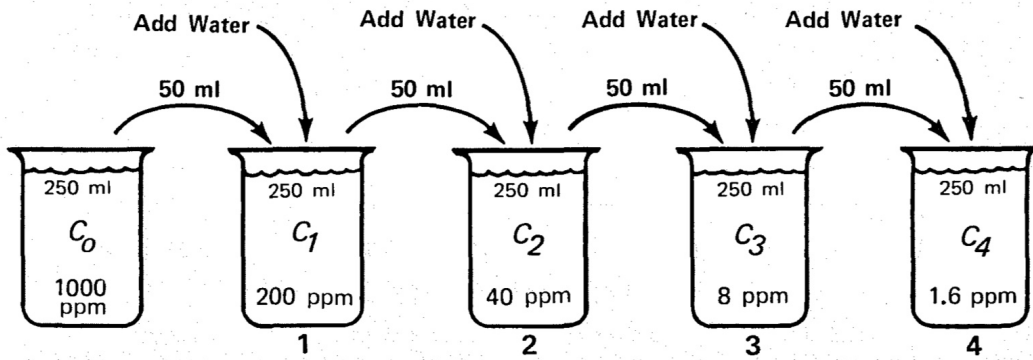
FIGURE 7.1: *Representation of the beaker experiment example in its "deterministic" case (from Ott, 1990).*
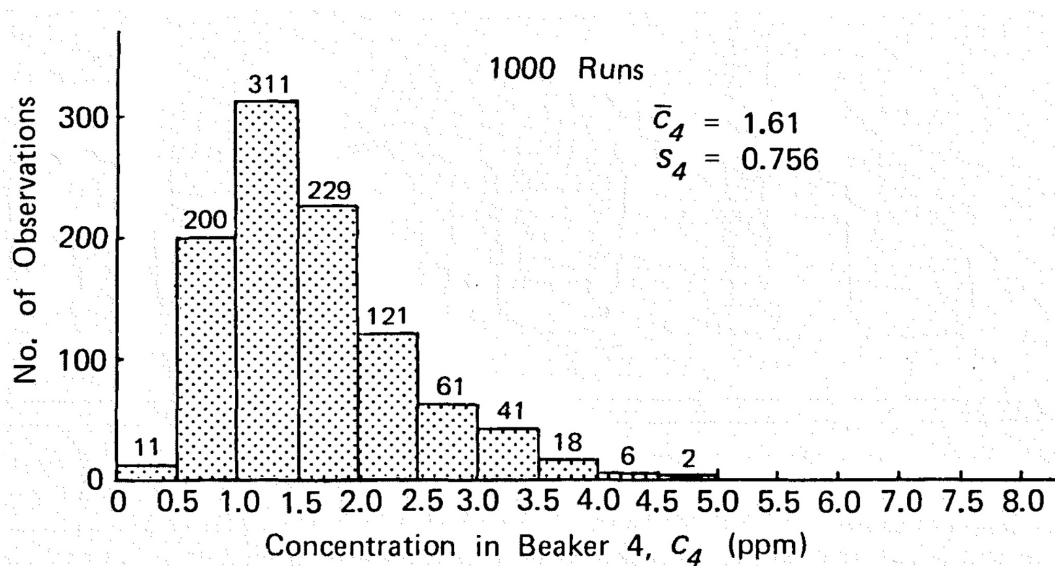
FIGURE 7.2: *Histogram of the final concentration after 1000 successive random dilution in the beaker experiment in the "stochastic" case (from Ott, 1990). A positively right-skewed distribution is observed.*

The same results were observed by Ott (1990) during an indoor air quality example: a pollutant was released into a room and numerous independent random ventilations took place, allowing the entry of a volume of fresh pollutant-free air and the removal of the same volume of contaminated air; the final concentration of the pollutant in the room was the product of the initial concentration and "n" independent successive random dilutions thus giving a log-normal distribution.

Considering all the fix spots at different distances from the source, the distribution of the H₂S-SO₂ data for each geothermal system shows a right-skewed frequency distribution with a mode at lower concentrations and a long tail to the right towards higher values. Some examples are shown in Fig. 7.3, 7.4, 7.5 and 7.6. Consequently, the log-normal distribution suggests that H₂S and SO₂ concentrations in the atmosphere were dependent on "dilution" processes. Nevertheless, in the air environment, these "dilution" processes include all the processes able to remove the S-compounds from the atmosphere, i.e. s.s. dilution processes and chemical reactions. Since the statistical analysis cannot quantify these processes or even distinguish them, a mathematical model (Chapter 6) was developed to better understand the

role possibly played by these dilution/chemical processes affecting the H_2S-SO_2 concentrations in the hydrothermal plumes.
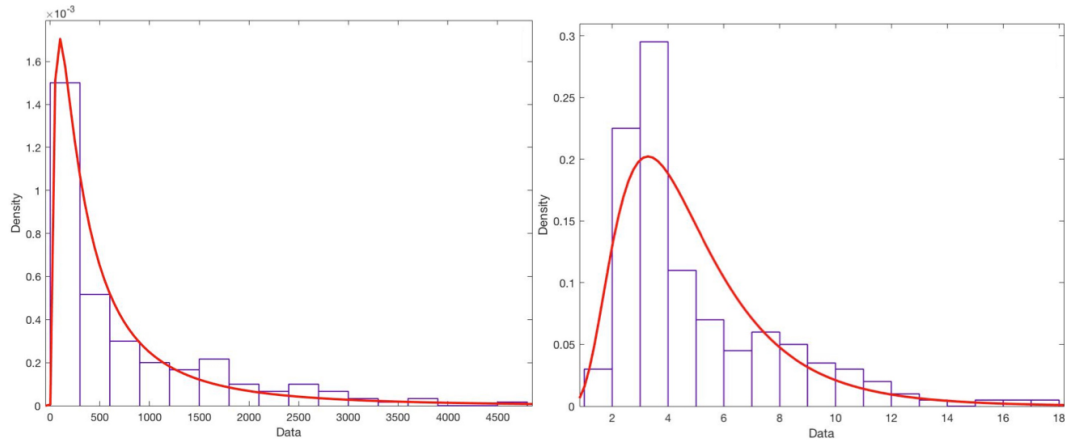
FIGURE 7.3: *Histograms for H_2S (left figure) and SO_2 (right figure), expressed in ppb, for BJARN(A). The log-normal fitted densities are indicated with the red line.*
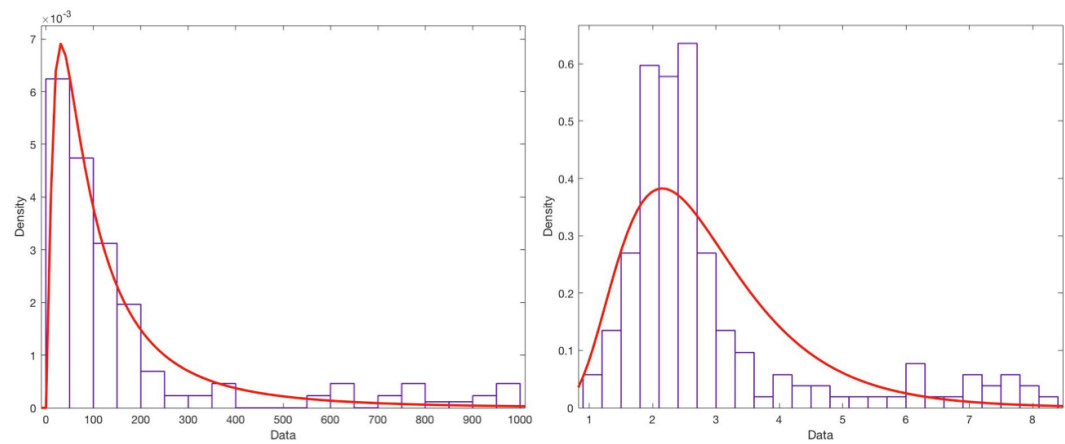
FIGURE 7.4: *Histograms for H_2S (left figure) and SO_2 (right figure), expressed in ppb, for REY(D). The log-normal fitted densities are indicated with the red line.*
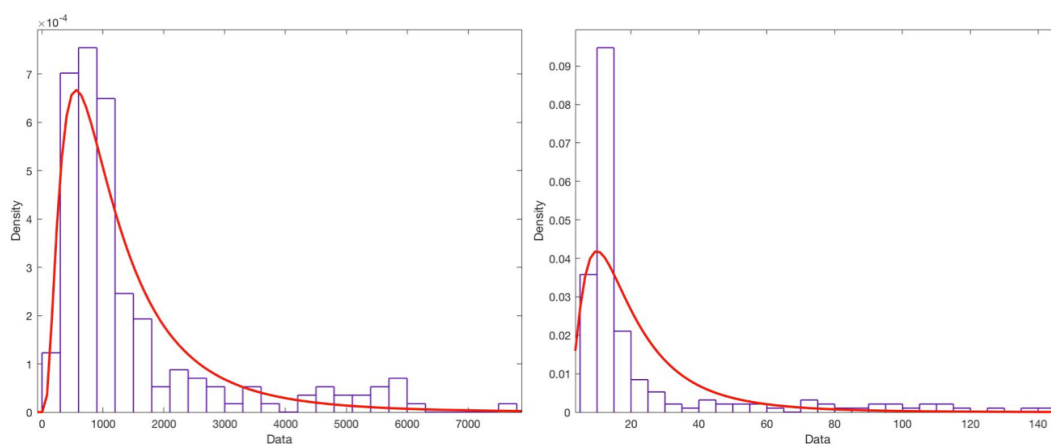
FIGURE 7.5: *Histograms for H_2S (left figure) and SO_2 (right figure), expressed in ppb, for NAM(D). The log-normal fitted densities are indicated with the red line.*
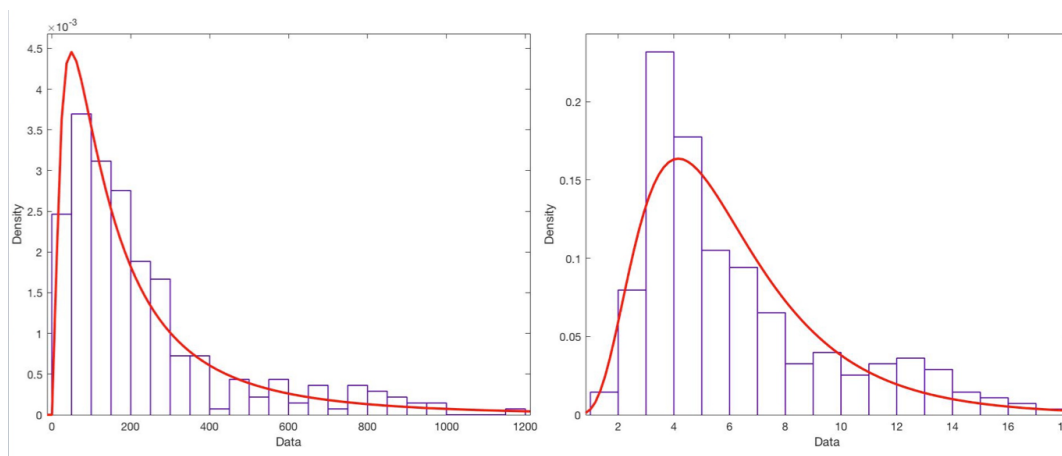
FIGURE 7.6: *Histograms for H_2S (left figure) and SO_2 (right figure), expressed in ppb, for HVITH(E). The log-normal fitted densities are indicated with the red line.*

7.2 Behaviour of S-compounds within the hydrothermal plume

7.2.1 Mathematical model: dilution vs. reaction

In the first step, the mathematical model (described in Chapter 6) was developed considering an independent H_2S and SO_2 evolution within the hydrothermal plume as the distance from the source was increasing. Before

considering the two compounds correlated (i.e. H_2S conversion to SO_2), their individual evolution was examined to understand the removal processes that affect these gases within the plume. The mass balance equation used in the model is, as follows:

$$\frac{\partial c}{\partial t} + v_{wind}\frac{\partial c}{\partial x} = \frac{\partial}{\partial z}\left(K\frac{\partial c}{\partial z}\right) - \alpha c \tag{7.1}$$

where:

   c = H_2S or SO_2 concentrations

   v = longitudinal constant mean wind velocity

   K = "eddy diffusivity" responsible for the dilution of S-gases in the atmosphere along the z axis

   α = "reaction rate": the rate of consumption of S-gases

To determine the best K (eddy diffusion) and α (reaction rate) values, we used the Nash-Sutcliffe efficiency coefficient (EF: optimization procedure; Chapter 6). When the model and the measured data are perfectly consistent, the EF coefficient is 1. We chose K and α in order to get an EF as close as possible to 1. For all the systems and for both H_2S and SO_2, the K term resulted to have a negligible influence in the fitting procedure. As shown in the Krýsuvík geothermal system for H_2S and SO_2 (Fig. 7.7), a determined value for α has to be chosen to get an EF coefficient of almost 1, while any values from 0 to 300 for K can be selected. This shows that vertical dilution processes seem to have negligible effect in the optimization procedure when compared to chemical reactions. Choosing the α fitted value and an arbitrary value for K, a good fitting with the measured data is computed by the model (Fig. 7.7). Some examples of K and α results for the other geothermal systems are graphically reported in Fig. 7.8,7.9, 7.10 and 7.11. The α values for all the geothermal systems vary in the range of 2-46 min^{-1} for SO_2 (Table 7.1) and in the of range 7-60 min^{-1} for H_2S (Table 7.2).
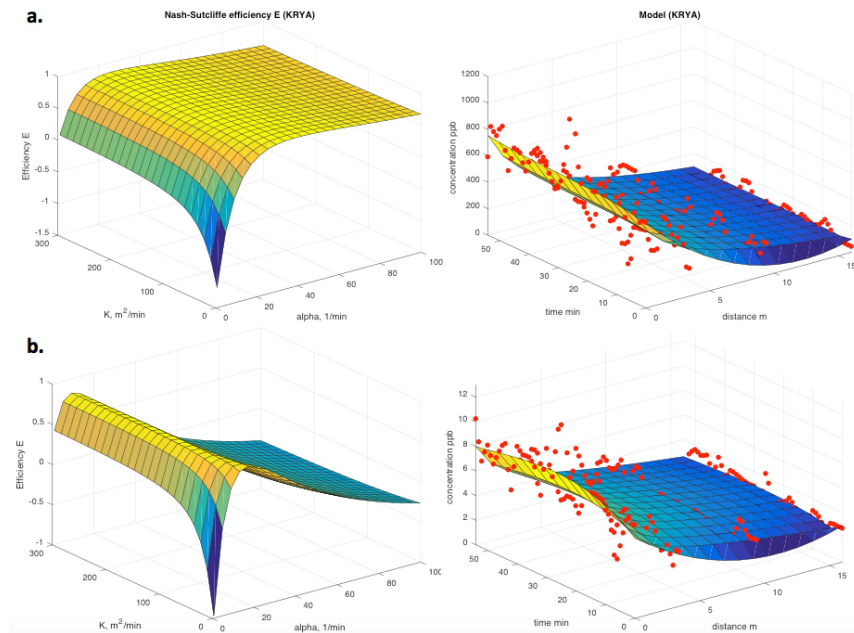
FIGURE 7.7: *Graphical representation of the optimization procedure to determine K and α values for H_2S (a) and SO_2 (b), using the Nash-Satcliffe efficiency coefficient (EF) (to the left) and the model fitted with the measured data (to the right) for KRY(A).*
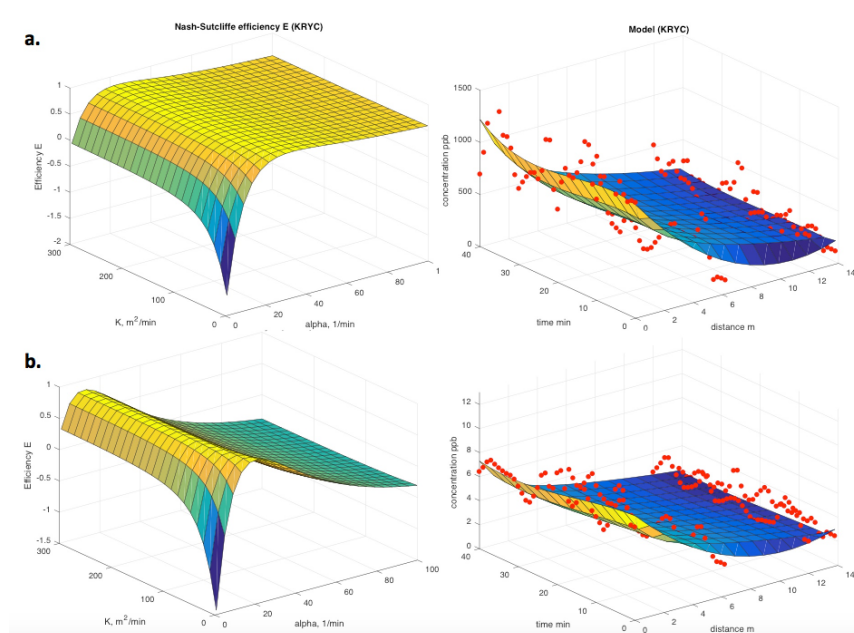
FIGURE 7.8: *Graphical representation of the optimization procedure to determine K and α values for H_2S (a) and SO_2 (b), using the Nash-Satcliffe efficiency coefficient (EF) (to the left) and the model fitted with the measured data (to the right) for KRY(C).*
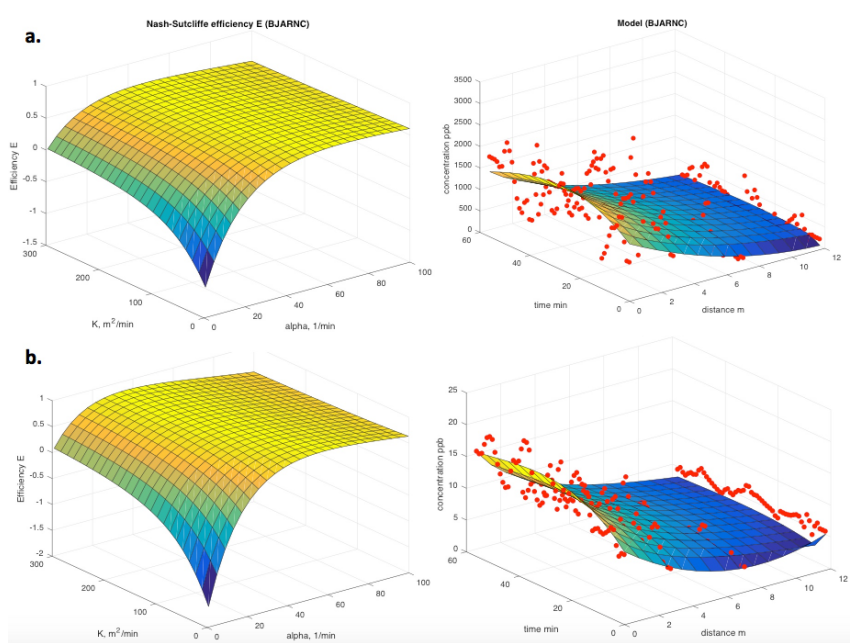
FIGURE 7.9: *Graphical representation of the optimization procedure to determine K and α values for H_2S (a) and SO_2 (b), using the Nash-Satcliffe efficiency coefficient (EF) (to the left) and the model fitted with the measured data (to the right) for BJARN(C).*
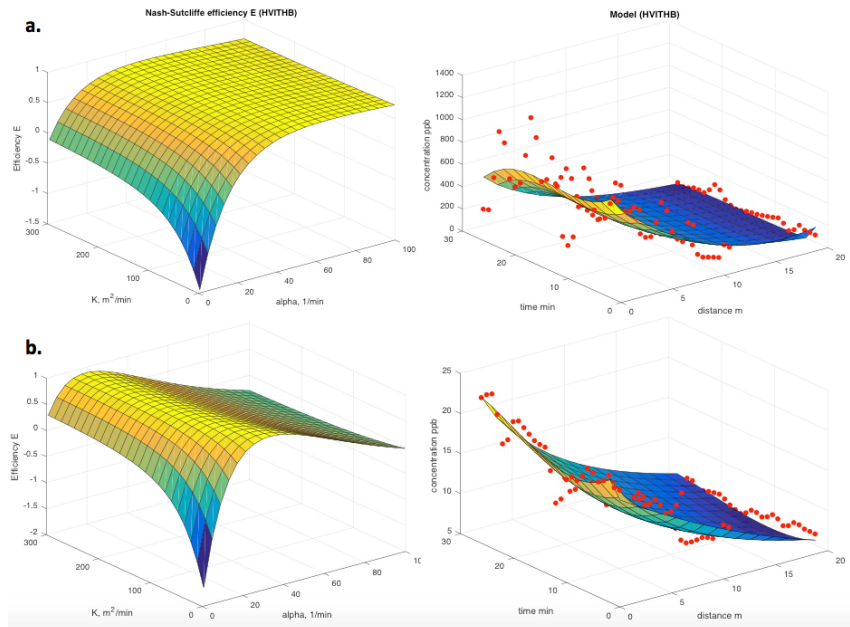
FIGURE 7.10: *Graphical representation of the optimization procedure to determine K and α values for H_2S (a) and SO_2 (b), using the Nash-Satcliffe efficiency coefficient (EF) (to the left) and the model fitted with the measured data (to the right) for HVITH(B).*
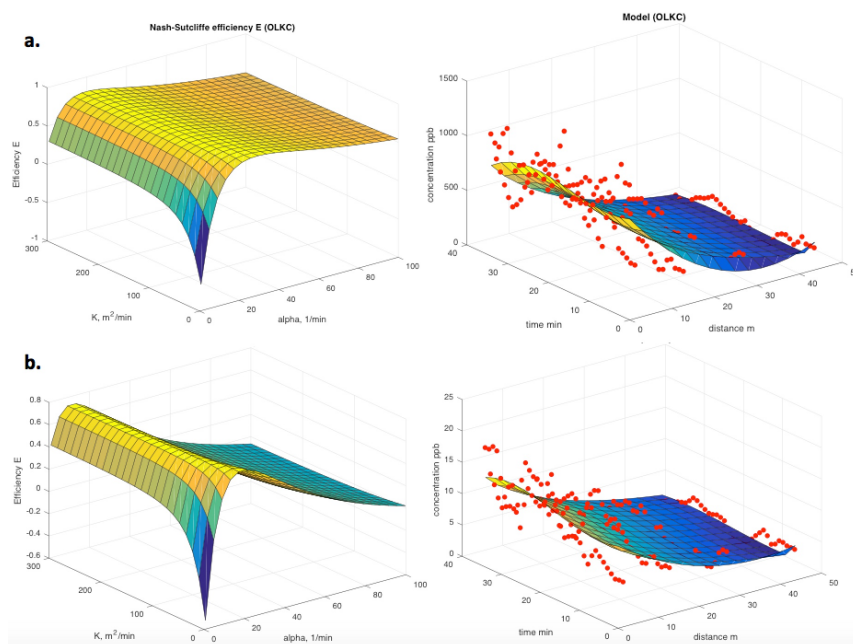
FIGURE 7.11: *Graphical representation of the optimization procedure to determine K and α values for H_2S (a) and SO_2 (b), using the Nash-Satcliffe efficiency coefficient (EF) (to the left) and the model fitted with the measured data (to the right) for OLK(C).*

SO_2

Site name	α (1/min)	EF	wind average (m/s)
KRY(A)	9.2	0.82	3.6
KRY(C)	13.3	0.84	3.7
OLK(A)	34	0.73	3.1
OLK(C)	13.4	0.73	9.0
OLK(E)	13.4	0.79	2.2
OLK(F)	46.4	0.62	3.4
REY(D)	21.6	0.7	6
REY(E)	29.9	0.71	4.4
BJARN(A)	2.2	0.67	6.8
BJARN(B)	6.3	0.46	4.4
BJARN(C)	38.1	0.81	6.4
HVITH(B)	21.6	0.9	7.3
HVITH(E)	9.2	0.69	4.6
SKI(B)	34	0.85	6.2
NAM(D)	17.5	0.66	4.9

TABLE 7.1: SO_2 α values (min^{-1}) for all the geothermal systems, the related EF coefficient (0-1) and the wind speed (m/s).

H$_2$S

Site name	α (1/min)	EF	wind average (m/s)
KRY(A)	25.8	0.84	3.6
KRY(C)	21.6	0.81	3.7
OLK(A)	38.1	0.74	3.1
OLK(C)	25.8	0.81	9.0
OLK(E)	21.6	0.72	2.2
OLK(F)	54.6	0.71	3.4
REY(D)	34.0	0.74	6
REY(E)	58.8	0.72	4.4
BJARN(A)	7.1	0.62	6.8
BJARN(B)	30.0	0.45	4.4
BJARN(C)	67.0	0.64	6.4
HVITH(B)	58.8	0.77	7.3
HVITH(E)	13.5	0.49	4.6
SKI(B)	54.6	0.88	6.2
NAM(D)	13.4	0.58	4.9

TABLE 7.2: H$_2$S α values (min^{-1}) for all the geothermal systems, the related EF coefficient (0-1) and the wind speed (m/s).

The EF values for both H$_2$S and SO$_2$ (Table 7.1 and 7.2) show that the model has a good fitting with the measured data, except for BJARN(B), HVITH(E) and NAM(D), the EF values being lower (<0.6). Considering all the geothermal systems, the α values seem consistent for both H$_2$S and SO$_2$ since they are in the same order of magnitude, suggesting that no correlation with the mean wind speed is present.

7.2.2 SO$_2$ and H$_2$S reaction rates

The average of the best SO$_2$ α values (EF > 0.6) calculated by our model is about 20 min^{-1} (Table 7.1), which corresponds to 3.3×10^{-1} s^{-1}. This α value suggests a faster reaction rate than those proposed by other authors (10^{-7}-10^{-5} s^{-1}; Jaeschke et al., 1980; Hobbs et al., 1982; Porter et al., 2002) for homogeneous reactions via hydroxyl radical within tropospheric volcanic plumes. Nevertheless, the α value computed in this study appears to be more consistent with the heterogeneous reaction rates determined for Soufriere Hills and Mt. Etna eruptions (10^{-3}-10^{-2} s^{-1}; Oppenheimer et al., 1998b) at particular conditions (i.e. presence of clouds and high ash content in the plume),

during which rapid steam condensation likely occurred, increasing SO_2 diffusion and dissolution in droplets.

On the other hand, the average of the best H_2S α values (EF > 0.6) calculated by our model (Table 7.2) is about 40 min^{-1}, which corresponds to 6.6 $\times$ 10^{-1} s^{-1}. In this case, the comparison with the reaction rates found in literature is not straightforward and requires some conversions of units of measure. The rate constant k_2, determined by laboratory experiments, referred to a second order reaction (x) and the most repeatable value for k_2 is considered to be about 5×10^{-12} cm^3 molecule^{-1} s^{-1} (see Chapter 2). In a second order reaction, the rate equation "r" is expressed as r = k[A][B] (in this case A = H_2S, B = OH and k is the constant rate) and the unit of measure is generally M^{-1}s^{-1}, where M is the molarity (mol L^{-1}). In the previously mentioned laboratory experiments, the concentrations were in molecule/cm^3 and, consequently, the constant rate was expressed in cm^3 molecule^{-1} s^{-1}. In our mathematical model, the H_2S concentrations are in ppb and the constant rate α is expressed in min^{-1}, since it refers to a first order reaction (r = k[A]). To compare the two constant rates, assuming that α describes the reaction (x), we have to multiply [OH] with k_2 (Spedding and Cope, 1984):

$$\alpha = k_2[OH] \tag{7.2}$$

The OH concentration in the atmosphere is variable (Watanabe et al., 1982), since it depends on a number of parameters (e.g., altitude, latitude, season, solar irradiation etc.), and some authors (Jaeschke et al., 1979; Servant and Delapart, 1982) suggested that the mean tropospheric concentration of OH is in the range of 2-9 $\times$ 10^6 molecule cm^{-3}. For example, Wine et al. (1981) considered a OH concentration of 2×10^6 molecule cm^{-3} (Chapter 2) and found a rate constant of 5.35 ($\pm$0.40) $\times$ 10^{-12} cm^3 molecule^{-1} s^{-1}:

$$\alpha = (5.35 \times 10^{-12} \ cm^3 \ molecule^{-1} \ s^{-1}) \times (2 \times 10^6 \ molecule \ cm^{-3}) \tag{7.3}$$

$$\alpha = 10.7 \times 10^{-6} \ s^{-1} \approx 1.1 \times 10^{-5} \ s^{-1} \tag{7.4}$$

The H_2S α value of our model (6.6 $\times$ 10^{-1} s^{-1}) differs from that of Wine et al. (1981) by at least 4 orders of magnitude. A lower but significant difference

can be observed with the constant rate determined by Jaeschke et al. (1982) in the Mt. Etna volcanic plumes (k = 2.1×10^{-4} s^{-1}). Finally, a difference of 2 orders of magnitude can be observed when the α computed in this study is compared with that one determined in a geothermal gas plume in New Zealand by Spedding and Cope (1984) (3.5×10^{-3} min^{-1}). The rate constant is often expressed in terms of half-life ($t_{1/2}$) or mean life-time (τ), as follow (Spedding and Cope, 1984):

$$t_{1/2} = \frac{0.693}{k} \tag{7.5}$$

$$\tau = \frac{1}{k} \tag{7.6}$$

In the literature, the mean life-time (τ) was calculated to be generally 12-27 h (Perry et al., 1976; Sprung, 1977; Graedel, 1977; Eggleton and Cox, 1978; Jaeschke et al, 1979; Wine et al., 1981; Servant and Delaport, 1982) or 1-2 h in one case (Hitchcock, 1977, 1978) whereas our α values computed a significantly much lower mean life-time, being of about 0.2 minutes. Three main scenarios can be suggested to explain the differences between the H_2S and SO_2 α values calculated by our mathematical model with respect to those reported in the literature:

i) the horizontal eddy diffusivity term (K_h), which was not considered in our 2D model (only K_v vertical is present; see Chapter 6), cannot be neglected and it has an important influence in the dilution of S-gases in the atmosphere (Fig. 7.12). Therefore, the α values for both H_2S and SO_2 resulted from both horizontal dilution processes (perpendicular to the plume) and photo-oxidation via the hydroxyl radical;
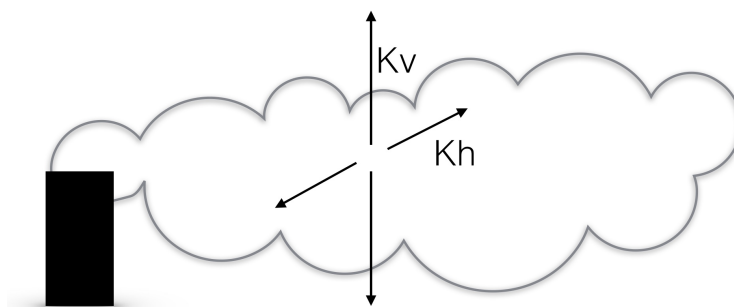
FIGURE 7.12: *K vertical and K horizontal*

ii) the photo-oxidation process via the hydroxyl radical is not the only removal mechanism that affects H_2S or SO_2 within the plume and the α value is due to the contribution of different chemical processes (e.g., photo-oxidation, wet and dry deposition);

iii) the α value is the combination of scenario i) and ii).

If the first scenario is verified, the eddy diffusivity K, along two perpendicular directions with respect to the plume ($K_h + K_v$; Fig. 7.12), is more influent than that assumed in our model. Consequently, the mathematical model must be re-written by including the K_h term and the model would be more complex to solve, since it becomes a 3D model, in the form:

$$\frac{\partial c}{\partial t} + v_{wind}\frac{\partial c}{\partial x} = \frac{\partial}{\partial y}\left(K_y \frac{\partial c}{\partial y}\right) + \frac{\partial}{\partial z}\left(K_z \frac{\partial c}{\partial z}\right) - \alpha c \qquad (7.7)$$

with K_y and K_z representing K_h and K_v, respectively. Furthermore, three terms are thus to be determined in the fitting procedure: K_h, K_z (or K_v) and α. Since is not possible to find an appropriate eddy diffusivity K in the literature, the literature α values were assumed to be correct and used to compute K_h and K_z by fitting with the measured data. However, as mentioned above, the model results suggested that K_z has a negligible influence in the fitting procedure, so that it is unlikely that K_h weights more than α, which seems to be the most important term.

Alternatively, if the second scenario is verified, our α value does not represent the photo-oxidation process alone, but it results by the sum of more chemical reactions that affect the S-compounds within the plume, which are able to accelerate their removal. Thus, the model should be re-written in the form:

$$\frac{\partial c}{\partial t} + v_{wind}\frac{\partial c}{\partial x} = \frac{\partial}{\partial z}\left(K \frac{\partial c}{\partial z}\right) - \alpha_1 c - \alpha_2 c - \alpha_3 c \qquad (7.8)$$

With α_1, α_2 and α_3 representing the constant rates of three possible chemical reactions. In this case, the eddy diffusivity term is only considered along the z-axis and, to solve the mass balance equation, we must know the reactions involved and their associated constant rates (α). As mentioned in Chapter 2, the α values for oxidation processes determined by laboratory experiments for both H_2S and SO_2 are generally slower (almost two

orders of magnitude) than those calculated by direct measurements in the field. This because the rates of transformation and removal of gas species in natural environments is not only influenced by the presence of oxidants (e.g., H_2O_2, O_3, OH) but also by the availability of condensed water and solid particles within the plume, the UV flux, and aerosol size, pH, and so forth (Horrocks et al., 2003). In fact, in volcanic and hydrothermal plumes, a quantity of suspended liquid-solid particles makes heterogeneous and multiphase (in droplets) reactions more important in controlling concentrations of soluble gases than slower homogeneous gas-phase reactions via the hydroxyl radical (Ravishankara, 1997). The plume conditions can determine the predominance of homogeneous or heterogeneous reactions, producing different α values: is the case for the Soufriere Hills volcano and Mt. Etna eruptions (Chapter 2, Fig. 2.3), where the presence of clouds and high ash content in the plume likely favored rapid condensation of steam and SO_2 dissolution in droplets, producing an α value up to 5 orders of magnitude higher than those recorded during the Mt. St. Helens and Pinatubo eruptions. These conditions can be important in geothermal-hydrothermal systems where the natural emissions, even if characterized by a generally low or absent ash content with respect to volcanic eruptions, mainly consist of water vapor (>98%). This means that heterogeneous reactions, i.e. dissolution in vapor droplets and wet deposition, can be significant for smaller and weaker hydrothermal emissions, especially when approaching the hydrothermal source where most steam condenses due to the rapid drop in temperature, particularly at high latitudes (3-10 °C in Iceland). Dry deposition, namely the transport of gaseous and particulate species from the atmosphere to surfaces with no precipitation, is probably a minor mechanism in hydrothermal plumes, because of the high H_2O content and the considered short distances around the source. Sulfur dioxide is a soluble gas in water and its removal rates in the troposphere dramatically increase in the presence of liquid water or when RH is greater than 75%, since it can be oxidized within cloud and fog droplets, producing sulfuric acid (Horrocks et al., 2003). Zhang and Tie (2011), during their study on gaseous SO_2 solubility in a polluted area in north China, observed a strong reduction (about 70-80%) of the measured SO_2 concentrations closely correlated to the appearance of fogs (not observed for other gaseous compounds not soluble in water

such as CO). The authors suggested that this decrease was resulting by the gaseous conversion of SO_2 to aqueous phase in fog droplets, showing a high solubility of SO_2 that cannot be explained by the Henry Law constant alone. As suggested by Ravishankara (1997), the solubility of chemical species can further increase relative to their aqueous reaction rate in droplets (Fig. 7.13): when SO_2 molecules are transported (diffused) into a liquid droplet, they react in water and they are converted into other chemical species. Consequently, more SO_2 is transported into water droplets increasing its solubility. Between the two most important aqueous-phase reactions for SO_2 suggested by Seinfeld and Pandis (1998), Zhang and Tie (2011) considered the reaction with O_3 not significant when compared with that one with H_2O_2, because of the very low solubility of O_3 respect to H_2O_2 (Sander et al., 2015).
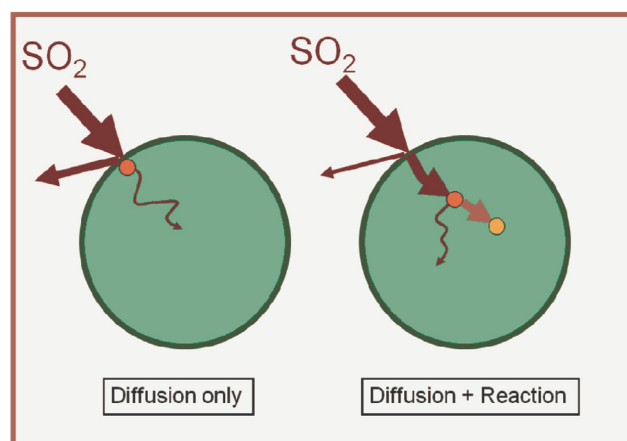
FIGURE 7.13: *Schematic comparisons between i) processes affecting SO_2 solubility without considering aqueous reactions (diffusion only) and ii) processes affecting SO_2 solubility considering aqueous reactions (diffusion + reaction), which lead to an increasing of SO_2 solubility (Zhang and Tie, 2011).*

Thus, the SO_2 solubility is described by the following reactions:

$$SO_{2(g)} \leftrightarrow SO_{2(aq)} \tag{7.9}$$

$$H_2O_{2(g)} \leftrightarrow H_2O_{2(aq)} \tag{7.10}$$

$$SO_{2(aq)} + H_2O_{2(aq)} \leftrightarrow H_2SO_{4(aq)} \tag{7.11}$$
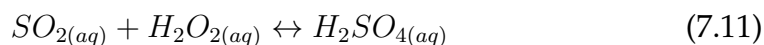
and it depends on the aqueous concentrations of SO_2 (aq) and H_2O_2 (aq) in droplets and the constant rate k of reaction (7.8), which is very fast (from 10^6 $M^{-1}s^{-1}$ to 10^2 $M^{-1}s^{-1}$ depending on pH; Seinfeld and Pandis, 1998). On this basis, Zhang and Tie (2011) suggested an "effective" Henry Law constant of SO_2 (H_e) expressed by:

$$H_e(SO_2) = H(H_2O_2) \times H_2O_{2(g)}/SO_{2(g)} \qquad (7.12)$$

where H is the Henry Law constant of H_2O_2. Calculating the partitioning between gas and aqueous phase concentrations of SO_2 with the "effective" Henry Law constant, they found that it is consistent with the SO_2 loss observed during fog periods. The results presented by Zhang and Tie (2011) support our findings, suggesting a faster removal of SO_2 from the water-rich hydrothermal plume by dissolution in water droplets. The same hypothesis can be applied for H_2S, even if this species is less soluble than SO_2 (Sander et al., 2015), since it can be readily oxidized by H_2O_2 below pH 7.5, as follows (Hoffmann, 1977):

$$H_2S_{(aq)} + H_2O_{2(aq)} \rightarrow 2H_2O + S \qquad (7.13)$$
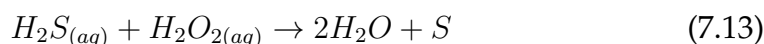
and characterized by a lower constant reaction with respect to that of SO_2, namely equal to 0.48 $M^{-1}min^{-1}$ (Hoffmann, 1977). Relatively few investigations of this reaction have been published. However, under proper conditions, H_2O_2 seems to be an effective reagent, controlling H_2S and its odor in aqueous systems and it is currently used in both industrial and municipal wastewater systems (Hoffmann, 1977). Nevertheless, further investigations on water droplets pH and H_2O_2 availability within hydrothermal plumes are necessary to support our hypothesis. Furthermore, the presence of S-bearing compounds (CS_2, C_4H_6S, C_4H_4S, C_5H_6S, C_6H_8S, C_2H_6OS and $C_2H_6O_2S$) among VOCs, suggests that H_2S can also partially be removed by chemical reactions to form these S-species. Another reaction path that can contribute to both SO_2 and H_2S removal in the vent area is the precipitation of native sulfur, according to the following disproportionation reaction (Mizutani and Sugiura, 1966; Giggenbach, 1987; Oppenheimer, 1992):

$$2H_2S_{(g)} + SO_{2(g)} = 2H_2O_{(g)} + 3/2\ S_{2(s)} \tag{7.14}$$
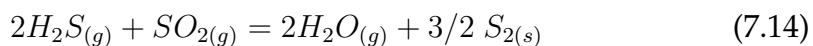
for which the consumption of H$_2$S$_{(g)}$ is doubled with respect to that of SO$_{2(g)}$. The appearance or disappearance of native sulfur is controlled by temperature, total pressure and chemical gas composition in equilibrium with native sulfur (Mizutani and Sugiura, 1966) and native sulfur deposits are common in low-temperature emissions (vent temperature below 150-200 °C; Gravelli et al., 1997; Aiuppa et al., 2005) rather than for high-temperature open-conduit volcanoes. However, the sublimation of sulfur is probably a major process close to the emission outlet, as shown by the presence of the typical sulfur deposits, and is unlikely a major process for SO$_2$ and H$_2$S removal within the hydrothermal plume, at > 5 m distance from the source. It can be concluded that the second scenario seems to be more reasonable than the first one, although our α values can also be determined by a combination of both (third scenario). To gather more information on which process is more likely to make our α values higher than those reported in the literature, the solutions of the mathematical models re-written for the three scenarios are to be investigated.

7.2.3   H$_2$S photo-oxidation to SO$_2$

As described in Chapter 2, photo-oxidation of H$_2$S via OH radicals likely proceeds in the daylight, as follows (Stuhl, 1974; Perry et al., 1976; Graedel, 1977a):

$$OH + H_2S \rightarrow H_2O + HS \tag{7.15}$$

$$HS + O_3 \rightarrow HSO + O_2 \tag{7.16}$$

$$HSO + O_3 \rightarrow HSO_2 + O_2 \tag{7.17}$$

$$HSO_2 + O_2 \rightarrow HO_2 + SO_2 \tag{7.18}$$
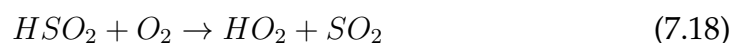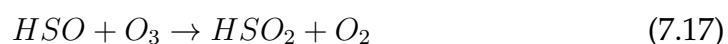
Based on a constant rate of 5×10^{-12} cm^3 molecule^{-1} s^{-1} at 298 K for reaction (7.15) (Perry et al., 1976; Cox and Sheppard, 1980; Wine et al., 1981), various authors suggested a H$_2$S lifetime in the troposphere ranging from 12 to 27 h (Perry et al., 1976; Sprung, 1977; Graedel, 1977; Eggleton and Cox, 1978; Jaeschke et al, 1979; Wine et al., 1981; Servant and Delaport, 1982). Based on these findings, it is unlikely that H$_2$S photo-oxidation reactions can occur immediately after the release of the hydrothermal gases into the atmosphere. Consequently, it is unlikely that variations of SO$_2$/H$_2$S ratios in hydrothermal plumes can be observed on timescales shorter than hours, even if kinetics of OH radical reactions in high-temperature volcanic gases could be much faster than in ambient air, as observed in the case of jet engine exhausts (Kärcher et al., 1996). Furthermore, the reaction rates described in Atkinson et al (1992) for reactions (7.16), (7.17) and (7.18) are even lower than that of (7.15), being 3.7×10^{-12} cm^3 molecule^{-1} s^{-1}, 1.1×10^{-13} cm^3 molecule^{-1} s^{-1} and 3.0×10^{-13} cm^3 molecule^{-1} s^{-1}, respectively, suggesting a relatively slow process to produce SO$_2$ from H$_2$S. On the other hand, assuming that H$_2$S conversion to SO$_2$ in hydrothermal plumes is faster than that previously suggested, it would be difficult to quantify this process since the fast removal of SO$_2$ hides its potential increase. Moreover, if we consider in the model a production term for SO$_2$, the resulting reaction term α would become more faster, because it would consume more SO$_2$, i.e. the one present in the plume and the one formed by the H$_2$S oxidation. If the H$_2$S oxidation via the hydroxyl radical within the plume are not an extremely fast process in the SO$_2$ production, it would pose some concern about the origin of SO$_2$. As explained by Giggenbach (1987), sulfur dioxide, because of its high chemical reactivity, can be affected by variable degree of re-equilibration with cooler wall rock in contact with the rising gas steam and, as a result of the fluid-rock interaction processes most magmatic SO$_2$ will be reduced to H$_2$S. The efficiency of the rock buffer in converting SO$_2$ to H$_2$S clearly depends on the intensity and duration of fluid-rock contact (residence time of the gases in the crust), but if any SO$_2$ survived to this rock matrix reduction, it would disproportionate into H$_2$S and H$_2$SO$_4$ in the presence of liquid water (hydrolysis reaction) before reaching the surface as the volcanic gases cool below 300-400 °C. This is what is suggested to happen

in hydrothermal systems, within which the presence of shallow water prevents SO_2 to reach the surface, which therefore is not measured in hydrothermal low-temperature emissions. However, some authors (e.g., Mizutani and Sugiura, 1966; Chiodini et al., 1993; Marini et al., 2011) suggested that secondary non–magmatic processes are potentially able to affect the concentrations of S-species when low-temperature gases are considered. Giggenbach (1987) argued that the deposition of elemental S during cooling and its remobilization during heating can play an important role in controlling the H_2S and SO_2 contents in low-temperature fumaroles, as recognized for White Island (New Zealand). The same hypothesis was suggested by Mizutani and Sugiura (1966) for the Nasudake Volcano solfataric gases (Japan), who proposed that the most S-bearing compounds at temperatures between 100-200 °C secondarily derived by subterranean native sulfur that accumulated through previous volcano solfataric activities. Furthermore, Mizutani and Sugiura (1966) also observed a correlation between higher H_2S/SO_2 ratios and low-temperature gases. Chiodini et al. (1993) suggested that the reduction and oxidation of pyrite, the most common hydrothermal sulfide, can be considered the main source of H_2S and SO_2 in the shallow hydrothermal component at Vulcano Island and they proposed various reactions (of pyrite reduction and oxidation) depending on temperature and redox conditions. Finally, some authors (Gerlach et al., 1996) proposed the boiling of sulfate-rich fluids of hydrothermal systems as another possible source of SO_2, while others (Devine et al., 1984; Sigurðsson, 1990) suggested that gaseous SO_2 can be produced by anhydrite decomposition, although high temperatures were occurring. Since findings from Stefánsson et al. (2015) and Gunnarsson-Robin et al. (2017) on the H_2S source in Icelandic hydrothermal systems are considered to be related predominantly to basalt upon rock leaching, probably a similar origin can be suggested for SO_2, as described by Giggenbach (1987) and Mizutani and Sugiura (1966).

7.2.4 SO_2/H_2S ratio

The SO_2/H_2S ratio is largely used as geochemical indicator for volcano monitoring since it reflects re-equilibration of magmatic gases within the colder, reducing hydrothermal system, during their migration from the deep-seated magmatic reservoir to the surface (Giggenbach, 1987; Symonds et al., 1996;

Symonds et al., 2001). Thus, hydrothermal processes can act as natural buffer that partially or totally hide the original information carried by magmatic volatiles and the speciation of sulfur in volcanic gases is considered an effective geochemical tool to quantify the hydrothermal versus magmatic contributions. As mentioned in the Introduction Chapter, SO_2 is the prevalent sulfur species in high-temperature volcanic gases (Gerlach and Nordlie, 1975; Symonds et al., 1994; Giggenbach, 1996), whereas H_2S dominates in low-temperature fumaroles and solfataras within hydrothermal systems (Giggenbach, 1980). The relative abundances of SO_2 and H_2S in the gas phase released from magmas are controlled by temperature, pressure and melt redox conditions, as described in the following reaction (Giggenbach, 1987; Carroll and Webster, 1994; Scaillet et al., 1998; Moretti et al., 2003):

$$log(SO_2/H_2S) = logK_{(1,T)} - 3R_H - logP \times X_{H_2O} \qquad (7.19)$$

where $K_{(1,T)}$ is the equilibrium constant at temperature T and $R_H = log(H_2/H_2O)$ relative to the reaction:

$$H_2S + 2H_2O = SO_2 + 3H_2 \qquad (7.20)$$
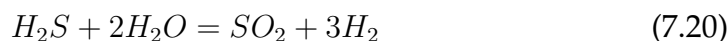
and X_{H_2O} is the mole fraction of water vapor in the gas phase. Consequently, the SO_2/H_2S ratio is higher for low values of R_H and high temperatures (magmatic conditions) and it is lower for high values of R_H and low temperatures (hydrothermal conditions). Changes in the magmatic versus hydrothermal contributions in a volcanic-hydrothermal system or a resuming volcanic activity of quiescent volcanoes are therefore expected to be preceded/accompanied by variations of the SO_2/H_2S ratio in the surface gas manifestations (e.g., Tassi et al., 2003; Aiuppa et al., 2005, 2006; Vaselli et al., 2010; Melián et al., 2012). On the contrary, as mentioned in Chapter 2, two main processes may alter the SO_2/H_2S ratios once fumarole gases are emitted in the atmosphere: oxidation of the gas phase (homogeneous reactions) and in the liquid/solid aerosol phase (heterogeneous reactions) (Seinfeld and Pandis, 1998). However, in hydrothermal systems, SO_2 was never detected with both the traditional direct gas sampling methods and more recent remote instrumentations (e.g., UV spectroscopy, Multi-gas) and

thus, no SO_2/H_2S ratios are available in such environments in neither fumarolic emissions nor in the air. In this study, a really highly sensitive H_2S-SO_2 analyzer was applied (see Chapter 4) and the SO_2/H_2S ratio within the hydrothermal plumes was determined for each system in both Iceland and Italy. The comparison among different systems, years (2017-2018) and emissions within the same system are discussed in this section.

By comparing the 2017 and 2018 measurements in the Hengill Ölkelduháls geothermal area (Fig. 7.14), we can observe that while the H_2S concentrations were comparable, those of SO_2 were significantly lower in 2018, OLK(E), with respect to those measured in 2017, OLK(A). This reflects on a different SO_2/H_2S ratio, i.e. 172×10^{-4} for 2017 and to 34×10^{-4} for 2018.
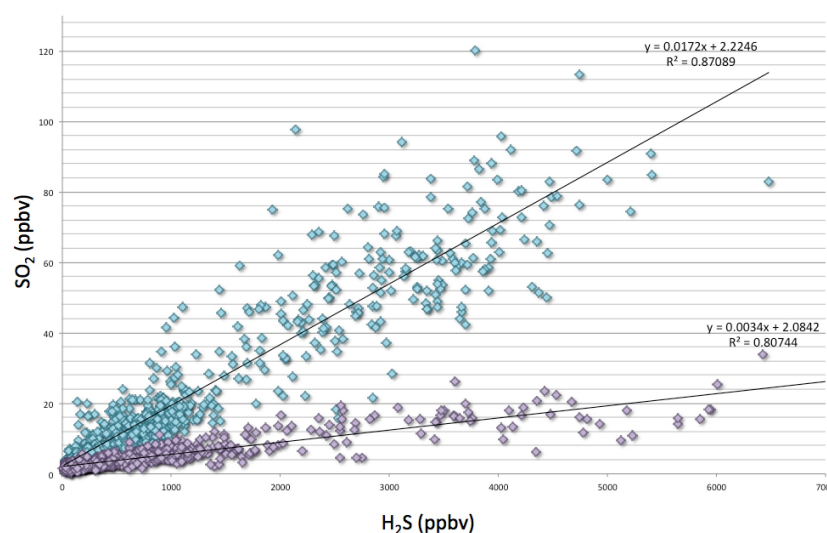
FIGURE 7.14: *SO_2 vs. H_2S concentrations from the Hengill Ölkelduháls geothermal area in 2017 (blue) and 2018 (violet). Linear regressions, the equations in the form y = mx + q and R^2, are also reported.*

Similar differences were observed in the Skidaskali geothermal area, where both SO_2 and H_2S concentrations in 2017, SKI(B), were higher than those recorded in 2018, SKI(D) (Fig. 7.15), producing a SO_2/H_2S ratio of 72×10^{-4} for 2017 and to 30×10^{-4} for 2018. A different SO_2/H_2S ratio can also be observed in 2017, in SKI(C), during the measurements around the same fumarolic emission (Fig. 7.16): the second and the third fix spots of measure shown a SO_2/H_2S ratio of 159×10^{-4}, whereas the first fix spot is aligned with SKI(B).
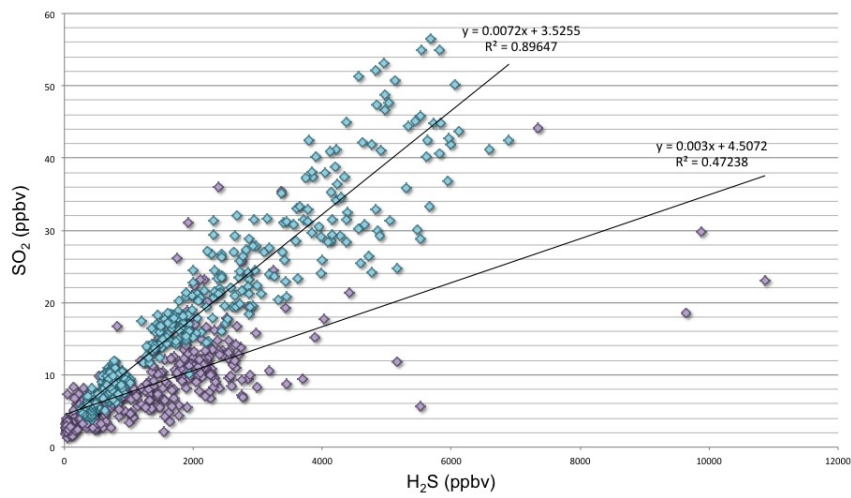
FIGURE 7.15: *SO$_2$ vs. H$_2$S concentrations from the Hengill Ski-daskali geothermal area in 2017 (blue), SKI(B), and 2018 (violet), SKI(D). Linear regressions, the equations in the form y = mx + q and R^2, are also reported.*
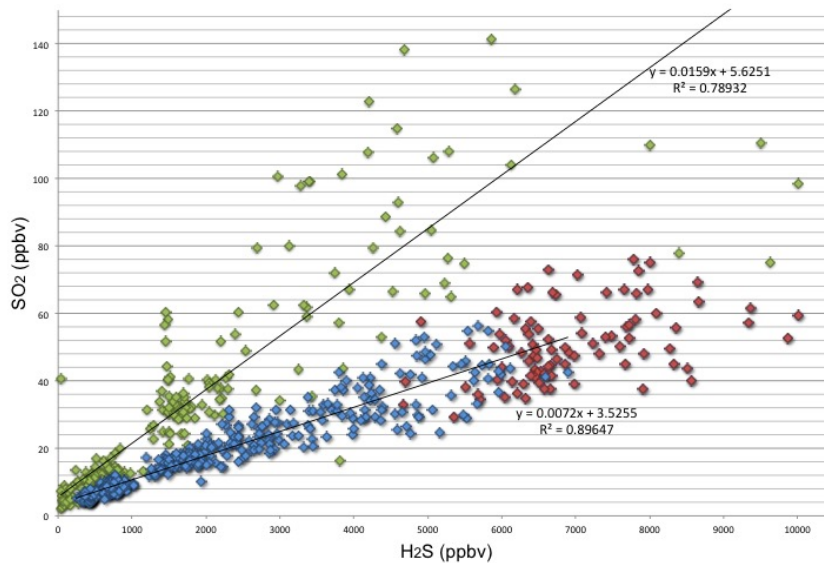
FIGURE 7.16: *SO$_2$ vs. H$_2$S concentrations from the Hengill Ski-daskali geothermal area in 2017: SKI(B) (blue) and SKI(C), first (red), second and third fix spots (green). Linear regressions, the equations in the form y = mx + q and R^2, are also reported.*

In the Reykjanes geothermal area, the 2017 measurements were consistent in terms of SO$_2$/H$_2$S ratio, being of 69×10^{-4} for REY(A) and of 78×10^{-4} for REY(C), even though REY(C) shown higher SO$_2$ and H$_2$S concentrations, respect to REY(A) (Fig. 7.17). The 2018 measurements, REY(D)

and REY(E), were not consistent in terms of SO_2/H_2S ratio and different H_2S-SO_2 concentrations were measured around the same fumarolic emission (Fig. 7.18). The 2017 SO_2/H_2S ratios are only consistent with one out of the measurements carried out in 2018 (Fig. 7.19), which correspond to 60×10^{-4}, whereas the other has a ratio of 184×10^{-4}.
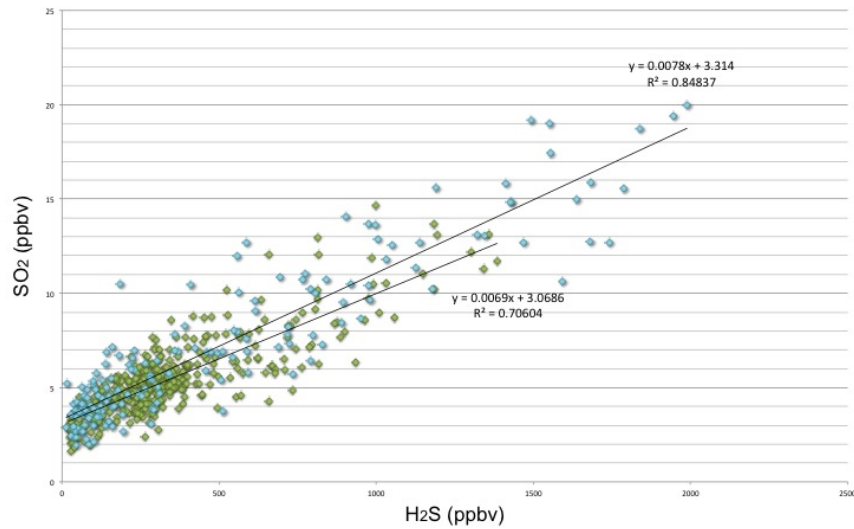
FIGURE 7.17: *SO_2 vs. H_2S concentrations from the Reykjanes geothermal area in 2017: REY(A), the Gunnuvher big steam vent (green) and REY(C), the small fumarole (blue). Linear regressions, the equations in the form $y = mx + q$ and R^2, are also reported.*
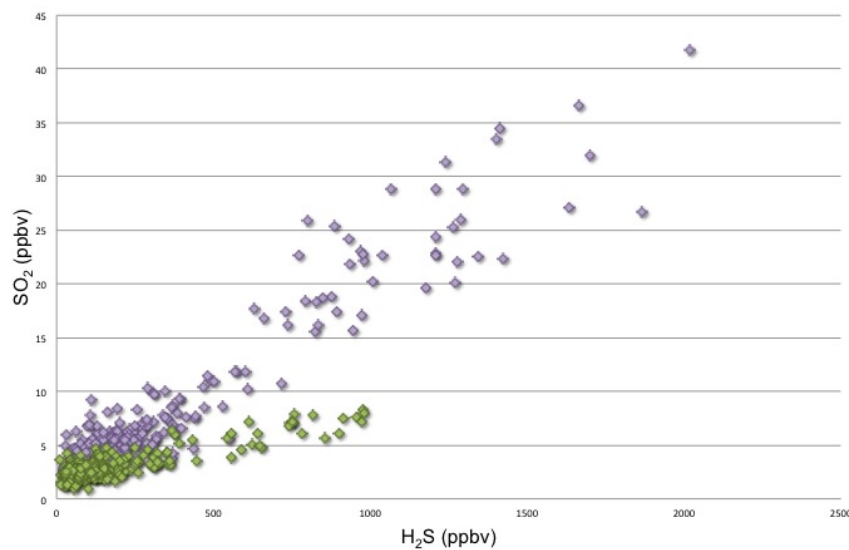
FIGURE 7.18: *SO_2 vs. H_2S concentrations from the Reykjanes geothermal area in three different repetitions around the same fumarole in 2018: REY(D) (green) and REY(E) (violet).*
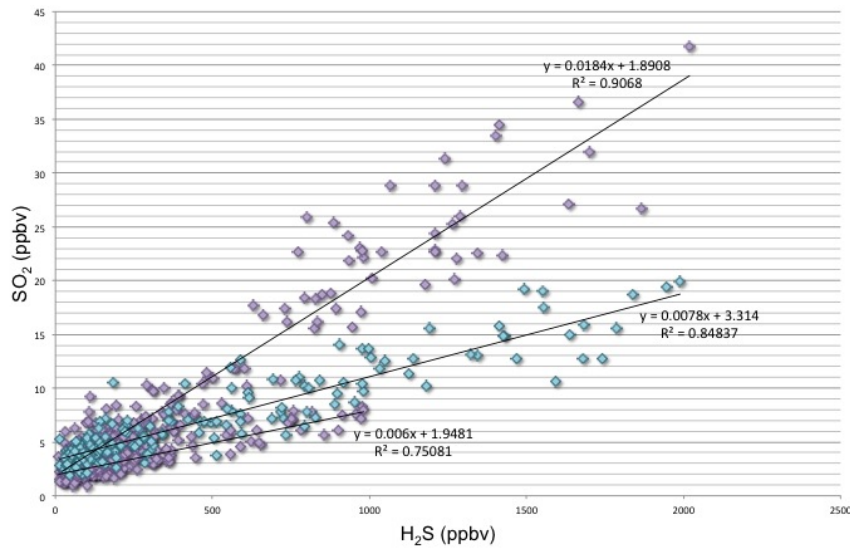
FIGURE 7.19: SO_2 vs. H_2S concentrations from the Reykjanes geothermal area in 2017 (blue) and 2018 (violet). Linear regressions, the equations in the form $y = mx + q$ and R^2, are also reported.

In the Bjarnaflag geothermal area, in 2017 and 2018, the H_2S and SO_2 concentration were consistent (Fig. 7.20) although slightly different SO_2/H_2S ratios are observed, i.e. 31×10^{-4} and 55×10^{-4} respectively.
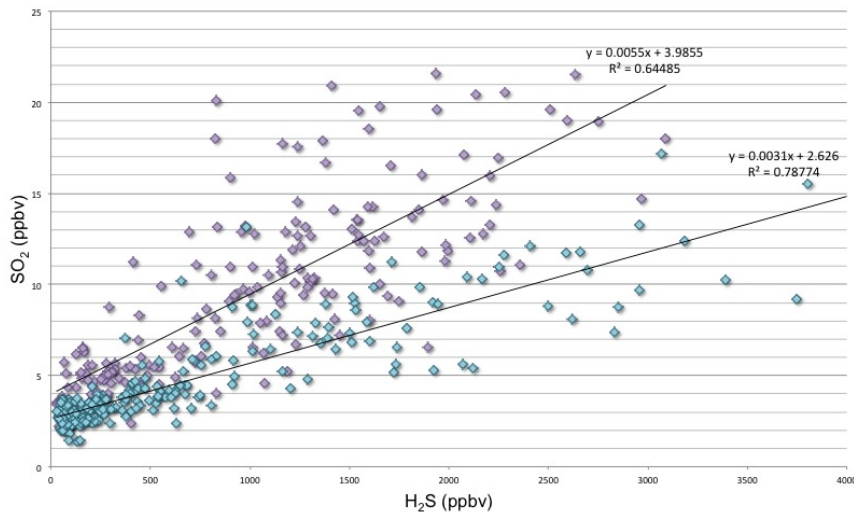
FIGURE 7.20: SO_2 vs. H_2S concentrations from Bjarnaflag geothermal area in 2017 (blue), BJARN(A), and 2018 (violet), BJARN(C). Linear regressions, the equations in the form $y = mx + q$ and R^2, are also reported.

In the Námafjall geothermal system, different SO_2/H_2S ratios are observed for the same system, though close to different emission sources (i.e.

well and boiling pools) in both 2017 and in 2018. The well SO_2/H_2S ratio measured in 2017, NAM(A), corresponds to 73×10^{-4}, whereas that of the small boiling pool, NAM(B), is 47×10^{-4} (Fig. 7.21) By comparing the 2017 measurements, NAM(A) and NAM(B), with that of 2018, NAM(C), a higher SO_2/H_2S ratio can be observed for the big boiling pool, being 129×10^{-4} (Fig. 7.22).
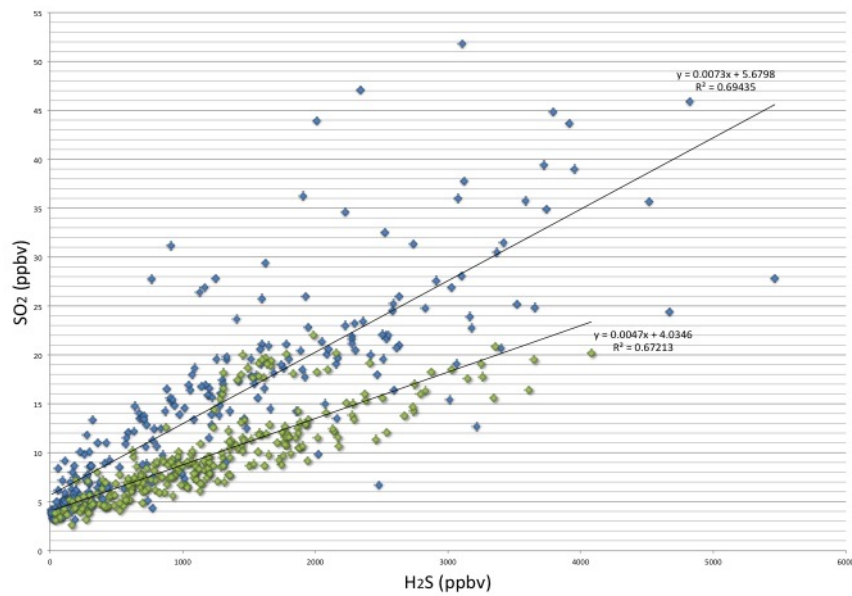
FIGURE 7.21: *SO_2 vs. H_2S concentrations from the Námafjall Hverir geothermal area in 2017, for well emission (blue), NAM(A), and small boiling pools (green), NAM(B). Linear regressions, the equations in the form y = mx + q and R^2, are also reported.*
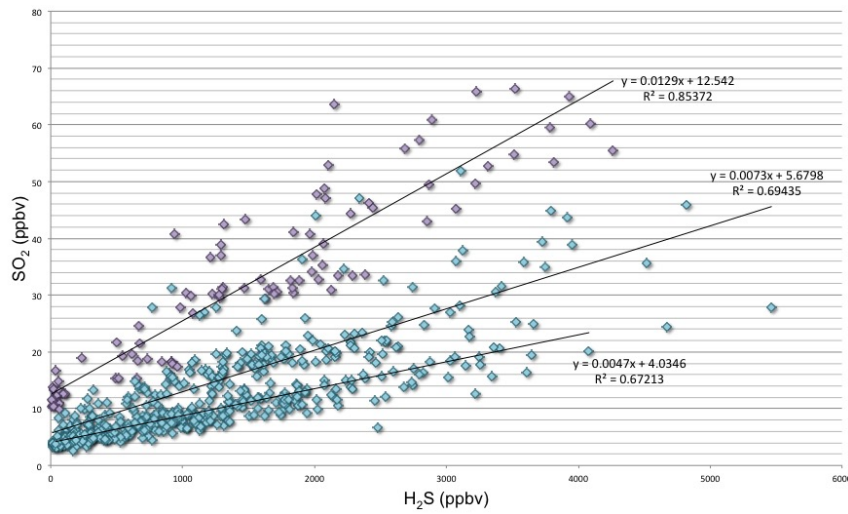
FIGURE 7.22: *SO$_2$ vs. H$_2$S concentrations from the Námafjall geothermal area in 2017 (blue), NAM(A) and NAM(B), and 2018 (violet), NAM(C). Linear regressions, the equations in the form y = mx + q and R^2, are also reported.*

At Hvíthólar, the H$_2$S and SO$_2$ concentrations were consistent during the 2017, HVITH(B), and 2018, HVITH(C), surveys (Fig. 7.23). A similar SO$_2$/H$_2$S ratio can also be observed, i.e. 105×10^{-4} and 128×10^{-4}, respectively. By comparing the Hvíthólar measurements with that of Leirbotnar, similar SO$_2$ concentrations and higher H$_2$S concentrations in the latter can be observed, producing a lower SO$_2$/H$_2$S ratio in Leirbotnar of 41×10^{-4} (Fig. 7.24).
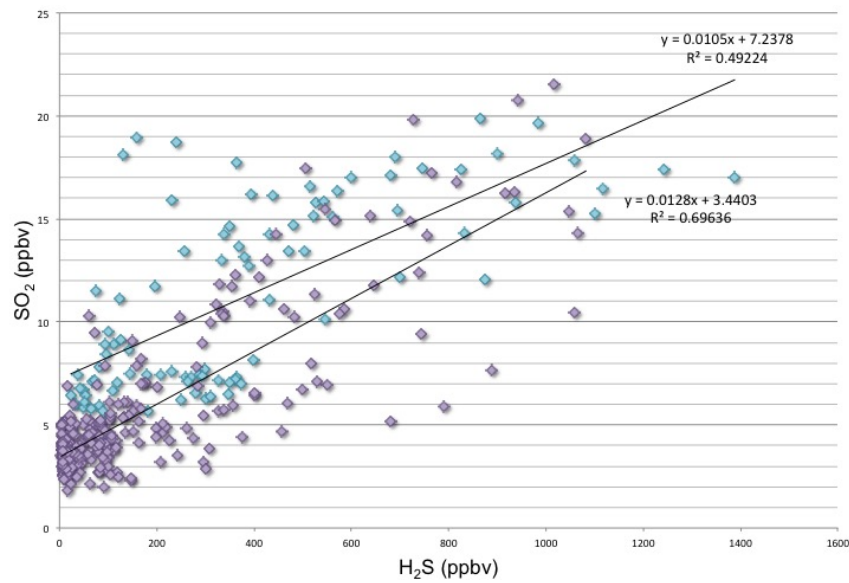
FIGURE 7.23: *SO$_2$ vs. H$_2$S concentrations from the Hvíthólar geothermal area in 2017 (blue), HVITH(B), and 2018 (violet), HVITH(C). Linear regressions, the equations in the form y = mx + q and R^2, are also reported.*
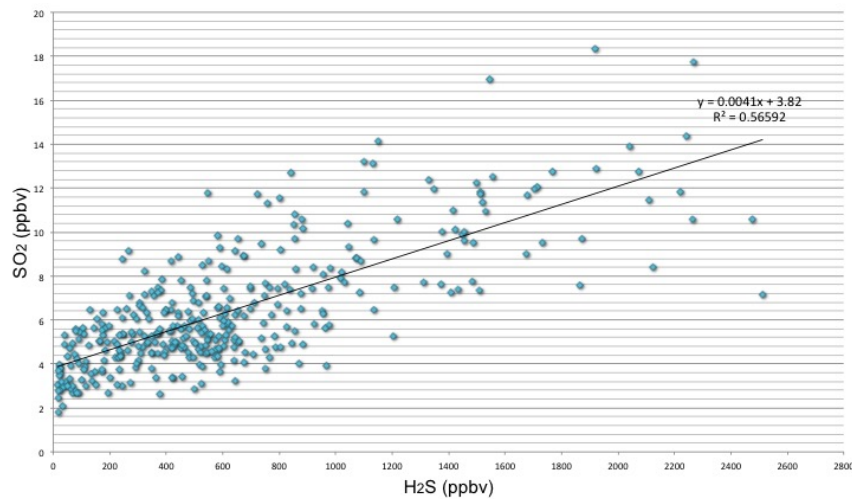
FIGURE 7.24: *SO$_2$ vs. H$_2$S concentrations from the Leirbotnar (Hveragil) geothermal area in 2018 (LEIRB). Linear regressions, the equations in the form y = mx + q and R^2, are also reported.*

At Krýsuvík, similar SO$_2$ and H$_2$S concentrations were measured around the same fumarolic emission, whereas different SO$_2$/H$_2$S ratio were observed: 84×10^{-4} for KRY(A) and 50×10^{-4} for KRY(C) (Fig. 7.25).
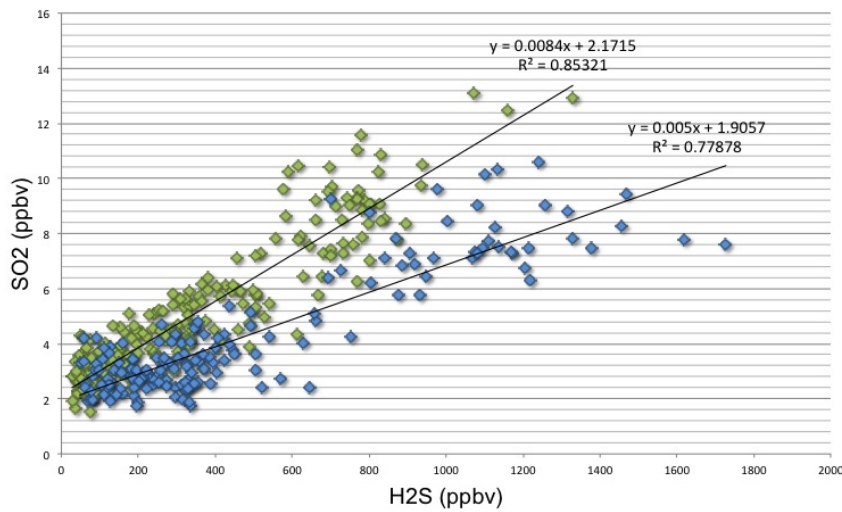
FIGURE 7.25: *SO$_2$ vs. H$_2$S concentrations from the Krýsuvík geothermal area in 2017: KRY(A) (green) and KRY(C) (blue). Linear regressions, the equations in the form y = mx + q and R^2, are also reported.*

As summarized in Fig. 7.26 and Fig. 7.27, the SO$_2$/H$_2$S ratio varies from 20 to 180 $\times$ 10^{-4} for both 2017 and 2018 measurements. Furthermore, the SO$_2$/H$_2$S ratio is different for each geothermal system and also varies within the same area, if different emissions from the same site are considered: this is the case of Námafjall, where the well emission has a higher SO$_2$/H$_2$S ratio with respect to that recorded close to the small boiling pools (Fig. 7.21). This can be explained in terms of the thick superficial water layer that SO$_2$ has to pass through to reach the surface in the boiling pools. Conversely, the water head is partially bypassed when fluids are rising up from the well. Owing to the high solubility of SO$_2$, the former manifestations recorded lower SO$_2$ concentrations than those shown at the well. The presence of surficial water can likely explain the reason why the SO$_2$/H$_2$S ratios are significantly differing among the various geothermal systems and within the same area in the 2017 and 2018 surveys. This implies that changes in the magmatic deep source can likely be excluded. In fact, the SO$_2$/H$_2$S ratio trends in 2017 and 2018 (Fig. 7.26 and Fig. 7.27) do not show any correlation with the magmatological setting of each area, since for example at Leirbotnar a higher SO$_2$/H$_2$S ratio would have been expected, due to the presence of a shallow magma chamber (Einarsson, 1978; Brandsdóttir et al., 1997, Schuler et al., 2015). Different SO$_2$/H$_2$S ratios for the same emission can also be observed when the

wind direction was changing: this is the case for the Reykjanes geothermal area, where two different SO_2/H_2S ratios are observed (78×10^{-4} and 184×10^{-4}) (Fig. 7.19). The higher SO_2/H_2S ratio is related to a NW wind direction, which forced different sources to overlap: the measurements were indeed carried out downwind with respect to multiple sources, producing a different SO_2/H_2S ratio with respect to what was expected by considering a single source. A similar process likely affected the measurements at Hengill Skidaskali and Námafjall, during which a temporary change in the wind direction favored the detection of a different emission source. In particular, in Námafjall, the hydrothermal gases released from the geothermal well were likely overlapping with those from the boiling pools, as shown in Fig. 7.21. Different conclusions can be made for the multiple SO_2/H_2S ratio observed for the same emission at Krýsuvík (Fig. 7.25). In this case, different weather conditions probably have affected the gas concentrations: the presence of rain during the KRY(C) measurements, probably has influenced mainly SO_2, which is more soluble than H_2S, producing a lower SO_2/H_2S ratio.
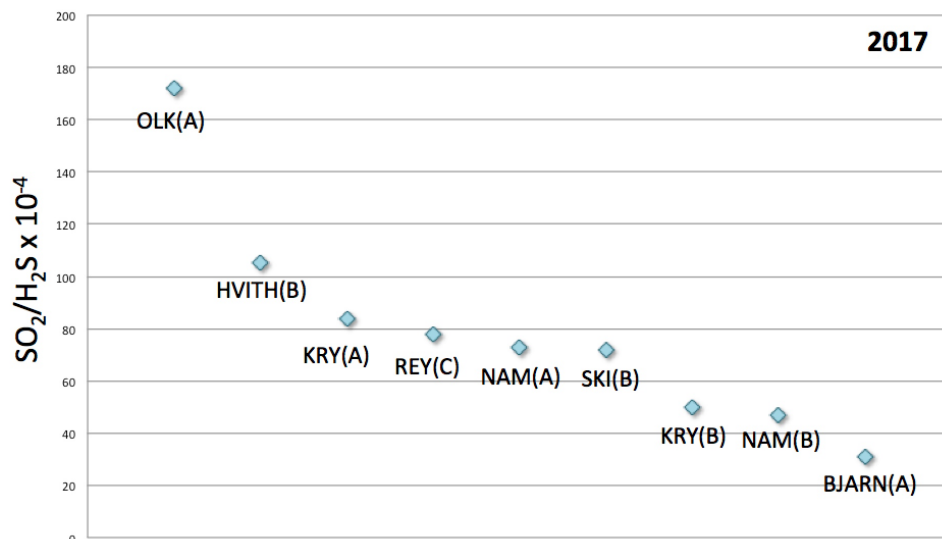
FIGURE 7.26: *The SO_2/H_2S ratio (y-axis), multiplied by 10^{-4}, for the Icelandic geothermal systems (ordered according to decreasing ratios) measured in 2017. Legend: OLK(A) = Ölkelduháls, HVITH(B) = Hvíthólar, REY(C) = Reykjanes small fumarole, NAM(A) = Námafjall well, SKI(B) = Skidaskali, NAM(B) = Námafjall boiling pools, BJARN(A)= Bjarnaflag.*
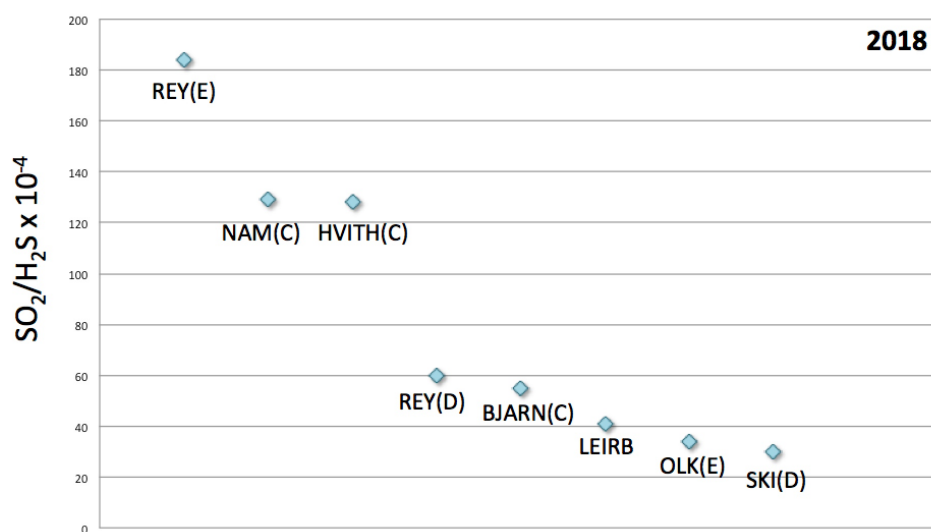
FIGURE 7.27: *The SO_2/H_2S ratio (y-axis), multiplied by 10^{-4}, for the Icelandic geothermal systems (ordered according to decreasing ratios) measured in 2018. Legend: REY(E) = Reykjanes small fumarole, NAM(C) = Námafjall big boiling pool, HVITH(C) = Hvíthólar; BJARN(C) = Bjarnaflag, OLK(E) = Ölkelduháls, SKI(D) = Skidaskali.*

Furthermore, different is also the case of Geysir geothermal area: even if it is considered an high-temperature geothermal system, it is located marginally respect to the active volcanic belts and it is characterized by lower gas concentrations compared to systems having higher reservoir temperatures (Stefánsson, 2017). These observations suggested that the low SO_2-H_2S concentrations measured, can probably be ascribed to multiple factors affecting the total gas concentrations, including the source of gases, rock and melt types and reactions within the geothermal systems.

Comparing the SO_2/H_2S ratios with those of Vulcano Island and La Solfatara crater, some differences can be recognized. The gas discharges at the beach of Vulcano Island are characterized by a SO_2/H_2S ratio of 230 $\times 10^{-4}$ (VULC(B), Fig. 7.28), a little bit higher than those recorded in Iceland, though quite consistent, suggesting that the Vulcano and Icelandic hydrothermal systems are possibly characterized by rather similar mechanisms of production for H_2S and SO_2. The differences between the SO_2/H_2S ratios are due to similar concentrations of SO_2 but with lower H_2S values with respect to those detected in the Icelandic geothermal systems.
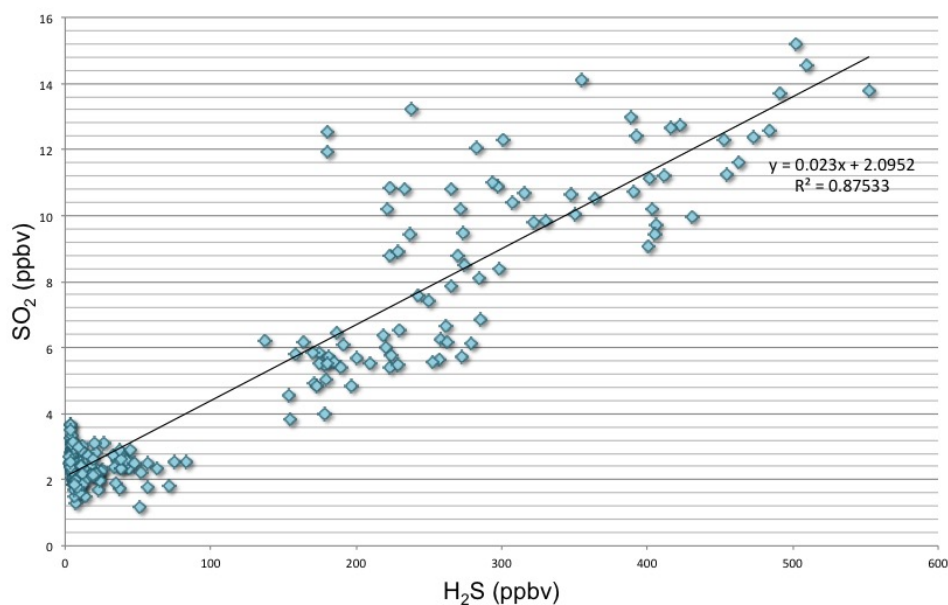
FIGURE 7.28: *Linear regression for SO$_2$ vs. H$_2$S measurements of VULC(B) at Vulcano Island.*

For the case study of Vulcano, the application of the mathematical model is more difficult, because of the complexity of the area where, for example, the presence of village buildings is likely controlling the pollutants distributions. At La Solfatara, two principal trends are observed (Fig. 7.29): the first one is characterized by relatively low SO$_2$ values and represents the first fix spot of measurements close to the Fangaia boiling pool (blue dots), the other one is characterized by higher SO$_2$ values and resulting by recordings obtained for fix spots located far from the emitting source (green dots). Accordingly, these trends present different SO$_2$/H$_2$S ratio: 75×10^{-4} and 1337×10^{-4}, respectively. The difference between the two ratios can be ascribed, as observed for Námafjall, to the overlapping of different gas sources: La Solfatara crater is an intensively altered area characterized by multiple fumarolic emissions, which present a higher flux and less water condensation at surface than the Fangaia boiling pool. Consequently, these fumarolic emissions can have contributed to the resulting ratio when measuring away from the Fangaia boiling pool source.
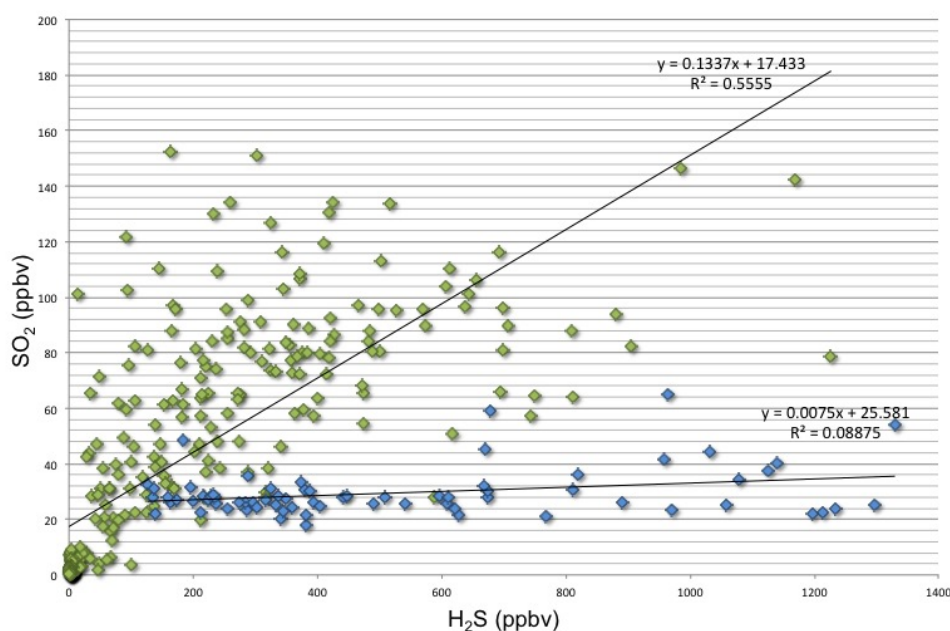
FIGURE 7.29: *Linear regression for SO$_2$ vs. H$_2$S measurements for La Solfatara crater (SOLF): first trend (green) and second trend (blue).*

7.2.5   SO$_2$ and H$_2$S spatial dispersion

As mentioned in Chapter 2, the World Health Organization (WHO, 2000) suggests a guideline value of 100 ppbv for H$_2$S in ambient air (24 h) and 4.6 ppbv to avoid significant odor annoyance (30 min), while a limit value for SO$_2$ of 125 ppbv (1 h) and 44 ppbv (1 day) are suggested for human health protection by WHO (2003) and 7 ppbv (1 year) for vegetation protection. In Iceland, the SO$_2$ emitted from the natural emissions considered in this study, rapidly decreases once released from the source and generally most sulfur dioxide is consumed within about 40-50 m from the emitting site where SO$_2$ reaches background values (1.5-2.0 ppbv). On the other hand, the initial H$_2$S concentrations are higher than those of SO$_2$, although the former does not reach low values as fast as SO$_2$, even if the depletion rate is twice faster. Thus, to predict the H$_2$S depletion with distance, the mathematical model was applied. The results show that for OLK(E), SKI(B) and HVITH(B) the distances at which H$_2$S reach the limit value proposed by WHO for odour annoyance are 95, 80 and 85 m from the source, respectively (Fig. 7.30, Fig.

7.31 and Fig. 7.32). It is worth to mention that these distances can be regarded as valid in accordance with the measured wind speed, assuming that the depletion rate is constant (so does not vary at increasing distance respect to the source) and no topographical obstacles are present. Thus, we can infer that, with these assumptions and conditions, over a distance of 100 m H_2S and SO_2 are expected not to exceed the limit values proposed by WHO (2003). In order to validate our simulation model, H_2S and SO_2 measurements at increasing distances (up to 100 m) are to be performed.
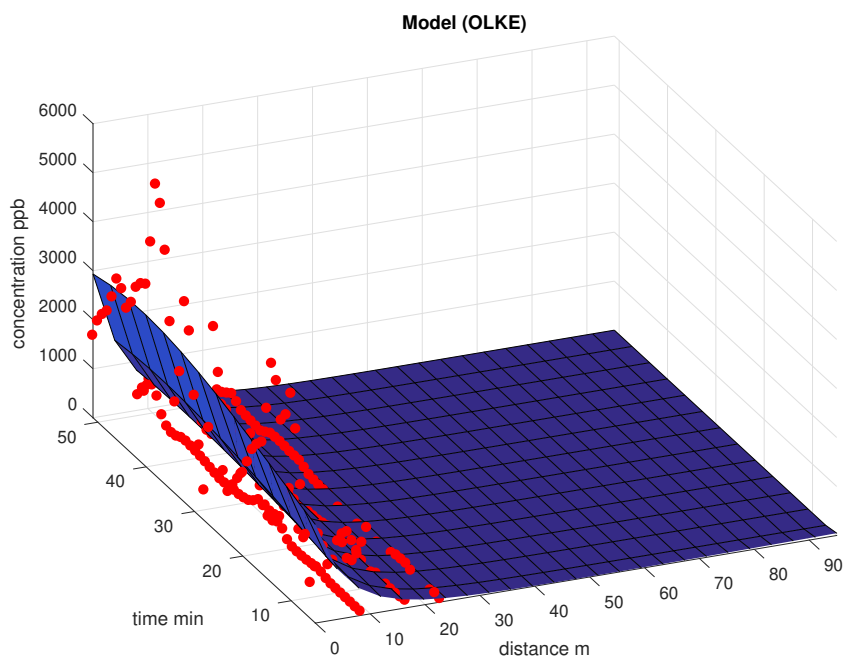
FIGURE 7.30: *Prediction of H_2S depletion with distance until 5 ppb for OLK(E).*
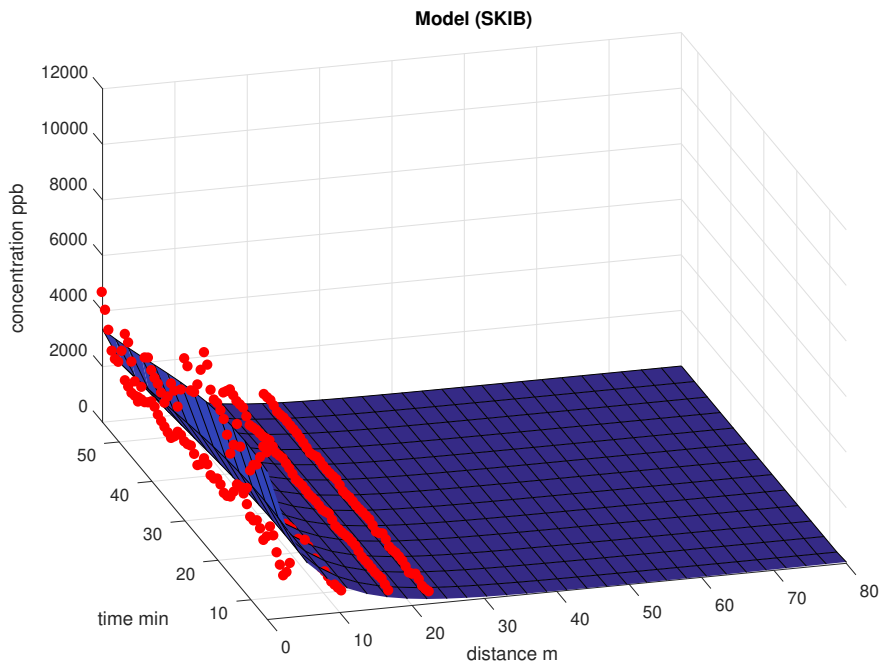
FIGURE 7.31: *Prediction of H_2S depletion with distance until 5 ppb for SKI(B).*
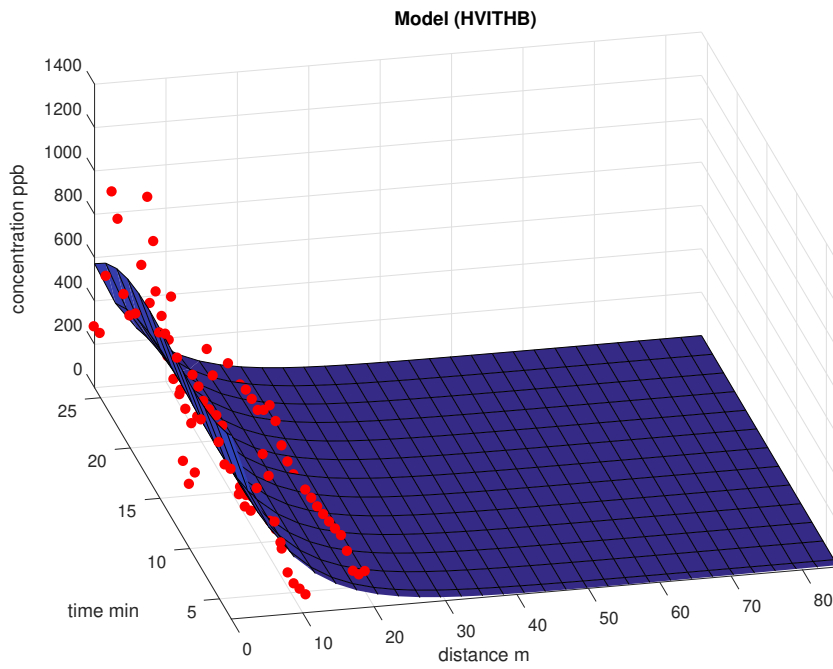
FIGURE 7.32: *Prediction of H_2S depletion with distance until 5 ppb for HVITH(B).*

7.3 Volatile organic compounds

Non-methane volatile organic compounds (VOCs) are released in volcanic and hydrothermal gas emissions (e.g., Capaccioni et al., 1993; Darling, 1998; Tassi, 2004; Tassi et al., 2009) in a complex mixture of a multitude of hydrocarbons (alkanes, alkenes, aromatics) and heteroatomic constituents (including O- and S-bearing compounds, and halocarbons) (Capaccioni et al., 1993, 1995; Taran and Giggenbach, 2003; Tassi et al., 2012c; Schwandner et al., 2013). The origin of VOCs in volcanic and hydrothermal systems is mainly ascribed to degradation of the organic material mainly buried in sedimentary rocks, by bacteria-driven (biogenic) reactions at low temperature (<150 °C) or by thermogenic processes at 150-350 °C, such as catalytic reforming and/or thermal cracking (e.g., Matsuo, 1961; Des Marais et al., 1981; Giggenbach et al., 1986; Martini et al., 1986; Capaccioni et al., 1993, 1995; Darling, 1998; Mango et al., 2009). The VOCs composition in the icelandic hydrothermal plumes is considered relatively homogeneous: aromatics are the most important group (up to 50% of the total VOC composition), followed by alkanes (20-25%), O-bearing (6-16%), cyclics (5-10%), S-bearing (4-7%), alkenes (1-6%) and halocarbons (up to 1% if present). For comparison, the VOC composition observed in "hydrothermal fluids" (e.g., Fournier, 1989; D'Amore et al., 1997; Lee et al., 2005) and in "low-temperature" fluids (Minissale et al., 1997) is reported in Fig. 7.33.
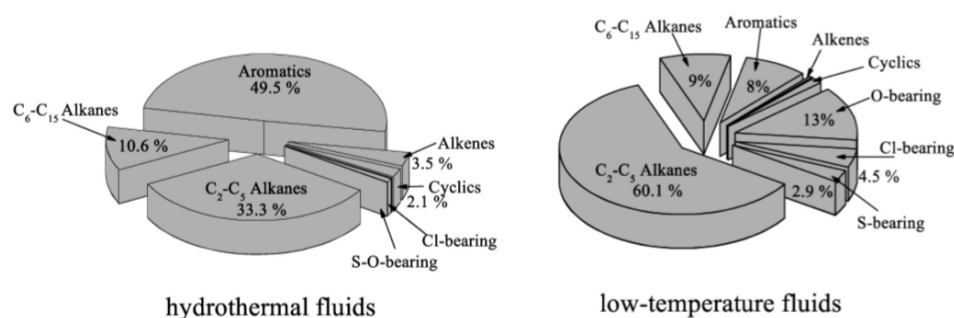
FIGURE 7.33: *Pie diagrams showing the relative abundances, expressed in % with respect to the total VOC concentrations, of the various groups of VOCs in fluid discharges of hydrothermal systems and of low-temperature systems.*

The composition of VOC in the icelandic hydrothermal plumes shows similarities with both hydrothermal and low-temperature fluids: on one

hand they are relatively rich in aromatics (50%) and alkanes (20-25%), on the other hand they present enrichments of O-bearing (6-16%) and S-bearing (4-7%) compounds. Thus, the VOC composition of icelandic hydrothermal plumes can be regarded as mainly hydrothermal, with anomalously high abundances of O-bearing and S-bearing compounds that can be ascribed to superficial reactions within the plume driven by the presence of atmospheric O_2 and H_2S.

Chapter 8

Concluding remarks

Large amounts of volcanic gases into the upper atmosphere are released during eruptive events, causing strong effects on climate and atmospheric and terrestrial environments. Non-eruptive periods are by the way able to contribute to extensive gas emissions through visible (i.e. fumaroles, solfataras and plumes) and non-visible (i.e. diffuse soil degassing) emanations. After CO_2, H_2S and SO_2 are the most prevalent gas species emitted from active volcanic/geothermal systems and their concentrations in the atmosphere can represent a significant hazard to human health, as described by the Word Health Organization guidelines (WHO, 2003). In hydrothermal systems, H_2S is the dominant species among S-compounds, while no magmatic SO_2 is expected to be detected, even if the conversion of H_2S to SO_2 has been suggested by many authors (Norrish and Zeelenberg, 1957; Cox and Sandalls, 1974; Stuhl, 1974; Perry et al., 1976; Graedel, 1977a). A number of studies, carried out on SO_2 concentrations emitted during strong volcanic eruptions and on H_2S emitted by geothermal power plants, have allowed to model the spatial dispersion and predict the distribution and impact on the environment of these two air pollutants (e.g., in the Imperial Valley in California, Gudiksen, 1979; in Cerro Prieto in Mexico, Gallegos-Ortega et al., 2000; in Rotorua, New Zealand, Horwell et al., 2004; and in Iceland: at Svartsengi, Kollikho, 1998; at Nesjavellir, Gíslason, 2000; at Nesjavellir, Nyagah, 2006 and at Hellisheidi power-plant, Ólafsdóttir, 2007). However, the mathematical models for H_2S in geothermal plumes are essentially "physically" simulated, since they do not take into account paths and rates of chemical reactions that can affect H_2S once it is released from the emitting source, despite the fact that they are critical considering the high chemical reactivity

in air of the S-bearing volatile compounds. Two main processes are suggested to favor the removal of H_2S and SO_2 within volcanic-hydrothermal plumes: a) oxidation in the gas phase (homogeneous reactions) and b) oxidation in the liquid/solid aerosol phase (heterogeneous reactions) (Seinfeld and Pandis, 1998). Nevertheless, although several laboratory experiments have been carried out, especially on the gas phase oxidation (Perry et al., 1976; Sprung, 1977; Graedel, 1977; Eggleton and Cox, 1978; Jaeschke et al, 1979; Wine et al., 1981; Servant and Delaport, 1982), few field studies have been dedicated to investigate the behavior of S-gases from hydrothermal plumes. Hydrothermal emissions can indeed persist for long periods and their contribution on the atmospheric impact can be substantial when compared to single large eruptions. The overriding purpose of this work is to increase the currently scarce scientific knowledge on the concentrations and behavior of H_2S and SO_2 from hydrothermal sources, which can be used to evaluate and predict health and vegetations hazards at a local scale. To accomplish this goal, an empirical method was applied to selected areas characterized by extensive emissions of geothermal fluids (e.g., Iceland) and a strategy of measurement in air was sett up, allowing the acquisition of an extended database that was used to develop a mathematical model able to describe the evolution of these gases in fumarolic plumes. The measurement strategy was tested during two field surveys at Vulcano Island and La Solfatara and then, extensively applied in Iceland. The strategy was that to place the portable battery-supplied high-sensitive device downwind with respect to the source to catch snapshots of H_2S and SO_2 concentrations within the plume to model as the hydrothermal plume was compositionally modifying at increasing distances. To develop the mathematical model, in collaboration with the Department of Mathematics of Florence "U. Dini", a simple mass balance equation able to describe the rate of H_2S and SO_2 depletion/enrichment observed in the field moving away from the emitting source was computed. Sulfur dioxide and H_2S were considered as independent variables and chemical reactions, such as photo-oxidation of H_2S to SO_2, were not considered in this first step. The field measurements and the modeling results firstly showed that: i) SO_2 is present in hydrothermal environments although at very low concentrations (<200 ppbv), suggesting why SO_2 was not previously detected in hydrothermal sites by adopting the

traditional gas sampling methods; ii) the physical dilution seems to affect both H_2S and SO_2 at a lower extent with respect to chemical reactions; iii) the reaction rates of oxidation processes in air for both H_2S and SO_2 calculated by the model are faster than those suggested in the literature. The modeling approach was specifically valid for low distances (up to 50 meters) with respect to the source due to the lack of physical obstacles along the gas pattern in air and almost stable wind directions. This implies that dispersion/dilution processes can play a pivotal role for higher distances (i.e. km), complex topography and extremely variable weather conditions. The reactions rates for SO_2 and H_2S calculated with our model corresponded to 3.3×10^{-1} s^{-1} and 6.6×10^{-1} s^{-1}, respectively, which are 3-4 orders of magnitude faster than that proposed for homogeneous gas phase oxidation via the hydroxyl radical calculated in laboratory experiments (Wine et al., 1981; Martin et al., 1986). As suggested by Ravishankara (1997), these differences can be related to the quantity of suspended liquid-solid particles largely present in volcanic and hydrothermal plumes, that renders heterogeneous and multiphase (in droplets) reactions more important in controlling the concentration of soluble gases than slower homogeneous gas-phase reactions via the hydroxyl radical. Moreover, the solubility of chemical species can further increase relative to their aqueous reaction rate in droplets (Ravishankara, 1997), which probably involve, in the case of S-compounds, H_2O_2, as suggested by Zhang and Tie (2011). The faster SO_2 reaction rates obtained by Oppenheimer et al. (1998), during Soufriere Hills volcano eruption (10^{-2} s^{-1}), support our findings, being calculated in particular conditions (i.e. presence of clouds and high ash content in the plume), since rapid condensation of steam is supposed to have occurred, increasing SO_2 diffusion and dissolution in droplets. Thus, in hydrothermal plumes, being weaker and lower respect to volcanic plumes, water vapor condensation and H_2S-SO_2 dissolution can even be faster. About the conversion of H_2S to SO_2, the constant rates for the photo-oxidation of H_2S via the hydroxyl radical suggested in the literature are rather slow to be observed near the emitting source. Consequently, this process probably does not represent the most important H_2S removal mechanism. Furthermore, the rates of SO_2 production related to the photo-oxidation of H_2S are difficult to be evaluated because

of the fast removal of SO_2 due to dissolution processes. Further investigations on reaction rates in presence of water droplets, through homogeneous and heterogeneous reactions, together with the availability of reagents such as OH and H_2O_2, are necessary to develop a more complex mathematical model, which should take into account all the contributions related to H_2S and SO_2 removal and interrelationship mechanisms. Futhermore, each studied geothermal system showed different SO_2/H_2S ratios considering both the 2017 and 2018 surveys and the same system around different emissions, e.g., when the geothermal well and the boiling pools were analyzes at Námafjall. The SO_2/H_2S ratios was varying from 20 to 190 $\times$ 10^{-4}, similarly to those suggested for epithermal environments at 250 °C and neutral pH (10^{-6}-10^{-4}) (Barton et al., 1977; Einaudi et al., 2003), whereas the SO_2/H_2S ratios in >500 °C volcanic fumaroles was measured up to 1.0 (Giggenbach, 1987). As explained by Giggenbach (1987), sulfur dioxide is a highly reactive gas species and its concentrations are largely affected by fluid-rock interactions and hydrolysis reactions in hydrothermal systems, during its uprising from the magmatic source to the surface. Consequently, it is unlikely that SO_2 can reach the surface in hydrothermal environments and that the different SO_2/H_2S ratios are likely reflecting variations in the deep magmatic source composition. Thus, we suggest that SO_2 is more probably produced by secondary processes e.g., photo-oxidation of H_2S via OH radicals (Spedding and Cope, 1984), remobilization of elemental S deposits (Giggenbach, 1987) or oxidation of pyrite (Chiodini et al., 1993), and different SO_2/H_2S ratios would be better explained by different rates and boundary conditions that control these processes in each hydrothermal system and in different years, but this was beyond the goals of this study. Furthermore, simulations carried out with the mathematical model shown that generally, considering the measured weather conditions, concentrations of <5 ppbv for both H_2S and SO_2 in air were reached at distances >100 meters from the emitting source. Nevertheless, it is not possible to rule out that different conditions or emissions, e.g., power plants, might be able to produce distinct H_2S and SO_2 concentrations and relative ratios. The plume emitted by geothermoeletrical plants is indeed higher and stronger than those released by natural hydrothermal plumes, as evidenced by Olafsdottir et al. (2014). These authors suggested that high H_2S concentrations were also found even

at high distances (i.e. km) from the power plants if correlated with high air stability, low wind speed and absence of precipitation. Further investigation on reaction rates of H_2S-SO_2 removal processes and the improvement of the mathematical model for the prediction of pollutants dispersion in the atmosphere and the assessment of the impact on the surrounding areas, including anthropogenic environments, will be matter of study of ongoing research projects and collaboration, started during the PhD program, with the Department of Mathematics of Florence, "U. Dini".

Appendix A

Published Papers

A multi-instrumental geochemical approach to assess the environmental impact of CO_2-rich gas emissions in a densely populated area: The case of Cava dei Selci (Latium, Italy)

S. Venturi[a,b,*], F. Tassi[a,b], J. Cabassi[a], O. Vaselli[a,b], I. Minardi[c], S. Neri[c], C. Caponi[b], G. Capasso[d], R.M.R. Di Martino[d], A. Ricci[e], F. Capecchiacci[b], M. Lelli[f], A. Sciarra[g], D. Cinti[g], G. Virgili[c]

[a] *Institute of Geosciences and Earth Resources (IGG), National Research Council of Italy (CNR), Via G. La Pira 4, 50121, Florence, Italy*
[b] *Department of Earth Sciences, University of Florence, Via G. La Pira 4, 50121, Florence, Italy*
[c] *West Systems Co. Ltd, Via Don Mazzolari 25, 56025, Pontedera, Italy*
[d] *Istituto Nazionale di Geofisica e Vulcanologia, Sezione di Palermo, Via Ugo La Malfa 153, 90146, Palermo, Italy*
[e] *Department of Biological, Geological and Environmental Sciences, University of Bologna, Porta S. Donato 1, 40136, Bologna, Italy*
[f] *Institute of Geosciences and Earth Resources (IGG), National Research Council of Italy (CNR), Via G. Moruzzi 1, 56124, Pisa, Italy*
[g] *National Institute of Geophysics and Volcanology (INGV), Via di Vigna Murata 605, 00143, Rome, Italy*

ARTICLE INFO

ABSTRACT

The Colli Albani volcanic complex (Lazio, Italy) hosts areas characterized by anomalously high emissions of CO_2-rich gases (e.g. Tivoli, Cava dei Selci, Tor Caldara, Solforata). The source of these gases is a regional aquifer within the Mesozoic carbonate rock sequences. These degassing zones release significant concentrations of H_2S and other toxic gases (e.g. GEM: Gaseous Elemental Mercury, and Rn) and represent a serious hazard for local inhabitants, especially for those living at Cava dei Selci (near Rome, Italy), where the emitting areas are nested inside residential neighborhoods. In April 2016, a comprehensive geochemical survey was carried out in an abandoned stone quarry nearby the urban settlement aimed to: (i) investigate the gas composition from both punctual discharges and anomalously high diffuse soil degassing sites, and (ii) evaluate their environmental impact on the local air quality. The spatial distribution of the soil CO_2 fluxes was mainly dependent on the local geostructural setting, whereas shallow secondary processes (e.g. oxidation and gas-water interaction) likely represent the main controlling factor on reactive and/or water-soluble gas species, such as CH_4 and H_2S. The total output of CO_2 from the abandoned stone quarry accounted for 0.53% of total CO_2 discharged from the whole Colli Albani volcanic district. The naturally emitted toxic gases (e.g. CO_2, H_2S, CH_4, GEM) largely affect the air quality and pose a serious threat for the health of the local residents. A mobile multi-instrumental station able to continuously and simultaneously acquire CO_2, H_2S, SO_2, CH_4, GEM and CO was deployed to verify the concentrations of both the main deep-originated gas compounds and potential secondary gaseous contaminants (i.e. SO_2) around and inside the urban settlement most exposed to the lethal gases. Hydrogen sulfide was found to be the most impacting gas, occasionally exceeding the 24-h air quality guideline for ambient air and causing odor annoyance at a distance up to more than 250 m downwind from the emitting area. In poorly ventilated basements, toxic gas accumulations up to hazardous levels were measured, producing anomalous outdoor air concentrations at the street level in front of the descending vehicular access to private garages and relatively far from the main emitting area. The geochemical survey, carried out via mobile station and soil gas measurements, resulted to be particularly efficient for evaluating the potential effects caused by gas emissions in inhabited areas. The multi-measurement approach adopted in the present study is of paramount importance for managing future urban development plans.

1. Introduction

Geogenic CO_2-rich gas emissions discharge from large sectors of the peri-Tyrrhenian segment in central and southern Italy (i.e. southern Tuscany, Latium and Campania; Chiodini et al., 2000, 2004; Chiodini, 2008; Chiodini et al., 2013), where degassing areas are favored by (i)

CrossMark

Active hydrothermal fluids circulation triggering small-scale collapse events: the case of the 2001–2002 fissure in the Lakki Plain (Nisyros Island, Aegean Sea, Greece)

Stefania Venturi[1,2] · Franco Tassi[1,2] · Orlando Vaselli[1,2] ·
Georges E. Vougioukalakis[3] · Heba Rashed[2] · Christos Kanellopoulos[4] ·
Chiara Caponi[2] · Francesco Capecchiacci[1,2] · Jacopo Cabassi[1,2] ·
Andrea Ricci[5] · Luciano Giannini[1,2]

Abstract In 2001–2002, two ground collapses occurred in the island of Nisyros (Aegean Sea, Greece), which formed a 600 m long and up to 5 m wide fissure in the vegetated central part of the Lakki Plain caldera. The fissure was alternatively ascribed to tensional stress release and hydrothermal alteration. In this study, we present original data of diffuse CO_2 soil fluxes, soil temperatures, mineralogical and chemical composition of the caldera-filling deposits exposed on the fissure walls, and chemical and isotopic composition of interstitial soil gases collected from: the bottom of the fissure, the adjacent vegetated areas,

✉ Stefania Venturi
stefania.venturi@igg.cnr.it

Franco Tassi
franco.tassi@unifi.it

Orlando Vaselli
orlando.vaselli@unifi.it

Georges E. Vougioukalakis
gvoug@igme.gr

Heba Rashed
hebaafef.rashed@unifi.it

Christos Kanellopoulos
ckanellopoulos@gmail.com

Chiara Caponi
chiara.caponi@unifi.it

Francesco Capecchiacci
francesco.capecchiacci@unifi.it

Jacopo Cabassi
jacopo.cabassi@igg.cnr.it

Andrea Ricci
ricciandrea89@gmail.com

Luciano Giannini
luciano.giannini@gmail.com

⚫ Springer

CrossMark

RESEARCH ARTICLE

The 2012–2016 eruptive cycle at Copahue volcano (Argentina) versus the peripheral gas manifestations: hints from the chemical and isotopic features of fumarolic fluids

F. Tassi[1,2] · M. Agusto[3] · C. Lamberti[3] · A. T. Caselli[4] · G. Pecoraino[5] · C. Caponi[1] ·
J. Szentiványi[3] · S. Venturi[1,2] · O. Vaselli[1,2]

Abstract This study presents the chemical and isotopic compositions of hydrothermal gases from fumaroles discharging around Copahue volcano (Argentina). Gas samples, including those from two fumaroles at the active summit crater, were collected during 13 surveys carried out by different research teams from 1976 to February 2016. The time-series of H_2, CO and light hydrocarbons showed episodic increases related to the main events of the last eruptive cycle that started on 19 July 2012. Concentration peaks were likely caused by enhanced input of hot magmatic fluids affecting the hydrothermal reservoir. These data contrast with the temporal variations shown by Rc/Ra and $\delta^{13}C\text{-}CO_2$ values in 2012–2014, which indicated an increasing input from a crustal fluid source. In 2015–2016, however, these isotopic parameters showed opposite trends; their composition became closer to that of the two summit fumaroles, which possibly corresponds to that of the deep magmatic-related end-member. The delayed and reduced compositional changes in the peripheral hydrothermal fluid discharge in response to the 2012–2016 eruptive events suggest that geochemical surveys of these emissions are unlikely to provide premonitory signals of volcanic unrest if the volcanic activity remains centered in the main crater. Instead, an instrument which is able to provide measurements of volcanic gases in the air (e.g. MultiGAS) may be used to detect changes at the summit crater. Otherwise, monitoring of seismic activity and ground deformation, as well as the periodic measurement of the chemistry of the water in the Rio Agrio, which is fed by thermal discharge from the summit crater, seem to represent the most reliable means of monitoring at Copahue. However, the relative compositional stability of the hydrothermal reservoir is a great advantage in terms of geothermal resource exploitation and could encourage new investments in the Copahue geothermal project which was abandoned in the 1990s.

✉ F. Tassi
    franco.tassi@unifi.it

1   Department of Earth Sciences, University of Florence, Via La Pira, 4,
    50121 Florence, Italy

2   Institute of Geosciences and Earth Resources of the National
    Research Council (CNR-IGG), Via La Pira, 4, 50121 Florence, Italy

3   GESVA-IDEAN, Dpto. Cs. Geológicas, FCEN, Universidad de
    Buenos Aires, Ciudad Universitaria, Pab.2, 1428 Buenos
    Aires, Argentina

4   LESVA, Universidad Nacional de Río Negro, Roca 1242,
    8332 General Roca, Argentina

5   Istituto Nazionale di Geofisica e Vulcanologia, Via U. La Malfa 153,
    90146 Palermo, Italy

Introduction

Fumarolic gases discharging from hydrothermal reservoirs hosted in quiescent volcanoes carry sensitive compounds (e.g. H_2, CO, CO_2, CH_4 and H_2O) that provide the means for investigating the chemical-physical conditions of the deep environment (e.g. Giggenbach 1987, 1996; Chiodini and Marini 1998). Noble gas isotopic signatures are useful tracers for identifying fluid source regions, especially in subduction zones (e.g. Poreda and Craig 1989; Giggenbach et al. 1993; Fischer et al. 2002; Hilton et al. 2002, 2010; Shaw et al. 2003; Sano and Fischer 2013). Accordingly, fluid discharge is periodically monitored to assess the degassing behavior of magmatic bodies (e.g. Menyailov et al. 1986; Tassi et al. 2016) and changes in volcanic activity (e.g. Chiodini et al.

🌐 Springer

The hydrothermal system of the Domuyo volcanic complex (Argentina): A conceptual model based on new geochemical and isotopic evidences

F. Tassi [a,b,*], C. Liccioli [c], M. Agusto [e], G. Chiodini [d], O. Vaselli [a,b], S. Calabrese [f], G. Pecoraino [g], L. Tempesti [a], C. Caponi [a], J. Fiebig [h], S. Caliro [i], A. Caselli [c]

[a] Department of Earth Sciences, University of Florence, Via La Pira 4, 50121 Florence, Italy
[b] CNR-IGG Institute of Geosciences and Earth Resources, Via La Pira 4, 50121 Florence, Italy
[c] Instituto de Paleobiología y Geología de la Universidad Nacional Rio Negro, Rio Negro, Argentina
[d] Istituto Nazionale di Geofisica e Vulcanologia, Via D. Creti 12, 40128 Bologna, Italy
[e] Facultad de Ciencias Exactas y Naturales, Universidad de Buenos Aires, Buenos Aires, Argentina
[f] Dipartimento di Scienze della Terra e del Mare, Università di Palermo, Palermo, Italy
[g] Istituto Nazionale di Geofisica e Vulcanologia, Sezione di PalermoVia Ugo la Malfa 153, 90146 Palermo, Italy
[h] Institut für Geowissenschaften, Goethe-Universität, Altenhöferallee 1, 60438 Frankfurt am Main, Germany
[i] Istituto Nazionale di Geofisica e Vulcanologia "Osservatorio Vesuviano", Via Diocleziano, Napoli 328-80124, Italy

ARTICLE INFO

ABSTRACT

The Domuyo volcanic complex (Neuquén Province, Argentina) hosts one of the most promising geothermal systems of Patagonia, giving rise to thermal manifestations discharging hot and Cl^--rich fluids. This study reports a complete geochemical dataset of gas and water samples collected in three years (2013, 2014 and 2015) from the main fluid discharges of this area. The chemical and isotopic composition (δD-H_2O and $\delta^{18}O$-H_2O) of waters indicates that rainwater and snow melting are the primary recharge of a hydrothermal reservoir located at relative shallow depth (400–600 m) possibly connected to a second deeper (2–3 km) reservoir. Reactive magmatic gases are completely scrubbed by the hydrothermal aquifer(s), whereas interaction of meteoric waters at the surface causes a significant air contamination and dilution of the fluid discharges located along the creeks at the foothill of the Cerro Domuyo edifice. Thermal discharges located at relatively high altitude (~3150 m a.s.l.), namely Bramadora, are less affected by this process, as also shown by their relatively high R/Ra values (up to 6.91) pointing to the occurrence of an actively degassing magma batch located at an unknown depth. Gas and solute geothermometry suggests equilibrium temperatures up to 220–240 °C likely referred to the shallower hydrothermal reservoir. These results, confirming the promising indications of the preliminary surveys carried out in the 1980's, provide useful information for a reliable estimation of the geothermal potential of this extinct volcanic system, although a detailed geophysical measurements is required for the correct estimation of depth and dimensions of the fluid reservoir(s).

© 2016 Elsevier B.V. All rights reserved.

1. Introduction

Preliminary geophysical and geochemical investigations carried out at the Domuyo volcanic complex by a Japan-Argentine joint agency in 1983 and 1984 (JICA, 1983, 1984), at the northern edge of the Cordillera del Viento chain in the Neuquén Province (Argentina), recognized a promising geothermal resource related to the possible occurrence of two hydrothermal aquifers located at ≤600 and 2000–3000 m depth. The exploration of this system was interrupted at the feasibility phase, mainly due to its remote location, i.e. far from the main electricity supplies, and the creation of a provincial natural park. Hence, the energy supply for the local communities currently consists of fossil fuels from the oil and gas fields in the neighboring Neuquén Basin, which have a high cost due to the lack of pipelines connecting this area with the production zones (Mas and Mas, 2015). In 2015, a renewed interest for geothermal resources caused by the economic crisis convinced the national government to financially support scientific projects aimed at investigating in more detail the Domuyo hydrothermal system. A recent study (Chiodini et al., 2014) carried out a preliminary evaluation of the thermal energy released from this system (~1 GW), based on the flux of Cl^--rich fluids discharged from the thermal springs emerging in the western-slope of the volcanic edifice. These results highlighted the enormous geothermal potential of Domuyo, encouraging further investigations.

This paper describes and discusses the first complete dataset of chemical and isotopic composition of gas and waters samples collected

---

* Corresponding author at: Department of Earth Sciences, University of Florence, Via La Pira 4, 50121 Florence, Italy.
 E-mail address: franco.tassi@unifi.it (F. Tassi).

Appendix B

Conference Proceedings

Session: S01.33 - Volcanic degassing: insights into volcanic processes, impacts and hazard

Behaviour of S-bearing compounds (H2S and SO2) emitted in air from the main hydrothermal-volcanic systems of Iceland

Corresponding Author: Chiara Caponi | email: chiaragcaponi@gmail.com

Author: Chiara Caponi | Franco Tassi (1,2) | Andri Stefánsson (3) | Lorenzo Fusi (4) | Antonella Buccianti (1) | Orlando Vaselli (1,2) | Fabio Rosso (4) | Niccolò Bonini (1) | Rikey Kjartansdóttir (3) | Jóhann Gunnarsson Robin (3)

Affiliation: (1) Department of Earth Sciences, Via La Pira 4, 50121 Florence, Italy | (2) CNR - Institute of Geosciences and Earth Resources, Via La Pira 4, 50121 Florence, Italy | (3) Science Institute, University of Iceland, Sturlugata 7, 101 Reykjavík, Iceland | (4) Department of Math "U. Dini", University of Florence, Viale Morgagni 67/A, 50134 Florence, Italy

The main sources of SO_2 and H_2S in air consist of (i) natural fluid emissions from active/quiescent volcanoes and (ii) anthropogenic activities. These gas compounds have a strong impact on air quality, since they are toxic and climate forcing agents. Notwithstanding, the behaviour of these S-compounds in air is poorly known, since relatively scarce are the available thermodynamic data as well as those deriving from direct measurements. Hydrogen sulphide is considered to be relatively reactive in the atmosphere as it tends to be oxidized to SO_2 by photochemical reactions, even though the efficiency of the H_2S to SO_2 conversion significantly decreases under dark, dry and relatively cold conditions. Oxidation processes are also affecting SO_2, since about 65% is transformed to SO_4^{2-} whilst the remaining 35% is removed by dry deposition.

This work presents the results of an empirical approach to investigate the behaviour of H_2S and SO_2 once they are released to the atmosphere from the main hydrothermal fluid discharges of Iceland, i.e. fumaroles, boiling and mud pools. Hydrogen sulphide and SO_2 measurements in air were carried out using a Thermo Scientific 450i Analyzer positioned at 4-6 fixed points at increasing distance and downwind from the emission sources, under different weather conditions.

The results showed significant variations in terms of H_2S/SO_2 ratios (from 30 up to 200) from the different gas emissions, which are not necessarily related to the composition of the emitting source. A mathematical model of the spatial distribution of air pollutants, coupled with a statistical elaboration of the measured data, has been applied to i) determine the rate of loss of H_2S and SO_2 at increasing distances from the source, and ii) discriminate the

Behaviour of volcanogenic S-bearing compounds (H_2S and SO_2) in air at Vulcano Island (Aeolian Archipelago, southern Italy)

Chiara Caponi (1), Franco Tassi (1,2), Andrea Ricci (3), Francesco Capecchiacci (1,2), Stefania Venturi (1,2), Jacopo Cabassi (1,2), Orlando Vaselli (1,2)

(1) Department of Earth Sciences, University of Florence, Florence, Italy, (2) Institute of Geosciences and Earth Resources, National Research Council (IGG-CNR), Florence, Italy, (3) Department of Biological, Geological and Environmental Sciences, University of Bologna, Bologna, Italy

The main sources of SO_2 and H_2S in air consist of both natural fluid emissions related to active/quiescent volcanoes and hydrothermal systems, and anthropogenic activities (e.g. gas and oil refineries, steel industries, urban traffic). These gas compounds have a strong impact on air quality, since they are strong toxic and climate forcing agents. Notwithstanding, the behaviour of these S-compounds in air once they are released from the contaminant source(s) is poorly known, due to the scarce available data from thermodynamics and direct measurements. Hydrogen sulfide is considered to be relatively reactive in the atmosphere, being easily oxidized to SO_2 by photochemical reactions, even though the efficiency of the H_2S to SO_2 conversion is significantly lowered under dark, dry and relatively cold conditions, leading to a residence time of H_2S in air up to 42 days in winter.

In this work, H_2S and SO_2 measurements in air carried out at the Levante beach (Vulcano Island, Aeolian Archipelago), where a number of hydrothermal fluid discharges consisting of fumaroles and submarine emissions occur, are presented and discussed. These volcanic fluids, characterized by an H_2S-rich chemical composition, are released in a close proximity to the touristic village of Vulcano Porto. The measurements were carried out using a Thermo Scientific™ Model 450i Analyzer coupled with a Davis® Vantage Vue weather station (air humidity and temperature, wind direction and speed) in 34 fixed spots and along 8 pathways, selected according to: (i) distance from the contaminant source, (ii) wind direction and (iii) accessibility by car (where the instrument was installed). The main aim was to provide empirical insights on the behavior of these air pollutants in relation to the physical and chemical processes controlling their spatial distribution. The measured data were elaborated using a statistical approach to construct spatial distribution maps and conceptual models able to forecast the dispersion of the S-compounds at different environmental conditions to define the potential hazard to human health.

Natural gas emissions affecting a densely populated area at Cava dei Selci (Latium, Italy): Insights into the environmental impact from multi-instrumental geochemical measurements

Franco Tassi (1,2), Jacopo Cabassi (1,2), Stefania Venturi (1,2), Ilaria Minardi (3), Simone Neri (3), Chiara Caponi (1), Andrea Ricci (4), Francesco Capecchiacci (1,2), Orlando Vaselli (1,2), and Giorgio Virgili (4)

(1) University of Florence, Earth Science Department, Earth Sciences, Florence, Italy (franco.tassi@unifi.it), (2) CNR – Institute of Geosciences and Georesources, National Research Council (IGG-CNR), Via G. La Pira 4, 50121 Florence (Italy), (3) WEST Systems Ltd., Via Don Mazzolari 25, 56025 Pontedera (Italy), (4) Department of Biological, Geological and Environmental Sciences, University of Bologna, Porta S. Donato 1, 40136 Bologna (Italy)

The Colli Albani volcanic complex (Lazio, Italy) shows areas (e.g. Tivoli, Cava dei Selci, Tor Caldara, Solforata) characterized by an anomalously high soil gas emission originated from a regional CO_2-saturated aquifer hosted within Mesozoic carbonate rock sequences. These natural gas manifestations, dominated by CO_2 and showing significant concentrations of CH4, H2S, and Rn, represent a serious hazard for local inhabitants, especially where residential zones are in a close proximity to the exhalations, such as at Cava dei Selci. Notwithstanding the insistent recommendations based on out- and in-door measurements of toxic gases clearly highlighting the strong hazard posed by this situation, the political authorities have not found any exhaustive solution. After the installation of a CO_2 measurement station that was prematurely dismissed, the main emission zone, consisting of a depression corresponding to an old quarry discharging up to 25 tons/day and 84 kg/day of CO_2 and H2S, respectively, was fenced and then abandoned.

In April 2016, a research team from the University of Florence and WEST Systems Ltd. (Italy) carried out a fieldtrip in this area for investigating the air quality. The measurement strategy was thought to provide a snapshot of the concentrations in air of the main deep-originated gas compounds along a pattern passing through the urban settlement mostly exposed to the lethal gases. A crawler mobile and remote-controlled vehicle was able to cover in 2 hours a grid within the inhabited center of Cava dei Selci, bringing high-sensitivity and synchronized instruments set at high-frequency acquisition, including: 1) a Tunable Diode Laser Absorption Spectroscopy (TDLAS) combined with a Herriot cell (CH4); 2) an infrared spectrometer with OA-ICOS technology (CO); 3) a Licor Li-820 infrared spectrometer (CO_2); 4) a Thermo Scientific Model 450i gas analyzer (H2S and SO_2); 5) a Lumex RA-915M analyzer (Hg0); 6) a Garmin GPS and a Davis Vantage Vue Weather station (position and the main meteorological parameters, respectively).

The dataset, consisting of up to 7,000 measurement spots, showed that concentrations of CO_2, H2S, CH4, and CO in the study area were, at a first approximation, consistent, whereas those of SO_2 and Hg0, not present in significant amounts in the contaminating source, were randomly distributed. A more detailed comparison of the gas concentration peaks revealed that in most cases the spatial distribution of CH4 surprisingly showed significant differences with respect to those of CO_2 and CO. This suggests that even at a relatively short distance from the gas source CH4 in air is affected by oxidation processes, masking the effects of the physical parameters (e.g. wind direction) that typically control the spatial distribution of air pollutants. On the contrary, H2S, which is supposed to rapidly turn to SO_2 by photochemical processes once emitted into the air, was in strong relation with the oxygenated carbon-bearing gases.

Although these promising results need to be integrated with those from further surveys, the multi-instrumental approach that was adopted seems to be particularly efficient for investigations aimed to assess the quality of air in contaminated areas

Stable carbon and hydrogen isotopes in CH_4 and light alkanes in magmatic and hydrothermal emissions from Vulcano Island (southern Italy)

Andrea Ricci (1), Jens Fiebig (2), Franco Tassi (3,4), Orlando Vaselli (3,4), Christoph Schreiber (2), Chiara Caponi (3), Sven Hofmann (2), Francesco Capecchiacci (3,4)

(1) Department of Biological, Geological and Environmental Sciences, University of Bologna, Bologna, Italy, (2) Institut für Geowissenschaften, Goethe-Universität, Frankfurt am Main, Germany, (3) Department of Earth Sciences, University of Florence, Florence, Italy, (4) Institute of Geosciences and Earth Resources, National Research Council (IGG-CNR), Florence, Italy

Vulcano Island, whose last eruption dates back to 1888-1890, is the southernmost island of the Aeolian Archipelago (southern Italy), a subduction-related volcanic arc in the Southern Tyrrhenian Sea. The active volcanic cone, namely La Fossa, displays an intense fumarolic activity, mostly occurring in its north-western sector. The fumaroles are characterized by outlet temperatures up to ∼400 ˚C, and a typical magmatic composition with relatively high concentrations of HCl, HF and SO_2. A second fumarolic area in the island occurs at Baia di Levante, the bay delimiting the eastern side of a flat isthmus that connects Vulcano to Vulcanello. In this area, low temperature (≤ 100˚C) fumaroles and bubbling gases are discharged, displaying the typical hydrothermal-type composition, i.e. being characterized by relatively high contents of H_2S and hydrocarbons and by the absence of acid gas constituents. We have investigated the chemical and isotopic ($\delta^{13}C$ and δD) compositions of CH_4 and light alkanes (C_2H_6, C_3H_8, C_4H_{10}) of the fumaroles venting from both the crater and the bay area. To the best of our knowledge, the isotopic data of CH_4 from La Fossa crater presented in this work are the first ones on terrestrial high-temperature fumaroles ever reported. The main aim is to use these geochemical parameters to identify the fluid source(s) and the processes controlling the isotopic composition of the hydrocarbons. Our analytical results highlight that the δD–CH_4 values of gases from La Fossa crater are extremely depleted in deuterium (down to -657‰ vs. V-SMOW), whereas those of the beach fumaroles range from -100‰ to -85‰ vs. V-SMOW. The $^{13}C/^{12}C$ ratios of CH_4 and C_{2+} n-alkanes in the crater fumaroles also strongly differ from the isotopic signature measured in the hydrothermal gases, with the carbon isotopic composition of the low-temperature gases occurring significantly enriched in ^{13}C relative to the magmatic gases. Assuming a deep source for light hydrocarbon common to both the crater and the beach fumaroles, these preliminary data suggest the occurrence of not well defined secondary processes able to strongly modify their primary isotopic signature. Alternatively, two distinct hydrocarbon sources characterized by dramatically different $\delta^{13}C$ and δD values, feeding the magmatic and the hydrothermal emissions, respectively, are to be invoked to explain the observed data.

ASSOCIAZIONE ITALIANA DI VULCANOLOGIA
in collaboration with
Istituto Nazionale di Geofisica e Vulcanologia

International Meeting
"Rittmann Young Researchers"

Dipartimento di Scienze della Terra e Geoambientali, Bari, Italy
December 13 – 15, 2016

Registration Form
To be mailed before November 18th, 2016 to:
ornella.cocina@ingv.it

Name and given name: Chiara Caponi

Institution: Università degli Studi di Firenze, Dipartimento di Scienze della Terra

Address: Via G. la Pira, 4 (Firenze)

E-mail: chiaragcaponi@gmail.com

Position: Ph.D (Student)

Abstract of poster presentation (max. 2000 characters):

ABSTRACT

Impact of C- and S-volatile compounds on air quality in areas affected by anthropogenic and natural contamination
Caponi C., Tassi F., Vaselli O., Capasso G., Lelli M., Sciarra A., Minardi I..

Significant amounts of VOCs (in particular benzene, toluene, ethylbenzene and xylenes; BTEX) and S-bearing compounds, such as sulphur dioxide (SO_2) and hydrogen sulphide (H_2S), are released into the atmosphere from both natural manifestations (volcanic, hydrothermal systems) and anthropogenic activities (e.g. refineries, steel industries, road traffic), causing a strong impact on air quality, climate forcing and human health. The behaviour of BTEX, SO_2, H_2S in air is difficult to be predicted due to (i) the complexity of direct measurements of these pollutants in air, and (ii) scarcity of thermodynamic data that could be used to model the chemical-physical processes controlling the fate of these gases in the atmosphere once they are released from the emitting source(s). In the framework of a collaboration between public/private institutions (University of Florence, University of Palermo, WEST SYSTEMS s.r.l., IGG-CNR, INGV), this study was aimed to test a procedure for synchronous, real-time, high-frequency and high-sensitivity measurements of BTEX and S-bearing gases in air. Other geochemical parameters, such as CO_2, CH_4, CO, Hg^0, NO_x and $\delta^{13}C$-CO_2-CH_4 were also measured applying the same approach and used as geochemical tracers to better refine the recognition of natural/anthropogenic contaminant sources. Different analytical instruments were assembled on a unique measurement station, and then inter-calibrated and synchronized through tests carried out in different volcanic, hydrothermal and urban areas characterized by the occurrence of natural fluid emissions having a strong impact on air quality: Solfatara di Pozzuoli (Campi Flegrei), Vulcano Island (Aeolian Islands) and Cava dei Selci (Rome).

Preliminary results obtained during three surveys showed that by combining different geochemical parameters, the various contaminant sources can exhaustively be distinguished and quantified. The next step will be that to model the spatial distribution of air pollutants via a sophisticated elaboration of the measured geochemical data, carried out with specific software, in collaboration with the supercomputing centre of Barcelona (Spain).

List of Figures

References

Adelinet, Dorbath C., Le Ravalec M., Fortin J. and Guéguen Y. (2011). Deriving microstructure and fluid state within the Icelandic crust from the inversion of tomography data. Geophys. Res. Lett. 38, L03305.

Aitchison J. (1982). The statistical analysis of compositional data (with discussion). Journal of the Royal Statistical Society Series B, 44 (2), 139–177.

Aiuppa A., Bonfanti P., Brusca L., D'Alessandro W., Federico C. and Parello F. (2001). Evaluation of the environmental impact of volcanic emissions from the chemistry of rainwater: Mount Etna area (Sicily). Applied Geochemistry, 16, 985-1000.

Aiuppa A., Inguaggiato S., McGonigle A. J. S., O'Dwyer M., Oppenheimer C., Padgett M. J., Rouwet D. and Valenza M. (2005a). H_2S fluxes from Mt. Etna, Stromboli and Vulcano (Italy) and implications for the global volcanic sulfur budget, Geochim. Cosmochim. Acta, 69, 1861–1871.

Aiuppa A., Franco A., Von Glasow R., Allen A. G., D'Alessandro W., Mather T. A., Pyle D. M. and M. Valenza (2006). The tropospheric processing of acidic gases and hydrogen sulphide in volcanic gas plumes as inferred from field and model investigations. Atmos. Chem. Phys. Discuss., 6, 11653–11680.

Aiuppa A., Federico C., Giudice G., Giuffrida G., Guida R., Guerrieri S., Liuzzo M., Moretti R. and Papale P. (2009). The 2007 eruption of Stromboli volcano; insights from real-time measurement of the gas volcanic plume CO2/SO2 ratio. J. Volcanol. Geotherm. Res. 182, 221–230.

Aiuppa A., Shinohara H., Tamburello G., Giudice G., Liuzzo M., Moretti R. (2011). Hydrogen in the gas plume of an open-vent volcano, Mount Etna, Italy. Journal of Geophysical Research, Vol. 116.

Ahrens L. H. (1954). The lognormal distribution of the elements a fundamental law of geochemistry and its subsidiary. Geochimica et Cosmochimica Acta, 6, 49–74.

Akdeniz N., Janni K. A., and Salnikov I. A. (2011). Biofilter Performance of Pine Nuggets and Lava Rock as Media, Bioresource Technol., 102, 4974–4980.

Al-Awadhi J.M. (2014). Measurement of air pollution in Kuwait city using passive samplers. Atmos. Clim. Sci. 4, 253e271.

Armienti P., Barberi F., Bizouard H., Clocchiatti R., Innocenti F., Métrich, N., Rosi, M. and Sbrana A. (1983). The Phlegrean Fields: magma evolution within a shallow chamber. In: Explosive Volcanism. J. Volcanol. Geotherm. Res. 17, 289–311.

Ármannsson H., Gudmundsson Á. and Steingrimsson B.S. (1987). Exploration and development of the Krafla geothermal area. Jokull, 37: 13-29.

Ármannsson H., Benjamínsson J. and Jeffrey A. W. A. (1989). Gas changes in the Krafla geothermal system, Iceland. Chem. Geol. 76, 175-196.

Ármannsson H. (1998). Oxarfjordur: Studies of Gas (In Icelandic). Orkustofnun OS- 98051, p. 14.

Ármannsson H. (1993). The Namafjall Geothermal System. An Overview of its Chemistry (In Icelandic). Orkustofnun OS-93053/JHD-29 B, p. 30.

Ármannsson H. (2011). EIA – example from Bjarnaflag in Iceland. University of Iceland, geothermal resources (JAR218), lecture notes.

Ármannsson H. (2015). The fluid geochemistry of Icelandic high temperature geothermal areas. Appl. Geochem. 66, 14–64.

Ármannsson H. (2016). The fluid geochemistry of Icelandic high temperature geothermal areas. Applied Geochemistry 66 , 14-64.

Árnason K., Haraldsson G. I., Johnsen G. V., Þorbergsson G., Hersir G. P., Sæmundsson K., Georgsson L. S., Rögnvaldsson S. Th. and Snorrason S. P. (1987a). Nesjavellir-Ölkelduháls. Surface Exploration in 1986. Orkustofnun Report OS- 87018/JHD-02, Reykjavik, Iceland, 112 pp. (in Icelandic).

Árnason K., Flóvenz Ó., Georgsson L. and Hersir G. P. (1987b). Resistivity structure of high-temperature geothermal systems in Iceland. In: International Union of Geodesy and Geophysics (IUGG) XIX General Assembly, Vancouver Canada, August 1–22, p. 477 (abstract V).

Árnason K., Eysteinsson H. and Hersir G. P. (2010). Joint 1D inversion of TEM and MT data and 3D inversion of MT data in the Hengill area, SW Iceland. Geothermics 39: 13–34.

Arnórsson S., Guðmundsson G, Sigurmundsson S, G., Björnsson A., Gunnlaugsson E., Gíslason G., Jónsson J., Einarsson P., Björnsson S. (1975). Systematic exploration of the Krísuvík high-temperature area, Reykjanes Peninsula, Iceland. Report, National Energy Authority, Reykjavik, Iceland. OS/JHD 7554, 127 pp.

Arnórsson S. (1978). Major element chemistry of geothermal sea-water at Reykjanes and Svartsengi, Iceland. Min. Mag. 42, 209-220.

Arnórsson S., Sigurdsson S. and Svavarsson H. (1982). The chemistry of geothermal waters in Iceland. I. Calculation of aqueous speciation from $0°C$ to 370 °C. Geochimica et Cosmochimica Acta 46, 1513-1532.

Arnórsson S., Gunnlaugsson E. and Svavarsson H. (1983). The chemistry of geothermal waters in Iceland. II. Mineral equilibria and independent variables controlling water compositions. Geochim. cosmochim. Acta 47, 547-566.

Arnórsson S. (1985). The use of mixing models and chemical geothermometers for estimating underground temperatures in geothermal systems. J. Volc. geotherm. Res. 23, 299-335.

Arnórsson S. and Gunnlaugsson E. (1985). New gas geothermometers for geothermal exploration - calibration and application. Geochim Cosm Acta, 49, 1307-1325.

Arnórsson S. (1987). Gas chemistry of the Krísuvík geothermal field, Iceland, with special reference to eveluation of steam condensation in upflow zones. Jökull 37, 30–47.

Arnórsson S. (1995). Geothermal systems in iceland: structure and conceptual models I. High-temperature areas. Geothermics, Vol. 24, No. 5/6, pp. 561-602.

Arnórsson S., Stefánsson A. and Bjarnason J. O. (2007). Fluid–fluid interactions in geothermal systems. Rev. Mineral. Geochem. 65, 259–312.

Arnórsson S., Angcoy E., Bjarnason J. Ö., Giroud N., Gunnarsson I., Kaasalainen H., Karingithi C., Stefánsson A. (2010). Gas chemistry of volcanic geothermal systems. Proceedings World Geothermal Congress, Bali Indonesia, 25-29 April.

Atkinson R., Balulch D. L., Cox R. A., Hampson R. F., Kerr J. A. and Troe J. (1992). Evaluated Kinetic and Photochemical Data for Atmospheric

Chemistry Supplement IV. IUPAC Subcommittee on Gas Kinetic Data Evaluation for Atmospheric Chemistry. J. Phys. Chern. Ref. Data, Vol. 21, No.6, 1125-1568.

Azzalini A. and Capitanio A. (1999). Statistical applications of the multivariate skew-normal distribution. Journal of the Royal Statistical Society, Series B, 61 (3), 579–602.

Badalamenti B., Liotta M., Valenza M. (2001). An automatic system for continuous monitoring of CO_2, H_2S, and SO_2 and meteorological parameters in the atmosphere of volcanic areas. Geochem. Trans. 5.

Balls P.W. and Liss, P.S. (1983). Exchange of H_2S between water and air. Atmospheric Environment 17, 735-742.

Barberi F., Corrado G., Innocenti F. and Luongo G. (1984). Phlegraean Fields 1982-1984: brief chronicle of a volcano emergency in a densely populated area. Bull. Volcanol. 47, 175-185.

Barberi F., Gandino A., Gioncada A., La Torre P., Sbrana A. and Zenucchini C. (1994). The deep structure of the Aeolian Arc (Filicudi-Panarea-Vulcano sector) In light of gravity magnetic and volcanological data. J. Volcanol. Geotherm. Res., 61, (3/4), 189-206.

Barnes I., Bastian V., Becker K. H., Fink E. H. and Nelson W. (1986). Kinetics and mechanisms of the reaction of OH radicals with dimethyl sulfide. J. Atmos. Chern. 4, 445.

Barth T. F. W. (1940). Geysir in Iceland. Americal Journal of Science Vol. 238, No 6.

Bates T.S., Lamb B.K., Guenther A., Dignon J. and Stoiber R.E. (1992). Sulfur emissions to the atmosphere from natural sources. Journal of Atmospheric Chemistry 14, 315–337.

Bates M. N., Garrett N. and Shoemack P. (2002). Investigation of health effects of hydrogen sulfide from a geothermal source. Archives of environmental health 57, 405-411.

Beblo M., Björnsson A., Arnason K., Stein B. and Wolfgram P. (1983). Electrical conductivity beneath Iceland: Constraints imposed by magnetotelluric results on temperature, partial melt, crust and mantle structure. J. Geophys. 53, 16-23.

Bellucci F. (2003). Geochimica di alcuni elementi in tracce nei condensati fumarolici dell'Isola di Vulcano. Tesi di Laurea in Scienze Geologiche,

Università degli Studi di Firenze.

Benkowitz C.M., Scholtz M.T., Pacyna J., Tarrason L., Dignon J., Voldner E.C., Spiro P.A., Logan J.A. and Graedel T.E. (1996). Global gridded inventories of anthropogenic emissions of sulfur and nitrogen. J. Geophys. Res., 101, 29239-29253.

Bernard N.L., Gerber M.J., Astre C.M. and Saintot M.J. (1999). Ozone measurement with passive samplers: validation and use for ozone pollution assessment in mont- pellier, France. Environ. Sci. Technol. 33, 217-222. http://dx.doi.org/10.1021/ es971140k.

Björnsson A., Saemundsson K., Einarsson P., Tryggvason E. and Grjönvold K. (1977). Current rifting episode in north Iceland. Nature 266, 318-323.

Björnsson A., Johnsen G., Sugurdsson S. and Thorbergsson G. (1979). Rifting of the plate boundary in North Iceland 1975-1978. J. Geophys. Res, 84, 30129-3038.

Björnsson A. (1985). Dynamics of crustal rifting in NE Iceland. J. Geophys. Res. 90, 151-162.

Björnsson G. and Steingrimsson B. (1991). Temperature and pressure in the Svartsengi geothermal system. Initial state and changes caused by exploitation. National Energy Authority Report OS-91016/JHD-IM, 119 pp. [in Icelandic].

Björnsson G., Hjartarson A., Bodvarsson G.S., Steingrimsson B. (2003). Development of a 3-D geothermal reservoir model for the Greater Hengill volcano in SW-Iceland. In: Proceedings, TOUGH Symposium. Lawrence Berkeley National Laboratory, Berkeley, CA.

Björnsson G., Olafsson M., Jonsson H. and Magnusson T.M. (2004). Production studies of wells RN-9, RN-10 and RN-12 in Reykjanes (2002-2004). Iceland GeoSurvey Report- ISOR-2004/2019.

Björnsson G., Gunnlaugsson E. and Hjartarson A. (2006). Applying Hengill geothermal in model in power plant decision making an environmental impact studies. In: TOUGH Symposium 2006.

Björnsson G. (2007). A Revised Conceptual Model of Hengill Geothermal Systems and a Simple Assessment of the Production Capacity of New Drillfields (In Icelandic) Orkuveita Reykjavíkur (Reykjavík Energy). Report No. 2007-3, p. 65.

Björnsson S., Arnorsson S. and Tomasson J. (1970). Exploration of the Reykjanes thermal brine area. Geothermics special issue 2, 1640–1650.

Björnsson S., Arnorsson S. and Tomasson J. (1972).Economic evaluation of the Reykjanes thermal brine area, Iceland. Bull. Am. Assoc. Petrol. Geol. 56, 2380-2391.

Blunden J. and Aneja V. P. (2008). Characterizing Ammonia and Hydrogen Sulfide Emissions from a Swine Waste Treatment Lagoon in North Carolina, Atmos. Environ., 42, 3277–3290.

Bluth G. J. S., Schnetzler C. C., Kreuger A. J. and Walter L. S. (1993). The contribution of explosive volcanism to global sulfur dioxide concentrations. Nature 366, 327–329.

Böðvarsson G. (1961). Physical characteristics of natural heat resources in Iceland. Jökull 11, 29-38.

Böðvarsson G. and Pruess K. (1984). The Krafla Geothermal Field, Iceland 2. The Natural State of the System. Water Resources Research, vol 20, No.11, 1531-1544.

Böðvarsson G., Bjornsson S., Gunnarsson A., Gunnlaugsson E., Sigurdsson O., Stefansson V., Steingrimsson B. (1990). The Nesjavellir geothermal field, Iceland. Part 1. Field characteristics and development, of a three-dimensional numerical model. Geotherm Sci & Tech 2(3): 189–228

Bolognesi L. and D'Amore F. (1993). Isotopic variation of the hydrothermal system on Vulcano Island, Italy. Geochim. Cosmochim. Acta 57, 2069-2082.

Bottenheim J. W. and Strausz O. P. (1980).Gas-phase chemistry of clean air at 55°N latitude. Environmental Science & Technology 14, 709-718.

Bourque C. (1996).Simulating sulfur dioxide plume dispersion and subsequent deposition downwind from a stationary point source: A model. Arp, P. Environ. Pollut. 91, 363-380.

Brandsdóttir B., Menke W., Einarsson P., White R. S. and Staples R. K. (1997). Faroe-Iceland Ridge Experiment 2. Crustal structure of the Krafla central volcano, J. Geophys. Res., 102, 7867–7886.

Brown K. L. and Webster J. G. (1994). H_2S oxidation in aerosols. In: Proceedings 15th PNOC- EDC Geothermal Conference, 37-44.

Brown R. H. (2000). Monitoring the ambient environment with diffusive samplers: theory and practical considerations. J. Environ. Monit. 2, 1-9.

Buccianti A. and Pawlowsky-Glahn V. (2005). New perspectives on water chemistry and compositional data analysis. Mathematical Geology, 37 (7), 703 – 727.

Buccianti A., Mateu-Figueras G. and Pawlowsky-Glahn V. (2006). Frequency distributions and natural laws in geochemistry. Compositional Data Analysis in the Geoscience: From Theory to Practice. Geological Society, London, Special Publications, 264: 175-189 pp.

Byanju R.M., Gewali M.B. and Manandhar K. (2012). Passive sampling of ambient nitrogen dioxide using local tubes. J. Environ. Prot. 3, 177-186.

Caliro S., Chiodini G., Moretti S., Avino R., Granieri D., Russo M. and Fiebig, J. (2007). The origin of the fumaroles of La Solfatara (Campi Flegrei, south Italy). Geochim. Cosmochim. Acta 71, 3040-3055.

Campos V.P., Cruz L.P.S., Godoi R.H.M., Godoi A.F.L., Tavares T.M., (2010). Development and validation of passive samplers for atmospheric monitoring of SO_2, NO_2, O_3 and H_2S in tropical areas. Microchem. J. 96 (1), 132-138. http://dx.doi.org/10.1039/b104622p.

Capaccioni B., Martini M., Mangani F., Giannini L., Nappi G. and Prati F. (1993). Light hydrocarbons in gas emissions from volcanic areas and geothermal fields. Geochem. J., 27, 7-17.

Capaccioni B., Martini M. and Mangani F. (1995). Light hydrocarbons in hydrothermal and magmatic fumaroles: hints of catalytic and thermal reactions. Bull. Volcanol., 56, 593-600.

Capaccioni B., Tassi F., Vaselli O. (2001). Organic and inorganic geochemistry of low temperature gas discharges at the Baia di Levante beach, Vulcano Island, Italy. J. Volcanol. Geotherm. Res. 108, 173-185 pp.

Capasso G., Dongarrà G., Hauser S., Favara R. and Valenza M. (1992). Isotope composition of rain water, well water, and fuma- role steam on the island of Vulcano, and their implications for volcanic surveillance. J. Volcanol. Geoth. Res. 49, 147-155.

Capasso G., Favara R. and Inguaggiato S. (1997). Chemical features and isotopic gaseous manifestation on Vulcano Island (Aeolian Island): an interpretative model of fluid circulation. Geochim. Cosmochim. Acta 61, 3425–3442.

Carapezza M., Nuccio P. M. and Valenza M. (1981). Genesis and Evolution of the Fumaroles of Vulcano (Aeolian Islands, Italy): a Geochemical

Model. Bull. Volcanol. Vol. 44-3.

Carapezza M., Dongarrà G., Hauser S. and Longinelli A. (1983) Preliminary isotopic investigations on thermal waters from Vulcano Island, Italy. Mineral. Petrogr. Ada 27, 22 l-232.

Carapezza M.L., Badalamenti B., Cavarra L. and Scalzo A. (2003). Gas hazard assessment in a densely inhabited area of Colli Albani volcano (Cava dei Selci, Roma). J. Volcanol. Geotherm. Res. 23, 81–94.

Carroll M. R. and Webster J. D. (1994). Solubilities of sulfur, noble gases, nitrogen, chlorine and fluorine in magmas. In Volatiles in Magmas (ed. M. R. Carroll and J. R. Halloway), pp. 231–279, Mineralogical Society of America.

Cheng L., Peake E. and Davis A. (1987). The Rate of SO2 to Sulfate Particle Formation in an Air Parcel from an Oil Sands Extraction Plant Plume. Atmos. Environ. 37: 163-167.

Chiodini G., Cioni R., Guidi M., Marini L. (1991). Geochemical variations at Fossa Grande crater fumaroles (Vulcano Island, Italy) in summer 1988. Acta Vulcanol 1: 179-192.

Chiodini G., Cioni R., Falsaperla S., Montalto A., Guidi M. and Marini L. (1992a). Geochemical and seismological investigations at Vulcano (Aeolian Islands) during 1978-1989. J Geophys Res 97:11025-11032.

Chiodini G., Cioni R., Guidi M., Marini L., Raco B. and Taddeucci G. (1992b). Gas geobarometry in boiling hydrothermal systems: a possible tool to evaluate the hazard of hydrothermal explosions. Acta Vulcanol., 2, 99-107.

Chiodini G., Cioni R., Marini L., Raco B. and Taddeucci G. (1993). Vulcano and Stromboli; gas geochemistry; fumarolic gases geochemistry. Acta Vulcanol., 3, 280-282.

Chiodini G. (1994). Temperature, pressure and redox conditions governing the composition of the cold CO2 gases discharged in north Latium (central Italy), Appl. Geochem., 9, 287–295.

Chiodini G., Cioni R., Marini L. and Panichi C. (1995). Origin of the fumarolic fluids of Vulcano Island, Italy and implications for volcanic surveillance. Bull. Volcanol. 57: 99-110.

Chiodini G., Cioni R., Magro G., Marini L., Panichi C., Raco B. and Russo M. (1996). Chemical and isotopic variations of Bocca Grande fumarole (Solfatara volcano, Phlegrean Fields). Acta Vulcanol. 8, 129–138.

Chiodini G. and Marini L. (1998). Hydrothermal gas equilibria; the H_2O –H_2 –CO_2 –CO– CH_4 system. Geochim. Cosmochim. Acta 62(15), 2673–2687.

Chiodini G., Frondini F., Cardellini C., Parello F. and Peruzzi L. (2000). Rate of diffuse carbon dioxide Earth degassing estimated from carbon balance of regional aquifers: the case of central Apennine, Italy. J. Geophys. Res. 105, 8423–8434.

Chiodini G., Frondini F., Cardellini C., Granieri D., Marini L. and Ventura G. (2001). CO_2 degassing and energy release at Solfatara volcano, Campi Flegrei, Italy. Journal of Geophysical Research, v. 106, no. B8, p. 16213–16221.

Chiodini G., Todesco M., Caliro S., Del Gaudio C., Macedonio G. and Russo M. (2003). Magma degassing as a trigger of bradyseismic events; the case of Phlegrean Fields (Italy). Geophysical Research Letters, v. 30, 1434.

Chiodini G., Granieri D., Avino R., Caliro S., Costa A. and Werner C. (2005). Carbon dioxide diffuse degassing and estimation of heat release from volcanic and hydrothermal systems, J. Geophys. Res., 110, B08204, doi:10.1029/2004JB003542.

Cihacek L. J. and Bremner J. M. (1993). Characterization of the sulfur retained by soils exposed to hydrogen sulfide. Communications in Soil Science and Plant Analysis, 24, 85–92.

Cioni R. and D'Amore F. (1984). A genetic model for the crater fumaroles of Vulcano Island (Sicily, Italy). Geothermics 13:375-384.

Cioni R., Corazza E., Fratta M., Guidi M., Magro G. and Marini L. (1989). Geochemical precursors at Solfatara Volcano, Pozzuoli (Italy). In Volcanic Hazard (ed. J. H. Latter). Springer Verlag, Berlin, pp. 384–398.

Cocks A. T., Kallend S. and Marsh A. R. W (1983). Dispersion limitations of oxidation in power plant plumes during long-range transport. Nature, 305: 122-123.

Cook A. and Weinstein P. (2011). Volcanic and Geothermal Processes: Health Effects. Reference Module in Earth Systems and Environmental Sciences - Encyclopedia of Environmental Health, pp. 664-671.

Colomer F. L., Morato H. E. and Iglesias E. M. (2012). Estimation of hydrogen sulfide emission rates at several wastewater treatment plants through experimental concentration measurements and dispersion modeling. J. Air & Waste Manag. Assoc. 62 (7), 758-766.

Cox R. A. and Sandalls F. J. (1974). The photo-oxidation of hydrogen sulphide and dimethyl sulphide in air. Atmospheric Environment 8, 1269-1281.

Cox R. A. and Sheppard D. (1980). Reactions of OH radicals with gaseous sulphur compounds. Nature 284, 330–331.

D'Alessandro W., Brusca L., Kyriakopoulos K., Michas G. and Papadakis G. (2009). Hydrogen sulphide as a natural air contaminant in volcanic/ geothermal areas: the case of Sousaki, Corinthia (Greece). Environmental Geology 57 (8), 1723–1728 http:// dx.doi.org/10.1007/s00254-008-1453-3.

D'Alessandro W., Aiuppa A., Bellomo S., Brusca L., Calabrese S., Kyriakopoulos K., Liotta M. and Longo M. (2013). Sulphur-gas concentrations in volcanic and geothermal areas in Italy and Greece: Characterising potential human exposures and risks. Journal of Geochemical Exploration Volume 131, 1-13.

D'Amore F., Giusti D. and Gizaw B. (1997). Tendaho, Ethiopia. Geothermal Project: a Geochemical Assessment. Proceedings 22nd Workshop Geothermal Reservoir Engineering, Stanford, January 27-29, pp. 435-445.

Darling W. G. (1998). Hydrothermal hydrocarbons gases: 1. Genesis and geothermometry. Appl. Geochem., 13, 815-824.

Davis G. H. (1966). Frequency distribution of dissolved solids in ground water. Ground Water 4:5.

Davis D. D., Ravishankara A. R. and Fischer S. (1979). SO2 oxidation via the hydroxyl radical at- mospheric fate of HSOx radicals. Geophys. Res. Lett. 6, 113–116.

De Astis G. (1995). Evoluzione vulcanologica e magmatologica dell' isola di Vulcano (IsoleEolie), Ph.D. thesis, Dip. Geomineral. Univ. di Bari, Bari, Italy.

De Kok L. J., Maas F. M., Stulen I. and Juiper P. J. C. (1988). Sulfur containing air pollutants and their effects on plant metabolism. Commission of European Communities, 11244, 620–625.

Delmelle P., Stix J., Bourque C. P. A., Baxter P., Garcia-Alvarez, J. and Barquero J. (2001). Dry deposition and heavy acid loading in the vicinity of Masaya volcano, a major sulfur and chlorine source in Nicaragua. Environmental Science & Technology, 7, 1289-1293.

Delmelle P. (2003). Environmental impacts of tropospheric volcanic plumes. In: Oppenheimer, C., Pyle, D.M., Barclay, J. (Eds.), Volcanic Degassing. Geological Society of London, pp. 381–389.

Delgado-Saborit J.M., Esteve-Cano V. (2006). Field study of diffusion collection rate coefficients of a NO_2 passive sampler in a Mediterranean coastal area. Environ. Monit. Assess. 120, 327-345.

Des Marais D. J., Donchin J. H., Truesdell A. H. and Nehring N. L. (1981). Molecular carbon isotopic evidence for the origin of geothermal hydrocarbons. Nature, 292, 826-828.

Devine J. D., Sigurdsson H., Davis A. N. and Self S. (1984). Estimates of sulfur and chlorine yield to the atmosphere from volcanic eruptions and potential climatic effects. Journal of Geophysical Research, v. 89, p. 6309-6325.

Di Vito M. A., Lirer L., Mastrolorenzo G. and Rolandi G. (1987). The 1538 Monte Nuovo eruption (Campi Flegrei, Italy). Bull. Volcanol. 49, 608-615.

Didana Y. L. (2010). Multidimensional Inversion of MT Data from Krýsuvík High Tempera- ture Geothermal Field, SW-Iceland, and a Study of how 1D and 2D Inversion can Re- produce a Given 2D/3D Resistivity Structure Using Synthetic MT Data. Unpublished MS Thesis. University of Iceland, Reykjavik, p. 119.

Dvorak J. J. and Berrino G. (1991). Recent ground movement and seismicity activity in Campi Flegrei, Southern Italy: episodic growth of a resurgent dome. J. Geophys. Res. 96, 2309-2323.

Dvorak J. J. and Gasparini P. (1991). History of earthquakes and vertical ground movements in Campi Flegrei caldera, Southern Italy: a comparison of precursor events to the A.D. eruption of Monte Nuovo and of activity since 1968. J. Volcanol. Geotherm. Res. 48, 77-92.

Dvorak J. J. and Mastrolorenzo G. (1991). The mechanisms of recent vertical crustal movements in Campi Flegrei Caldera, southern Italy, Special Paper – Geological Society of America, 263, 47.

Eatough D. J., Hansen L. D., Izatt R. M. and Mangelson N. F. (1977). Analysis of Sulfite Species in Aerosols. A.C.S. Abstracts, Division of Enviromental Chemistry, 173rd Annual Meeting, New Orleans, March 20-27, pp. 57-60.

Eatough D. J., Caka F. M. and Farber R. J. (1994). The conversion of SO2 to sulphate in the atmosphere. Isr. J. Chem. 34, 301–314.

Eggleton A. E. J. and Cox R. A. (1978). Homogeneous oxidation of sulphur compounds in the atmosphere. Atmospheric Environment 12, 227-230.

Einarsson P. (1978). S-wave shadows in the Krafla caldera in NE-Iceland, evidence for a magma chamber in the crust. Bull. Volcanol.,41, 187 – 195.

Einarsson P. (1989). lntraplate earthquakes in Iceland. In Earthquakes at North Atlantic Passive Margins: Neotectonic and Postglacial Rebound (Edited by Gregersen, S. and Basham, P. W.), pp. 329-344. Kluwer, Dordrecht.

Einarsson P. (1991). Earthquakes and present-day tectonism in Iceland. Tectonophysics 189, 261-279.

Einarsson P. (2008). Plate boundaries, rifts and transforms in Iceland. Jökull 58, 35-58.

Elders W., Friðleifsson G. O., Zierenberg R. A., Pope E. C., Mortensen A. K., Guðmundsson Á., Lowenstern J. B. Marks N. E., Owens L., Bird D. K., Reed M., Nellie J. O. and Schiffman P. (2011). Origin of a rhyolite that intruded a geothermal well while drilling at the Krafla volcano, Geology, 39, 231–234.

Ellam R. M., Menzies M. A., Hawkesworth C. J., Leeman W. P., Rosi M. and Serri G. (1988). The transition from calc-alkaline to potassic orogenic magmatism in the Aeolian Islands, southern Italy, Bull. Volcanol., 50, 386-398.

Erickson R. E., Yates L. M., Clark R. L. and McEwen D. (1977). The reaction of sulfur dioxide with ozone in water and its possible atmospheric significance. Atmos. Environ. 11, 813-817.

Ewart J. A., Voight B. and Björnsson A. (1991). Elastic deformation models of Krafla Volcano, Iceland, for the decade 1975 through 1985. Bull. Volcanol. 53, 436–459.

Federico C., Capoasso G., Paonita A. and Favara R. (2010).Effects of steam-heating processes on a stratified volcanic aquifer: Stable isotopes and dissolved gases in thermal waters of Vulcano Island (Aeolian archipelago). Journal of Volcanology and Geothermal Research 192 (2010) 178–190.

Ferrucci F., Gaudiosi G., Milano G., Nercessian A., Vilardo G. and Luongo G. (1991). Seismological exploration of Vulcano (Aeolian Islands, southern Tyrrhenian Sea): case history, Acta Vulcanol. 1. 143–152.

Finlayson-Pitts B. J. and Pitts J. N. Jr. (1986). Atmospheric Chemistry: Fundamentals and Experimental Techniques. Wiley, New York.

Finlayson-Pitts B. J. and Pitts J. N. (2000). Chemistry of the upper and lower atmosphere. USA: Academic Press.

Fisher T. P. and Chiodini G. (2015). Chapter 45 - Volcanic, Magmatic and Hydrothermal Gases. The Encyclopedia of Volcanoes, Pages 779-797.

Flores M.I., Ray J.D. and Joseph D.B. (1996). Passive Sampling Devices: a Cost-effective Method of Obtaining Air Quality Data in Protected Areas. National Park Ser- vice Strategic Plan, Final Draft, NPS D-1151, September 1996.

Flóvenz Ó. G. and Sæmundsson K. (1993). Heat flow and geothermal processes in Iceland. Tectonophysics 225, 123-138.

Foulger G. R. (1988a). The Hengill triple junction, SW Iceland: 1. Tectonic structure and the spatial and temporal distribution of local earthquakes. J. Geophys. Res., 93: 493-506.

Foulger G. R. (1988b). The Hengill triple junction, SW Iceland: 2. Anomalous earthquake focal mechanisms and implications for process within the geothermal reservoir and at accretionary plate boundaries. J. Geophys. Res., 93: 507-523.

Foulger G. R. and Toomey D. R. (1989). Structure and evolution of the Hengill-Grensdalur central volcano complex, Iceland: Geology, geophysics and seismic tomography. J. Geophys. Res., 94: 17511-17522.

Foulger G. R. and Arnott. S. A. (1993). Local Tomography: volcanoes and the accretionary plate boundary in Iceland. In: H.M. lyer and K. Hirahara (Editors), Seismic Tomography: Theory and Practice. Chapman and Hall, London, pp. 644-675.

Fournier R. O. (1989). Geochemistry and dynamics of the Yellowstone National Park hydrothermal system. Annu. Rev. Earth Planet. Sci., 17, 13-53.

Francis P., Burton M. R. and Oppenheimer C. (1998). Remote measurements of volcanic gas compositions by solar occultation spectroscopy. Nature 396, 567–570.

Franzson H., Thordarson S., Bjornsson G., Gudlaugsson S. Th., Richter B., Fridleifsson G.O. and Thorhallsson S., (2002). Reykjanes high-temperature field SW-Iceland. Geology and hydrothermal alteration of well RN-10. In:

Proceedings of the 27th Workshop Geothermal Reservoir Engineering, Stanford University.

Franzson H., Kristjánsson B. R., Gunnarsson G., Björnsson G., Hjartarson A., Steingrímsson B., Gunnlaugsson E. and Gíslason G. (2005). The Hengill–Hellisheiði geothermal field. Development of a conceptual model. In: Proceedings World Geothermal Congress 2005.

Franzson H., Gunnlaugsson E., Arnason K., Saemundsson K., Steingrimsson B., Hardarson B.S. (2010). The Hengill geothermal system, conceptual model and- thermal evolution. In: World Geothermal Congress, Bali, Indonesia.

Freedman B. and Hutchinson T.C. (1980). Pollutant inputs from the atmosphere and accumulations in soils and vegetation near a nickel-copper smelter at Sudbury, Ontario, Canada. Canadian Journal of Botany, 58, 108-132.

Freiberg J. (1975).The mechanism of iron catalyzed oxidation of SO2 in oxygenated solution. Atmospheric Environment 9, 661-672.

French S.W. and Romanowicz B. (2015). Broad plumes rooted at the base of the Earth's mantle beneath major hotspots. Nature 525, 95–99.

Frenklach M., Lee J. H. White J. N. and Gardiner W. C. (1981). Oxidation of hydrogen sulfate. Combustion and Flame, 41, 1,16.

Friðleifsson I. B. (1979). Geothermal activity in Iceland. jokull 29, 47-56.

Friðleifsson G. Ó. and Richter B (2010). The geological significance of two IDDP-ICDP spot cores from the Reykjanes geothermal field, Iceland. In: Proceedings of the World Geothermal Congress 2010, Bali, Indonesia, p. 6. Also available at: www. iddp.is.

Friðleifsson G. Ó., Albertsson A., Elders W. A., Sigurdsson Ó., Karlsdóttir R., Pálsson B. (2011). The Iceland deep drilling project (IDDP): planning for the second deep well at Reykjanes. Geotherm. Resour. Counc. Trans. 35, 347–354.

Friðleifsson G.Ó., Sigurdsson Ó., Þorbjörnsson D., Karlsdóttir R., Gíslason Þ., Albertsson A., Elders W.A. (2014). Preparation for drilling well IDDP-2 at Reykjanes. Geothermics 49, 119–126 (Iceland Deep Drilling Project:The first well, IDDP-1, drilled into Magma).

Fridriksson Th., Kristjansson B. R., Armannsson H., Margretardottir E., Olafsdottir S. and Chiodini G. (2006). CO_2 emissions and heat flow through

soil, fumaroles, and steam heated mud pools at the Reykjanes geothermal area, SW Iceland. Appl. Geochem. 21, 1551–1569.

Fridriksson Th., Stefánsson A., Óskarsson F., Eyjólfsdóttir E. and Sigurðsson Ó. (2015). Fluid chemistry scenarios anticipated for IDDP-2 to be drilled in Reykjanes, Iceland. Proc. World Geothermal Congress (8 pp.).

Friedlander S. K. (1977). Smoke, Dust, and Haze: Fundamentals of Aerosol Behavior. Wiley, New York.

Galle B., Oppenheimer C., Geyer A., McGonigle A. J. S., Edmonds M. and Horrocks L. A. (2003). A miniaturised ultraviolet spectrometer for remote sensing of SO2 fluxes: a new tool for volcano surveillance. J. Volcanol. Geotherm. Res. 119, 241–254.

Gallegos-Ortega R., Quintero-Nuñez M. and García-Cueto O. (2000). H2S dispersion model at Cerro Prieto geothermoelectric power plant in Mexico. World Geothermal Congress 2000, Kyushu - Tohoku, Japan, 579-584.

Gebrehiwot K. (2005). Geothermal mapping in western Ölkelduháls field, Hengill area, SW-iceland. Geothermal training programme, The United Nations University, Internal reports, 7.

Geilert S., Vroon P. Z., Keller N. S., Gudbrandsson S., Stefánsson A. and Van Bergen M. J. (2015). Silicon isotope fractionation during silica precipitation from hot-spring waters: evidence from the Geysir geothermal field, Iceland. Geochim. Cosmochim. Acta 164, 403–427.

Gerlach T. M. and Nordlie B. E. (1975). The C-O-H-S gaseous system, Part II: temperature, atomic composition and molecular equilibrium in volcanic gases. Am. J. Sci. 275, 377–394.

Gerlach T. M., Westrich H. R. and Symonds R. B. (1996). Preeruption Vapor in Magma of the Climactic Mount Pinatubo Eruption: Source of the Giant Stratospheric Sulfur Dioxide Cloud. FIRE and MUD contents: Eruptions and Lahars of Mount Pinatubo, Philippines.

Gerlach T. M. (2004). Volcanic sources of tropospheric ozone-depleting trace gases. Geochem. Geophys. Geosyst., 5, Q09007.

Giggenbach W.F. (1975b). A simple method for the collection and analysis of volcanic gas samples. Bull. Volcanol. 39, 132-145.

Giggenbach W.F. (1980). Geothermal gas equilibria. Geochim. Cosmochim. Acta 44, 2021-2032.

Giggenbach W.F. (1981). Geothermal mineral equilibria. Geochim. Cosmochim. Acta 45, 393-410.

Giggenbach W. F., Martini M. and Corazza E. (1986). The effects of hydrothermal processes on the chemistry of some recent volcanic gas discharges. Per. Mineral., 55, 15-28.

Giggenbach W.F. (1987). Redox processes governing the chemistry of fumarolic gas discharges from White Island, New Zealand. Applied Geochem., Vol. 2. pp. 143-161.

Giggenbach W.F. (1996). Chemical composition of volcanic gases. In: Monitoring and Mitigation of Volcano Hazards, Springer, Berlin, Heidelberg pp 221-256.

Gíslason G. (2000) Nesjavellir co-generation plant, Iceland. Flow of geothermal steam and non- condensable gases. Proceedings of World Geothermal Congress 2000, Kyushu-Tohoku, Japan, 585- 590.

Goff F. and Janik C.J. (2000). Geothermal systems. In: Sigurdsson H., Houghton B., McNutt S.R., Rymer H., Stix J. (Eds.), Encyclopedia of Volcanoes. Vol. 2000. Academic Press, San Diego, California, pp. 817–834.

Graedel T. E. (1977a). The homogeneous chemistry of atmospheric sulfur. Rev. Geophys Space Phys., 15, 421-428.

Graedel T. E., (1977b). The oxidation of ammonia, hydrogen sulfide, and methan in nonurban troposphere. J. Geophys. Res., 82, 5917-5922.

Garavelli A., Laviano R. and Vurro F. (1997). Sublimate deposition from hydrothermal fluids at the Fossa crater - Vulcano, Italy. European Journal of Mineralogy, 9, 423–432.

Gudiksen P.H. (1979). The potential air quality impact of geothermal power production in the Imperial Valley. Lawrence Livermore Laboratory, University of California, 38 pp.

Gudjónsdóttir S.R., Ilyinskaya E., Hreinsdóttir S., Bergsson B., Pfeffer M.A., Michalczewska K., Aiuppa A. and Óladóttir A.A. (2018). Gas emissions and crustal deformation from the Krýsuvík high temperature geothermal system, Iceland. Journal of Volcanology and Geothermal Research, In Press.

Guðmundsson G., Arnórsson S., Sigurmundsson S. G., Björnsson A., Gunnlaugsson E., Gíslason G., Jónsson J., Einarsson P. and Björnsson S. (1975).

The Krýsuvík area, report on geothermal observations (in Icelandic). Report OSJHD 7554, November 1975, 71 pp.

Guðmundsson A. (1983). The geology of the Krafla Sudurhlıdar field. On the status of the Krafla geothermal power station. Proceedings of Meeting Held in Akureyri, Iceland 2–3 March 1983, pp 86–101 (in Icelandic).

Guðmundsson A. (1987). Formation and mechanisms of magma reservoirs in Iceland. Geophys. J. R. astr. Soc. 91, 27-41.

Guðmundsson A. (1993a). Cross section between wells BJ-11 and BJ-12 in Bjarnarflag. National Energy Authority Report OS-93071/JHD-35 B, 46 pp (in Icelandic).

Guðmundsson A., Mortensen A. K, Hjartarson A., Karlsdottir R. and Armannsson H. (2010). Exploration and utilization of the Namafjall high temperature area in N-Iceland. In: Proceedings World Geothermal Congress 2010 Bali, Indonesia, 25- 29 April 2010, p. 9.

Guðmundsson A. (1995). Infrastructure and mechanics of volcanic systems in Iceland. J. Volcanol. Geotherm. Res., 64, 1–22.

Guðmundsson B. T. and Arnórsson S. (2002). Geochemical monitoring of the Krafla and Namafjall geothermal areas, N-Iceland. Geothermics 31, 195–243.

Guðmundsson O. (2003). The dense root of the Iceland crust. Earth Planet. Sci. Lett., 206, 427–440.

Gunnarsson-Robin J., Stefánsson A., Ono S. and Torssander P. (2017). Sulfur isotopes in Icelandic thermal fluids. Journal of Volcanology and Geothermal Research 346, 161–179.

Gurtin M.E. (1981). An introduction to continuum mechanics. Mathematics in Science and Engineering, 158.

Hardarson B. S. and Fitton J. G. (1997). Mechanisms of crustal accretion in Iceland, Geology, 25, 1043–1046.

Hangartner M. (2000). Limits and Advantages of Diffusion Sampling in Ambient Air Pollution Monitoring. 7th International Conference on Atmospheric Science and Applications to Air Quality, 31 October e 2 November 2000, Taipeh, Taiwan.

Hansell A. and Oppenheimer C. (2004). Health Hazards from Volcanic Gases: A Systematic Literature Review. Arch.Env. Health 59, 628-639.

Harðardóttir S., Halldórsson S. A. and Hilton D.R. (2017). Spatial distribution of helium isotopes in Icelandic geothermal fluids and volcanic materials with implications for location, upwelling and evolution of the Icelandic mantle plume. Chemical Geology, doi: 10.1016/j.chemgeo.2017.05.012.

Heber A., Bogan B., Ni J. Q., Lim T. T., Cortus E., Ramirez-Dorronsoro J., Diehl C., Hanni S., Xiao C., Casey K., Gooch C., Jacobson L., Koziel J., Mitloehner F., Ndegwa P., Robarge W., Wang L. and Zhang R. (2009). The National Air Emissions Monitoring Study: overview of barn sources, in: Livestock Environment VIII, Am. Soc. Ag. Bio. Eng., 1990–2206.

Henley R.W. and Ellis A.J. (1983). Geothermal systems ancient and modern: a geochemical review. Earth-Sci. Rev. 19, 1±50.

Henry R. C. and Hidy G. M. (1980). Potential for atmospheric sulphur from microbiological sulphate reduction. Atmospheric Environment 14, 1091-l103.

Hersir G. P., Björnsson A. and Pedersen L. B. (1984). Magnetotelluric survey across the active spreading zone in southwest Iceland. J. Volc. Geothermal Res. 20, 253– 265.

Hersir G. P., Björnsson G. and Björnsson A. (1990a). Volcanism and Geothermal Activity in the Hengill Area. Geophysical Exploration. Orkustofnun Report OS- 90031/JHD-06, Reykjavik, Iceland, 93 pp. (in Icelandic).

Hersir G.P., Björnsson G., Björnsson A. and Eysteinsson H. (1990b). Volcanism and Geothermal Activity in the Hengill Area. Geophysical Exploration – Resistivity Data. Orkustofnun Report OS-90032/JHD-16 B, Reykjavik, Iceland, 89 pp. (in Icelandic).

Hersir G., Árnason K. and Vilhjálmsson A. (2013). 3D inversion of magnetotelluric (MT) resis- tivity data from Krýsuvík high temperature geothermal area in SW Iceland. Proceed- ings, Thirty-eighth workshop on Geothermal Reservoir Engineering, Stanford University, Stanford, California, February 11–13, 2013. SGP-TR-198, p. 14.

Hitchcock D. (1977). Biogenic sulfur sources and air quality in the United States. Final Report, NSF Contract AEN- 7514571, Arthur, D. Little, Inc., Cambridge, Massachusetts.

Hitchcock D., Black M. S. and Herbst R. P. (1978). Sulfur isotope studies of biogenic sulfur emissions at Wallops Island, Virginia. Prepared for the National Science Foundation, Environmental.

Hjartardóttir Á. R., Einarsson P., Bramham E. and Wright T. J. (2012). The Krafla fissure swarm, Iceland, and its formation by rifting events, Bull. Volcanol., 74, 2139–2153. Research and Technology document P-2058, Concord, Massachusetts.

Hjartarson A., Sigurdsson O., Gudmundsson A., Armannsson H. and Karlsdottir R. (2004). A Numerical Simulation Model for the Namafjall Geothermal System and Predictions about its Reaction to 30-90 MW Power Production in Bjarnarflag (In Icelandic). Iceland GeoSurvey, ISOR 2004/009, p. 123.

Hobbs P. V., Tuell J. P., Hegg D. A., Radke L. F. and Eltgroth M. W. (1982). Particles and gases in the emissions from the 1980-81 eruptions of Mount St. Helens. J. Geophys. Res. 87, 11062–11086.

Hoffmann M. R. (1977). Kinetics and Mechanism of Oxidation of Hydrogen Sulfide by Hydrogen Peroxide in Acidic Solution. Environmental Science & Technology, Volume 11, Number 1, 61-66.

Honnorez J., Honnorez-Guerstein B., Vallette. J. and Wauschkuhn A. (1973). Present Day Formation of an Exhalative Sulfide Deposit at Vulcano (Tyrrhenian Sea). Part. II: Active Crystallization of Fumarolic Sulfides in the Volcanic Sediments of the Baia di Levante. In: Ores in Sediments, Amstutz G. C. and Bernard A. J. (eds.). Springer-Verlag, New York, 1973, p. 139-16.

Horrocks L. A., Oppenheimer C., Burton M.R. and Duffell H. J. (2003). Compositional variation in tropospheric volcanic gas plumes: evidence from ground- based remote sensing. In: Oppenheimer, C., Pyle, D.M., Barclay, J. (Eds.), Volcanic Degassing. Geological Society of London, pp. 349–369.

Horwell C. J., Paterson J. E., Gamble J. A. and Allen A. G. (2004). Monitoring and mapping of hydrogen sulphide emissions across an active geothermal field. J. of Volcanology and Geothermal Research, 139, 259-269.

Huang J., Lyman S.N., Hartman J.S. and Gustin M.S. (2014). A review of passive sampling systems for ambient air mercury measurements. Environ. Sci. Process. Impacts 16, 374-392.

Ilyinskaya E., Aiuppa A., Bergson B., Di Napoli R., Fridriksson T., Óladottir A. A., Óskarsson F., Grassa F., Pfeffer M., Lechner K., Yeo R. and Giudice G. (2015). Degassing regime of Hekla volcano 2012-2013. Geochim. Cosmochim. Acta 159, 80–99.

Isabyrie E. (1994). Borehole geology and hydrothermal alteration in well

B-9, Námafjall geothermal field, NE-Iceland. Report 5 in: Geothermal Training in Iceland 1994. UNU-GTP, Iceland, 89-121.

Italiano F. and Nuccio P. M. (1997). Variazioni del rapporto isotopico dell'elio nelle esalazioni fumaroliche di Vulcano, in: La Volpe, Dellino, Nuccio, Sbrana (Eds.), Progetto Vulcano: Risultati dell'Attivita' di Ricerca 1993–95, Felici Editore, Pisa, pp. 124–127.

Italiano F., Pecoraino G. and Nuccio P. M. (1997). Steam output from fumaroles of an active volcano: Tectonic and magmatic-hydrothermal controls on the degassing system at Vulcano (Aeolian arc). J. Geophys. Res., 103, 29, 829–842.

IUPAC Subcommittee on Gas Kinetic Data Evaluation for Atmospheric Chemistry (1989). Atkinson R., Baulch D. L., Cox R. A., Hampson R. F., Kerr J. A. and Troe J.. J. Phys. Chern. Ref. Data 18, 881.

Jaeschke W., Claude H., Herrmann J. and Vogler D. (1979). Messung und Verteilung von Schwefelwasserstoff in reiner und verunreinigter Atmosphere. Staub-Reinhalt. Luft 39, 174177.

Jaeschke W., Claude H. and Herrmann J. (1980). Sources and sinks of atmospheric H2S. J. geophys. Res. 85, 5639-5644.

Jaeschke W., Berresheim H. and Georgii H-W. (1982). Sulfur emissions from Mt. Etna. J. Geophys. Res. 87, 7253–7261.

Jakobsson S. P., Jonsson J. and Shido F. (1978). Petrology of the western Reykjanes Peninsula, Iceland. J. Petrol. 19, 669– 705.

Janni K. A., Jacobson L. D., Hetchler B. P., Oliver J. P. and Johnston L. J. (2014). Semi-Continuous Air Sampling versus 24-Hour Bag Samples to Evaluate Biofilters on a Swine Nursery in Warm Weather, Transactions of the American Society of Agricultural and Biological Engineers, 57, 1501–1515.

Jóhannesson H. and Saemundsson K. (1998). Geological map of Iceland. Bedrock geology, scale 1:500.000. Nátturufraedistofnun Islands, Reykjavík (2nd edition).

Jónsson J. (1968). Changes in the geothermal area at Reykjanes in 1967. National Energy Authority Report 10421 OST 5.

Kaasalainen H. and Stefánsson A. (2012). The chemistry of trace elements in surface geothermal water and steam, Iceland. Chem. Geol. 330–331, 60–85.

Kaasalainen H., Stefánsson A., Giroud N. and Arnórsson S. (2015). The geochemistry of trace elements in geothermal fluids, Iceland. Appl. Geochem. 62, 207–223.

Kärcher B., Hirschberg M. M. and Fabian P. (1996). Small-scale chemical evolution of aircraft exhaust species at cruising altitudes. J. Geophys. Res. 101, 15169–15190.

Keller J. (1970). Studio geovulcanologico delle isole di Salina e Vulcano e carta geologica. Rapp. Tecrk, Ist. Int, Vulcan., C.N.R. Catania.

Keller J. (1980). The Island of Vulcano. Rend. Soc. Ital. Mineral. Petrogr., 36, 369-414.

Klanova J., Kohoutek J., Hamplova L., Urbanova P., Holoubek I. (2006). Passive air sampler as a tool for long-term air pollution monitoring: Part 1. Performance assessment for seasonal and spatial variations. Environ. Pollut. 144, 393e405. http://dx.doi.org/10.1016/j.envpol.2005.12.048.

Kourtidis K., Kelesis A., Maggana M. and Petrakakis M. (2004). Substantial traffic emissions contribution to the global H_2S budget. Geophys. Res. Lett. 31, L18107.

Kourtidis K., Kelesis A. and Petrakakis M. (2008). Hydrogen sulfide (H_2S) in urban ambient air. Atmospheric Environment 42, 7476 -7482.

Kristmannsdóttir H. and Armannsson H. (1999). Environmental studies of Iceland's unexploited geothermal areas. Geothermal Resources Council Bulletin 28, 25–28.

Kristmannsdóttir H. and Ármannsson H. (2004). Groundwater in the Lake Mývatn area, northern Iceland. Chemistry, Origin and Interaction, Aquatic Ecology, 115-128.

Krupa S. V. and Legge A. H. (2000). Passive sampling of ambient, gaseous air pollutants: an assessment from an ecological perspective. Environ. Pollut. 107, 31-45.

Lafage C., Pauwels J. F., Carlier M. and Devolder P. (1987). Rate constant for the reaction OH + H_2S in the range 243–463 K by discharge-flow laser-induced fluorescence. J. Chern. Soc. Faraday Trans. 2, 83, 731.

Larsen R. I. (1971). A mathematical model for relating air quality measurements to air quality standards. U.S. Environmental Protection Agency, Research Triangle Park, NC, Publication No. AP-89, November.

Larsen G., Gronvold K. and Thorarinsson S. (1978). Volcanic eruption through a geothermal borehole at Námafjall, Iceland. Nordic Volcanological Institute, Science Institute, Reykjavik, report RH-78-10, 22 pp.

Larson E.W.F. and Ekström, G. (2001). Global models of surface wave group velocity. Pure Appl. Geophys. 158 (8), 1377-1400.

Lee H.F., Yang T.F., Lan T.F., Song S.R. and Tsao S. (2005). Fumarolic gas composition of the Tatun volcano group, northern Taiwan. TAO. 16, pp. 843–864.

Leu M. T. and Smith R. H. (1982). Rate constants for the gas-phase reaction between hydroxyl and hydrogen sulphide over the temperature range 228-518 K. J. phys. Chem. 86, 73-81.

Levy H. (1971. Normal atmosphere, Large radical and formaldehyde concentrations predicted. Science 173, 141-143.

Levy H. (1973). Photochemistry of minor constituents of the troposphere. J. Atmos. Sci.

Libbey R. B. and Williams-Jones A. E. (2016). Relating sulfide mineral zonation and trace element chemistry to subsurface processes in the Reykjanes geothermal system, Iceland. Journal of Volcanology and Geothermal Research, 310: 225–241.

Li W., Powers W. and Hill G. M. (2011). Feeding Distillers Dried Grains with Solubles and Organic Trace Mineral Sources to Swine and the Resulting Effect on Gaseous Emissions, J. Anim. Sci., 89, 3286–3299.

Lim T. T., Jin Y., Ni J. Q., and Heber A. J. (2012). Field Evaluation of Biofilters in Reducing Aerial Pollutant Emissions from a Com- mercial Pig Finishing Building, Biosyst. Eng., 112, 192–201.

Lin X. J., Cortus E. L., Zhang R., Jiang S. and Heber A. J. (2012). Ammonia, Hydrogen Sulfide, Carbon Dioxide and Particulate Mat- ter Emissions from California High-Rise Layer Houses, Atmos. Environ., 46, 81–91.

Lin Y. L., Wang N.S. and Lee Y. P. (1985). Temperature dependence of the rate constant for the reaction OH + H_2S in He, N_2, and O_2. Int. J. Chem. Kinet. 17, 1201.

Liu C., Liu J., Li J., He H., Peng S., Li C. and Chen Y. (2013). Removal of H_2S by Co-Immobilized Bacteria and Fungi Biocatalysts in a Bio-Trickling Filter, Process Saf. Environ., 91, 145– 152.

Liu Z., Powers W., Oldick B., Davidson J., and Meyer D. (2012). Gas Emissions from Dairy Cows Fed Typical Diets of Midwest, South, and West Regions of the United States, J. Environ.l Qual., 41, 1228–37.

Lonker S.W., Franzson H. and Kristmannsdóttir H. (1993). Mineral-fluid interactions in the Reykjanes and Svartsengi geothermal systems, Iceland. Amer. J. Sci. 293, 605-670.

Mango F., Jarvie D. and Herriman E. (2009). Natural gas at thermodynamic equilibrium. Implications for the origin of natural gas. Geochem. Trans., 10(6), doi: 10.1186/1467-4866-10-6.

Mather T. A., Allen A. G., Oppenheimer C., Pyle D. M. and McGonigle A. J. S. (2003). Size-resolved characterisation of soluble ions in the particles in the tropospheric plume of Masaya volcano, Nicaragua: origins and plume processing. Journal of Atmospheric Chemistry 46, 207–237.

Marani M., Tole M. and Ogalo L. (2000). Concentrations of H2S in air around the Olkaria geothermal field, Kenya. Proceedings World Geothermal Congress 2000, Kyushu-Tohoku, Japan, 649-661.

Marini L., Moretti R. and Accornero M. (2011). Sulfur Isotopes in magmatic-hydrothermal systems, melts and magmas. Reviews in Mineralogy and Chemistry, Vol. 73 pp. 423-492.

Martin D., Ardouin B., Bergametti G., Carbonelle J., Faivre-Pierret R., Lambert G., and Le Cloarec M. F. (1986). Geochemistry of sulfur in Mt. Etna plume. J. Geophys. Res. 91, 12249–12254.

Martini M., Cellini Legittimo P., Piccardi G. and Giannini L. (1986). The fumaroles of Vulcano (Italy): differences in chemical compositions produced by the surface environment. Geothermics, 15, 205-209.

Marty B., Gunnlaugsson E., Jambon A., Óskarsson N., Ozima M., Pineau F. and Torssander P. (1991). Gas geochemistry of geothermal fluids, Hengill area, southwest rift zone of Iceland. Chem. Geol. 91, 207-225.

Matsuo S. (1961). On the chemical nature of fumarolic gases of Vulcano Showashinzan, Hokkaido, Japan. J. Earth Sci. Nagoya Univ., 8, 80-100.

Mazor E., Cioni R., Corazza E., Fratta M., Magro G., Matsuo S., Hirabayashi J., Shinohara H., Martini M., Piccardi G. and Cellini P. (1988). Evolution of fumarolic gases–boundary conditions set by measured parameters: Case study at Vulcano, Italy. Bull. Volcanol. 50, 71-85.

Mazzuoli R., Tortorici L. and Ventura G. (1995). Oblique rifting in Salina, Lipari and Vulcano islands (Aeolian islands, southern Italy). Terra Nova 7:444-452.

Melián G., Tassi F., Pérez N., Hernández P., Sortino F., Vaselli O., Padrón E., Nolasco D., Barrancos J., Padilla G., Rodríguez F., Dionis S., Calvo D., Notsu K. and Sumino H. (2012). A magmatic source for fumaroles and diffuse degassing from the summit crater of Teide Volcano (Tenerife, Canary Islands): a geochemical evidence for the 2004-2005 seismic-volcanic crisis. Bullettin of Volcanology, vol. 74, issue 6, pp 1465-1483.

McDougall J.W.G. and Garland T.O. (1954). Hydrogen sulphide gas poisoning at Rotorua. The New Zealand Medical Journal 53, 471–475.

McGonigle A. J. S., Oppenheimer C., Tsanev V.I., Saunders S., Mulina K., Tohui S., Bosco J., Nahou J., Kuduon J. and Taranu F. (2004). Sulphur dioxide fluxes from Papua New Guinea's volcanoes. Geophys. Res. Lett. 31, L08606.

McKeen S. A., Liu S. C. and Kiang C. S. (1984). On the chemistry of stratospheric SO_2 from volcanic eruptions. Journal of geophysical research, vol. 89, NO. D3 pages 4873-4881, June 20, 1984.

Michalczewska K., Hreinsdottir S., Arnadottir T., Hjaltadottir S., Agustsdottir T., Gudmundsson M. T., Geirsson H., Sigmundsson F. and Gudmundsson G. (2012=. Inflation and Deflation Episodes in the Krisuvik Volcanic System, Abstract V33A-2843, Am. Geophys. Un. Fall Meeting, San Francisco, December 2012.

Minissale A., Evans W. C., Magro G. and Vaselli O. (1997). Multiple source components in gas manifestations from north-central Italy. Chem. Geol., 142, 175-192.

Mizutani Y. and Sugiura T. (1966). The chemical equilibrium of the $2H_2S + SO_2 = 3S + 2H_2O$ reaction in solfataras of the Nasudake volcano. Bulletin of the Chemical Society of Japan, Vol. 39, 2411-2414.

Montegrossi G., Tassi F., Vaselli O., Buccianti A. and Garofalo K. (2001). Sulfur species in Volcanic Gases. Anal. Chem., 73, No. 15, 3709-3715.

Möller D. (1980). Kinetic model of atmospheric SO2 oxidation based on published data. Atmos. Environ. 14, 1067–1072.

Moretti R., Papale P., and Ottonello G. (2003). A model for the saturation of C-O-H-S fluids in silicate melts. In Volcanic Degassing, Special Publication 213 (ed. C. Oppenheimer et al.) pp. 81–101. Geological Society of

London.

Moreira D.M. and De Almeida Albuquerque T.T. (2016). Solution of the atmospheric diffusion equation with longitudinal wind speed depending on the source distance. Rev. Bras. Metereol., 31, 202-210.

Mortensen A., Egilson T., Gautason B., Gunnarsson H. and Ingólfsson T. (2008). Bjarnarflag-well BJ-14. 3rd stage: Drilling of production section from 847 m to 2506 m depth. ÍSOR – Iceland GeoSurvey, Reykjavik, report ÍSOR -2008/039 (in Icelandic).

NASA Panel for Data Evaluation, Chemical Kinetics and Photochemical Data for Use in Stratospheric Modeling (1990). Evaluation Number 9, De-More W. B., Sander S. P., Goldn D. M., Molina M. J., Hampson R. F., Kurylo M. J., Howard C. J. and Ravishankara A. R., JPL Publication 90-1.

Nash J. E. and Sutcliffe J. V. (1970). River flow forecasting through conceptual models, Part I - A discussion of principles. J. Hydrol., 10, 282-290.

Nash D.G. and Leith, D. (2010). Use of passive diffusion tubes to monitor air pollutants. J. Air & Waste Manag. Assoc. 60, 204-209. http://dx.doi.org/10.3155/1047-3289.60.2.204.

National Energy Authority (2014). The Resource. Viewed 08.09.2014 from http://www.nea.is/geothermal/the-resource/.

Ni J. Q., Chai L., Chen L., Bogan B. W., Wang K., Cortus E. L., Heber A. J., Lim T. T., and Diehl C. (2012). Characteristics of Ammonia, Hydrogen Sulfide, Carbon Dioxide, and Particulate Matter Concentrations in High-Rise and Manure-Belt Layer Hen Houses, Atmos. Environ., 57, 165–174.

Nicholson K. (1993). Gas chemistry. In Nicholson K., Geothermal fluids chemistry and ezploration techniques. Berlin Heidelberg Springer-Verlag, 87-117.

NIST(2005). NIST/EPA/NIH Mass Spectral Library, 2005.

Norrish R. G. W. and Zeelenberg A. P. (1957). The combustion of hydrogen sulphide studied by flash photolysis and kinetic spectroscopy. Proc. R. Soc. A240, 292-303.

Norton D. and Knight J. (1977). Transport phenomena in hydrothermal systems: cooling plutons. Am. J. Sci. 277, 937–981.

Ólafsdóttir S. (2007). Modelling of hydrogen sulphide concentration in Reykjavík city due to emissions from geothermal power plants. University of Iceland, MSc thesis, web page: www.verk.hi.is/page/msub0701, 114 pp.

Ólafsdóttir, S. and Gardarsson, S.M. (2013). Impacts of meteorological factors on hydrogen sulfide concentration downwind of geothermal power plants. Atmospheric Environment 77, 185-192.

Ólafsdóttir S., Gardarsson S.M. and Andradóttir H.O. (2014). Spatial distribution of hydrogen sulfide from two geothermal power plants in complex terrain. Atmospheric Environment 82, 60-70.

Oppenheimer C. (1992). Sulphur eruptions at Volcan Poas, Costa Rica. J. Volcan. Geotherm. Res, 49, 1-21.

Oppenheimer C., Francis P. and Stix J. (1998b). Depletion rates of sulfur dioxide in tropospheric volcanic plumes. Geophys. Res. Lett. 25, 2671–2674.

Oppenheimer C. (2003a). Climatic, environmental, and human consequences of the largest known historic eruption: Tambora volcano (Indonesia) 1815. Prog. Phys. Geogr. 27, 230–259.

Óskarsson N., Steinthorsson S. and Sigvaldason G. E. (1985). Icelandic geochemical anomaly: origin, volcano-tectonics, chemical fractionation and isotopic evolution of the crust. J. geophys. Res. 90, 10011-10025.

Ott W. R. (1990). A physical explanation of the log-normality of pollutant concentrations. Journal of Air & Waste Management Associaties, 40 (10), 1378 – 1383.

Pálmason G. and Sæmundsson K. (1974). Iceland in relation to the Mid-Atlantic Ridge. Ann. Rev. Earth Plan. Sci. 2, 25-50.

Pálmason G., Johnsen G. V., Torfason H., Saemundsson K., Ragnars K., Haraldsson G. I. and Halldorsson G. K. (1985). Evaluation of geothermal resources in Iceland. National Energy Authority Report OS-85076/JHD-10, 134 pp. (in Icelandic).

Palsson S. (1945). Ferdabok (Travel book), Snaelandsutgafa.

Parungo F., Kopcewicz B., Nagamoto C., Schnell R., Sheridan P., Zhu C. and Harris J. (1992). Aerosol particles in the Kuwait oil fire plumes: Their morphology, size distribution, chemical composition, transport, and potential effect on climate. J. Geophys. Res. 97: 15867-15882.

Pavilonis B.T., O'Shaughnessy P.T., Altmaier R., Metwali N., Thorne P.S. (2013). Passive monitors to measure hydrogen sulfide near concentrated animal feeding operations. Environ. Sci. Process. Impacts 15 (6), 1271-1278.

Peate D. W., Baker J. A., Jakobsson S. P., Waight T. E., Kent A. J. R.,

Grassineau N. V., Skovgaard A. C. (2009). Historic magmatism on the Reykjanes Peninsula, Iceland: a snap shot of melt generation at a ridge segment. Contrib. Mineral. Petrol. 157, 359-382.

Penner J.E., Andreae M., Annegarn H., Barrie L., Feichter J., Hegg D., Jayaraman A., Leaitch R., Murphy D., Nganga J. and Pitari G. (2001). Aerosols, their direct and indirect effects. In: Climate Change 2001: The Scientific Basis. Contribution of Working Group I to the Third Assessment Report of the Intergovernmental Panel on Climate Change [Houghton, J.T., Y. Ding, D.J. Griggs, M. Noguer, P.J. van der Linden, X. Dai, K. Maskell, and C.A. Johnson (Eds.)]. Cambridge University Press, Cambridge, United Kingdom and New York, NY, USA, 881 pp.

Perry R. A., Atkinson R. and Pitts J. (1976). Rate constants for the reactions OH + H2S → H_2S + SH and OH + NH_3 → H_2O + NH_2 over the temperature range 297-427 K. The Journal of Chemical Physics. Vol. 64. No. 8.

Piccardi G. (1982). Fumaroles Gas Collection and Analysis. Bull. Volcanol., Vol. 43-3.

Pope E. C., Bird D. K., Arnórsson S., Fridriksson T., Elders W. A. and Friðleifsson G. Ó. (2009). Isotopic constraints on ice age fluids in active geothermal systems: Reykjanes, Iceland. Geochim. Cosmochim. Acta 73, 4468–4488.

Pope E. C., Bird D. K. and Arnorsson S. (2013). Evolution of low-18O Icelandic crust. Earth and Planetary Science Letters, 374, 47–59.

Pope E. C., Bird D. K. and Arnorsson S. (2014). Stable isotopes of hydrothermal minerals as tracers for geothermal fluids in Iceland. Geothermics, 49, 99–110.

Poreda R., Craig G., Arnorsson S. and Welhan J. (1992). Helium isotopes in Icelandic geothermal systems. Geochim. Cosmochim. Acta 56, 4221-4228.

Porter J. N., Horton K. (2002). Sun photometer and lidar measurements of the plume from the Hawaii Kilauea volcano Pu'u O'o vent: aerosol flux and SO2 lifetime. Geophysical Research Letters, 28.

Ragnars K., Saemundsson K., Benediktsson S. and Einarsson S. S. (1970). Development of the Namafjall area - northern Iceland. Geothermics 2, 925–936.

Ravishankara A. R. (1997). Heterogeneous and multiphase chemistry in the troposphere. Science 276, 1058–1065.

Reimann C. and Filzmoser P. (1999). Normal and log-normal data distribution in geochemistry: death of a myth. consequences for the statistical tretment of geochemical and environmental data. Environmental Geology, 39 (9), 1001–1014.

Richards M. A., Duncan R. A. and Courtillot V. E. (1989). Flood basalts and hot-spot tracks: plume heads and tails. Science 246, 103–107.

Robock A. (2000). Volcanic eruptions and climate. Rev. Geophys. 38(2), 191–219.

Robock A. and Oppenheimer C. (2003). Volcanism and the Earth's Atmosphere, AGU Geophysical Monograph, 139. American Geophysical Union.

Rosi M. and Santacroce R. (1984). Volcanic hazard assessment in the Phlegrean Fields: a contribution based on stratigraphic and hysterical data. Bull. Volcanol. 47, 359– 370.

Saemundsson K. (1979). Outline of the geology of Iceland. Jökull 29, 7-28.

Saemundsson K. and Einarsson S. (1980). Geological map of Iceland 1:250.000. Sheet 3, 2nd ed. Museum of Natural History and Iceland Geodetic Survey.

Saemundsson K. (1991). Geology of the krafla system (In icelandic). In: Gardarsson, A, Einarsson, P (Eds.), Nattúra Mývatns (The Natural History of Lake Mývatn). The Icelandic Natural History Society, Reykjavík, pp. 24-95.

Saemundsson K. (2006). The 1789 rifting event in the Hengill volcanic system, SW-Iceland. Am Geophys Union, Fall Meeting, Abstract T41B-1568.

Saemundsson K. (2011). Geological map of Western Reykjanes Peninsula. Iceland GeoSurvey and HS Orka hf. 1:50,000/1:18,000, 1 sheet.

Saemundsson K. and Sigurgeirsson M. Á. (2013). The Reykjanes Peninsula. In Sólnes, J (editor in chief)., Sigmundsson F., Bessason B. 2013. Natural hazards in Iceland, volcanic eruptions and earthquakes (in Icelandic). Reykjavík, Viðlagatrygging Íslands/Háskólaútgáfan, 379-403.

Samarskii A. A. and Tikhonov A. N. (1963). Equations of Mathematical Physics. International Series of Monographs on Pure and Applied Mathematics, vol. 39. Pergamon Press.

Sander R. (2015). Compilation of Henry's law constants (version 4.0) for water as solvent. Atmos. Chem. Phys., 15, 4399–4981.

Santo A. P., Chen Y., Clark A. H., Farra E. and Tsegaye A. (1995). 40Ar/39Ar ages of the Filicudi Island volcanics: Implication for the volcanogical history of the Aeolian Arc, Italy, Acta Vulcanol., 7, 13-18, 1995.

Scaillet B., Clemente B., Evans B. W., and Pischavant M. (1998). Redox control on sulfur degassing of silicic magmas. J. Geophys. Res. 103, 23937–23949.

Schuler J., Greenfield T., White R. S., Roecker S. W., Brandsdóttir B., Stock J. M., Tarasewicz J., Martens H. R. and Pugh D. (2015). Seismic imaging of the shallow crust beneath the Krafla central volcano, NE Iceland. J. Geophys. Res. Solid Earth, 120, 7156–7173.

Schwandner F. M., Seward T. M., Gize A. P., Hall A. and Dietrich V. J. (2013). Halocarbons and other trace heteroatomic organic compounds in volcanic gases from Vulcano (Aeolian Islands, Italy). Geochim. Cosmochim. Ac., 101, 191-221, doi: 10.1016/j.gca.2012.10.004.

Scott S., Gunnarsson I., Arnorsson S. and Stefansson A. (2013). Gas chemistry, boiling and phase segregation in a geothermal system, Hellisheidi, Iceland. Geochimica et Cosmochimica Acta 124: 170–189.

Seinfeld J. H. and Pandis S. N. (1998). Atmospheric Chemistry and Physics: From Air Pollution to Climate Change, John Wiley and Sons, New York.

Servant J. and Delapart M. (1982). Daily variations of the H2S content in atmospheric air at ground-level in France. Atmospheric Environment 16, 1047-1052.

Sethi D. S. (1971). Photo-oxidation of sulfur dioxide. J. Air Pollut. Control Ass. 21, 418-420.

Shooter D., Watts S.F. and Hayes J. (1995). A passive sampler for hydrogen sulfide. Environ. Monit. Assess. 38, 11-23.

Sicardi L. (1955). Captazione ed analisi chimica dei gas della esalazione solfidrico-solforosa dei vulcani in fase solfatarica. Bull. Volcanol. 17, 107–112.

Sidebottom H. W., Badcock C. C, Jackson G. E., Calvert J. G., Reinhardt G. W. and Damon E. K. (1972b). Photooxidation of sulfur dioxide. Envir. Sei. Technol. 6, 72-79.

Sigmundsson F., Vadon H. and Massonnet D. (1997). Readjustment of the Krafla spreading segment to crustal rifting measured by satellite radar interferometry. Geophys. Res. Lett. 24 (15), 1843–1846.

Sigurðsson F. (1986). Hydrogeology and groundwater on the Reykjanes Peninsula. Jokull 36, 11–29.

Sigurðsson H. (1990). Assessment of the atmospheric impact of volcanic eruptions. In Sharpton V. L., and Ward P. D., eds., Global catastrophies in Earth history: Geological Society of America Special Paper 247, p. 99-110.

Sigurðsson O. (1993). The geothermal system in Bjarnaflag. Evaluation of temperature, pressure and well productivity. National Energy Authority Report OS-93016/JHD-08 B, 45 pp (in Icelandic).

Sigurðsson O. (2010). The Reykjanes seawater geothermal system — its exploitation under regulatory constraints. Proc. World Geothermal Congress (7 pp.).

Sigurðsson H., Houghton B., McNutt S., Rymer H. and Stix J. (2015). The Encyclopedia of Volcanoes, second ed. Academic Press.

Somma R., Granieri D., Troise Cl., Terranova C., De Natale G., Pedone M. (2017). Modelling of hydrogen sulfide dispersion from the geothermal power plants of Tuscany (Italy). Science of the Total Environment, In Press.

Sommaruga C. (1984). Le ricerche geotermiche svolte a Vulcano negli anni '50. Rend. Soc. ltaliana Mineral. Petrol 39, 355-366.

Spedding D. J. and Cope D. M. (1984). Field measurements of hydrogen sulfide oxidation. Atmospheric Environment 18, 1791- 1795.

Sprung J. L. (1977), Tropospheric oxidation of H_2S. Advances in environmental science and technology.

Stefánsson V. (1981). The Krafla geothermal field, North-east Iceland. In: L. Rybach and L.J.P. Muffler (Editors), Geothermal Systems: Principles and Case Histories, Ch. 10. Wiley, New York, N.Y., pp. 273-294.

Stefánsson A. and Arnórsson S. (2002). Gas pressures and redox reactions in geothermal fluids in Iceland. Chem. Geol. 190, 251–271.

Stefánsson A., Keller N. S., Gunnarsson-Robin J. and Ono S. (2015). Multiple sulfur isotope systematics of Icelandic geothermal fluids and the source and reactions of sulfur in volcanic geothermal systems at divergent plate boundaries. Geochim. Cosmochim. Acta 165, 307–323.

Stefánsson A., Keller N. S., Gunnarsson-Robin J., Kaasalainen H., Björnsdóttir S., Pétursdóttir S., Jóhannesson H., and Hreggvidsson G.Ó. (2016b). Quantifying mixing, boiling, degassing, oxidation and reactivity of thermal waters at Vonarskard, Iceland. J. Volcanol. Geotherm. Res. 309, 53–62.

Steingrimsson S B., Gudmundsson As., Sigurdsson O. and Gunnlaugsson E. (1986a). Nesjavellir–well NJ-11. National Energy Authority Report OS86025/JHD-05, 60pp. (in Icelandic).

Steingrimsson B., Fridleifsson G. O., Sverrisdottir G., Tulinius H., Sigurdsson O. and Gunnlaugsson E. (1986b). Nesjavellir, well NJ-15, Drilling, investigations and production characteristics. National Energy Authority Report OS-86029/JHD-09, 119pp. (in Icelandic).

Stevenson D. S., Johnson C. E., Collins W. J. and Derwent R. G. (2003). The tropospheric Sulphur Cycle and the role of Volcanic SO_2. Geological Society, London, Special Publications, 213, 295-305.

Stockwell W. R. and Calvert J. G. (1983). The mechanism of the HO-SO2 reaction. Atmos. Environ. 17, 2231-2235.

Stoiber R. E., Malinconico L. L., Williams S. N. (1983). Use of the correlation spectrometer at volcanoes. In: Tazieff, H., Sabroux, J.C. (Eds.), Forecasting Volcanic Events. Elsevier, Amsterdam, pp. 425–444.

Stuhl F. (1974). Determination of the rate constant for the reaction OH + H2S by a pulsed photolysis-resonance fluorescence method. Ber. Bunsenges. Phys. Chem. 78, 230-232.

Sveinbjörnsdóttir A.E., Coleman M.L. and Yardley B. W. D. (1986). Origin and history of hydrothermal fluids of the Reykjanes and Krafla geothermal fields, Iceland - a stable isotope study. Cont. Min. Petrol. 94, 99-109.

Symonds R. B., Rose W. I., Bluth G. J. S. and Gerlach T. (1994). Volcanic-gas studies: methods, results, and applications. In: Carroll, M.R., Holloway, J.R. (Eds.), Volatiles in Magmas. Reviews in Mineralogy, vol. 30. Mineralogical Society of America, pp. 1–66.

Symonds R., Mizutani Y. and Briggs P. H. (1996). Long term geochemical surveillance of fumaroles of Showa-Shinzan dome, Usu volcano, Japan. J. Volcanol. Geotherm. Res. 73, 177–211.

Symonds R., Gerlach T. M., and Reed M. H. (2001). Magmatic gas scrubbing: Implications for volcano monitoring, J. Volcanol. Geotherm. Res., 108, 303–341.

Tang H., Sandeluk J., Lin L. and Lown J.W. (2002). A new all-season passive sampling system for monitoring H_2S in air. Sci. World J. 2, 155-168. http://dx.doi.org/ 10.1100/tsw.2002.87.

Taran Y. A. and W. F. Giggenbach (2003). Geochemistry of light hydrocarbons in subduction-related volcanic and hydrothermal uids. In: Volcanic, Geothermal, and Ore-Forming Fluids: Rulers and Witnesses of Processes Within the Earth, Spec. Publ., 10, S. F. Simmons and I. J. Graham (Eds.), Soc. of Econ. Geol., Littleton, Colorado, 61–74.

Tassi F., Vaselli O., Capaccioni B., Macias J. L., Nencetti A., Montegrossi G., Magro G. (2003). Chemical composition of fumarolic gases and spring discharges from El Chicho'n volcano, Mexico: causes and implications of the changes detected over the period 1998-2000. Journal of Volcanology and Geothermal Research 123, 105-121.

Tassi F., (2004). Fluidi in ambiente vulcanico: Evoluzione temporale dei parametri composizionali e distribuzione degli idrocarburi leggeri in fase gassosa. Ph.D. thesis, Univ. of Florence, Florence, Italy, pp. 292 (in Italian).

Tassi F., Capaccioni B., Capecchiacci F. and Vaselli O. (2009). Non-methane Volatile Organic Compounds (VOCs) at El Chichón volcano (Chiapas, México): Geochemical features, origin and behavior. Geofísica Internacional 48 (1), 85-95.

Tassi F., Capecchiacci F., Buccianti A. and Vaselli O. (2012c). Sampling and analytical procedures for the determination of VOCs released into air from natural and anthropogenic sources: A comparison between SPME (Solid Phase Micro Extraction) and ST (Solid Trap) methods. Applied Geochemistry 27, 115–123.

Tedesco D. (1995). Fluid geochemistry at Vulcano Island: A change in the volcanic regime or continuous fluctuations in the mixing of different systems?. J. Geophys. Res., 100, 4157–4167.

Thermo Fisher Scientific: Model 450i – Instruction Manual, 2008.

Thordarson T. and Larsen G. (2007). Volcanism in Iceland in historical time: Volcano types, eruption styles and eruptive history. J. Geodyn. 43, 118-152.

Thorkelsson T. (1925). On thermal activity in Iceland and geyser action. Soc. Sci. Isl. XXV, 139. Reykjavik.

Thornton D.C., Bandy A.R., Blomquist B.W., Davis D. D. and Talbot R.W (1996). Sulfur dioxide as a source of condensation nuclei in the upper troposphere of the Pacific Ocean. J. Geophys. Res, 101, 1883-1890.

Thorsteinsson T., Hackenbruch J., Sveinbjörnsson E. and Jóhannsson T. (2013). Statistical Assessment and Modeling of the Ef- fects of Weather Conditions on H2S Plume Dispersal from Ice- landic Geothermal Power Plants, Geothermics, 45, 31–40.

Thunell R., Federman A., Sparks S., Williams D. (1979). The origin and volcanological significance of the Y-5 ash layer in the Mediterranean. Quat. Res. 12, 241–253.

Todesco M. (1997). Origin of fumarolic fluids at Vulcano (Italy). Insights from isotope data and numerical modeling of hydrothermal circulation. J. Volcanol. Geotherm. Res. 49 (1997) 63–85.

Todesco M., Chiodini G. and Macedonio G. (2003). Monitoring and modelling hydrothermal fluid emission at La Solfatara (Phlegrean Fields, Italy); an interdisciplinary approach to the study of diffuse degassing, J. Volcanol. Geotherm. Res., 125, 57-79.

Trønnes R. G. (2012). Basaltic melt evolution of the Hengill Volcanic System, SW Iceland, and evidence for clinopyroxene assimilation in primitive tholeiitic magmas. J. Geophys. Res. 95, 15893-15910.

Tryggvason K., Husebye E. S. and Stefánsson R. (1983). Seismic image of the hypothesized Icelandic hot spot. Tectonophys. 100, 97-118.

Tryggvason A., Rögnvaldsson S.Th. and Flóvenz Ó.G. (2002). Three dimensional imaging of P- and S-wave velocity structure and earthquake locations beneath Southwest Iceland. Geophys. J. Int. 151, 848–866.

Urone P., Schroeder W. H. and Miller S. R. Reactions of sulfur dioxide in air. In Proc. 2nd IUAPPA Clean Air Congress, Washington D.C., December 1970, Academic Press, New York, 1971, pp. 370-374.

US Environmental Protection Agency (EPA) (2003). Toxicological review of hydrogen sulfide. EPA/635/R-03/005. Washington, DC.

Vaselli O., Tassi F., Duarte E., Fernandez E., Poreda R. J. and Delgado Huertas A. (2010). Evolution of fluid geochemistry at the Turrialba volcano (Costa Rica) from 1998 to 2008. Bull Volcanol, 72: 397–410.

Ventura G. (1994). Tectonics, structural evolution and caldera formation in Vulcano Island (Aeolian Archipelago, southern Tyrrhenian Sea). J. Volcanol. Geotherm. Res., 60, 207-224, 1994.

Vink G. E., Morgan, W. J. and Vogt P. R. (1985). The earth's hot spots. Sci. Am. 252, 50-57.

Walker C. L. (1992). The volcanic history and geochemical evolution of the Hveragerdi region, SW Iceland. Ph.D. thesis, Univ. Dur- ham, 365 pp.

Wallace J. M. and Hobbs P. V. (2006). Atmospheric Science. An introductory survey (2nd ed). Canada: Academic Press.

Wang D. K. W. and Austin C. C. (2006). Determination of complex mixtures of volatile organic compounds in ambient air: an overview. Anal. Bioanal. Chem., 386: 1089–1098.

Ward Alter H., Oswald R. A. (1983). Results of indoor radon measurements using the track etch method. Health Physics, 45: 425.

Ward P. L. and Björnsson S. (1971). Microearthquakes, swarms, and the geothermal areas of Iceland. J. Geophys. Res. 76, 3953-3982.

Watanabe T., Yoshida M., Fujiwara S., Abe K., Onoe A., Hirota M. and Igarashi S. (1982). Spin trapping of hydroxyl radicals in the troposphere for determination by electron spin resonance and gas chromatography/mass spectrometry. Analyl. Chem. 54, 2470-2474.

Wesely M. L. and Hicks B. B. (2000). A review of the current status of knowledge on dry deposition. Atmospheric Environment, 34, 2261-2282.

WHO (2000). Air quality guidelines for Europe, second ed. WHO Regional Publications. European Series, No. 91.

WHO (2003). Hydrogen Sulfide: Human Health Aspects. Concise International Chemical Assessment Document 53. World Health Organization, Geneva, Switzerland.

Williams-Jones G. and Reimer H. (2015). Hazards of Volcanic Gases. The Encyclopedia of Volcanoes, second ed. Elsevier Inc, pp. 985-992.

Wine P. H., Kreutter N. M., Gump C. A. and Ravishankara A. R. (1981). Kinetics of OH reactions with the atmospheric sulphur compounds H2S, CH3SH, CH3SCH3 and CH3SSCH3. J. phys. Chem. 85, 2660-2665.

Witham C. S. (2005). Volcanic disasters and incidents: a new database. Journal of Volcanology and Geothermal Research 148, 191–233.

Xie Z. D. (1992). Formation mechanism of condensation nuclei in nighttime atmosphere and the kinetics of the sulfur dioxide-ozone-nitrogen dioxide system. J. Phys. Chem., 96 (4), pp 1543–1547.

Yin F., Grosjean D. and Seinfeld J. (1990). Photooxidation of dymethyl sulfide and dimethyl disulfide. I: mechanism development. Journal of Atmospheric Chemistry 11: 309-364.

Yu Z., Jang M. and Park J. (2017). Modeling atmospheric mineral aerosol chemistry to predict heterogeneous photooxidation of SO_2. Atmos. Chem. Phys., 17, 10001–10017.

Zabiegala B., Urbanowicz M., Szymanska K. and Namiesnik J. (2010). Application of passive sampling technique for monitoring of BTEX concentration in urban air: field comparison of different types of passive samplers. J. Chromatogr. Sci. 48, 167-175.

Zhang Q. and Tie X. (2011). High solubility of SO_2: evidence in an intensive fog event measured in the NCP region, China. Atmos. Chem. Phys. Discuss., 11, 2931–2947.

Zierenberg R. A., Schiffman P., Barfod G. H., Lesher C. E., Marks N. E., Lowenstern J. B., Mortensen A. K., Pope E. C., Bird D. K., Reed M. H., Fridleifsson G. O. and Elders W. A. (2013). Composition and origin of rhyolite melt intersected by drilling in the Krafla geothermal field, Iceland. Contributions to Mineralogy and Petrology, 165, 327–47.